Dissertation zur Erlangung des Doktorgrades

der Fakultät für Chemie und Pharmazie

der Ludwig-Maximilians-Universität München

Advancing DNA-PAINT super-resolution microscopy to uncover the structural basis of membrane receptor biology

Isabelle Rita Sophie Pachmayr (geb. Baudrexel)

aus

Gräfelfing, Deutschland

2025

Erklärung

Diese Dissertation wurde im Sinne von § 7 der Promotionsordnung vom 28. November 2011 von Herrn Prof. Dr. Ralf Jungmann betreut und von Herrn PD Dr. Christian Klein von der Fakultät für Chemie und Pharmazie vertreten.

Eidesstattliche Versicherung

Diese Dissertation wurde eigenständig und ohne unerlaubte Hilfe erarbeitet.

München, 16.07.2025

Isabelle Rita Sophie Pachmayr

Dissertation eingereicht am: 17.07.2025

1.Gutachter: PD Dr. Christian Klein

2.Gutachter: Prof. Dr. Ralf Jungmann

Mündliche Prüfung am: 21.10.2025

Table of Contents

Summary

Super-resolution microscopy methods have revolutionized fluorescence imaging by surpassing the diffraction limit of light, a breakthrough recognized with the Nobel Prize in Chemistry in 2014. One class of these techniques is single-molecule localization microscopy (SMLM), which routinely achieves resolutions of ~20 nm by temporally separating fluorophores through stochastic on- and off-switching ("blinking") and localizing subsets of single molecules with high precision.

DNA-PAINT (DNA Points Accumulation for Imaging in Nanoscale Topography) has emerged as a powerful SMLM technique that relies on the transient binding of dye-labeled imager strands to complementary DNA docking strands. DNA-PAINT offers several advantages: it is resistant to photobleaching due to the continuous supply of imager strands in solution, follows predictable DNA hybridization kinetics, and enables high multiplexing. However, in the cellular context, its resolution is typically limited to ~10 nm, primarily due to the limited number of photons that can be collected per localization.

Accessing sub-10 nm resolution is critical for detecting and resolving cell membrane receptors. These receptors are key regulators of cellular fate, processing external signals through the cell membrane, and are highly specific drug targets. The nanoscale organization of membrane receptors, and its modulation by ligand or drug binding, governs the activation of downstream cellular processes.

To understand molecular arrangements within cells, the first part of my thesis advances DNA-PAINT imaging to the molecular scale in a cellular context by introducing Resolution Enhancement by Sequential Imaging (RESI) (**Publication 1**). Through stochastic labeling and sequential imaging of sparse subsets, RESI achieves Ångström-resolution in DNA-origami structures. Applying RESI at ~1 nm resolution in cells enabled the detection of antibody-induced rearrangements of the membrane receptor CD20 at the molecular scale.

In the second part of my thesis, I extended RESI to two-target imaging in 3D to visualize CD20 in complex with therapeutic antibodies (**Publication 2**). Anti-CD20 antibodies are classified into Type I and Type II based on their functional properties. To investigate how these differences relate to receptor organization, I quantitatively analyzed RESI data before and after antibody treatment, uncovering the distinct structural arrangements of Type I and Type II antibodies. Combining RESI with functional assays revealed a distinct pattern of CD20 oligomerization that drives the shift from Type II to Type I antibody

function. These findings support a minimal model describing a continuum between oligomerization state and antibody function for anti-CD20 antibodies.

The third part of my thesis presents a novel strategy for DNA-PAINT and RESI imaging of small extracellular ligands, using Epidermal Growth Factor (EGF) as a model system (**Publication 3**). Understanding the molecular arrangement of EGF during its interaction with the Epidermal Growth Factor Receptor (EGFR) is essential for dissecting receptor signaling pathways that govern cell survival and proliferation. To enable functional ligand labeling for super-resolution imaging, two tagged EGF constructs – ALFA-EGF and DNA-EGF – were compared. The ALFA-tagged variant more effectively preserved EGFR binding and dimerization, showing that ALFA-tagging maintains EGF function while enabling stoichiometric labeling. This establishes ALFA-tagging as a broadly applicable strategy for ligand labeling in DNA-PAINT and RESI microscopy.

Together, these advances establish RESI as a powerful method for achieving molecular-scale resolution in cells and expand the capabilities of DNA-PAINT for studying receptor-ligand interactions.

List of Publications

Publications that are part of this cumulative thesis

Publication 1: Susanne C. M. Reinhardt*, Luciano A. Masullo*, **Isabelle Baudrexel***, Philipp R. Steen*, Rafal Kowalewski, Alexandra S. Eklund, Sebastian Strauss, Eduard M. Unterauer, Thomas Schlichthaerle, Maximilian T. Strauss, Christian Klein & Ralf Jungmann. Ångström-resolution fluorescence microscopy. *Nature* 617, 711-716 (2023). https://doi.org/10.1038/s41586-023-05925-9. (* equal contribution)

Publication 2: **Isabelle Pachmayr**, Luciano A. Masullo, Susanne C.M. Reinhardt, Jisoo Kwon, Maite Llop, Ondřej Skořepa, Sylvia Herter, Marina Bacac, Christian Klein & Ralf Jungmann. Resolving the structural basis of therapeutic antibody function in cancer immunotherapy with RESI. *Accepted at Nat. Commun.* (2025).

Publication 3: Monique Honsa*, **Isabelle Pachmayr***, Larissa Heinze*, Levent Bas, Luciano A. Masullo, Jisoo Kwon, Ana Perovic, Brenda Schulman & Ralf Jungmann. Imaging Ligand-Receptor Interactions at Single-Protein Resolution with DNA-PAINT. *Small Methods*. 9, 2401799 (2025). doi: https://doi.org/10.1002/smtd.202401799. (* equal contribution)

Publications that are not covered in this thesis

Eduard M. Unterauer*, Eva-Maria Schentarra*, **Isabelle Pachmayr***, Taisha Tashrin*, Jisoo Kwon, Sebastian Strauss, Kristina Jevdokimenko, Rafal Kowalewski, Felipe Opazo, Eugenio F. Fornasiero, Luciano A. Masullo & Ralf Jungmann. Left-handed DNA for efficient highly multiplexed imaging at single-protein resolution. *Under review*. (* equal contribution)

Luciano A. Masullo*, Karim Almahayni*, **Isabelle Pachmayr**, Monique Honsa, Larissa Heinze, Sarah Fritsche, Heinrich Grabmayr, Ralf Jungmann & Leonhard Möckl. Ångström-resolution imaging of cell-surface glycans. *bioRxiv* 2025.02.07.637003; doi: https://doi.org/10.1101/2025.02.07.637003. *Accepted at Nat. Nanotech.* (* equal contribution)

Luciano A. Masullo*, Rafal Kowalewski*, Monique Honsa, Larissa Heinze, Shuhan Xu, Philipp R. Steen, Heinrich Grabmayr, **Isabelle Pachmayr**, Susanne C. M. Reinhardt, Ana Perovic, Jisoo Kwon, Ethan P. Oxley, Ross A. Dickins, Maartje M. C. Bastings, Ian A. Parish & Ralf Jungmann. Spatial and stoichiometric in situ analysis of biomolecular oligomerization at single-protein resolution. *Nat. Commun.* 16, 4202 (2025). https://doi.org/10.1038/s41467-025-59500-z. (* equal contribution)

Alexey Ferapontov*, Marjan Omer*, **Isabelle Baudrexel**, Jesper Sejrup Nielsen, Daniel Miotto Dupont, Kristian Juul-Madsen, Philipp Steen, Alexandra S. Eklund, Steffen Thiel, Thomas Vorup-Jensen, Ralf Jungmann, Jørgen Kjems & Søren Egedal Degn. Antigen footprint governs activation of the B cell receptor, *Nat. Commun.* 14, 976 (2023). https://doi.org/10.1038/s41467-023-36672-0. (* equal contribution)

List of Figures

Abbreviations

(d)STORM	(direct) stochastic optical reconstruction microscopy
(m)RNA	(messenger) ribonucleic acid
A	adenine
ADCC	antibody-dependent cellular cytotoxicity
ADCP	antibody-dependent cellular phagocytosis
BCR	B cell receptor
BODIPY	boron-dipyrromethene
C	cytosine
CD	Cluster of Differentiation
CDC	complement-dependent cytotoxicity
CDR	complimentary determining regions
DARPin	designed ankyrin repeat protein
DBCO	dibenzocyclooctyne
DNA-PAINT	DNA-points accumulation for imaging in nanoscale topography
DR	death receptor
dsDNA	double-stranded DNA
ExM	expansion microscopy
ECL	extracellular loop
EGF	epidermal growth factor
EGFR	epidermal growth factor receptor
EM	electron microscopy
EPI	epifluorescence
Fab	Fragment antigen binding
Fc	Fragment crystallizable
FcγRs	Fcγ receptors
FLASH-PAINT	fluorogenic labeling in conjunction with transient adapter-mediated switching for high-throughput DNA-PAINT
FWHM	full width at half maximum
G	guanine
GFP	green fluorescent protein

GPCR	G-protein coupled receptor
HC	heavy chain
HILO	highly inclined and laminar optical sheet
Ig	Immunoglobulin
LC	light chain
LS	least-squares
mAb	monoclonal antibody
MAPK	mitogen-activated protein kinase
mEGFP	monomeric enhanced green fluorescent protein
MINFLUX	minimal photon fluxes
MLE	maximum likelihood estimator
NA	numerical aperture
Nb	nanobody
NeNA	nearest neighbor based analysis
NK cells	natural killer cells
NPC	nuclear pore complex
OBZ	obinutuzumab
OCR	ocrelizumab
OFA	ofatumumab
p-HOBDI	p-hydroxybenzylidene-2,3-dimethylimidazolinone
PAINT	points accumulation for imaging in nanoscale topography
PALM	photoactivated localization microscopy
PD	programmed cell death protein
PD-L	programmed cell death protein ligand
PEG	polyethylene glycol
PFA	paraformaldehyde
PNA	peptide nucleic acid
PSF	point spread function
RESI	resolution enhancement by sequential imaging
RFP	red fluorescent protein
RTK	receptor tyrosine kinase
RTX	rituximab

scFv	single chain variable fragment
SMLM	single-molecule localization microscopy
SNR	signal to noise ratio
SOMAmers	slow off rate modified aptamers
SPAAC	strain-promoted [3 + 2] azide-alkyne cycloaddition click chemistry
ssDNA	single-stranded DNA
STED	stimulated emission depletion
SUM-PAINT	secondary label-based unlimited multiplexed DNA-PAINT
T	thymine
TCE	T cell engager
TIRF	total internal reflection fluorescence
TNFR	tumor necrosis factor receptors
TOS	tositumomab
Tregs	regulatory T cells

1. Theoretical background

Cells are the universal units of living organisms and they are continuously carrying out vital processes: DNA is constantly replicated and repaired, proteins are synthesized and transported, and energy is both stored and consumed to sustain life.

The discovery of both unicellular and multicellular organisms became possible through the invention of the light microscope by Antonie van Leeuwenhoek in the 17th century. By enabling objects to be magnified and visible to the human eye, he accurately described protozoa, bacteria, and human blood cells.[1,2]

1.2 Fluorescence microscopy

Conventional light microscopy relies on the natural contrast of membrane structures within samples, but it lacks the specificity necessary for selectively visualizing biochemical activity. Fluorescence microscopy overcomes this restriction by combining optical imaging with targeted fluorescent labeling, allowing for the precise, high-resolution imaging of biological processes. Consequently, fluorescence microscopy has emerged as a vital instrument in life science research.

1.2.1 Fluorescence

Fluorescence is a process in which molecules emit light of specific wavelengths to return from an excited to a relaxed state. The process requires the previous absorption of a photon with a certain wavelength, leading to the excitation of an electron from the singlet ground state (S_0) to a vibrationally excited singlet state ($S_{i\geq1}$), typically within ~10^{-15} s (Fig. 1a).[3] This is immediately followed by vibrational relaxation within the excited state, mainly by collisions with the surrounding solvent molecules. If $S_{i>1}$, this is followed by a subsequent internal conversion into a vibrationally excited state of the next lower electronically excited state (S_{i-1}). This relaxation cascade is repeated until a vibrationally relaxed state of S_1 is reached which typically takes ~10^{-12}s. Fluorescence is emitted once the electron returns from the excited S_1 state to the ground state S_0, with a typical lifetime of the S_1 amounting to ~10^{-8}s. Once S_0 is reached again, the absorption and emission cycle can restart.[4]

Instead of emitting fluorescence by directly returning from S_1 to S_0, the electron can also undergo intersystem crossing to reach a triplet state (T_1). This encompasses a spin flip to reach a vibrationally excited triplet state, eventually vibrationally relaxing to its triplet ground state. This triplet state is exceptionally long-lived (10^{-6} s to hours), as an electron can only return to S_0 if it flips its spin again. The resulting energy is emitted as a photon in a process called phosphorescence (P).[4]

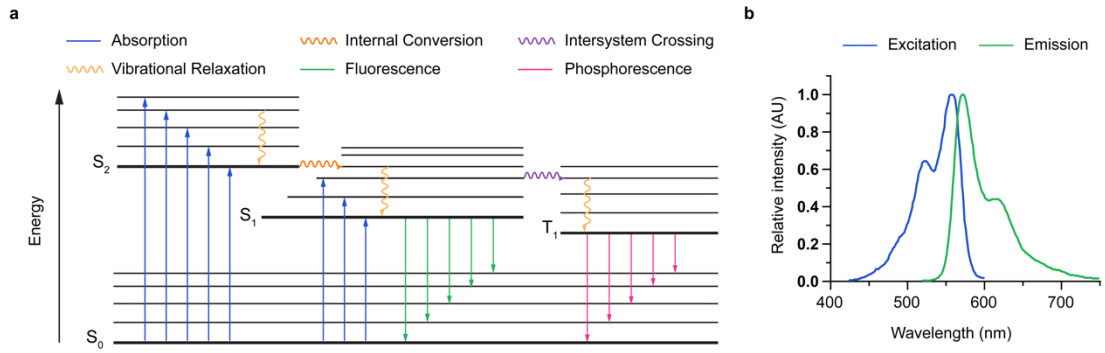

Figure 1: Fluorescence. **a**, An electron is excited from the ground state (S_0) to the first or higher excited state (S_1, S_2,…) by absorption of visible light (blue arrows). Vibrational relaxation (yellow) from higher to lower vibrational levels allows the electron to return to the ground vibrational state (v=0). Internal conversion (orange) allows for the radiation-less transfer of an electron from the ground vibrational state of S_2 to a vibrationally excited state of S_1. Fluorescence (green) of characteristic wavelengths is emitted when the electron relaxes from S_1 to S_0. Alternatively, the electron can undergo intersystem crossing (purple), by spin transition to reach the long-lived triplet state. The electron can return from the triplet state to the singlet relaxed state by emitting light as phosphorescence (magenta). **b**, Excitation (blue) and emission (green) spectra of the Cy3B fluorescent dye with maxima at 558 nm and 572 nm, respectively.

In addition, both fluorescence and phosphorescence can be prevented if there is a nonradiative decay from S_1 to S_0 or from T_1 to S_0 respectively, via further collision with neighboring solvent molecules.[4]

All excited states, but especially T_1 due to its long-lived nature, can undergo chemical reactions, irreversibly damaging the fluorescent the molecule in a process called photobleaching. To prevent photobleaching and extended dark states in fluorescence microscopy, triplet state quenchers can be added to return the molecule to S_0 and quickly as possible.

Each fluorescent molecule has characteristic excitation and fluorescence emission spectra, according to the energy differences between S_0 and S_1 states (Fig. 1a). Due to the vibrational relaxation in the excited state before fluorescence emission, the emitted light always has lower energy that the absorbed light. This resulting shift from a lower wavelength excitation maximum to a higher wavelength emission maximum is called the

"Stokes-shift".[5] S_0 to S_1 energy transitions allow for the absorption of several wavelengths to reach different vibrational states of S_1. Accordingly, S_1 to S_0 transitions can result in several emission wavelengths, when relaxing to different S_0 vibrational states. Because vibrational levels of S_0 and S_1 normally have a similar structure, this leads to approximate mirror images of excitation and emission spectra (Fig 1b).[6]

1.2.2 Fluorescent dyes

The most common fluorescent molecules applied in microscopy are organic dyes and fluorescent proteins. Organic dyes were developed in the 19th and 20th century, after the discovery of the first fluorescent molecule quinone.[7] All organic dyes are planar molecules that are 1-2 nm in size and contain systems of conjugated π-electrons with excitation spectra in the ultraviolet (UV)- to near infra-red range.

For fluorescence imaging, organic fluorophores either stain certain organelles based on their chemical composition, are directly coupled to molecules of interest, or can be covalently conjugated to antibodies for immunofluorescence staining.

Fluorophores can be separated into the following groups based on their core structures: coumarins, boron-dipyrromethene (BODIPY) dyes, xanthene-based dyes, such as rhodamines and fluoresceins, and cyanines (Fig. 2).[4] In general, a more extended conjugated electron system lowers the energy required for excitation, resulting in absorption at higher wavelengths. Hence, cyanines as well as rhodamines generally absorb light at higher wavelengths than coumarins or BODIPY dyes (Fig. 2).

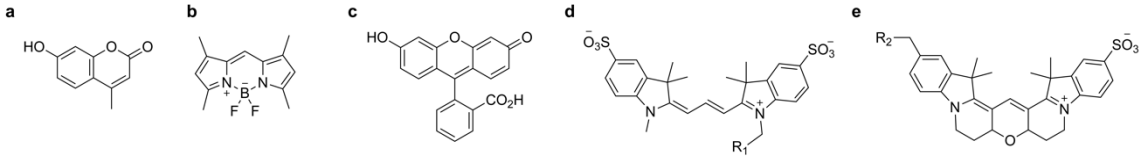

Figure 2: Fluorescent dyes. **a**, 2h-chromene-2-one, a representative coumarin dye. **b**, Boron-dipyrromethene, a representative BODIPY dye. **c**, Fluorescein, a representative Xanthene dye. **d**, Sulfonated Cy3, a representative cyanine dye. R_1 is a chemical moiety for conjugation. **e**, Cy3B, a cyanine dye with stabilized conjugated electron system. R_2 is a chemical moiety for conjugation.

Coumarins are used for chemical sensing and organelle staining and have excitation spectra in the UV to green range. BODIPY dyes have highly tunable excitation and emission spectra, ranging all the way from blue to near-infrared light, making them broadly applicable in biosensing, single-molecule imaging and live cell imaging.[4]

Cyanine (Cy) dyes have multiple applications in diffraction limited microscopy but also in super-resolution microscopy due to their photo-switching capabilities, with popular representatives being Alexa Fluor 647 and Cy3/Cy5. However, because of their linear connecting chain, most cyanine dyes exhibit lower photostability and quantum yields compared to rhodamines, driving the development of more robust derivatives. For instance, Cy3B features a more planar and stabilized π-electron system than Cy3, enhancing its photostability and making it well-suited for single-molecule studies and super-resolution microscopy (Fig. 2d,e).[7] Rhodamines are the basis for silicon-rhodamine as well as Janelia Fluor dyes, which are especially photostable and bright and therefore well-suited for live cell and super-resolution microscopy.[8,9]

All dyes have advantages and disadvantages depending on the exact applications in fluorescence microscopy. Rhodamine dyes have excellent photostability but they are often more hydrophobic than cyanines and conjugation of these dyes to a protein can lead to proximity-induced dye aggregation reducing fluorescence.[10] Next-generation rhodamines and cyanines are therefore heavily modified e.g. by sulfonation, rendering them more hydrophilic.[10]

Despite the wide range of suitable molecules, the application of organic fluorophores for live cell imaging remains limited. Organic fluorophores do not readily diffuse inside organelles within living cells and there are few chemical modalities for covalent protein labeling. Most importantly, the hydrophobic nature of organic dyes impacts protein function in living cells.

1.2.3 Fluorescent proteins

This limitation was fundamentally lifted with the discovery of the green fluorescent protein (GFP) from the jellyfish *Aequorea victoria* by Shimomura in 1962.[11] In 1994, Chalfie et al. demonstrated that GFP could be used as a fluorescent reporter when expressed under the beta-tubulin promoter in cells.[12] Now, all kinds of GFP-fusion proteins are used to study the function and localization of proteins in live cells and fixed tissue. Since its discovery, brighter, more photostable variants of GFP, such as (monomeric) enhanced GFP ((m)EGFP) were developed and the toolbox of fluorescent proteins was has been

dramatically extended: Cyan, Blue and Yellow fluorescent protein are variants of GFP, that can be exited with UV, blue and yellow light, respectively.[13]

The basis for excitation and emission in visible spectrum in the case of GFP is the same as for organic fluorescent dyes: a conjugated π-electron system. This π-electron system is formed by a post-translational maturation of amino acids inside the folded GFP barrel (Fig. 3a,b). The adjacent amino acids serine, tyrosine and glycine (S65, Y66, and G67) undergo cyclization, oxidation and dehydration to form the mature chromophore p-hydroxybenzylidene-2,3-dimethylimidazolinone (p-HOBDI) (Fig. 3c). This matured chromophore only exhibits green fluorescence when conformationally restrained by the abundant hydrogen-bonding within the GFP barrel.[13]

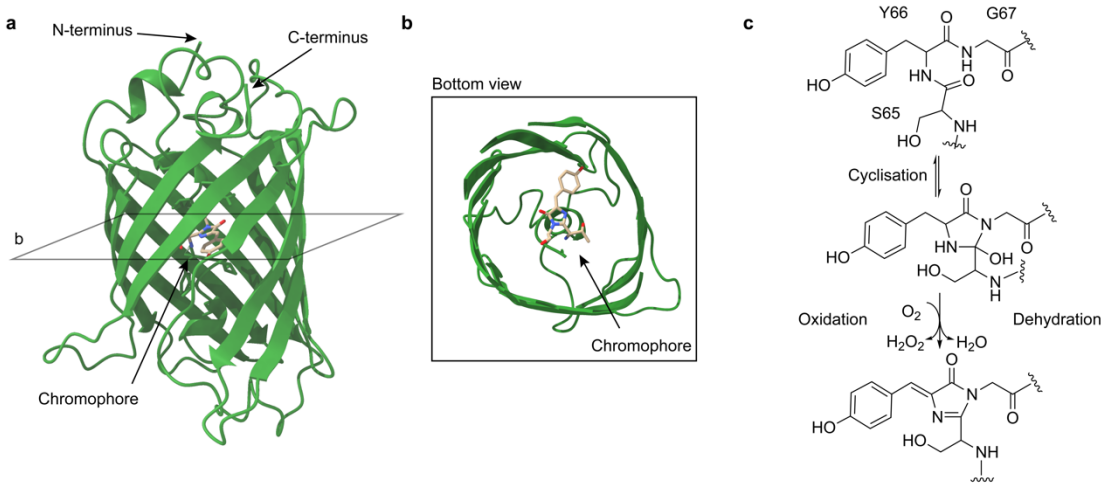

Figure 3: Green Fluorescent Protein (GFP). ***a****, Structure of GFP (PDB: 1EMA) with the chromophore in the center. Graphic was generated with Chimera X.* ***b****, Bottom view of GFP showing the p-HOBDI. Graphic was generated with Chimera X.* ***c****, Cyclization, oxidation and dehydration yields the mature GFP chromophore. Graphic was generated with ChemDraw.*

The success of GFP prompted the isolation of other fluorescent proteins such as red fluorescent protein (RFP)/mCherry from coral *Discosoma*[14] or TagRFP, derived from the sea anemone *Entacmaea quadricolor*[15].

This wide variety of fluorescent dyes and fluorescent proteins enables spectral multiplexing. However, the partly overlapping excitation as well as emission spectra require sets of optimal filters for efficient detection with minimal bleed through, effectively limiting spectral multiplexing to around 6 targets in fluorescence microscopy.

1.2.4 The fluorescence microscope

The detection of fluorescent dyes or proteins with an optical microscope requires the excitation of the fluorescent molecule and the separation of excitation and emission wavelengths to allow efficient detection of the relatively weak fluorescence emission. This is possible due to the Stokes shift to higher wavelengths in fluorescence emission.

There are several different types of fluorescence microscopes all differing in the optical path and in the specific way the fluorophores are exited and detected.[4]

In epifluorescence (EPI) microscopy, excitation light from a laser or an LED is first passed through an excitation filter, to select for the appropriate wavelengths for excitation (Fig. 4).[4] This excitation light is focused on the sample by a e.g. high-NA objective lens. After excitation, fluorophores within the sample emit fluorescence, which is again collected by the same objective. Before fluorescence detection, emitted light is separated from the excitation light by passing it through a dichroic mirror that reflects the excitation wavelengths but allows for the transmission of the lower energy emission wavelengths. Finally, the emission light is passed through an emission filter just before detection with a camera or photon detector.

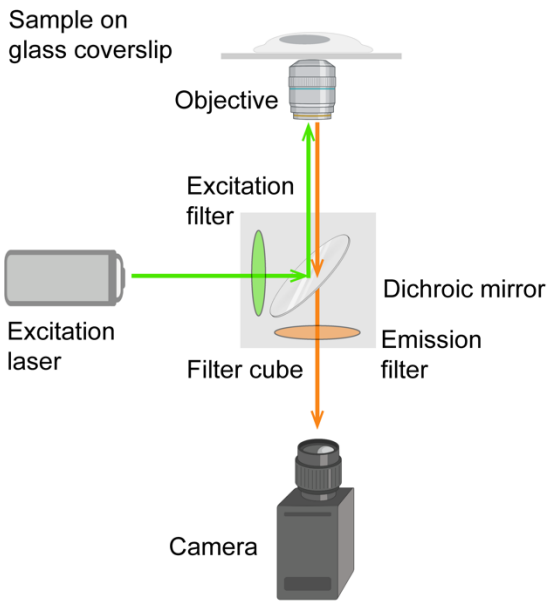

Figure 4: Inverted fluorescence microscope. The excitation laser is passed through the excitation filter and reflected by the dichroic mirror in the filter cube. The excitation light is focused on the sample by an objective. The emission light can pass through the dichroic mirror, is filtered by the emission filter before detection with a camera.

Classical epifluorescence microscopy has a relatively low signal-to-noise ratio because the excitation laser passes through the objective in a perpendicular manner. This illumination of the whole sample in z-direction results in out-of-focus fluorescence detection. This is partly circumvented by confocal microscopy in which out-of-focus excitation and emission light are reduced using a pinhole, and the sample is scanned with this reduced confocal volume. Moreover, selective volume illumination to avoid out-of-focus excitation and fluorescence detection can be achieved with spinning disk or light sheet microscopes. For samples, in which the processes of interest happen close to the glass coverslip, selective illumination of the first hundreds of nm can be achieved by total internal reflection fluorescence (TIRF).

1.2.5 Total internal reflection fluorescence microscopy

TIRF illumination involves a change in the incident angle of fluorescent light at the interface of glass and water at the coverslip. Instead of directing the laser beam centrally through the objective, leading to an incident angle of $\theta_1 \sim 0°$ at the coverslip (epifluorescence), the laser beam can be shifted from the center to the edge of the back focal plane of the objective.[16] This shift results in a change in the incident angle of the laser beam at the glass coverslip. Due to the difference in the refractive indices of glass and water in the sample, this leads to bending of the laser light at this border. The relationship between the angle of incidence θ_1, the angle of refraction θ_2, the refractive index of the incident medium n_1, and the refractive index of the refracting medium n_2 can be described with Snell's law (Fig. 5a):

$$n_1 \cdot \sin\theta_1 = n_2 \cdot \sin\theta_2 \qquad 1$$

In microscopy, glass has a refractive index of n_1=1.52 and water of n_2=1.33. The fact that in this case $\frac{n_1}{n_2}$>1 means that θ_2>θ_1 and thus the laser light is refracted away from the optical axis.

Therefore, when the incident light approaches the so-called critical angle θ_c, the angle of refraction will reach $\theta_2 = 90°$. For incident angles above the critical angle, the beam is totally internally reflected at the glass water interface. According to Snell's law the critical angle θ_c is:

$$\theta_c = \arcsin\left(\frac{n_2}{n_1} \cdot \sin 90°\right) = \arcsin\left(\frac{1.33}{1.52}\right) = 61.04° \qquad 2$$

The total internal reflection (TIRF) generates a so-called evanescent wave penetrating into the lower refractive index medium with a limited depth (Fig. 5b).[17]

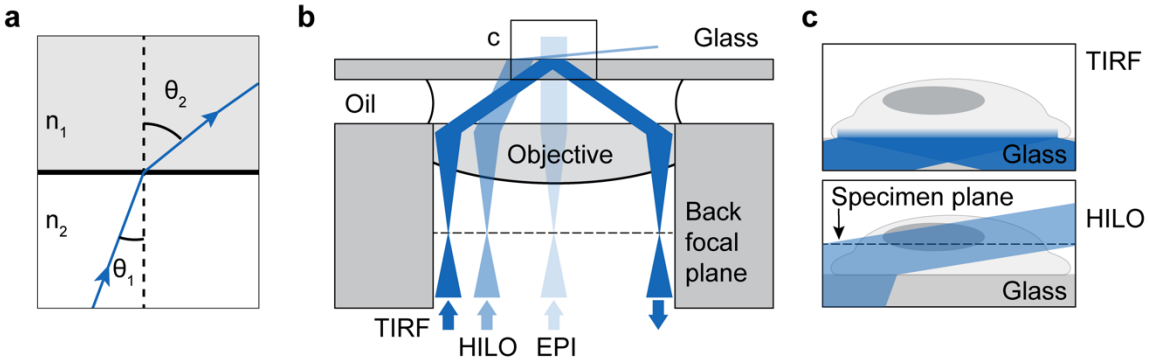

Figure 5: Selective plane illumination. **a**, Snell's law. **b**, Moving the laser from the center towards the edge of the back focal plane changes the illumination from epifluorescence (EPI), to highly inclined and laminated optical sheet (HILO), and then to total internal reflection fluorescence (TIRF). **c**, TIRF illuminates only the first few 100 nm close the cover glass. HILO illuminates the sample with a higher depth in z.

There is an exponential decrease of the light intensity I within the sample, depending on the distance z from the interface.

$$I = I_0 \cdot exp\left(\frac{-z}{d(\theta_1)}\right) \qquad 3$$

The "penetration depth" d of the laser in TIRF microscopy is defined as the distance at which the intensity drops to $\frac{1}{e} I_0$ which is 37% of its value at the interface ($z = 0$), according to the following equation:

$$d(\theta_1) = \frac{\lambda}{4\pi\sqrt{n_1^2 sin^2(\theta_1) - n_2^2}} \quad (4)$$

For an excitation laser of λ=561 nm, a refractive index n_1 of glass of 1.52 and a refractive index n_2 of water of 1.33, when keeping θ_1 between 62° and 65°, the penetration depth varies between 248 nm and 124 nm, respectively.

Due to this exponential decrease in intensity, the background fluorescence is reduced, which increases the signal-to-noise ratio (SNR) of the measurement. Therefore, TIRF illumination is often used for singe molecule studies of surface immobilized nanostructures or for events happening at the cell membrane close to the coverslip (Fig. 5b,c).

This illumination mode however fails when high SNR measurements of events further (>300 nm) from the coverslip is desired. For this, a modified version of TIRF can be employed, termed “highly inclined and laminated optical sheet” (HILO) microscopy (Fig. 5b,c).[18] When choosing an incident angle close to total internal reflection but below the critical angle, the laser beam at the glass-water interface is not reflected but inclined to form a laminated light sheet. This thin sheet penetrates the sample for up to ~10 μm in depth while only illuminating a fraction of the total z-plane, thus reducing the background fluorescence as opposed to EPI illumination.[18] The sheet thickness dz can be calculated from the diameter of the illuminated area R at the specimen and the refracted angle θ_2:

$$dz = \frac{R}{tan(\theta_2)} \quad (5)$$

The HILO sheet passes through the center of the illuminated sample and is therefore applicable for imaging in 3D.[18]

Taken together, the optimized sample illumination in TIRF and HILO result in a reduced SNR in fluorescence microscopy, leading to a significantly improved detection efficiency of low fluorescence intensity and single molecule events. However, one fundamental limit of microscopy cannot be overcome by this: The diffraction limit of light.

1.2.6 The diffraction limit of light

Diffraction encompasses all processes, in which electromagnetic waves interact with objects. According to its wave-like properties, light is always diffracted when passing through an aperture, or when interacting with nanoscopic particles. This results in bending and spreading of the diffracted light waves, consequently forming constructive and destructive interference patterns. In the case of fluorescence microscopy, light is diffracted when passing through the aperture of an objective and forms a concentric interference pattern. This means that every point-like light source in the imaged sample is convoluted by the so-called point-spread function (PSF) so that it can only be detected as its diffracted pattern.[4] The two-dimensional manifestation of this pattern is the Airy disk, showing concentric rings of light surrounding a central, high intensity spot with alternating maxima and minima along x- and y-axis (Fig. 6a).

In standard fluorescence microscopy all point-like emitters are ON at the same time and the emission PSFs overlap during image detection. This PSF convolution results in an effectively blurred image. Consequently, two point-sources of light cannot be distinguished (i.e. resolved) if they are closer than the resolution limit of the system.[3,4]

The resolution limit was first defined by Ernst Abbe by investigating minimal resolvable distance in optical grids in 1873, and is since known as the “Abbe limit”. He observed that “the resolution of a microscope will not exceed half the wavelength of the incident [blue] light”.[19] The Abbe resolution limit d_A is dependent on the wavelength of the incident light λ_i as well as on the half opening angle α of the objective and the refractive index n of the objective, according to:

$$d_A = \frac{\lambda_i}{2n \cdot sin\alpha} = \frac{\lambda_i}{2NA} \qquad 6$$

NA is the numerical aperture (NA) of the imaging system.

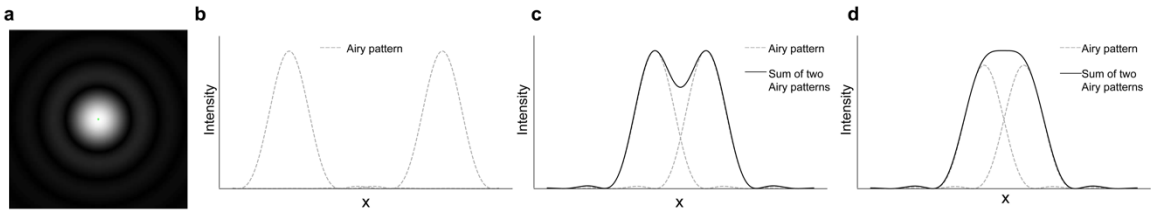

Figure 6: Airy disk and resolution limits. **a**, Airy pattern in 2D.[22] **b**, Two point objects with distance greater than the Rayleigh limit (d_R) are well resolved. **c**, Two point objects spaced with a distance equal to d_R. **d**, Two point objects spaced with a distance equal to the Sparrow limit (d_S).

Lord Rayleigh further refined the resolution limit based on overlapping Airy disks. According to Rayleigh, the minimal distance for which two point-like light sources can be distinguished, is reached if the maximum of one Airy disk overlaps with the first minimum of the other Airy disk (Fig. 6c).[20] This results in the following equation for the Rayleigh limit d_R, dependent on the wavelength of the fluorescence emission light λ_e:

$$d_R = 0.61 \frac{\lambda_e}{NA} \qquad 7$$

Another definition by Sparrow states that the resolution limit is reached when the overlapping Airy disks no longer show a minimum within the resulting intensity graph (Fig. 6d).[21]

$$d_S = 0.47 \frac{\lambda_e}{NA} \qquad 8$$

However, the Sparrow limit fundamentally requires that the number of molecules within the spot is known. The Sparrow limit is mainly used in astronomy, whereas Abbe and Rayleigh limit are more frequently applied in fluorescence microscopy. The exact definition of resolution in fluorescence microscopy is still heavily debated and can only be demonstrated experimentally.

The PSF is narrower in xy and wider in the z dimension, thereby decreasing the resolution in the axial dimension at least 2-fold. This is due to the fact that the axial resolution can be estimated with $d_z = \frac{2\lambda}{NA^2}$ as opposed to $d_{xy} = \frac{0.61\lambda}{NA}$ for typical high-NA objectives.[19,22]

No matter which resolution limit is applied in the end, the resolution of fluorescence microscopes is fundamentally limited by the wavelength λ of visible light not going below 400 nm as well as by the half opening angle α limited to 90°, when the numerical aperture equals the refractive index of the objective n=1.52. Electron microscopy (EM), with much lower wavelengths down to a few pm, can surpass the resolution of light microscopy and reach 1 Å resolution.[23] However, in EM, sample integrity can be compromised by the extensive preparation process, labeling of specific structures is challenging and the throughput is limited.[23] To address both the limitations of classic fluorescence microscopy and EM, super-resolution fluorescence microscopy methods have been developed.

1.3 Super-resolution microscopy

In the mid to late 1990s, the basic concepts of two fundamentally different approaches to super-resolution microscopy were introduced, with stimulated-emission depletion (STED) and single-molecule localization microscopy (SMLM), both awarded a Nobel Prize in 2014. All super-resolution approaches circumvent the resolution limit by essentially preventing the PSF overlap of nearby fluorophores.

For conciseness, I will mostly focus on super-resolution methods which significantly and routinely go below the 100 nm resolution limit.

1.3.1 Point scanning-based methods

The first group of super-resolution microscopy methods, the so-called coordinate-targeted versions, are based on point-scanning the sample, similar to confocal microscopy.

1.3.1.1 STED

For instance, in stimulated emission depletion (STED) microscopy, individual fluorophores are separated from nearby molecules while scanning over the sample. This is achieved by stimulated emission depletion of fluorescence around the maximum of the excitation spot, using a red-shifted donut-shaped laser (Fig. 7a).[24,25] Fluorophores illuminated with excitation and depletion laser undergo the following steps: First, an electron is excited from S_0 to S_1 by the excitation laser. Second, a photon originating from the depletion laser, with slightly lower energy than the expected fluorescence emission, triggers the return of the electron from S_1 to S_0. Third, two photons with the same wavelength of the incoming depletion photon are emitted (Fig. 7b). Thereby, the fluorescence is quenched and the

depletion wavelengths can be filtered out before fluorescence detection (Fig. 7c). This essentially results in the decrease in size of the PSF.

The STED concept was first introduced by Stephan Hell in 1994 and practically implemented in 1999, using a phase-plate to generate the donut-shaped beam (Fig. 7d).[25,26] In order to generate the donut-shaped depletion beam, it is modulated with a phase mask to obtain a nanometric center of zero intensity with an exponential increase of laser intensity around that center.

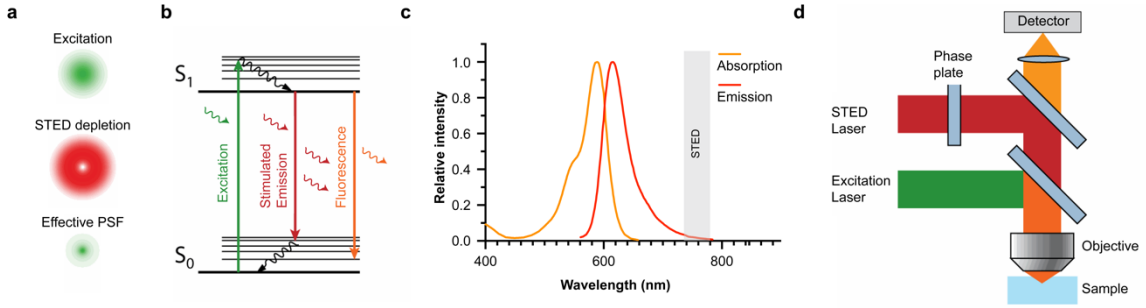

Figure 7: STED microscopy. **a**, The excitation laser (green) is depleted with a donut-shaped STED depletion laser (red) to obtain an effective PSF with a reduced size. **b**, Jablonsky diagram of the involved states during STED transitions. **c**, Absorption (orange) and emission (red) spectra of the STED dye Aberrior STED ORANGE. STED depletion lasers are at higher wavelengths than the STED detection. **d**, Simplified STED setup. A phase mask is used to generate the donut-shaped STED laser and both excitation and STED laser are focused on the sample through the same objective. Adapted with permission from[27].

STED is relatively fast and can perform optical sectioning with a 3D engineered depletion laser. Therefore, STED is suitable for live cell and deep tissue imaging. It is even possible to perform sub-70 nm resolution imaging in a living mouse, thereby observing dendritic spine dynamics in the cerebral cortex.[28]

The achievable STED precision σ_{STED} scales with the intensity of the STED laser I_{STED} over the saturation intensity I_{sat}.

$$\sigma_{STED} = \frac{\sigma_{PSF}}{\sqrt{1 + {I_{STED}}/{I_{sat}}}} \qquad 9$$

However, high STED laser intensities quickly lead to dye photobleaching. Therefore, STED resolution is mainly limited by the stability of the dye molecule.

1.3.1.2 MINFLUX

This need for high depletion laser powers is omitted in minimal photon fluxes (MINFLUX) nanoscopy[29], by essentially "flipping nanoscopy on its head"[30]. As opposed to localizing a molecular emitter by detecting its emission maximum, MINFLUX aims to localize a molecule near the signal minimum (Fig. 8). This allows for super-resolution imaging and tracking with minimal photon emission required.

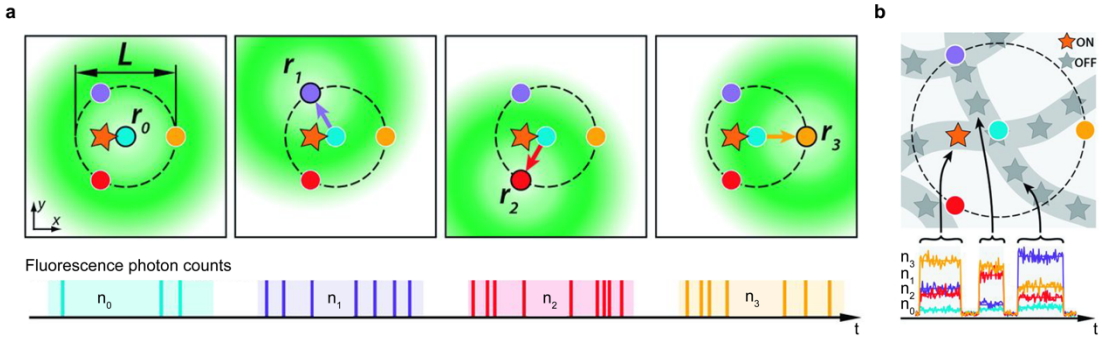

Figure 8: MINFLUX nanoscopy. **a**, The donut-shaped excitation laser, featuring a center of zero intensity, is placed at four different locations r_0, r_1, r_2, r_3 and the photon counts n_0, n_1, n_2, n_3 are detected. **b**, A nanoscale object of interest can be imaged with MINFLUX, if it is labeled with photo-switchable fluorophores, that are tuned so that only one of the fluorophores within the excitation range is on at the same time. Individual molecules can be distinguished by changes in the ratios between the different photon counts or by intermissions in emission. Adapted with permission from[29].

MINFLUX is implemented using a donut-shaped excitation laser, featuring a center of zero intensity and exponential increase of intensity towards the donut ring. The relative distance of fluorophores from the known zero-intensity-center can be calculated from the number of detected photons (N).

Assuming an ideal measurement with a perfect donut-zero devoid of background photons, the two-dimensional MINFLUX localization precision σ_{MIN} is:

$$\sigma_{MIN} = \frac{L}{\sqrt{8N}} \qquad 10$$

It can therefore be improved by decreasing the donut diameter L, or increasing the number of detected photons N.

Practically, MINFLUX uses diffraction-limited *a priori* information on the fluorophore location and then determines its position by circling the donut minimum within 50-150 nm around the expected position. By determining the fluorescence intensity at four different positions around a single fluorophore, MINFLUX reaches sub-1 nm precisions and true molecular resolution (2 to 3 nm). However, the serial point-scanning approach currently limits the throughput for whole-cell imaging, as it takes minutes to hours to image a 1x1 μm^2 FOV.[31]

1.3.2 Single-molecule localization microscopy

A fundamentally different approach to coordinate-targeted super-resolution approaches, such as STED and MINFLUX, are coordinate-stochastic approaches, more commonly referred to as single-molecule localization microscopy (SMLM) methods. SMLM relies on a basic concept that was first introduced by Eric Betzig to increase resolution when imaging dense samples. He proposed that, if you find any way to differentiate and thereby isolate diffraction limited-spots of single molecules, this allows you to find the centers of each spot with a precision much better than the width of the spot. Eventually, this permits the retrieval of the molecular coordinates.[32]

In SMLM, single molecules within the sample are isolated by stochastically switching them on and off over the whole field of view, while illuminating in wide-field mode. Switching conditions are tuned so that only a small subset of fluorophores are ON at a given time. Thus, two or more adjacent unresolvable molecules are temporarily separated, allowing single-molecule detection with much higher precision. Each molecule has to be detected at least once, and ideally multiple times during the measurement, which requires imaging over thousands of consecutive frames.[33]

SMLM images are reconstructed by first detecting local photon maxima within in each image frame. For these identified single-molecule pixel regions, the emission center has to be estimated.[34] This is commonly achieved by either fitting Gaussian profiles with a least squares (LS) algorithm or maximum-likelihood estimators (MLE).[35,36] Extensive comparisons have shown that, while LS is about 25% less precise that MLE at low photon counts, LS performs as well as MLE at higher photon counts.[37] From this fitting procedure, a list of xy-coordinates is obtained – featuring properties such as photon count, localization precision, and background values – from which the final image can be reconstructed (Fig. 9).

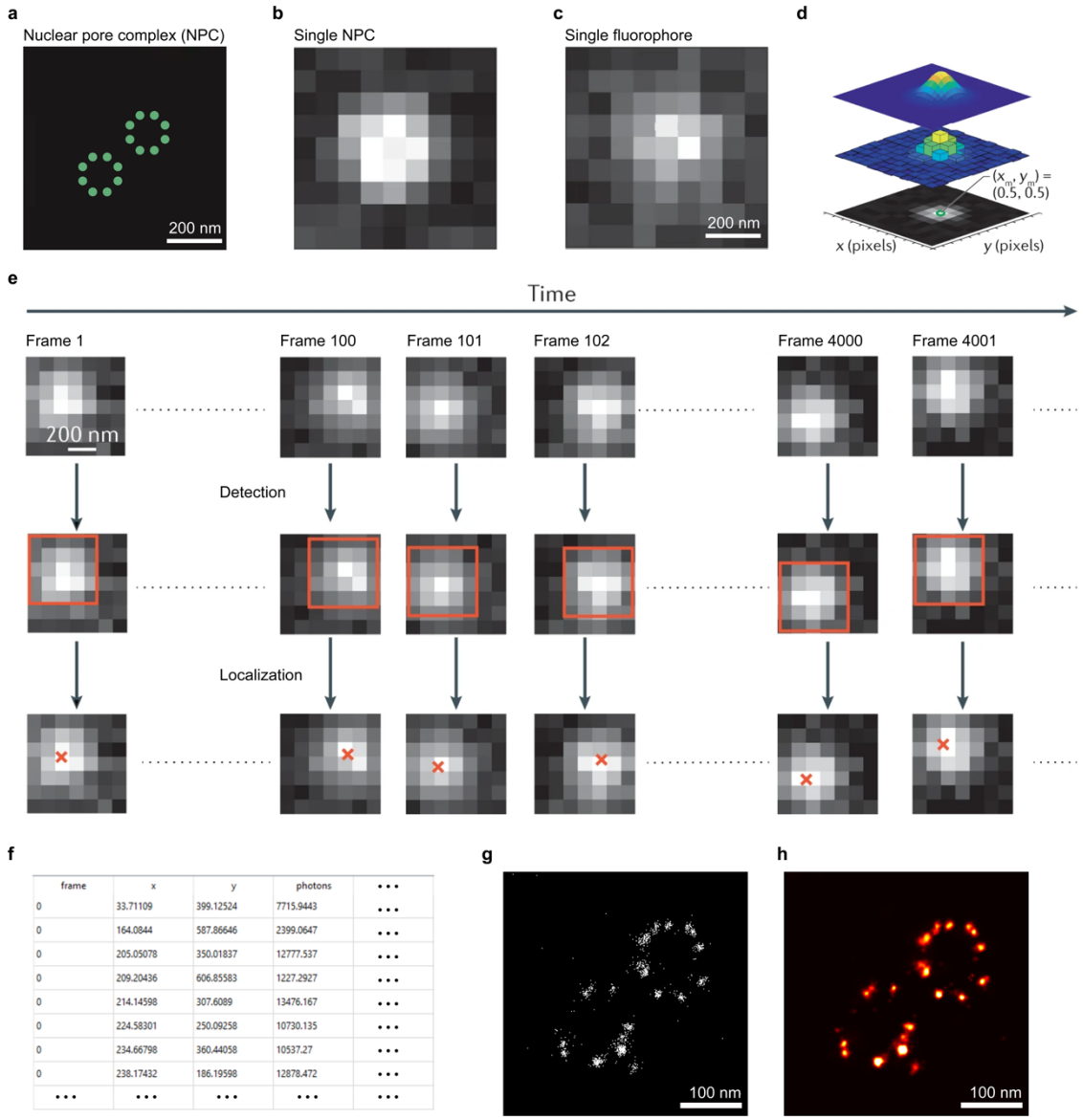

Figure 9: Single-molecule localization microscopy. **a**, Schematic representation of a typical nanoscale structure in cells, the nuclear pore complex (NPC). **b**, PSFs are overlapping when all fluorescent molecules within the NPC structure are on at the same time, resulting in a blurred image. **c**, PSF of a single molecule. **d**, For a single molecule, x- and y-coordinates (x_m, y_m) can be computed with high precision. **e**, On- and off-switching of fluorophores yields single-molecule blinking over several thousands of frames. In each frame, single molecules are first detected and can then be localized with high precision. **f**, SMLM results in a localization table, where each row represents a distinct localization event and columns indicate x/y-coordinates and additional information such as frame number and the number of photons. **g**, Accumulated localizations visualized as one pixel blur, where each dot represents a single localization. **h**, Final SMLM image for which localizations are rendered with the individual localization precision, revealing the ring-like structure of nuclear pores. Adapted with permission from[33].

The gain in resolution by performing SMLM is critically dependent on the localization precision (σ_{SMLM}) of these single-molecule events, which is fundamentally limited by the Cramér-Rao lower bound, that can be simplified as:[38,39]

$$\sigma_{SMLM} \geq \frac{\sigma_{PSF}}{\sqrt{N}} \qquad 11$$

Thus, the precision of the estimated coordinates is dependent on the standard deviation of the PSF (σ_{PSF}) and increases with the number of photons N collected by the camera.[40]

More advanced models to estimate σ_{SMLM} include the non-Gaussian shape of the PSF, read and amplification noise, background signal, finite pixel size and dipole orientation, that all reduce precision.[39] Taking into account the pixel size a and the background intensity b, σ_{SMLM} can be calculated as follows:

$$\sigma_{SMLM} \geq \sqrt{\left(\frac{\sigma_{PSF}^2 + {a^2}/{12}}{N}\right) \cdot \left(\frac{16}{9} + \frac{8\pi\left(\sigma_{PSF}^2 + {a^2}/{12}\right) b^2}{Na^2}\right)} \qquad 12$$

A commonly used and generally applicable method to estimate σ_{SMLM} in experimental data is Nearest Neighbor based Analysis (NeNA). Single-molecule blinking events usually last several frames. Therefore, analyzing the distribution of nearest-neighbor distances between localizations in consecutive frames can be used to approximate σ_{SMLM}. By fitting this distribution with a model accounting for true and false nearest neighbors, NeNA provides a robust, experiment-specific measure of σ_{SMLM}, even in dense or dynamic samples.[38]

A practical approach to determine the experimental resolution from the measured precision σ_{SMLM}, is calculating the full width at half maximum (FWHM) of the PSF, according to:

$$d_{FWHM} \approx 2.35\sigma_{SMLM} \qquad 13$$

Thus, to increase resolution in SMLM, the localization precision σ_{SMLM} can be improved by narrowing the PSF, increasing the number of detected photons, reducing pixel size, and minimizing background intensity, among other factors.

1.3.2.1 PALM

SMLM relies on reversible on- and off-switching of fluorescent molecules (the so called "blinking") which can be achieved in several different ways. Already in 1997, the group of W.E. Moerner performed single-molecule experiments on GFP and observed that they undergo repeated cycles of fluorescent emission ("blinking") upon illumination with a 488 nm laser. [41] This eventually results in a long-lasting dark state, from which they can be switched back to their emissive state by irradiation at 405 nm.[41] In photoactivated localization microscopy (PALM), this effect is used to image several sparse single-molecule subsets of fluorescent proteins. This allows fitting of single protein positions and reconstruction into a super-resolved image.[42] The first-generation PALM-compatible proteins could only be photoconverted once during the measurement. Later, reversibly photo-switchable fluorescent proteins have been introduced, allowing the repeated detection over the course of the measurement, thereby increasing sampling of the imaged structures.[43] The possibility to fuse a photo-convertible or -switchable fluorescent protein directly to the protein of interest makes PALM generally well suited for live-cell applications. However, low photon yield, premature bleaching or incomplete labelling can limit the effective resolution. Photoactivatable fluorescent proteins typically only emit a few hundred photons before they bleach, whereas synthetic fluorophores can emit more than 1,000 photons per cycle.[44]

1.3.2.2 (d)STORM

This is why in stochastic optical reconstruction microscopy (STORM), the blinking is generated by photophysically or chemically switching small organic fluorescent molecules.[33] In the original STORM concept, Rust et al. used Cy5 that is converted to a dark state with a red laser, and is switched on again by Cy3 in close proximity, after excitation with green light.[45] Later, this was extended to 3-color multiplexed STORM imaging by not only using Cy3, but also Alexa 405 and Cy2, to activate Cy5.[46]

The now more commonly used direct STORM (dSTORM) achieves photo-switching with only one dye but requires special buffers to reversibly switch molecules.[44] Carbocyanine dyes, such as Cy3, Cy5, and Alexa Fluor 647, as well as most Alexa Fluor dyes and ATTO

dyes, are photoswitchable.[47] More specifically, the dyes can be transferred to a non-fluorescent dark state by reacting with thiol-containing reducing agent – such as β-mercaptoethylamine, dithiothreitol, or glutathione – after reaching the triplet state (Fig. 10). From this reduced form, they can be switched back ON by irradiation with low wavelength laser light. Tuning the laser power can be used to regulate the number of molecules that are simultaneously in a bright state. Since the thiolate competes with oxygen in terms of triplet state quenching, it is crucial to fine tune the pH value to obtain thiolate anions, control the thiol concentration and/ or use oxygen scavenging reagents.[47] dSTORM is an efficient dye-based super-resolution method routinely achieving ~20 nm resolution.

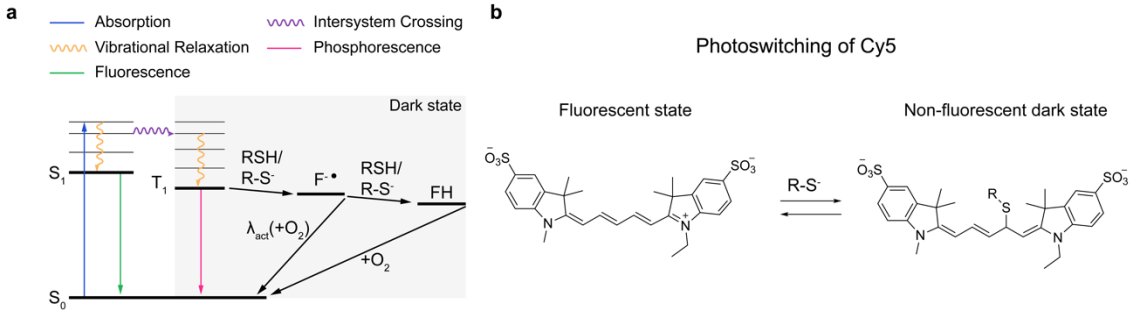

Figure 10: Photoswitching in (d)STORM. **a**, Jablonski diagram for reversible photoswitching of organic fluorophores in the presence of reducing agents. From the first excited state S_1, either fluorescence emission, or intersystem crossing into the triplet state T_1 occurs. The long-lived triplet state can react with reducing agents (such as thiols) to form a radical anion ($F^{\bullet-}$). The singlet ground state can be recovered by oxidization with oxygen or excitation of the radical with near-UV light. Some fluorophores can become fully reduced (FH), and can also return to the ground state by reaction with oxygen. **b**, Reversible reduction of Cy5 by thiol-containing reagents leads to a non-fluorescent dark state.[48]

1.3.2.3 PAINT

Single-molecule blinking does not necessarily have to be generated by photoswitching of fluorophores. It can also be generated by dynamic binding and unbinding of fluorescent probes in the points accumulation for imaging in nanoscale topography (PAINT) method.[49] This was first implemented with Nile Red, a hydrophobic dye that transiently associates with individual lipid vesicles, changing from a non-fluorescent to a highly fluorescent state in hydrophobic environments. By adjusting the probe concentration or the excitation light intensity, the number of Nile Red molecules associating with lipid membranes at any time can be tuned so that fluorescent signals are distinct and well-separated, enabling SMLM.

The PAINT concept is not limited to organic molecules. Any fluorescent molecule that transiently binds to a location of interest can theoretically be used to detect single-molecule events. This is demonstrated in universal PAINT (uPAINT), in which low concentration of fluorescent ligands in the extracellular medium achieve a constant rate of membrane molecules being labeled.[50] To minimize background fluorescence of diffusing ligands in the solution, HILO or TIRF illumination have to be used. uPAINT is applicable for live cell single-molecule tracking and is not limited by photobleaching since the continuous binding of and unbinding allows for the replacement of photobleached ligands for intact molecules from the solution. The PAINT concept can theoretically be exploited for any affinity reagent with sufficient specificity. In lectin-PAINT, the reversible binding of dye-labeled lectins to carbohydrates allows for PAINT imaging the cell's glycocalyx.[51,52] In LIVE-PAINT, direct transient binding of dye-labeled peptides to proteins of interest enables SMLM, of which the most commonly used reagent is the Actin-targeting LifeAct protein.[53] A more general approach is peptide-PAINT, in which proteins of interested are tagged with a short peptide-tag.[54,55] These "direct" PAINT approaches have the advantage that they are highly biocompatible and can be applied in live cell settings. However, they suffer from low versatility due to the need to develop a specific binder for each target in the right affinity range and therefore have limited multiplexing abilities. Moreover, binding and blinking kinetics have limited tuneability, requiring the optimization of imaging conditions for each target individually.

1.4 DNA-PAINT super-resolution microscopy

These limitations are overcome with DNA-PAINT super-resolution microscopy, in which the blinking is generated by transient binding of dye-labeled DNA "imager" strands to complimentary DNA "docking" strands. It makes use of the high tunability and programmability of DNA-DNA interactions.

1.4.1 The DNA molecule

DNA is the fundamental building block of life, the way genetic information is stored in every cell of the human body. According to the central dogma of molecular biology, DNA encodes for (messenger) ribonucleic acid ((m)RNA), that is then translated to proteins.

With the help of X-ray crystallography images taken by Rosalind Franklin; James Watson, Francis Crick, and Maurice Wilkins described the double-helical structure of DNA in 1953, for which the latter three were eventually awarded with the Nobel Prize in Physiology or Medicine (Fig. 11a).[56,57]

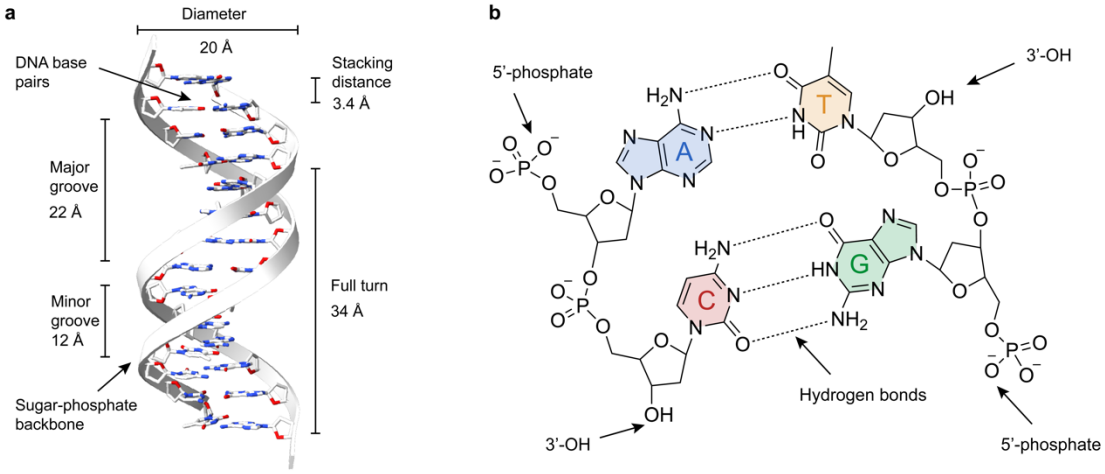

Figure 11. Structure of the B-DNA double helix. **a**, Double-stranded DNA consists of two single strands, featuring a sugar-phosphate backbone, equipped with DNA bases. The double helix is stabilized by DNA base pairing. It has a major and a minor groove and a full turn is 34 Å, or 10-10.5 base pairs with 3.4 Å stacking distance from base pair to base pair. The DNA double helix was generated with Chimera X. **b**, DNA base pairing in B-DNA. Adenine (A in blue) can specifically pair with Thymine (T in yellow) by forming 2 hydrogen bonds. Cytosine (C in red) can specifically pair with Guanine (G in green) by forming 3 hydrogen bonds. Molecular structures were generated with ChemDraw.

The DNA-double helix consists of two single DNA-strands, each a polymer with a specific sequence of four different nucleotides that are connected via a sugar-phosphate backbone (Fig. 11). Each of these nucleotides consists of a phosphate-group, a deoxyribose molecule and one out of four nitrogenous bases, which are adenine (A), cytosine (C), thymine (T) and guanine (G). Two single-stranded DNA (ssDNA) molecules with complementary sequence can form a double-stranded DNA (dsDNA) helix by specific base pairing. This is achieved by formation of two selective hydrogen bonds in A-T pairs and three selective hydrogen bonds in G-C pairs (Fig. 11b). The most common form of dsDNA in cells and in aqueous solution is the right-handed B-DNA. It features an average of 10 base pairs per turn with a 3.4 Å base stacking distance, a 7.0 Å distance along the backbone between two nucleotides and a diameter of 20 Å. The right-handed A-DNA mostly forms in anhydrous environments but is also found in cells, and is slightly broader and more compacted along the helix-axis. Alternative DNA-base pairing results in noncanonical left-handed Z-DNA with a “zigzag” backbone, which plays a role in

transcription regulation or mitochondrial DNA stability.[58,59] The naturally occurring left-handed Z-DNA should not be confused with synthetic left-handed L-DNA. L-DNA is an exact mirror-image of natural right-handed B-DNA. It is generated by synthesizing DNA nucleotides in the L-form, instead of the naturally occurring D-form of deoxyribose.[60,61]

In DNA-double strand formation, the electrostatic repulsions of the negatively charged phosphate backbones and the entropic cost ($-T\Delta S° >> 0$) of the highly ordered double-helix structure are overcome by hydrogen bonding as well as π-π-stacking between adjacent base pairs, providing a favorable enthalpy ($\Delta H° << 0$).[62]

1.4.2 DNA nanotechnology

The programmability, stability and Ångström scale addressability of DNA can be exploited for nanotechnology applications. Already in 1982, Ned Seeman generated stable versions of the 2D Holliday junction and proposed that it is "possible to generate covalently joined three-dimensional networks of nucleic acids which are periodic in connectivity and […] in space" [63]. 24 years later, Paul Rothemund described a highly programmable method for assembling DNA into arbitrary two-dimensional shapes, termed DNA origami.[64] By designing over 200 short ssDNA 'staple strands', a long ssDNA scaffold strand could be folded into nearly any shape of about 100 nm in size (Fig. 12a). With this bottom-up folding approach, each staple strand can be individually addressed and functionalized with (bio)molecules with nm-resolution (Fig. 12b).

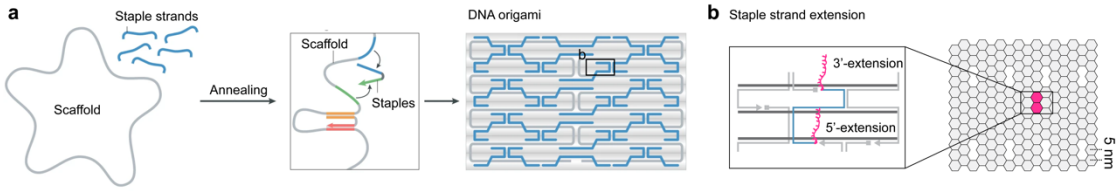

Figure 12: DNA origami. **a**, A single stranded DNA scaffold can be folded into a 2D or 3D shape using short single stranded DNA staple strands by thermal annealing. **b**, Each of these staples can be individually modified with a DNA extension or other chemical moieties. Adapted with permission from[65].

1.4.3 DNA-PAINT imaging

The first implementation of DNA-PAINT super-resolution microscopy was performed on exactly these DNA origami structures [66], by designing staple strands in a way that ssDNA docking strands with lengths of 7 and 10 bases were protruding from the origami.

Immobilizing these on glass slides and introducing a solution with complementary ATTO655 or Cy3B-labeled DNA imager strands yielded a characteristic blinking, with a spot being ON while the imager was bound to the docking strand, and the spot switching OFF when the transiently bound imager dissociated (Fig. 13a,b). In DNA-PAINT, the few 100 ms of imager binding permits the collection of enough photons (signal) over the background of quickly diffusing imager strands. Imager background detection was minimized by TIRF imaging, and the intramolecular dye-quenching by guanine bases in diffusing imagers. DNA-PAINT imaging enables the detection of tens of single-molecule binding events over several thousands of frames, allowing for the deduction of single-molecule binding kinetics.

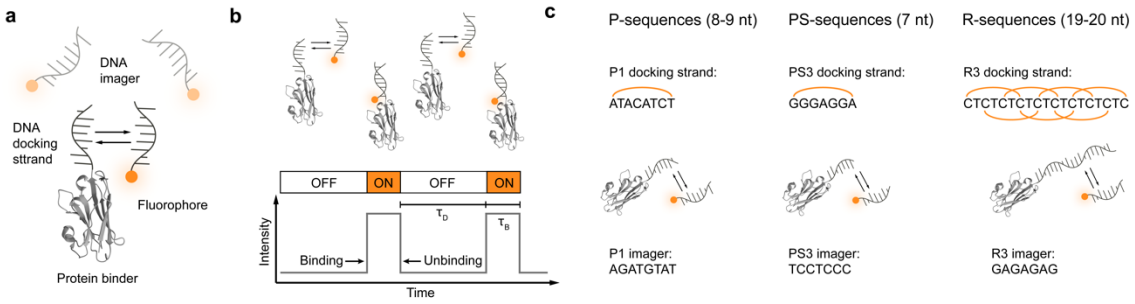

Figure 13: DNA-PAINT super-resolution microscopy. **a**, DNA docking strands are immobilized on the structure of interest, for example via a protein binder. Complementary fluorophore-conjugated DNA imager strands are added in solution. **b**, DNA-PAINT generates blinking for SMLM, with the spot being 'ON' while the transiently binding dye-labeled imager is bound to docking strands immobilized on the sample, and the spot being 'OFF' when the imager diffuses freely. The binding is characterized by distinct bright times (τ_B) and dark times (τ_D). **c**, The first generation of DNA-PAINT docking strand-imager pairs, P sequences, were 8-9nt long and used the full sequence spectrum, reducing apparent on-rates. The second-generation PS-sequences feature a 5x-10x increase in imaging speed, compared with P sequences, by reducing the length to 7nt and using only two non-complementary bases per sequence. The third generation R-sequences increase the imaging speed by up to 100x, by concatenating several imager-binding sites on the docking strand.

The DNA docking strand-imager interactions can be described as a second-order reaction according to:

$$c_i c_d \underset{k_{off}}{\overset{k_{on}}{\rightleftharpoons}} c_{id} \qquad 14$$

Binding event life times ("bright times") τ_B and interevent lifetimes ("dark times") τ_D (Fig. 13b) can be detected from single molecule binding sites. The association rate (k_{on}) can then be derived from τ_D and the imager concentration c_i according to:

$$k_{on} = \frac{1}{\tau_D c_i} \qquad 15$$

The dissociation rate k_{off} can be approximated as a first-order reaction and can thus directly be derived from the binding event lifetime (τ_b) according to:

$$k_{off} = \frac{1}{\tau_B} \qquad 16$$

Typical association rates for 7-10 nt docking strand-imager interactions are around 10^6 $M^{-1}s^{-1}$ and are only weakly dependent on the ssDNA length[66]. Dissociation rates are around 1 s^{-1}, but strongly dependent on the length of the docking strand-imager duplex formed, with the dissociation rate of the 9-mer being ~8 times higher than that of the 10-mer. DNA-duplex lengths and sequences have to be tuned for appropriate bright times of ~200-500 ms, as too short bright times prevent the harvesting of enough photons above the background, and too long bright times increase the probability for a PSF overlap of two imagers bound within a diffraction-limited spot.

This robust kinetic performance of DNA-DNA interactions of docking strands and imagers allows a precise molecular counting of the number of DNA-docking strands within a certain image area, also if they are below the resolution limit of DNA-PAINT.[67] If the imager influx rate $\xi = k_{on} c_i$ of a single binding site has been calibrated, the number of binding sites n_b can be calculated from the measured dark time τ_D^* according to:

$$n_b = \frac{1}{\tau_D^* \cdot \xi} \qquad 17$$

DNA-PAINT has many advantages over traditional (dye-based) super-resolution methods. Firstly, it is not limited by photobleaching, allowing the collection of tens to hundreds of blinking events in a measurement. Secondly, the programmability of DNA allows for a fine

tuning of the binding kinetics. Thirdly, due to its specificity, DNA allows for sequence-based multiplexing.

However, the first generation of DNA-PAINT sequences suffered from a major limitation: imaging was inherently slow.

1.4.4 Speed-optimized DNA-PAINT

When considering how to improve the kinetics for faster imaging, we have to first understand which parameters to optimize for. For optimal detection efficiency in DNA-PAINT, binding sites have to be "sampled" by an imager about 5-10 times during the measurement, to reliably detect the single binding site. So essentially, in order to increase speed, we need to achieve more sampling events (or "ON-events") within the same imaging time. To achieve this, both the bright times and the dark times have to be reduced. Bright times can be shortened relatively easily by reducing the length of imager strand, with the only limitation that bright times <<50 ms prevent sufficient photon collection. When aiming at reducing the dark time, the most straightforward strategy is increasing the imager concentration, which also quickly reaches a limit due to increasing background fluorescence.

Thus, Schueder et al. aimed at reducing the dark time by optimizing buffer salinity as well as DNA sequence design.[68] Increasing the $MgCl_2$ concentrations from 10 mM to 75 mM yielded a two-fold speed increase. However, optimizing the sequence design was the key to significantly improving k_{on}. The original P sequences had a reduced apparent k_{on} because they contained complementary bases, forming intramolecular hairpins. Hence, to prevent hairpin formation in speed-optimized sequences, they were designed to either contain only T and C or only A and G bases. The best-performing sequence (termed 'PS3') led to an approximately 5x shorter dark time, translating to a 10x speed increase when combined with the 2x salt-based speed increase.[68]

Last but not least, Strauss et al. even further increased DNA-PAINT imaging speed by introducing >1 imager binding motif per docking strand.[69] Instead of just stringing together the same docking strand sequence several times, periodic overlapping sequence motifs within a concatenated docking strand generated 5 possible binding motifs while only increasing the docking strand length by ~2.7-fold.[69] The binding kinetics linearly increased with the number of binding motifs introduced into the docking strand, ultimately resulting in 6 orthogonal speed-optimized sequences (R1-R6), with optimal properties for speed-optimized DNA-PAINT imaging.

1.4.5 Exchange-PAINT

The first generation of DNA-PAINT docking strand-imager pairs (P sequences) had very high direct multiplexing capabilities since they used all DNA bases within these sequences, tolerating intramolecular hairpin formation. This was powerfully implemented in Exchange-PAINT: Labeling 10 different origami with 10 orthogonal DNA-sequences (P1-P10), and addressing those with 10 different imager strands (P1*-P10*) allowed for the first 10-plex super-resolution image, which was later extended to 52 orthogonal P sequences.[70,71] The sequence orthogonality allowed for sequential imaging with only one optimal dye (Cy3B) and virtually no crosstalk between sequences. Moreover, due to the high photon yield during the bright times, and repetitive binding of imagers, docking strands can be localized with sub-2 nm precision, enabling up to 5 nm resolution in vitro.

Exchange-PAINT is universally applicable to cellular imaging, allowing for multiplexed imaging of organelles, such as mitochondria (Fig. 14).

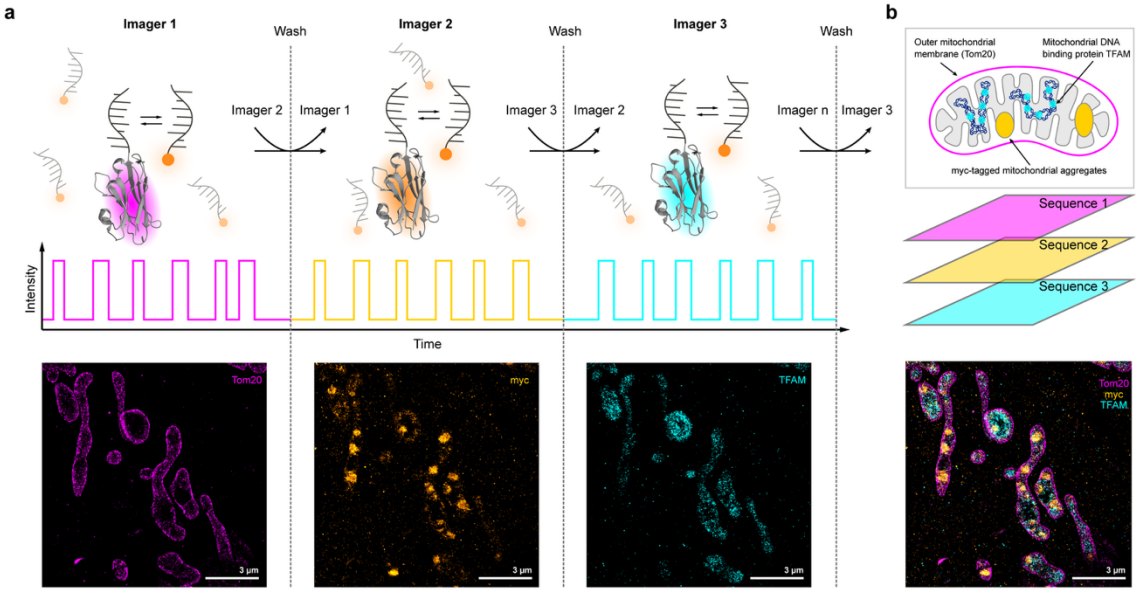

Figure 14: Exchange-PAINT. **a**, In this example, three orthogonal DNA docking strands are immobilized on the sample, each via an antibody specifically binding to a target of interest. In the first imaging round, complementary DNA imager strands to sequence 1 are introduced and the target is imaged. Then, imager 1 is washed away and imager 2, complementary to sequence 2, is introduced. After imaging target 2, the same washing and imaging cycles are repeated until all targets have been imaged sequentially. **b**, After the acquisition of all imaging rounds for three different targets in mitochondria, all channels have to be aligned to generate the final multiplexed image.

However, for speed-optimized Exchange-PAINT, the multiplexing is limited to 6 targets, due to only two non-complementary bases present per docking strand sequence, limiting the direct application in highly-multiplexed applications.[69]

Recent work from the Ganji laboratory showed that the speed-sequences can be extended to a total of 12-plex imaging with some risk of crosstalk.[72] However, extending speed-optimized DNA-PAINT imaging well beyond 12-plex required the application of secondary sequences.

This multiplexing limit was recently overcome by two studies introducing either transient[72] or stable[73] secondary adaptor sequences, called fluorogenic labeling in conjunction with transient adapter-mediated switching for high-throughput DNA-PAINT (FLASH-PAINT) and secondary label-based unlimited multiplexed DNA-PAINT (SUM-PAINT), respectively. SUM-PAINT allowed for the sequential readout of several sets of the 6 speed-optimized R-sequences, enabling up to 30-plex high-throughput DNA-PAINT imaging in cells and 42-plex imaging in DNA origami.[73,74]

1.4.6 3D imaging

SMLM relies on estimating the xy-coordinates from fitting a 2D Gaussian of single-molecule blinking events. This is sufficient for 2D DNA origami measurements since these structures are close to the surface and do not extend in the z-dimension. In biological samples, however, obtaining the 3D coordinate is of high importance.

In diffraction-limited microscopy, the 3D coordinates are usually obtained by scanning 2D slices of the sample sequentially, producing so called z-stacks with ~500 nm resolution. This is also possible for SMLM, but there is an additional need for improved resolution in z below 500 nm.[75]

One approach to retrieve both axial and lateral positions from a 2D blinking events recorded on a camera, is the introduction of optical astigmatism, as introduced by Huang et. al in 2008 (Fig. 15).[76] Inserting a weak cylindrical lens into the optical path creates two slightly different focal planes for the x and y directions, resulting in a broadening of the single-molecule spot, depending on the z-plane (Fig. 15a). When the single-molecule event is recorded exactly between the x- and y-focal planes, the PSF has equal widths in the x- and y-direction. When the fluorophore is above or below the average focal plane, it displays a PSF broadening along the x-axis or the y-axis, respectively.

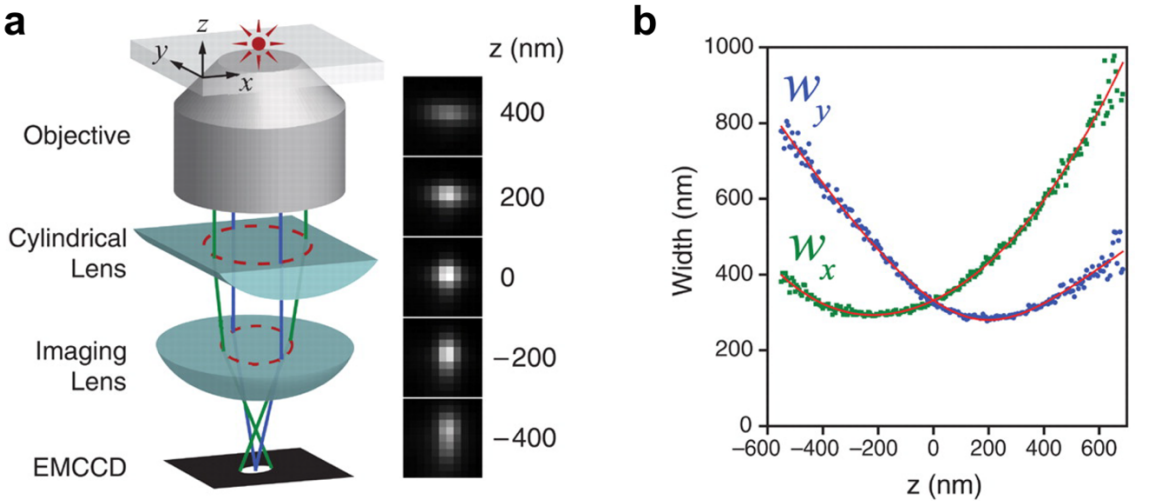

Figure 15: Astigmatism-based 3D imaging in SMLM. **a**, A cylindrical lens in the optical path changes focal planes depending on the x- and y-positions, resulting in recording an elliptical PSF. **b**, Calibrating the z-position depending on the PSF width in x (w_x) and y (w_y) allows the retrieval of z-coordinates with nm-precision. Reprinted with permission from[76].

Thus, the xy-coordinates are encoded in the peak position and the z-coordinate can be retrieved from the peak widths w_x and w_y (Fig. 15b). The axial resolution in astigmatic lens-based 3D SMLM imaging is about 2-3x worse than the lateral resolution, resulting in ~50 nm in standard SMLM, while also slightly reducing the precision in xy, due to the PSF broadening.

Astigmatism-based 3D SMLM is widely applied for convenient implementation in most standard TIRF microscopes, with a z-depth of up to ~1 μm.

1.5 Cell imaging with DNA-PAINT super-resolution microscopy

The DNA-PAINT toolbox theoretically enables unlimited multiplexing with sub-10 nm resolution in aqueous systems, making it an ideal tool to achieve true spatial proteomics with single-protein resolution. Speed-optimized imaging typically takes 10-50 minutes per channel and requires the sample to be completely immobilized over the whole measurement. This prevents live cell imaging and requires biological samples to be chemically fixed before imaging.

1.5.1 Sample preparation

Sample preparation for DNA-PAINT begins with standard cell culture techniques. Cells are seeded on suitable imaging surfaces such as high-precision glass coverslips or specialized imaging chambers compatible with total internal reflection fluorescence (TIRF) microscopy. Following this, cells undergo treatments relevant to the experimental design, including transfection, stimulation, or drug application.

To preserve structural integrity and epitope accessibility, cells are fixed using paraformaldehyde (PFA) and/or glutaraldehyde. The fixation process must maintain both the target protein's localization and accessibility for labeling probes. High-quality fixation is particularly crucial for DNA-PAINT, where prolonged imaging requires exceptional sample stability over hours.

1.5.2 Labeling probes

To visualize proteins of interest in fixed cells, DNA-docking strands have to be immobilized at the target of interest. Typically, DNA-conjugated labeling probes are used, which have to fulfil certain requirements for optimal DNA-PAINT imaging: (1) high specificity with little off-target binding, (2) high affinity with a low off rate, (3) small size with little linkage error, (4) stoichiometric binding of the target and (5) high availability for easy implementation.

1.5.2.1 Antibodies

The most commonly used labeling reagents are Immunoglobulin G (IgG) antibodies, mainly because of their high availability, affinity and specificity.

Antibody generation usually starts with immunizing animals with the antigen of interest. As a response to immunization, immature B cells with antigen-specific B cell receptors (BCR) become activated and start developing. Repeated immunization leads to clonal expansion and affinity maturation of antigen-specific BCRs, accompanied by a transition from IgM-BCR to IgG-BCR.[77] Ultimately, B cells develop into plasma cells, secreting antigen-specific IgG antibodies that are released into the animals' blood stream. Antibodies can then be isolated in two different qualities, polyclonal or monoclonal antibodies. To obtain polyconal antibodies, all the antigen-specific IgGs are purified from the animals' plasma and directly used for imaging or detection.

Polyclonal antibodies are normally directed against several different epitopes, increasing detection efficiency of the targeted protein in imaging applications.[78] However, the biological variability in polyclonal sera can result in low batch-to-batch consistency, and once the animals die, the antibody source disappears. To overcome these limitations, purified monoclonal antibodies (mAbs) can be generated from hybridoma cells, that are generated by fusion of individual B cell clones with melanoma cells, ensuring a high reproducibility and unlimited mAb supply.[77]

IgGs are large 150 kDa Y-shaped proteins, consisting of 2 identical copies of a heavy chain (HC) (50 kDa each) and 2 identical copies of the light chain (LC) (25 kDa) (Fig. 16a,b).[79] One HC forms a heterodimer with one LC, via disulfide bridge formation between the constant heavy chain (CH)1 and the constant light chain (CL) region. Two of these heterodimers dimerize via the CH2 and CH3 regions towards the HC C-terminus, thereby forming the so-called Fragment crystallizable (Fc)-region. This heterotetramer is further stabilized by covalent disulfide bonds between the HCs, in the so-called hinge region between CH1 and CH2 domains (Fig. 16b). The Fragment antigen-binding (Fab) region, located at the “arms” of the antibody Y-shape, consists of the variable domains of both HC and LC, as well as the CH1 and the variable light chain (VL). The combination of two antigen-binding regions in one molecule results in a high-affinity and high-avidity bivalent binder (Fig. 16b). The antigen-binding regions are located at the “tip” of the Fabs, more specifically in the complimentary-determining regions (CDRs). There are 3 unique CDRs in each variable region, with CDR3 of the HC being the largest (>20 amino acids), thus key for specificity.[80]

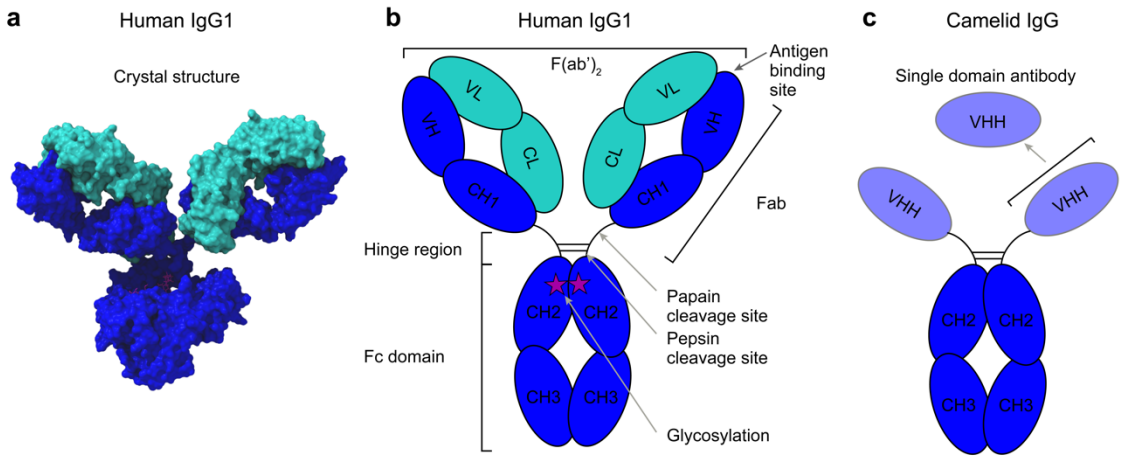

Figure 16: IgG antibodies. **a**, X-ray crystallography structure 1IGY of human IgG1. **b**, Schematic representation of human IgG1. The heavy chain (blue) consists of constant heavy chain (CH)3, CH2, CH1 and variable heavy chain (VH) domains with glycosylation (magenta) at the CH2 domain. The heavy chains are linked at the hinge region via 2 disulfide bonds. The light chain (turquoise) consists of constant light chain (CL) and variable light chain (VL) domains. Both variable chains make up the antigen binding site. **c**, Schematic representation of a camelid heavy chain only IgG, featuring only CH3 and CH2 domains as well as a variable heavy chain, responsible for antigen binding. This VHH is the basis for a single domain antibody (also termed nanobody).

For DNA-PAINT, primary antibodies can be labeled with DNA-conjugated secondary antibodies. However, antibodies are large, with a primary-secondary antibody “sandwich” displacing the fluorophore from the actual epitope by ~20 nm, thereby compromising detection accuracy, and spatial resolution (Fig. 17a). This linkage error can be reduced by directly conjugating antibodies with DNA, limiting displacement to ~10 nm (Fig. 17a). Direct antibody conjugation can be achieved in a stoichiometric and quantitative way, through enzymatic methods modifying the glycosylation sites, or through genetically encoded tags.[81]

A more cost-efficient and modular alternative are monovalent secondary binders, such as DNA-conjugated Fabs, or secondary Nbs. Secondary Nbs can also be used to stably label the primary antibodies by performing pre-incubation before labeling the sample, enabling the multiplexed imaging of several antibodies raised in the same species.[82]

Nevertheless, the bivalent nature of IgGs limits the stoichiometric labeling since it can be bound either in a 1:1 or 1:2 IgG:target stoichiometry.

1.5.2.2 Small monovalent binders

Consequently, the application of small monovalent binders is favorable for stoichiometric target labeling with minimal linkage error. To achieve this, there are several monovalent derivatives of IgG antibodies. IgGs can be digested with proteases such as papain to

directly obtain Fab fragments, or with pepsin to obtain F(ab')2 fragments, that can be further reduced to obtain monovalent F(ab'). These binders can be generated from any IgG and feature a reduction in size of about 67% when compared with the full IgG (Fig. 17a).

Other, recombinantly expressed IgG derivatives are single-chain variable fragments (scFv), comprising the variable regions of HC and LC, connected by a flexible linker. Their smaller size (~25–30 kDa) compared to full-length antibodies allows better tissue penetration and reduced steric hindrance, which is advantageous for super-resolution imaging. scFvs can be genetically fused to DNA docking strands or tags facilitating site-specific conjugation, whereas Fabs and F(ab')s have to be conjugated via their free sulfhydryl groups or NHS-chemistry.

However, these IgG derivatives are facing challenges such as lower stability compared with the very stable IgG molecules, necessitating optimization for each monovalent binder.

Non-IgG affinity reagents are small proteins such as affimers or designed ankyrin repeat proteins (DARPins), both between 12 and 18 kDa in size. They can be engineered to bind specific targets with high affinity and specificity and expressed recombinantly, allowing for site-specific modifications with DNA. Their monovalent nature and minimal cross-reactivity make them ideal for imaging closely spaced targets in crowded environments, however the availability for several targets is still limited. Affimers have been used to specifically label cytoskeletal proteins as well as receptor tyrosine kinases (RTK), significantly reducing linkage errors in super-resolution microscopy.[83,84]

Besides protein-based labeling reagents, there are DNA- and RNA-based reagents that are able to specifically bind to cellular with high affinity, when folded into defined three-dimensional structures. These so-called aptamers are synthesized in vitro allowing for a seamless incorporation of DNA docking strands directly into their structure, thereby eliminating the need for additional conjugation steps. Due to their highly negatively charged nature, they require specialized blocking conditions in immunofluorescence staining and can suffer from relatively high off-rates reducing labeling efficiency. Thus, for DNA-PAINT, slow off-rate modified aptamers (SOMAmers) have been successfully used to perform multiplexed imaging and quantitative labeling and even live cell tracking of EGFR molecules.[85]

The most commonly used monovalent binders in advanced imaging applications are Nbs, which combine the advantages of both conventional IgG antibodies and non-IgG protein scaffolds. Nbs, also known as single-domain antibodies, are derived from the unique class of heavy-chain-only antibodies found naturally in camelids (e.g., llamas and alpacas).[86]

Unlike traditional IgGs, which consist of both heavy and light chains, camelid heavy-chain antibodies are composed solely of heavy chains, and their antigen-binding region is a single variable domain known as VHH (Fig. 16c). VHH domains can function independently, since they have a longer CDR3 loop compensating for the missing VL domain.[86] Nbs are essentially these isolated VHH domains, with a molecular weight of approximately 12-15 kDa, making them about one-tenth the size of a full IgG. Despite their small size, Nbs retain high binding affinity and specificity to their target epitopes. Their robust structural stability, resistance to denaturation, and ease of recombinant expression make them ideal for use in super-resolution microscopy techniques.[87,88]

In DNA-PAINT, Nbs are increasingly favored due to their ability to minimize linkage error, achieving precise and accurate molecular localization at the nanoscale.[85] Nbs can be conjugated to DNA docking strands either via chemical crosslinking or through site-specific enzymatic labeling methods, such as sortase-mediated transpeptidation or click chemistry.

1.5.2.3 Genetically Encoded Tags

Another widely used strategy for site-specific labeling in DNA-PAINT super-resolution microscopy involves the use of genetically encoded tags that can be fused directly to the protein of interest via genetic engineering. These tags include self-labeling enzymes, such as SNAP-tag and HaloTag, allowing direct labeling in a 1:1 labeling stoichiometry of a protein of interest. The corresponding ligands can be pre-functionalized with DNA docking strands, enabling their direct use in DNA-PAINT imaging. Alternatively, fluorescent proteins, such as GFP, RFP and TagFP, can also serve as specific tags, since they can be addressed with their cognate Nbs, enabling high labeling efficiency and precise targeting of the protein of interest. The tag-complex is about 7-9 nm in size and features stoichiometric binding both for self-labeling enzymes, making both ideal tools for super-resolution microscopy (Fig. 17a).

Perhaps the most suitable approach for super-resolution microscopy are peptide tags, that can be targeted with cognate Nbs. Due to their small size of below 5 kDa, peptide tags introduce minimal spatial displacement, which is advantageous over larger tags like GFP or HaloTag. The BC2 tag is a short peptide sequence (PDRKAAVSHWQQ) recognized by the anti-BC2-nanobody (Nb), that however needs the Nb to be bivalent to reach sufficient affinity for super-resolution imaging.[89] The ALFA-tag is a rationally designed 15-amino-acid peptide (SRLEEELRRRLTE) that adopts a stable α-helical structure and is specifically recognized by the anti-ALFA Nb with low picomolar affinity.[90] This high-affinity interaction

allows for efficient labeling of ALFA-tagged proteins even after PFA fixation with minimal labeling uncertainty because of the small size of the ALFA-tag-Nb complex (Fig. 17a).

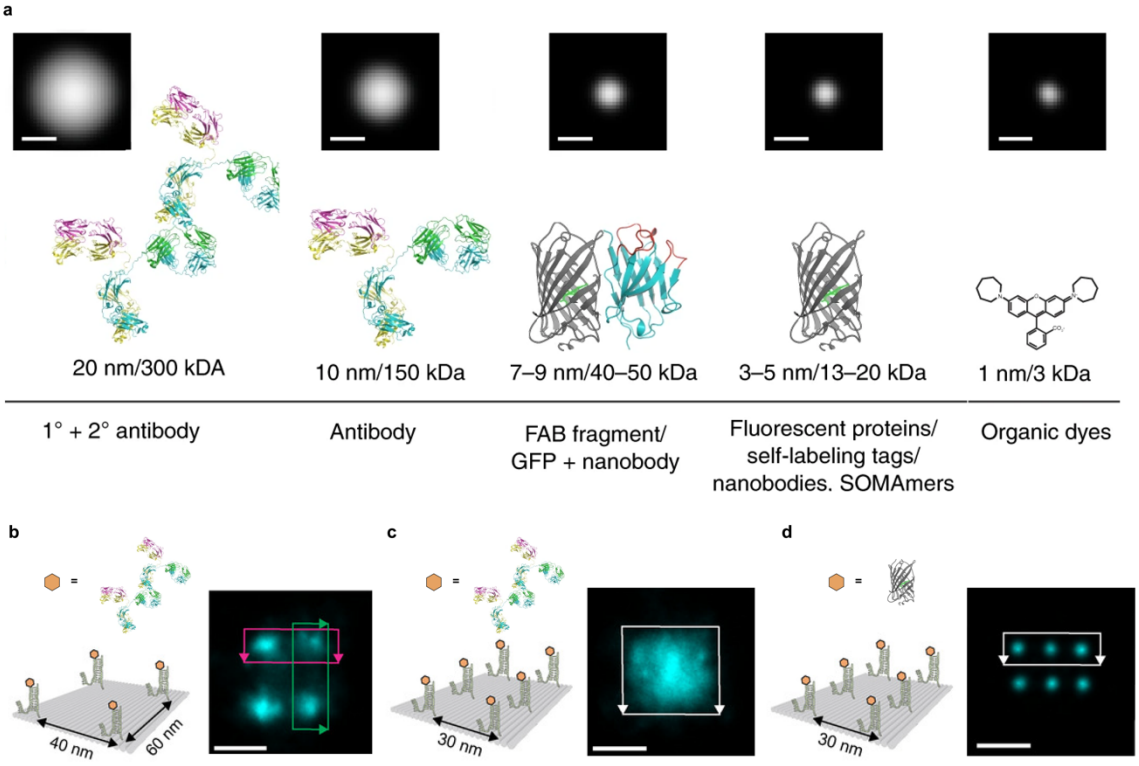

Figure 17: Label size in DNA-PAINT. **a**, Primary and secondary antibody "sandwiches" result in a decrease in labeling accuracy and precision by effectively displacing the label from the target molecule by ~20 nm. Directly labeled primary antibodies result in an improved labeling accuracy and precision, displacing the label by ~10 nm. Genetically encoded tags labeled with Nbs or Fab fragments with sizes of 7-9 nm further reduce the labeling uncertainty. Direct Nbs or SOMAmers reduce the labeling uncertainty even further to ~3-5 nm. Direct labeling with organic dyes induces minimal displacement of the label by ~1nm. **b**, Primary and secondary antibody complexes, labeling antigens immobilized on a DNA origami with 40 nm and 60 nm distances, can be resolved with DNA-PAINT. **c**, Primary and secondary antibody complexes labeling antigens deposited on a DNA origami with 30 nm distances, cannot be resolved with DNA-PAINT, due to the size of the label. **b**, Labeling antigens, deposited on a DNA origami with 30 nm distances, with anti-ALFA Nb can be resolved with DNA-PAINT. Reprinted with permission from[91,92].

The linkage error depending on the labeling strategy is impressively demonstrated by measuring different distances on DNA origami (Fig. 17b-d). For antigens labeled with primary and secondary antibodies, only distances above 30 nm could be reliably measured (Fig. 17b,c).

In the case of monovalent binders, such as aptamers and Nbs, the width of the distributions is considerably smaller due to the reduced linkage error and allows to resolve distances of 30 nm and beyond (Fig. 17d).[87,92]

To summarize, all of the abovementioned labeling strategies are used in DNA-PAINT super-resolution microscopy. Antibodies are mostly applied for their high specificity, high affinity and high availability for easy implementation. Combined with secondary Nbs, they have been impressively used for 30-plex imaging of neuronal targets.[74] Direct small binders are employed for specific targets, such as cytoskeletal proteins and receptor tyrosine kinases (RTK), when suitable reagents are available, offering high precision and spatial resolution due to minimal linkage error and stoichiometric binding to their targets.[83] Genetically encoded tags offer the strong benefit that they can be in principle attached to any protein of interest in the cell, allowing for monovalent and specific targeting with minimal linkage error in cellular systems, with high affinity Nbs. However, the ideal labeling approach for DNA-PAINT, are small, monovalent, high affinity, direct binders –such as Nbs or aptamers – that are currently not available for every protein in the cell.

1.5.3 Labeling chemistry

For detection in DNA-PAINT, monovalent binders have to be site-specifically conjugated with ssDNA docking strands. Since scFvs, affimers, DARPINs and Nbs can all be recombinantly expressed in bacteria, this allows for the placement of short amino acid sequences to allow for site-specific conjugation.

1.5.3.1 Single cysteine

One approach uses the high reactivity of the sulfhydryl group in single C-terminal cysteines towards maleimide-linkers. A carbon atom adjacent to the double bond of the maleimide ring undergoes nucleophilic attack by the thiolate anion, resulting in the formation of a stable addition product.[93] The pH of the reaction medium has a critical impact on the rate of the conjugation as it requires deprotonated thiols to react with the maleimide ring. Thiolate formation increases with pH, typically above pH~8.0-9.0 for free thiols. However, maleimides are susceptible to hydrolysis at alkaline pH, forming maleamic acid derivatives that are unreactive toward thiols.[93] As a result, the optimal pH range is 6.5 to 7.5, balancing the availability of reactive thiolates with maleimide stability and thereby slightly reducing the speed of the reaction.[93]

Even though it is theoretically possible to directly react cysteines with Maleimide-DNA in a one-step-reaction, in practice the negatively DNA molecule leads to electrostatic repulsion and reduces reaction efficiency. To circumvent that, the cysteine-containing protein can first be reacted with a polyethylene glycol (PEG)yalted maleimide-linker, carrying another

reactive unit (Fig. 18). This reactive unit is often an alkyne derivative that can undergo click chemistry with azides under ambient conditions.[94] While earlier click chemistry implementations required metal catalysts, such as copper cations to perform the cycloaddition, the strain-promoted [3 + 2] azide-alkyne cycloaddition click chemistry (SPAAC) between cyclooctynes and azides now allows for conjugation under physiological conditions without the need for a catalyst.[95] Thus, in a second step, the maleimide-conjugated linker bearing a Dibenzocyclooctyne (DBCO) molecule can be reacted with an azide-modified DNA docking strand (Fig. 18). It enables rapid, high-yield chemical conjugation under mild and biocompatible conditions, even with the negatively charged DNA attached to the azide. Even though reaction rates in SPAAC are mostly $<10^0$ $M^{-1}s^{-1}$ [96] and thus about 100-10000-fold slower than the maleimide-cysteine reaction[97,98], the almost complete absence of competing reactions in the former results in a high conjugation efficiency, approaching 100% in ideal systems.[99]

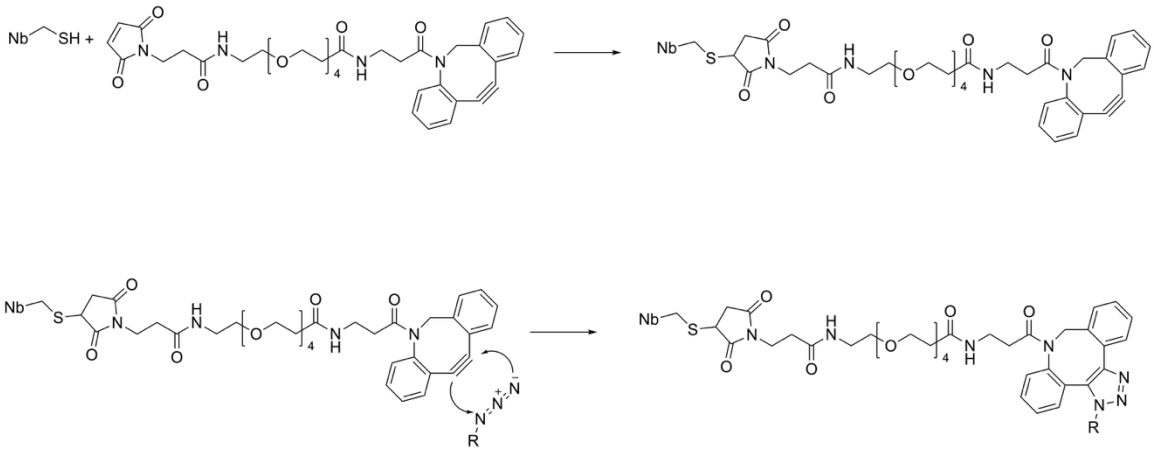

Figure 18: Functionalization of molecules carrying a free sulfhydryl group (e.g. cysteine). In the first step, the sulfhydryl group reacts with the maleimide-containing, polyethylene glycol (PEG)ylated linker (top). In a second step, the dibenzocyclooctyne (DBCO) on the other side of the linker can be reacted with an azide-containing molecule (R is DNA in the case of DNA-conjugation for DNA-PAINT) in a so-called strain-promoted azide-alkyne cycloaddition click (SPAAC)-reaction (bottom). Structures were generated with ChemDraw.

1.5.3.2 Sortase-mediated conjugation

To circumvent the need for a single C-terminal cysteine, sometimes impacting the solubility and causing dimerization of the target protein, enzymatic site-specific conjugation methods can be employed. The most commonly used enzymatic conjugation strategy is sortase-mediated labeling.[100]

Sortase A is an enzyme derived from *Staphylococcus aureus*, that recognizes the short peptide motif LPXTG encoded at the N- or the C-terminus of the protein of interest. The enzyme catalyzes a transpeptidation reaction, cleaving between the threonine and glycine in this motif and catalyzing the formation of a new covalent amide bond between the cleaved protein and an incoming GGG-modified DNA docking strand. This results in a site-specific, stable linkage between the DNA label and the target protein (Fig. 19).[101]

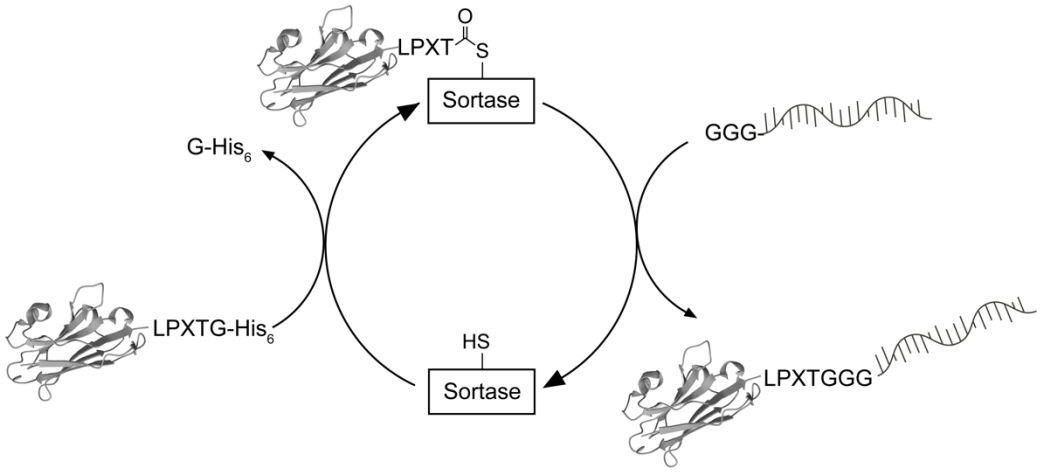

Figure 19: Sortase-mediated labeling. A binder (e.g. a Nb) with a the LPXTG recognition motif for sortase reacts with the enzyme (left). Sortase cleaves the threonine-glycine bond in the motif via its active site cysteine residue (HS), removing the C-terminal glycine and forming an acyl intermediate with the binder (left). This intermediate can then react with a poly-glycine-functionalized molecule (here DNA), thereby conjugating the binder with the poly-glycine functionalized molecule via the LPXT-motif. This regenerates the active site cysteine on the sortase.[101,102]

Most sortase versions are dependent on Ca^{2+} in the buffer and are relatively slow, but some mutants have sufficient catalytic activity without the need for Ca^{2+} in the buffer. For example, sortase heptamutants have shown an almost 100-fold increase in the enzymes k_{cat}, when compared with the wild-type enzyme, making it very well suitable for bioconjugation applications.[103] Nevertheless, sortase-mediated labeling is gentler than maleimide-cysteine chemistry, as there is no need to reduce disulfide bonds. In addition, the separate step of adding a maleimide-DBCO-linker can be omitted by directly reacting protein-LPXTG with GGG-DNA, increasing the speed and the yield of the conjugation reaction.

To summarize, both maleimide-cysteine-based and sortase-mediated conjugation strategies can be employed for site-specific and stoichiometric conjugation of binders for the application in super-resolution microscopy.

1.6 Membrane receptors in cancer immunotherapy

In order to integrate into the complex unity of a multicellular system, cells have to constantly exchange with the cells around them. This is required to regulate the growth, differentiation, migration, and elimination of cells. Their contact with the environment is regulated by transmembrane proteins, spanning across the lipid bilayer with their extracellular, transmembrane, and intracellular domains. Transmembrane proteins fulfill various functions, including signaling, regulating the transport of small molecules and ions, catalyzing reactions, and maintaining cellular stability and tissue integration.[104]

Cellular signaling is mediated by cell membrane receptors, which are key regulators of cellular fate. This positions them among the most important targets for drug development, with over 50% of current pharmaceutical targets being membrane receptors.[105] Among these are G protein-coupled receptors (GPCR), regulating a wide range of physiological processes, including sensory perception, immune responses, and neurotransmission. Due to their central role in cell signaling and their accessibility on the cell surface, GPCRs alone account for approximately one-third of all approved pharmaceuticals.[106]

Due to their precise control over cell fate, membrane receptors are key targets in cancer immunotherapy.[107,108] The intramolecular structural changes involved in receptor activation and signaling have been extensively studied *in vitro* using structural biology methods such as X-ray crystallography and cryo-EM. To investigate the nanoscale structural changes accompanying activation in the cell membrane, super-resolution microscopy techniques can be employed, with the ultimate goal of linking receptor structure to function in a cellular context.

1.6.1 Ligands and receptors in cellular signaling

One of the most extensively studied groups of membrane receptors is the ErbB/HER family, a subset of RTKs. These receptors are key targets in cancer therapy due to their critical role in regulating cell proliferation, differentiation and migration.[109] The first ligand-receptor pair to be discovered was epidermal growth factor (EGF) and the corresponding EGF receptor (EGFR).[110] EGFR (also known as HER1) is one of four members of the ErbB/HER family, which also includes HER2 (ErbB2), HER3 (ErbB3), and HER4 (ErbB4). All four receptors are frequently implicated in oncogenesis and therapeutic resistance due to their dysregulation, overexpression, or mutation across a range of cancers, including breast, lung, brain, and gastrointestinal malignancies.[111]

On a molecular level, EGF specifically binds to the EGF receptor (EGFR/HER1) at the extracellular domain, thereby inducing intracellular signaling, via intracellular tyrosine phosphorylation.[112] EGF binding first causes a conformational change in EGFR, followed by a specific dimerization of two EGFR molecules.[113] The two EGFRs in the dimer phosphorylate each other on specific tyrosine residues in their intracellular domain, also referred to as cross-phosphorylation.[114] The phosphorylated tyrosines serve as docking sites for downstream signaling molecules, activating pathways such as mitogen-activated protein kinase (MAPK) cascade, phosphatidylinositol 3-kinase and STAT signaling.[115] In cancer, mutations or overexpression of ErbB/HER receptors can lead to ligand-independent activation or hypersensitivity to low ligand concentrations, promoting tumor growth.[111] Many oncogenic EGFR mutations stabilize EGFR in an active state or weakly self-associate without needing a ligand, thus eliminating the need for ligand-induced dimerization to activate downstream signaling.[116] Downstream of activation, EGFR signaling is downregulated by internalization and recycling of EGFR and EGF.[117]

It is still debated if EGFR dimerization is only induced upon EGF binding or if EGF binding activates pre-formed inactive EGFR dimers.[117,118] Super-resolution microscopy studies of EGFR in the cellular context indicate EGFR monomers that dimerize only upon EGF treatment.[118] Besides EGFR dimers, higher order structures of EGFR and bound EGF have been postulated.[119] Single-molecule studies of EGF when bound to EGFR on cells, indicate linear EGFR multimers with EGF bound only at the ends of these arrangements.[119] Contradicting super-resolution microscopy studies postulate EGFR-multimers with EGF bound on all EGFR binding sites, forming clusters in an offset rectangular arrangement.[118]

EGFR not only homo-oligomerizes but also hetero-oligomerizes with other HER/ErbB family receptors and thereby influences signaling outcomes: HER2 cannot be activated by ligands, but acts through hetero-dimerization with one of the other HER-family proteins, and is often overexpressed in breast cancer.[120] HER3 on the other hand lacks intrinsic kinase activity and relies entirely on heterodimerization, particularly with HER2, to activate downstream pathways.[121] Dysregulated oligomerization of these receptors, is strongly associated with aggressive forms of cancer.[122]

Targeting the ligand-receptor interaction, or the receptor homo-or heterodimerization by monoclonal antibodies, has emerged as a successful therapeutic strategy. Agents like trastuzumab (targeting HER2/ErbB2) and cetuximab (targeting EGFR) are able to block ligand-mediated RTK activation in cancer therapy.[123,124] Thus, the precise regulation of ligand-receptor interactions at the cell surface remains a crucial focus in the development of targeted anticancer therapies.

1.6.2 CD20 in cancer immunotherapy

Before targeting EGFR, the first ever membrane receptor target exploited for cancer immunotherapy was the Cluster of Differentiation (CD)20 membrane receptor.[125] CD20 is a general B cell marker, expressed starting from late pre-B lymphocytes and terminated by plasma cell differentiation.[126] Apart from B cells, a small subset of $CD20^+$ T cells with immune-regulatory and pro-inflammatory activity has been described.[127,128]

Due to its almost exclusive and relatively high expression in most B cell development stages, CD20 is a prime target for tumors of the B cell lineage. Both “healthy” B cells and CD20-positive tumors are rapidly and almost completely depleted by anti-CD20 antibody administration for ~6 months.[129]

CD20 is a phosphorylated, non-glycosylated membrane protein of 33-37 kDa with no known ligand.[126] It is a member of the membrane-spanning 4-domain family A (MS4A) family of proteins, with N- and C-terminus residing in the cytosol (Fig. 20). CD20 features a small and a large extracellular loop (ECL), ECL1 and ECL2, respectively, with the latter providing the major epitope for antibody binding (Fig. 20).[130] In situ chemical crosslinking in lymphoma cell lines, as well as native immunoprecipitation of CD20 mutants in Burkitt lymphoma cell lines indicated the presence of CD20 monomers, homo-dimers as well as -tetramers on the cell surface.[131,132]

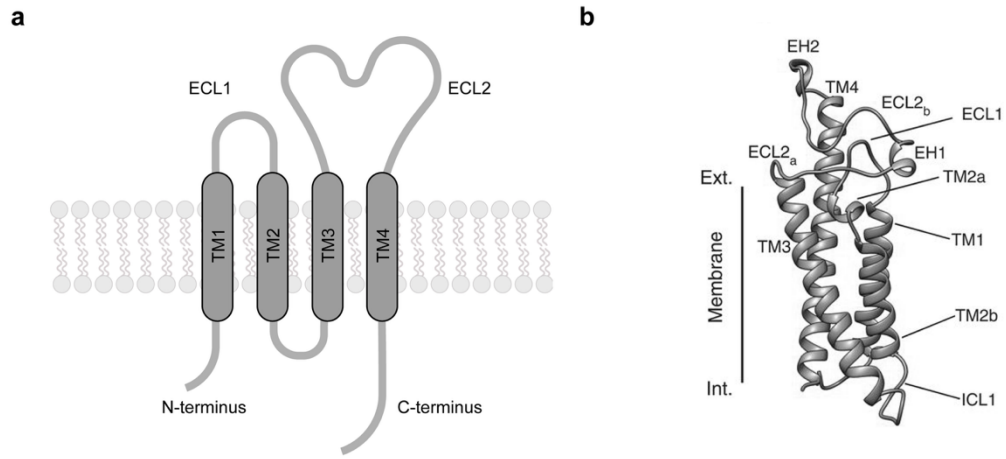

Figure 20**:** Structure of the CD20 membrane protein. **a**, Schematic representation of CD20. It has 4 transmembrane domains with the N- and the C- terminus located in the cytosol. **b**, Cryo-EM structure of CD20. Reprinted with permission from[133].

Early studies described CD20 as a Ca^{2+} channel regulating B cell activation.[134] $CD20^{-/-}$ mice and humans without any CD20 surface expression do not have an obvious phenotype and show normal B cell development.[135,136] However, an impaired response to both T cell-dependent and -independent antigens in the case of CD20 absence suggests a vital function in the formation of long term immunity.[135-137]

Biochemical investigations have shown that CD20 is heavily involved in B cell activation, as direct CD20 crosslinking induces acute signaling similar to BCR crosslinking, with overlapping transcription patterns in human lymphoma cell lines.[138] In addition, the IgM-BCR was found to associate with CD20 in unstimulated cells and rapidly dissociates upon anti-IgM crosslinking.[132,139] Contrasting data obtained with proximity ligation assays describes CD20 co-localization with the IgM-BCR in lipid rafts upon B cell activation.[140] In these lipid domains, CD20 further co-localizes with CD19, CD81, CD20, CD40, and CXCR4.[141,142]

Klaesener et al. showed that CD20 prevents B cell activation by localizing to IgD nanoclusters, separately from the IgM-BCR.[143] CD20 knockout (KO) or downregulation provokes a loss of the B cell resting state, ultimately leading to a differentiation into plasma cells, introducing CD20 as a gatekeeper of the B cell resting state.[143] This implies that anti-CD20 mAbs can interfere with B cell activation cascade, thereby influencing signaling outcomes and the mechanism of action in cancer therapy.

The anti-CD20 mAb rituximab (RTX) was approved in 1997, and since then, it has been widely applied in the treatment of B cell derived leukemia and lymphoma cases. It

improves overall survival rates and progression-free survival when added to standard chemotherapy (CHOP).[125,126,144] RTX's success prompted the development of several anti-CD20 mAbs, including tositumomab (TOS), ocrelizumab (OCR), ofatumumab (OFA), and obinutuzumab (OBZ).[144] Besides cancer, anti-CD20 immunotherapies have been extended for autoimmune diseases such as rheumatic arthritis, systemic lupus erythematodes as well as multiple sclerosis, for their ability to fully deplete B cells.[145-147]

Anti-CD20 mAbs are known to evoke (cancer) cell depletion mechanisms to different degrees, which is why they are sub-classified into Type I and Type II antibodies.[126,148,149] RTX, OCR and OFA are classified as Type I, with abilities to cluster CD20 and induce complement activation, whereas OBZ and TOS are classified as Type II with the ability to induce direct cell death.[126,149-151]

Type I mAbs evoke src family kinase-dependent, caspase-mediated apoptosis[152,153], whereas Type II CD20 antibodies induce lysosome-mediated cell death through actin reorganization, independent of caspase pathways.[144,150] Perhaps the most quantitative difference among the two types of mAbs is the ability of Type I mAbs to bind around twice as many CD20 molecules on each cell than Type II mAbs.[154]

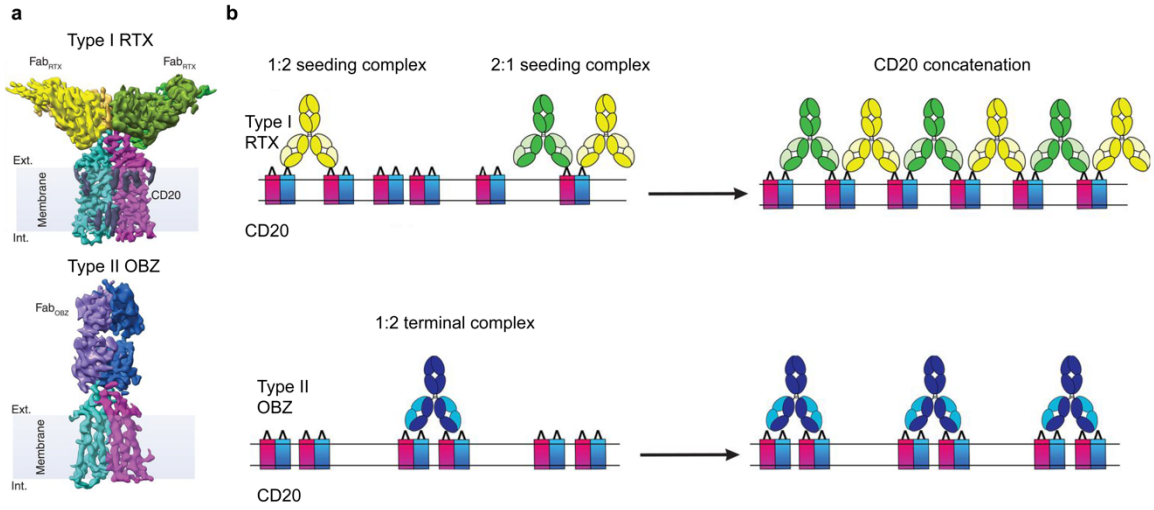

Figure 21: Cryo-EM structures of CD20 dimers bound to therapeutic antibody Fabs. **a**, Two Type I RTX Fabs bind to one CD20 dimer. One Type II OBZ-Fab binds to one CD20 dimer. **b**, Proposed models for Type I and Type II monoclonal antibody (mAb) binding to CD20 in cells. Type I mAbs are proposed to form concatenated CD20 assemblies. Type II mAbs are proposed to bridging two CD20 dimers to induce CD20 tetramers. Reprinted with permission from [155].

In 2020, detailed Cryo-EM structures of Type I and Type II-Fab fragments bound to CD20 provided a molecular reason for differences in function.[133,155] CD20 was detected as a tightly packed dimer co-crystallized with either two Type I Fabs (derived from RTX or OFA) or one Type II Fab (derived from OBZ) bound per CD20 dimer (Fig. 21a).[133,155] This explains the 2:1 ratio of Type I:Type II binding to $CD20^+$ cells lines. More strikingly, this suggests an ability of Type I RTX IgGs to bridge individual CD20 dimers on the B cell surface, therefore leading to CD20 concatenation and highly clustered CD20 molecules (Fig. 21b, top).[155] OBZ, on the contrary, is theoretically limited to bringing two CD20 dimers into close proximity, leading to dimeric assemblies of CD20 dimers and no big CD20 clusters (Fig. 21b, bottom).[155]

Overall, there appears to be a close relationship between structure and function in anti-CD20-directed cancer immunotherapy, which strongly depends on the specific properties of the therapeutic antibody.

1.6.3 Therapeutic antibodies

As introduced previously in chapter 1.5.2, antibodies can be generated against almost every target with high specificity and affinity. In addition, IgGs have a high biocompatibility for human treatment paired with a long half-life. This has made mAbs against membrane receptors a cornerstone of targeted treatment in autoimmune diseases, infectious diseases and cancer. Over the past four decades, the number of therapeutic antibodies entering clinical trials has increased exponentially. While in the 1980s and 90s, only a few such antibodies were introduced per year, the annual number has surpassed 300 in recent years, showing the increasing importance of these targeted therapies.[156,157] This shows both the relevance of these biologics and also the advances that have been made in the past years.

1.6.3.1 From murine to human antibodies

The first FDA-approved therapeutic mAb, OKT3, was a murine mAb targeting CD3, developed to prevent transplant rejection.[158] However, it triggered strong human anti-mouse antibody responses, reducing efficacy and causing adverse effects due to its fully murine protein structure.[159] To overcome this, chimeric antibodies were developed by combining murine variable regions with human constant regions, improving effector functions and reducing immunogenicity, with rituximab (anti-CD20) and cetuximab (anti-EGFR) being key examples.[124,160] Further reduction of immunogenicity led to the creation

of humanized antibodies, where only the murine CDRs are grafted onto human IgG frameworks, as seen with trastuzumab (Herceptin) for HER2-positive breast cancer.[161] Today, fully human antibodies can be generated through humanized transgenic mice, phage display libraries, or directly from human B cells.[162]

1.6.3.2 Human IgG subclasses

IgGs have four distinct subclasses, IgG1, IgG2, IgG3, and IgG4, with differences in their constant regions.[80] IgG1 isoforms particularly differ in their hinges and upper CH2 domains. IgG1 has a very flexible 15 amino acid hinge region, only surpassed by IgG3 whose hinge region is about four times as long.[163] The IgG4 hinge region is a bit shorter than the IgG1 hinge, reducing the flexibility. The least flexible hinge is that of IgG2, featuring rigid, poly-proline sequences and four inter-HC disulfide bridges that can also undergo alternative disulfide bond formation, resulting in disulfide bond isomers.[163]

IgG1 remains the most widely used isotype for therapeutic antibodies due to its strong binding to Fcγ receptors (FcγRs) on effector cells, and efficient activation of the complement system via C1q, combined with favorable developability attributes such as stability, manufacturability, and a long serum half-life. In some applications however, such as receptor blockade or bispecific antibodies, no Fc-mediated downstream effects are desired but the extended serum half-live via neonatal Fc receptor-recycling is still desired. For this purpose, IgG4 is the preferred isotype, since this subclass shows no C1q binding and reduced Fc receptor binding compared with IgG1.[80,164] Apart from that, only a limited number of IgG2-based therapeutics are used, as they exhibit even lower binding to FcγRs and minimal C1q binding. Nevertheless, the complex IgG2 structure, including hinge-region isoforms, presents manufacturing challenges that limit its applicability. As opposed to IgG4 and IgG2, IgG3 exhibits even stronger FcγR and C1q binding than IgG1, making it, in principle, a strong candidate for immunotherapy. However, it is prone to proteolysis and aggregation, and sometimes displays a reduced half-life in the body.[165] Therefore, there are currently no IgG3-based therapeutics on the market.

To summarize, IgG4 is preferred when immune activation is not desired. IgG2 and IgG3 are rarely used due to structural complexity and, in the case of IgG3, a short half-life. Thus, IgG1 is the most widely used antibody isotype due to its strong effector functions, stability, and long half-life.

1.6.3.3 Mechanism of action

Many monospecific antibodies directed against cancer cells mainly act through FcγR recognition, ultimately leading to tumor cell depletion.

Antibody-dependent cellular cytotoxicity (ADCC) is a mechanism mainly mediated through FcγRIIIa on natural killer (NK) cells, that then secrete granzyme and perforin to promote apoptosis in cancer cells (Fig. 22).[166]

Antibody-dependent cellular phagocytosis (ADCP) can be performed by macrophages and monocytes expressing high-affinity FcγRI and medium-affinity FcγRIIa, and by neutrophils expressing FcγRIIa and FcγRIIIb (Fig. 22).[167]

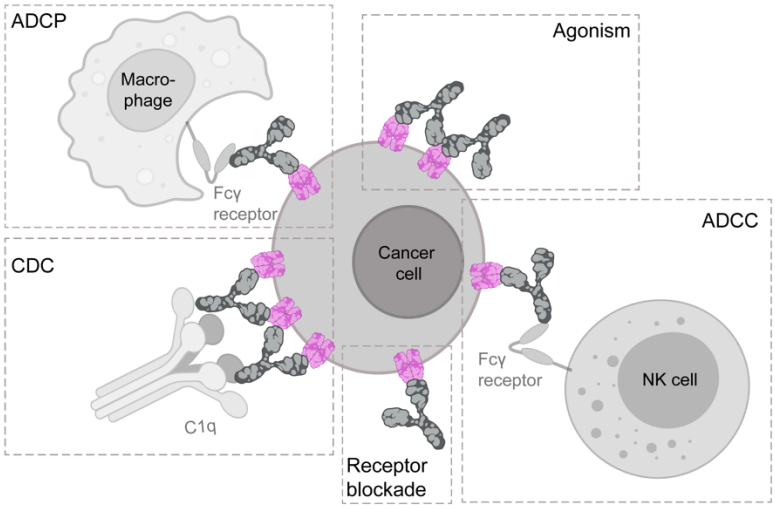

Figure 22: Mechanism of action of therapeutic antibodies. Cancer cells can be depleted by mechanisms such as Antibody-dependent cellular phagocytosis (ADCP), Antibody-dependent cellular cytotoxicity (ADCC), Complement-dependent cytotoxicity (CDC), receptor blockade, or by agonism exerted by therapeutic antibodies.

There is also a cell-independent Fc-mediated mechanism, called complement-dependent cytotoxicity (CDC) (Fig. 22). Soluble complement proteins are constantly present in the blood and play essential roles in both innate and adaptive immunity. The classical complement pathway is activated by C1 complex binding (composed of C1q, C1r and C1s) to oligomerizing therapeutic antibodies on cell surfaces. Since the flexible hinge region is accessible for C1q binding, IgG1 antibodies show the highest capabilities of triggering strong complement activation. The C1q protein is a hexameric molecule, connected at the "stalk" region and capable of binding with its six globular heads. Each of the heads has a

low (micromolar) affinity for a region close to the CH2 domain of IgG1 Fc, thus requiring high avidity to stably bind to cells. It carries 2 copies each of the serine proteases C1r and C1s that are activated after C1 binding. This starts a proteolytic cascade, leading to the cleavage of C4 and C2 and formation of the C3 convertase (C4b2a). The convertase cleaves C3, which promotes C5 cleavage and ultimately leads to the formation of the membrane attack complex, resulting in target cell lysis.[168,169]

Research by Diebolder et al. showed that introducing mutations in the Fc region of IgG1s, such as E345R (optionally combined with E430G and S440Y), can lead to IgG1 hexamer formation *in vitro* which in turn promotes C1q binding.[170] Similar mutations are applied by Genmab to generate IgG1-based therapeutic antibodies with enhanced effector functions.[171]

An Fc-independent mAb-function is to simply block the binding of a membrane receptor to its soluble or membrane-bound ligand that is involved in disease progression, thereby acting as an antagonist (Fig. 22). This is the main mechanism for mAbs blocking either Programmed Cell Death Protein (PD)-1 or PD-L1, on T cells or tumor cells, respectively. The blockade reduces PD-1-PD-L1 interactions that can, in the untreated case, stop T cells from killing the tumor. PD-1-PD-L1 checkpoint blockade has revolutionized cancer treatment, with the anti-PD-1 antibody pembrolizumab being the current “blockbuster” drug for PD-L1-positive tumors, approved for a wide range of advanced tumors, such as melanoma, Non-Small Cell Lung Cancer, B cell lymphoma and Triple-Negative Breast Cancer, among others.[172] Additionally, this receptor blockade mechanism is exploited in antibodies blocking the interaction between the ligand vascular endothelial growth factor and its receptors, thereby reducing angiogenesis in tumors and abnormal vessel growth in eye diseases.

Besides just blocking receptors, therapeutic antibodies can also exert direct effects after binding with two Fabs at the same time. Due to their bivalent nature, certain antibodies can act as receptor agonists by effectively cross-linking and clustering them on the cell surface (Fig. 22).[173-175] This plays a role for tumor necrosis factor receptors (TNFR), in which antibodies can mimic the activating ligand function. For example, CD40-agonist antibodies can lead to B cell activation[175], whereas Death receptor (DR)5 agonists can induce tumor cell killing[173]. Depending on the therapeutic purpose, agonists have to be fine-tuned to either activate or suppress immune responses and therefore have a huge potential to treat cancer and autoimmune diseases, respectively.[176,177] However, in practice antibody-agonists are challenging to develop as they tend to show weak on-target but high off-target effects. One famous case is the superagonistic anti-CD28 antibody, designed to expand regulatory T cells (Tregs). However, first-in-human studies resulted in severe

cytokine release syndrome within hours, as also additional T cell subsets besides Tregs, were strongly activated.[178] Agonism is often mediated or potentiated by Fc domain-mediated effects as binding of Fc receptors on immune effector cells to the antibodies bound on target cells can lead to more pronounced crosslinking.[179]

Apart from monospecific antibodies, there are also bispecific antibodies, recognizing two different antigens with two different Fab fragments combined on the same molecule. From an antibody engineering perspective, this poses additional challenges as heavy and light chains from two specificities can mispair. This mixture of both monospecifics and bispecifics is challenging to separate. To circumvent that, heavy chain heterodimers can be favored by knob-into-Hole (KiH) technique. By engineering CH3 domains with one having a "knob" mutation and the other one having a "hole" mutation, heterodimerization at the CH3-CH3-interface can be promoted. Bulky “knobs” were constructed by replacing small amino acids with the largest amino acids, tyrosine or tryptophan. Holes of similar size to the knobs were constructed by replacing large side chains with alanine, valine serine or threonine.[180] T366W as a knob and a combination of T366S, L368A, Y407V as a hole, yielded a 87% efficiency in correct pairing.[181] This just leaves the problem of LC mispairing which can be solved with the CrossMab technology, in which correct LC pairing is ensured by swapping domains between the variable or constant regions of one Fab arm.[182]

In receptor blockade and bispecific approaches, FcγR or complement engagement is often not desired, requiring a shift from IgG1 to IgG4. Alternatively, to combine the favorable stability and half-life of IgG1 with Fc-silenced properties, the so-called LALA mutation (L234A, L235A), which reduces FcγR binding, can be introduced into the Fc domain.[183]

However, if enhanced effector functions like ADCC are desired, FcγRIIIa engagement can be promoted by either introducing mutations such as S239D/I332E, or by removing fucose from the Fc glycan. This so-called “afucosylation” is used in cancer antibodies such as the anti-CD20 OBZ to enhance immune cell effector mechanisms through an increase in affinity for FcγRIIIa receptors.[184]

To summarize, therapeutic mAb engineering encompasses many aspects to achieve the desired functional outcome. Key factors such as antibody isotype, affinity for FcγRs and complement proteins, antigen-binding domains, as well as hinge region flexibility collectively determine the mechanism of action. All of these properties must be carefully selected and optimized to ensure maximal therapeutic efficacy.

2. Aims and objectives

DNA-PAINT super-resolution microscopy has overcome many limitations of traditional SMLM. By utilizing the constant exchange of dye-labeled imager strands, DNA-PAINT bypasses the dye-photobleaching limitations inherent to techniques like PALM and (d)STORM. This allows for virtually unlimited accumulation of localizations over extended imaging periods, enabling super-resolution imaging with exceptionally high precision. Furthermore, the predictable kinetics of DNA-DNA hybridization support truly quantitative imaging. Finally, DNA-PAINT exceeds the traditional multiplexing limit of ~3 targets in super-resolution microscopy, achieving simultaneous imaging of up to ~30 targets in cells.

In ideal systems, such as DNA-origami measurements *in vitro*, DNA-PAINT can reach ~1 nm precision and sub-5 nm-resolution. However, in more challenging environments, such as intact cells or tissues, background levels are higher and diffusion of imager strands can be limited, resulting in cell measurements with ~10 nm resolution. This prevents the reliable detection of protein oligomers with distances below 10 nm, especially in dense environments.

In the case of membrane receptors, accessing these distances is of central importance, as their spatial organization directly influences cellular signaling and downstream function. While structural biology techniques like X-ray crystallography and cryo-EM achieve Ångström-resolution of membrane receptors, they are obtained in vitro and therefore lack whole-cell context. Bridging this methodological gap is essential for understanding how nanoscale receptor behavior in the cell membrane is connected with functional outcomes. Ultimately, this knowledge can guide the structure-informed design of drugs targeting membrane receptors.

Thus, the overarching aim of this thesis is to advance DNA-PAINT to true quantitative single-protein imaging of membrane receptors and to visualize their interactions with therapeutic antibodies or ligands at 1-nm resolution in the native cellular context. This will be achieved through the following specific objectives:

Achieve cellular imaging at 1 nm-resolution

Achieving 1 nm-resolution in cells with DNA-PAINT is not straightforward, as, according to equations 11 and 12, the localization precision is constrained by photon counts, background, and pixel size, all of which have practical limits and cannot be optimized indefinitely. Thus, when localizations of two adjacent molecules below the resolution limit

are detected, individual localizations cannot be unambiguously assigned to one or the other molecule. To overcome this limit, the first aim of this thesis is to introduce DNA-barcoding as a way to unambiguously assign the localizations to their targets to resolve distances below 1 nm in DNA origami. Furthermore, I will implement this for Ångström-precision imaging in cells to assess membrane receptor organization of CD20, before and after treatment with the therapeutic antibody RTX.

Determine organization of Type I and Type II mAbs in cells

Structural studies have provided high-resolution cryo-EM data for Type I and Type II anti-CD20 antibody fragments in complex with CD20 dimers.[133,155] However, how these structures relate to the nanoscale receptor re-organization upon Type I or Type II therapeutic mAb treatment in the cellular context, is still unclear. Moreover, how the nanoscale arrangement correlates with functional outcomes has not been investigated.

To address this, I aim to perform quantitative two-plex imaging of both CD20 and the bound therapeutic antibodies in intact cells in 3D. By investigating different variants of Type I and Type II mAbs when bound to CD20, and modeling the oligomeric structure, I set out to explain how Type I mAbs can form complement binding platforms and Type II mAbs lead to direct cell death. This will deepen our understanding of therapeutic mechanisms at the molecular level and inform the targeted design of next-generation antibody therapies.

Develop labeling methods for small ligands

DNA-PAINT imaging is ultimately limited by the specificity, the size, the accuracy and precision of the labeling strategy. Labeling small proteins such as extracellular ligands, such as the EGF ligand, remains particularly challenging, since the label can impact its functionality and accessibility. However, to fully understand how the EGFR signaling is regulated on a nanoscale basis, both EGFR and EGF ligand have to be quantitatively labeled.

To address this challenge, an aim of this thesis is to establish robust labeling protocols for small ligands to enable their visualization in super-resolution imaging. In particular, strategies to directly label the EGF ligand with DNA or peptide-tags will be implemented and the impact of these labeling strategies on EGF functionality will be assessed.

Implementing this labeling strategy will allow for Ångström-precision imaging of the EGF ligand and lay the groundwork for future studies to resolve the currently incomplete picture of EGFR-ligand interactions in the cellular context.

3. Summary of Publications

3.1 Publication 1: Ångström-resolution fluorescence microscopy

Susanne C. M. Reinhardt*, Luciano A. Masullo*, **Isabelle Baudrexel***, Philipp R. Steen*, Rafal Kowalewski, Alexandra S. Eklund, Sebastian Strauss, Eduard M. Unterauer, Thomas Schlichthaerle, Maximilian T. Strauss, Christian Klein & Ralf Jungmann. (* equal contribution)

Super-resolution microscopy has significantly advanced biological research by surpassing the traditional diffraction limit of optical microscopy, allowing visualization of biomolecules at unprecedented spatial resolutions. Conventional single-molecule localization microscopy (SMLM) techniques, however, are fundamentally restricted by the number of photons captured per localization, setting a practical limit to achievable resolution. To overcome this intrinsic limitation, we developed Resolution Enhancement by Sequential Imaging (RESI) that pushes fluorescence microscopy into the Ångström-scale resolution range.

This is achieved by sequentially imaging sparse subsets of identical molecules labeled with orthogonal DNA barcodes, allowing for precise grouping and averaging of localizations. RESI essentially applies the concept of SMLM again by grouping individual blinking events linked to specific molecular targets to determine their center with an improved precision. As a result, localization precision scales inversely with the square root of the number of localizations, facilitating Ångström-level spatial resolution even with limited individual event precision.

RESI was first implemented using DNA origami structures with two orthogonal adjacent docking strands emerging from the same DNA double helix within the origami. These two strands featured a designed distance of ~7 Å, the distance of DNA base pairs along the axis of the sugar-phosphate backbone. With RESI, we measured distance of 8.5 ± 1.7 Å, demonstrating direct visualization of molecular features at Ångström-scale resolution. Furthermore, RESI was validated in cells by visualizing individual Nup96 proteins within nuclear NPCs, resolving protein copies with an average lateral precision of 1 nm across thousands of complexes.

To illustrate RESI's utility in biomedical research, we studied the spatial organization of CD20 receptors on untreated versus RTX-treated cells. RESI resolved individual receptor

dimers and allowed the precise quantification of their distribution, revealing drug-induced formation of linear, higher-order receptor structures in treated cells, previously undetectable with conventional methods.

RESI significantly advances fluorescence microscopy, bridging the gap between super-resolution imaging and structural biology. RESI's compatibility with standard widefield microscopy, stable performance under ambient conditions, and high-throughput imaging capabilities make it a promising tool for biomedical research, with potential applications in molecular diagnostics and therapeutic development.

3.2 Publication 2: Resolving the structural basis of therapeutic antibody function in cancer immunotherapy with RESI

Isabelle Pachmayr, Luciano A. Masullo, Susanne C.M. Reinhardt, Jisoo Kwon, Maite Llop, Ondřej Skořepa, Sylvia Herter, Marina Bacac, Christian Klein & Ralf Jungmann.

Determining the nanoscale organization with RESI for only one target – CD20 – does allow to visualize changes in CD20 organization and infer the biological effects on CD20-expressing B lymphocytes. However, visualizing the nanoscale arrangement of the antibodies themselves is of equal importance, as the Fc domains prime and regulate the downstream effects of immune system components, such as FcγR binding or C1q binding.

To achieve this, we extended RESI to multiplexed, 3-dimensional imaging of two targets with four RESI rounds each. In this study, we utilized this approach to explore how therapeutic mAbs modulate the nanoscale organization of CD20 receptors.

Therapeutic anti-CD20 mAbs, categorized as Type I (e.g., RTX and OFA) and Type II (e.g., OBZ), differ notably in their mechanisms of action. However, until now, their in situ spatial arrangements at single-protein resolution remained unresolved. By harnessing RESI's ability to achieve Ångström-level precision, we mapped individual CD20 molecules and quantified their spatial distributions in intact cells, revealing striking differences in clustering patterns induced by different antibody types.

We observed that Type I mAbs such as RTX and OFA facilitated extensive higher-order clustering of CD20 receptors into flexible chain-like oligomers beyond hexamers. By introducing a chain-like model for Type I-CD20 arrangements that accounts for the flexibility of antibody hinge regions, and by comparing simulations of these arrangements with experimental data, we demonstrate that flexible chains provide a suitable model for the observed structures. In addition, we show that flexible chains facilitate configurations

favorable for binding complement protein C1q, in good agreement with efficient complement activation detected for Type I antibodies. This model even accounts for differences in Fab binding angles and hinge flexibility. For instance, OFA's shorter chain segment lengths uncovered with simulations of the flexible chain-like model, aligned with its steeper Fab binding angle and superior complement engagement compared to RTX.

Conversely, Type II OBZ treatment predominantly resulted in CD20 monomers, dimers, trimers and a low percentage of tetramers. Moreover, we excluded the presence of OBZ-higher order structures, and demonstrated minimal formation of C1q binding platforms, which is in good agreement with limited complement activation for Type II mAb-treatment.

To further probe the relationship between structural modulation and antibody function, we investigated different Type II OBZ-derived antibody formats, differing in their hinge region flexibility. These were CD20-CD3 T cell engagers (TCEs) with the classical (c-TCE) having a similar flexibility to OBZ, and inverted (i-TCE) being more flexible. RESI revealed that i-TCE promoted more substantial CD20 trimer- and tetramerization compared to c-TCE and OBZ. Excitingly, this correlated with a functional shift from Type II to Type I characteristics, exemplified by a reduced direct cytotoxicity of i-TCE. These findings indicate that therapeutic function is governed by the extent of receptor oligomerization. We show that this shift from Type II to Type I function can occur through efficient CD20 tetramer formation, without requiring extensive higher-order clustering as observed by other Type I antibodies. By integrating RESI-derived structural insights with functional assays, we established a continuum of antibody behaviors rather than a rigid Type I/II dichotomy.

In summary, this study provides an in-depth structural foundation for understanding how therapeutic antibodies engage and modulate their membrane targets at the molecular scale. This method can be universally applied to any receptor-antibody pair, paving the way for single-molecule in situ structural characterization of antibody-based immunotherapy. Multi-target 3D RESI emerges as a powerful imaging platform offering significant potential for antibody screening, biosimilar development, and targeted immunotherapeutic optimization.

3.3 Publication 3: Imaging Ligand-Receptor Interactions at Single-Protein Resolution with DNA-PAINT

Monique Honsa*, **Isabelle Pachmayr***, Larissa Heinze*, Levent Bas, Luciano A. Masullo, Jisoo Kwon, Ana Perovic, Brenda Schulman & Ralf Jungmann. (* equal contribution)

While DNA-PAINT super-resolution microscopy has enabled nanoscale visualization of membrane receptors, and RESI allows to access the single-protein scale, its application to small extracellular ligands is still limited. Achieving stoichiometric labeling of ligands, such as Epidermal Growth Factor (EGF), while maintaining their biological activity presents a significant challenge. Conventional detection of EGF or its receptor EGFR often relies on sub-stoichiometric labeling to isolate individual molecules but remains largely restricted to single-target imaging, preventing detailed structural analysis of ligand-receptor complexes in their activated states.

To overcome these limitations, we developed a robust and generalizable method for imaging small extracellular ligands with DNA-PAINT at single-protein resolution. Specifically, we engineered site-specifically labeled, functional human EGF ligands by introducing two alternative tagging strategies: a directly DNA-conjugated EGF construct (DNA-EGF) and an ALFA-tagged EGF construct (ALFA-EGF).

Since inducing EGFR dimerization is one of the main functions of EGF, we performed DNA-PAINT imaging and quantitatively compared EGFR dimerization after treatment with the tagged EGF versions, to treatment with untagged EGF. While DNA-EGF retained partial EGFR dimerization capabilities, ALFA-EGF demonstrated almost complete preservation of native receptor clustering, making it the best strategy for EGF labeling. In addition, when imaging both ligands and receptors, ALFA-EGF exhibited specific co-localization to EGFR, while DNA-EGF showed less specificity for EGFR.

The functional ALFA-EGF enabled 3D DNA-PAINT imaging of early EGF-EGFR oligomerization and later activation stages, characterized by vesicle formation and internalization. Furthermore, ALFA-EGF is compatible with RESI, allowing the visualization of two EGF ligands bound to EGFR dimers at distances of ~11 nm.

Taken together, this approach establishes the ALFA-tag as a minimally invasive and broadly applicable labeling strategy for small extracellular ligands, compatible with both DNA-PAINT and RESI imaging. By preserving biological function while enabling nanoscale imaging, the method extends super-resolution studies to a wider range of ligand-receptor systems. This opens up new avenues for dissecting how ligand-induced spatial organization influences signaling pathways in health and disease.

4. Conclusion and Outlook

This work advances DNA-PAINT super-resolution microscopy towards true single-protein imaging in native cellular environments. By introducing RESI as an extension of DNA-PAINT, Ångström-level resolution is achieved through sequential imaging of sparse protein subsets and molecular averaging. This enables direct 3D visualization of receptor re-organization at ~1 nm resolution in intact cell membranes.

Quantitative single-protein imaging of CD20 receptors upon therapeutic antibody treatment, reveals distinct clustering patterns for Type I and Type II anti-CD20 antibodies. By combining RESI and functional studies, we show that, rather than Type II and Type I being two distinct groups, there is a Type II-Type I oligomerization-function continuum. Furthermore, a robust and generalizable labeling strategy for small extracellular ligands such as EGF was developed using ALFA-tagging, which preserves biological activity while enabling quantitative, multiplexed imaging.

Together, these advances bridge the gap between structural biology and cellular imaging, allowing for in situ characterization of receptor-ligand and receptor-antibody interactions at single-protein resolution. Ultimately, these methods lay the foundation for future studies to dissect molecular mechanisms of signaling and therapeutic action, and to guide the structure-informed development of next-generation targeted therapies.

Advancing RESI

One limitation of RESI is that it relies on the stochastic labeling with orthogonal docking strands. This means that, if all molecules within an oligomer are DNA-PAINT-unresolvable, all molecules have to be labeled with an orthogonal strand, in order to be detected as the correct oligomer. More importantly, if two or more adjacent molecules within a DNA-PAINT-unresolvable oligomer are labeled with the same docking strand, they are detected

as one molecule. This reduces the apparent the fraction of detectable oligomers $F(m,n)$ in RESI measurements, depending on the number of orthogonal sequences used for RESI n, and the number of molecules in a DNA-PAINT unresolved volume m, according to:[185]

$$F(m,n) = \frac{n!}{(n-m)!\, n^m} \qquad 18$$

This means that, e.g. with the six speed-improved R-sequences for RESI – when neglecting the labeling efficiency – only ~55% of trimers can be detected as a trimer. In practice, this effect is mitigated in cellular measurements due to the natural distribution of dimer distances and the size of the labeling tag-Nb complex, making a fraction of the intra-oligomer distances resolvable by DNA-PAINT. Nevertheless, in order to detect oligomers with efficiencies closer to 100%, RESI rounds have to be increased to >30 which can so far only be achieved by using secondary sequences as introduced in the SUM-PAINT approach.[74] Extending RESI to more rounds will enable the precise detection of highly clustered oligomers in high-density environments and further improve the detection efficiency of multimers that are unresolvable with DNA-PAINT.

RESI features a relatively high throughput with ~3 cells within a ~100x100 μm^2 FOV imaged in ~2.5 h. This throughput can be further improved by increasing the FOV with flat-top imaging[186] or further increasing imaging speed[68,69]. By combining these advances and automating imaging with liquid exchange, this could be used for therapeutic antibody screening. Performing RESI for several mAbs with known functions in cells and training machine learning models, could predict mAb function from oligomeric patterns detected with RESI. Thus, RESI-based analysis has the potential not only to identify drug candidates, but also to provide a feedback loop for improving the structure of mAb candidates based on imaging data.

C1q binding

To describe the molecular basis for complement activation in the case of Type I anti-CD20 antibodies in more detail, C1q binding has to be imaged in addition to CD20-mAb complexes. To date, the mechanism of C1 activation is still debated as structural data points both towards intra-complex C1r/C1s cleavage and C1 inter-complex cross-activation.[187-189]

The flexible chain-like arrangements with several C1q binding platforms close together could explain a molecular mechanism for C1 (C1q with proteases C1r and C1s bound)

inter-complex cross-activation. Preliminary DNA-PAINT data in CD20-expressing CHO cells, treated with OFA, indicates that a chain-like arrangement of Type I-mAbs indeed allows for C1q deposition, with C1q bound within a “bulls-eye”-structure of an OFA-CD20-chain wrapped around it (Fig. 23).

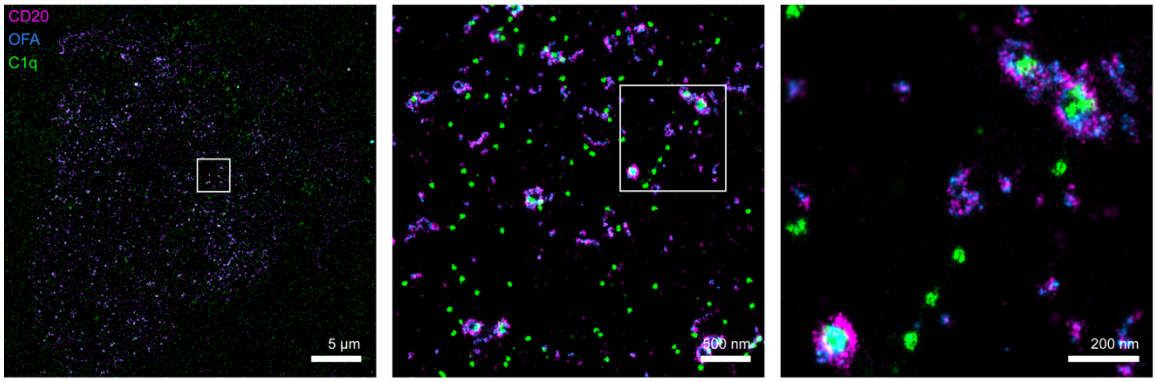

Figure 23: The formation of C1q platforms. DNA-PAINT images of mEGFP-CD20 (magenta), Ofatumumab (OFA, blue) and C1q (green) in CHO cells. Co-incubation of OFA and C1q on CD20-expressing cells results in the development of C1q-binding platforms with OFA-CD20 chains forming U-shaped clusters.

Multiplexed imaging of CD20 and interacting proteins

To further link the CD20 RESI data to functional outcomes in therapeutic antibody treatment, multiplexed imaging of CD20 interactors before and after treatment can be performed.

CD20 has an important role in BCR signaling, and is described to act as a gate-keeper of the resting state.[143] This suggests that changing the CD20 nanoscale arrangement with therapeutic antibodies modulates BCR signaling, which, depending on the context, is either beneficial or bad for therapeutic outcomes. CD20 clustering by Type I-mAbs could either remove CD20 from its natural function, thereby losing its gatekeeping ability, or Type I-induced CD20 concatenation could co-cluster other proteins involved in BCR signaling. To test these hypotheses, multiplexed imaging in the B cell context should be performed.

Preliminary 3D DNA-PAINT results show that for both Type I and Type II-treatment, CD20 interactions with CD19 are maintained, indicating that Type I-mediated CD20 clustering co-clusters interacting proteins and could remove them from the IgM-BCR (Fig. 24). The influence of therapeutic mAbs on molecular interactions of CD20 with the BCR have to be investigated in more detail, as this has important implications on personalized medicine or combination therapies targeting other B cell proteins.[190]

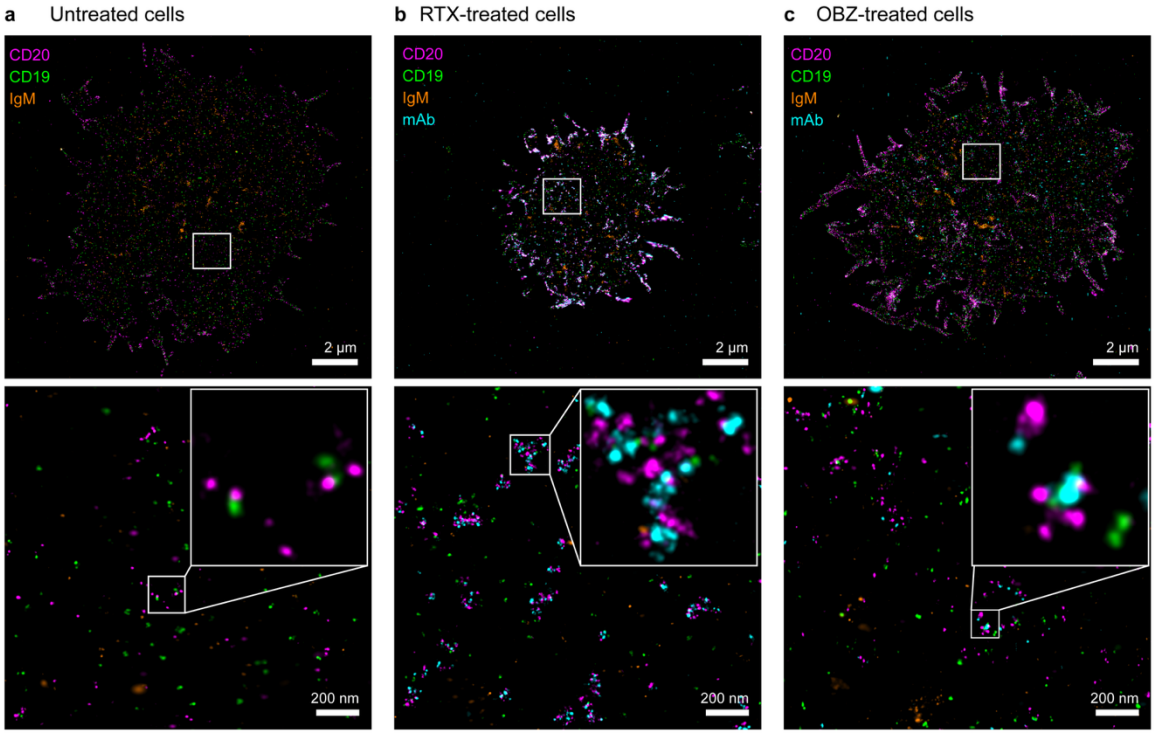

Figure 24: Multiplexed imaging of CD20 and other membrane proteins in B cells. **a**, DNA-PAINT imaging of GFP-CD20 (magenta), CD19 (green), IgM (orange) and in untreated cells show CD20 and CD19 homo- and heterodimers. **b**, DNA-PAINT imaging of GFP-CD20, CD19, IgM and monoclonal antibodies (mAb, cyan) after RTX-treatment, show RTX-CD20 clusters, also containing CD19. **c**, DNA-PAINT imaging of GFP-CD20, CD19, IgM and mAbs after OBZ-treatment, show CD19 in close proximity to CD20 oligomers.

DNA-PAINT imaging in whole cells and biological tissues

To fully understand the whole picture of CD20 re-arrangement after mAb-treatment, DNA-PAINT and RESI have to be advanced to the whole-cell level. Recently, Two-dye imager (TDI) PAINT in combination with single-objective light sheet illumination, has enabled whole-cell imaging of DNA-labeled therapeutic antibodies while binding to CD20 on B cells.[191] This 3D imaging showed that the mAb clustering on CD20-positive cells was detected mainly at the rod-like microvilli, which is in agreement with the observations that also untreated CD20 is localized at microvilli and most of the membrane in these kind of cell lines consists of protrusions.[134,192] Nevertheless, with lateral and axial resolutions of approximately 50 nm and 140 nm, respectively, no significant differences in nanoscale arrangements of mAbs were detectable between Type I and Type II antibodies.[191] In addition, mAb-induced clusters were not compared to CD20 in the untreated case. Collectively, this indicates that TDI-PAINT assisted light-sheet imaging has yet to demonstrate sufficient sensitivity to resolve nanoscale differences in oligomerization relevant to this context.

Implementing 3D-RESI for whole-cell imaging, either with light-sheet illumination, spinning-disk confocal or biplane setups[193,194], will overcome these limitations and allow for whole-cell imaging at single protein resolution. Furthermore, these advances will also enable RESI beyond the single-cell context, which is necessary to image membrane protein organization at cell-cell contact sites, e.g. in the context of T cell engagers (TCE) or immune cell activation.

Eventually, super-resolution microscopy findings regarding membrane receptor organization should also be validated in the biological context of tissue samples. This poses additional challenges for DNA-PAINT imaging: Tissues are thick, heterogeneous assemblies of many different kinds of cells, that are densely packed and are embedded in an extracellular matrix. This crowded environment limits the diffusion of DNA-conjugated binders to their targets of interest and reduces staining efficiency. Therefore, permeabilization and staining protocols have to be optimized for DNA-PAINT tissue imaging. In addition, the diffusion of dye-labeled imagers during DNA-PAINT is limited, leading to photobleaching. To circumvent this, optimized fluorogenic imagers have to be used for tissue imaging.[195]

Alternatively, these crowding challenges could further be alleviated by combining DNA-PAINT with expansion microscopy (ExM), a chemical process that physically expands tissues by ~4 to 10-fold.[196] However, the expansion process encompasses proteolytic digestion and free-radical polymerization of the hydrogel, which can destroy epitopes for immunolabeling, fluorophores as well as ssDNA.[197] Given that specific protein epitopes are preserved during the expansion process, post-expansion antibody labeling offers a potential solution for implementing DNA-PAINT in ExM, as this has previously been applied for dSTORM imaging.[197] To achieve DNA-PAINT in ExM, the expansion factor of the expanded tissue has to be carefully monitored, since high salt buffers – such as those needed for optimal DNA binding kinetics – can lead to tissue shrinkage during imaging.[197]

Studying the dynamics of CD20 clustering

Apart from the missing information of the whole-cell context, information about clustering dynamics is also not accessible in fixed-cell super-resolution imaging. We could show that the direct cytotoxicity of Type II-mAbs correlates with their ability to induce CD20 oligomers above dimers. However, we do not know if the more flexible linker in i-TCE leads to a greater degree of freedom for CD20 diffusion as opposed to c-TCE, and if that in turn affects CD20-directed cytotoxicity. This could be investigated further by single-molecule tracking or fluorescence recovery after photobleaching (FRAP) studies of CD20 after mAb treatment in living cells. This dynamic information could contribute to the understanding if

it is the CD20 oligomerization itself or rather the stiffness of the oligomers driving the direct cytotoxicity of Type II mAbs.

Labeling approaches in DNA-PAINT

Ultimately, the resolution in DNA-PAINT and RESI is still limited by the label. As introduced in chapter 1.5.2, antibodies are ~10 nm in size, and tag-Nb complexes still add ~2-5 nm in uncertainty in labeling, thus reducing both accuracy and precision in super-resolution imaging. The label itself does not only impact imaging but can also influence protein function. In the case of CD20, it cannot be excluded that the bulkiness of the mEGFP-tag affects diffusion or interactions with other proteins in the cell membrane. This is even more problematic for small soluble proteins ligands such as EGF for which the tag has to be as small as possible, while only minimally disturbing the function.

Directly attaching the DNA-docking strand at the protein of interest is, in theory, the best labeling strategy for imaging as this is per definition the most accurate label. However, even with site-specific DNA-conjugation of EGF opposite from the EGFR-binding pocket, our EGF-study shows that DNA-tagging reduces functionality. This is most likely due the 19-nt long, negatively charged DNA, reducing apparent EGF-affinities to EGFR. In accordance with this, it has been shown that affinities of Fabs to their targets are significantly reduced after DNA-conjugation.[198] Peptide-nucleic acid (PNA) is an uncharged DNA analogue, that could be tested to determine whether the negative charge is the reason for this impact on function.[199] Treating live cells with ssDNA comes with additional caveats, especially in the immune cell context, since ssDNA activates innate immunity pathways.[200] This means that the impact of direct ssDNA conjugation on protein function and affinity, always has to be carefully evaluated.

An alternative to direct DNA-labeling before treatment, is the ssDNA attachment after cell treatment and fixation. Click chemistry approaches allow for direct DNA attachment with high efficiency under ambient conditions.[96] To achieve this, the EGF ligand could be functionalized with e.g. Azide, through the introduction of unnatural amino acids during protein expression.[201] We recently used this approach for direct DNA-labeling of metabolically incorporated azido-sugars, for Ångström-resolution imaging of the glycocalyx.[202]

So far, the small ALFA-tag is the best approach for functional EGF labeling, allowing for detection of EGF-mediated EGFR rearrangement. Future efforts should focus expanding the toolbox of small peptide tags with high affinity cognate Nbs. Alternatively, high-affinity direct binders, such as Nbs, Affimers or SOMAmers have to be developed, individually for

each protein of interest. In the future, such binders will be more accessible with the advancements in de novo protein design and in situ screening methods.[203]

Most monovalent binders exhibit relatively low target affinities, limiting their direct applicability for DNA-PAINT imaging. Developing strategies to adapt these binders for DNA-PAINT would expand the range of suitable reagents available from existing literature.

ErbB/HER signaling

ErbB/HER signaling is regulated by both ligand binding and by homo- and hetero-dimerization of ErbB proteins. For example, EGF treatment also induces EGFR-Her2 heterodimerization in addition to EGFR homodimerization (Fig. 25). Structural and single-molecule data demonstrated HER2-HER3-heterodimers as well as interactions of HER4 with all other HERs.[204,205] While EGFR and HER2 are well-established anti-tumor targets, the roles of HER3 and HER4 remain less clearly defined, with their expression either correlating with more or less favorable outcomes in cancer.[206,207] The formation of specific HER protein dimerization patterns could regulate signaling in different cancer contexts and could even account for treatment resistance to EGFR-/HER2-directed cancer therapies.

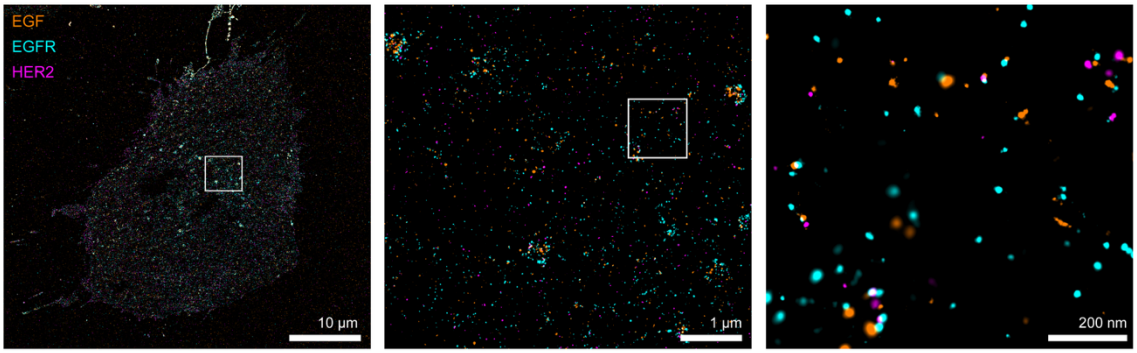

Figure 25: EGFR-Her2 interactions in transiently transfected CHO cells. DNA-PAINT imaging of EGFR-mEGFP (cyan), HER2-TagBFP2 (magenta) and ALFA-EGF (orange) shows that EGF-treatment induces EGFR clustering and heterodimerization of EGFR and HER2.

Studying how ligand binding, regulates receptor interactions, both in healthy and diseased cells, is essential to advance our understanding of ErbB/HER-driven signaling networks. Future studies should also investigate the effects of other ligands binding to ErbB/HER proteins, such as Neuregulins, Transforming Growth Factor-α or Epiregulin, in order to better understand the sensitive regulation of the ErbB/HER signaling network.[109]

Examining how cancer-associated mutations affect oligomerization behavior, will provide deeper insights into the dysregulation of signaling in malignancies. To narrow down, which homo- or heterodimers are actively signaling and are therefore relevant in the disease context, multiplexed HER imaging has to be combined with readouts of activation, for example by staining EGFR phosphorylation sites or downstream kinases and phosphatases, that are all modulating signaling outcomes.[109] Visualizing the molecules recruited downstream of receptor multimerization induced signaling can deliver valuable information for combination therapies with small molecule inhibitors.[111]

Super-resolution imaging for improvement of targeted immunotherapies

Super-resolution microscopy offers valuable insights that can improve current immunotherapies and guide the rational design of novel drugs in multiple ways.

One application is the measurement of Fc-to-Fc distances between bound antibodies on target cells, which can predict complement activation.[208] The spatial configuration of C1q head domains is critical for activation, and optimizing Fab-to-Fab distances could enhance or suppress C1q deposition, depending on therapeutic goals. Additionally, engineered antibody multimers can increase local Fc density, promoting more robust C1q cross-activation.[188] This approach could refine existing strategies, including pentameric IgM-based binders, antibody cages, or hexabodies.[171,209,210]

The arrangement of Fc domains on antibody-treated cancer cells also influences their interaction with Fcγ receptors (FcγRs) on immune effector cells like T cells and NK cells. By identifying FcγR expression patterns unique to specific immune cell subsets, it is possible to design IgGs that induce matching Fc configurations on cancer cells. Such precise pattern matching could enhance the specificity and predictability of ADCC and ADCP.

Beyond analyzing therapeutic IgGs and their receptors, multiplexed DNA-PAINT imaging can be used to identify novel membrane receptor targets for bi- and multispecific therapeutics. By mapping receptor patterns exclusive to cancer cells, and absent in healthy tissue, drugs with defined geometries and binder distances can be engineered for selective targeting and depletion.

This imaging strategy is also valuable for designing antibody-cytokine fusion proteins. Systemic delivery of cytokines often leads to off-target effects.[211] Hence, localizing cytokine receptors in close proximity to antibody targets allows for rational fusion designs. For instance, IL-2 variants fused to anti-PD-1 antibodies have improved T effector

responses in cancer treatment.[212] Spatial mapping of cytokine receptors relative to antibody binding sites could guide modifications to cytokine affinity, thereby minimizing side effects.

Multiplexed DNA-PAINT imaging could also be key in analyzing tumor evasion strategies. This is particularly important in hard-to-treat cancers such as triple-negative breast cancer, where resistance to PD-1/PD-L1 blockade is common.[213] Identifying molecules that compensate for blocked PD-L1 function, such as alternative immune checkpoints or other compensatory pathways, could guide the development of combination therapies to overcome resistance.

To further connect structural arrangements of membrane receptors and bound therapeutic molecules with functional outcomes, multiplexed DNA-PAINT imaging of phosphorylation sites and signaling molecules has to be implemented. This is important e.g. for antibodies targeting TNFR agonists, as introduced in chapter 1.6.3.3 Mechanism of action. These agonists have potential to improve cancer immunotherapy but to face significant challenges regarding off-target toxicity, currently limiting their application.[214] Precisely imaging and defining the signaling pathways, that are switched on during antibody-binding, will allow to tightly control the desired degree of agonism and to advance TNFR agonists for drug treatment.

In the future, multiplexed DNA-PAINT and RESI super-resolution microscopy will be central to advancing personalized medicine. These techniques enable detection of low-abundance targets, reveal resistance mechanisms, and provide detailed insights into receptor-mediated signaling. By combining intracellular and extracellular information at single-protein resolution in intact cells, these techniques uniquely bridge structural and functional understanding. This will not only deepen our mechanistic knowledge of current immunotherapies but also lay the groundwork for the rational development of next-generation receptor-targeted therapies with enhanced specificity and efficacy. Ultimately, integrating these insights with emerging technologies such as structure-guided drug design will pave the way for more precise, efficient, and personalized treatment strategies.

5. References

1 Lane, N. The unseen world: reflections on Leeuwenhoek (1677) 'Concerning little animals'. *Philosophical Transactions of the Royal Society B: Biological Sciences* **370**, 20140344 (2015). https://doi.org/10.1098/rstb.2014.0344

2 Davis, I. M. "Round, red globules floating in a crystalline fluid" – Antoni van Leeuwenhoek's observations of red blood cells and hemocytes. *Micron* **157**, 103249 (2022). https://doi.org/10.1016/j.micron.2022.103249

3 Vlastimil Fidler, P. K. in *Fluorescence Spectroscopy and Microscopy in Biology* (ed Mariana Amaro Radek Šachl) (Springer Cham, 2023).

4 Dobrucki, J. W. in *Fluorescence Microscopy* 97-142 (2013).

5 Stokes, G. G. XXX. On the change of refrangibility of light. *Philosophical Transactions of the Royal Society of London* **142**, 463-562 (1997). https://doi.org/10.1098/rstl.1852.0022

6 Lakowicz, J. R. *Principles of Fluorescence Spectroscopy*. (Springer New York, NY, 2006).

7 Herschel, J. F. W. On a case of superficial colour presented by a homogeneous liquid internally colourless. *Philosophical Transactions of the Royal Society of London* **135**, 143-145 (1997). https://doi.org/10.1098/rstl.1845.0004

8 Lukinavičius, G. *et al.* Fluorescent dyes and probes for super-resolution microscopy of microtubules and tracheoles in living cells and tissues. *Chemical Science* **9**, 3324-3334 (2018). https://doi.org/10.1039/C7SC05334G

9 Grimm, J. B. *et al.* A general method to improve fluorophores for live-cell and single-molecule microscopy. *Nature Methods* **12**, 244-250 (2015). https://doi.org/10.1038/nmeth.3256

10 Joshi, A., Mukherjee, N. & Pandey, M. Water-soluble organic fluorescence-based probes for biomolecule sensing and labeling. *Biosensors and Bioelectronics: X* **19**, 100510 (2024). https://doi.org/10.1016/j.biosx.2024.100510

11 Shimomura, O., Johnson, F. H. & Saiga, Y. Extraction, Purification and Properties of Aequorin, a Bioluminescent Protein from the Luminous Hydromedusan, Aequorea. *Journal of Cellular and Comparative Physiology* **59**, 223-239 (1962). https://doi.org/10.1002/jcp.1030590302

12 Chalfie, M., Tu, Y., Euskirchen, G., Ward, W. W. & Prasher, D. C. Green Fluorescent Protein as a Marker for Gene Expression. *Science* **263**, 802-805 (1994). https://doi.org/10.1126/science.8303295

13 Kong, J. *et al.* Green fluorescent protein inspired fluorophores. *Advances in Colloid and Interface Science* **285**, 102286 (2020). https://doi.org/10.1016/j.cis.2020.102286

14 Matz, M. V. *et al.* Fluorescent proteins from nonbioluminescent Anthozoa species. *Nature Biotechnology* **17**, 969-973 (1999). https://doi.org/10.1038/13657

15 Subach, O. M. *et al.* Structural Characterization of Acylimine-Containing Blue and Red Chromophores in mTagBFP and TagRFP Fluorescent Proteins. *Chemistry & Biology* **17**, 333-341 (2010). https://doi.org/10.1016/j.chembiol.2010.03.005

16 Tokunaga, M., Kitamura, K., Saito, K., Iwane, A. H. & Yanagida, T. Single Molecule Imaging of Fluorophores and Enzymatic Reactions Achieved by Objective-Type Total Internal Reflection Fluorescence Microscopy. *Biochemical and Biophysical Research Communications* **235**, 47-53 (1997). https://doi.org/10.1006/bbrc.1997.6732

17 Axelrod, D., Burghardt, T. P. & Thompson, N. L. Total Internal Reflection Fluorescence. *Annual Review of Biophysics* **13**, 247-268 (1984). https://doi.org/10.1146/annurev.bb.13.060184.001335

18 Tokunaga, M., Imamoto, N. & Sakata-Sogawa, K. Highly inclined thin illumination enables clear single-molecule imaging in cells. *Nature Methods* **5**, 159-161 (2008). https://doi.org/10.1038/nmeth1171
19 Abbe, E. Beiträge zur Theorie des Mikroskops und der mikroskopischen Wahrnehmung. *Archiv für Mikroskopische Anatomie* **9**, 413-468 (1873). https://doi.org/10.1007/BF02956173
20 Rayleigh, L. LVI. Investigations in optics, with special reference to the spectroscope. *The London, Edinburgh, and Dublin Philosophical Magazine and Journal of Science* **8**, 477-486 (1879). https://doi.org/10.1080/14786447908639715
21 Sparrow, C. M. On Spectroscopic Resolving Power. *The Astrophysical Journal* **44**, 76 (1916). https://doi.org/10.1086/142271
22 Booth, M. J. Microscope Resolution Estimation and Normalised Coordinates. *Zenodo* (2020). https://doi.org/10.5281/zenodo.4302488
23 Joy, D. C., Ford, B.J., Bradbury, S. in *Encyclopedia Britannica.* (2025).
24 Harke, B., Bianchini, P., Vicidomini, G., Galiani, S. & Diaspro, A. in *Encyclopedia of Biophysics* (ed Gordon C. K. Roberts) 2470-2475 (Springer Berlin Heidelberg, 2013).
25 Klar, T. A., Jakobs, S., Dyba, M., Egner, A. & Hell, S. W. Fluorescence microscopy with diffraction resolution barrier broken by stimulated emission. *Proceedings of the National Academy of Sciences* **97**, 8206-8210 (2000). https://doi.org/10.1073/pnas.97.15.8206
26 Klar, T. A. & Hell, S. W. Subdiffraction resolution in far-field fluorescence microscopy. *Opt. Lett.* **24**, 954-956 (1999). https://doi.org/10.1364/OL.24.000954
27 Huang, B., Bates, M. & Zhuang, X. Super-Resolution Fluorescence Microscopy. *Annual Review of Biochemistry* **78**, 993-1016 (2009). https://doi.org/10.1146/annurev.biochem.77.061906.092014
28 Berning, S., Willig, K. I., Steffens, H., Dibaj, P. & Hell, S. W. Nanoscopy in a Living Mouse Brain. *Science* **335**, 551-551 (2012). https://doi.org/10.1126/science.1215369
29 Balzarotti, F. *et al.* Nanometer resolution imaging and tracking of fluorescent molecules with minimal photon fluxes. *Science* **355**, 606-612 (2017). https://doi.org/10.1126/science.aak9913
30 Xiao, J. & Ha, T. Flipping nanoscopy on its head. *Science* **355**, 582-584 (2017). https://doi.org/10.1126/science.aam5409
31 Ostersehlt, L. M. *et al.* DNA-PAINT MINFLUX nanoscopy. *Nature Methods* **19**, 1072-1075 (2022). https://doi.org/10.1038/s41592-022-01577-1
32 Betzig, E. Proposed method for molecular optical imaging. *Opt. Lett.* **20**, 237-239 (1995). https://doi.org/10.1364/OL.20.000237
33 Lelek, M. *et al.* Single-molecule localization microscopy. *Nature Reviews Methods Primers* **1**, 39 (2021). https://doi.org/10.1038/s43586-021-00038-x
34 Schnitzbauer, J., Strauss, M. T., Schlichthaerle, T., Schueder, F. & Jungmann, R. Super-resolution microscopy with DNA-PAINT. *Nature Protocols* **12**, 1198-1228 (2017). https://doi.org/10.1038/nprot.2017.024
35 Cheezum, M. K., Walker, W. F. & Guilford, W. H. Quantitative Comparison of Algorithms for Tracking Single Fluorescent Particles. *Biophysical Journal* **81**, 2378-2388 (2001). https://doi.org/10.1016/S0006-3495(01)75884-5
36 Abraham, A. V., Ram, S., Chao, J., Ward, E. S. & Ober, R. J. Quantitative study of single molecule location estimation techniques. *Opt. Express* **17**, 23352-23373 (2009). https://doi.org/10.1364/OE.17.023352
37 Small, A. & Stahlheber, S. Fluorophore localization algorithms for super-resolution microscopy. *Nature Methods* **11**, 267-279 (2014). https://doi.org/10.1038/nmeth.2844
38 Endesfelder, U., Malkusch, S., Fricke, F. & Heilemann, M. A simple method to estimate the average localization precision of a single-molecule localization

microscopy experiment. *Histochemistry and Cell Biology* **141**, 629-638 (2014). https://doi.org/10.1007/s00418-014-1192-3

39 Mortensen, K. I., Churchman, L. S., Spudich, J. A. & Flyvbjerg, H. Optimized localization analysis for single-molecule tracking and super-resolution microscopy. *Nature Methods* **7**, 377-381 (2010). https://doi.org/10.1038/nmeth.1447

40 Ober, R. J., Ram, S. & Ward, E. S. Localization Accuracy in Single-Molecule Microscopy. *Biophysical Journal* **86**, 1185-1200 (2004). https://doi.org/10.1016/S0006-3495(04)74193-4

41 Dickson, R. M., Cubitt, A. B., Tsien, R. Y. & Moerner, W. E. On/off blinking and switching behaviour of single molecules of green fluorescent protein. *Nature* **388**, 355-358 (1997). https://doi.org/10.1038/41048

42 Betzig, E. *et al.* Imaging Intracellular Fluorescent Proteins at Nanometer Resolution. *Science* **313**, 1642 (2006). https://doi.org/10.1126/science.1127344

43 Shcherbakova, D. M., Sengupta, P., Lippincott-Schwartz, J. & Verkhusha, V. V. Photocontrollable Fluorescent Proteins for Superresolution Imaging. *Annual Review of Biophysics* **43**, 303-329 (2014). https://doi.org/10.1146/annurev-biophys-051013-022836

44 van de Linde, S. *et al.* Direct stochastic optical reconstruction microscopy with standard fluorescent probes. *Nature Protocols* **6**, 991-1009 (2011). https://doi.org/10.1038/nprot.2011.336

45 Rust, M. J., Bates, M. & Zhuang, X. Sub-diffraction-limit imaging by stochastic optical reconstruction microscopy (STORM). *Nature Methods* **3**, 793-796 (2006). https://doi.org/10.1038/nmeth929

46 Bates, M., Huang, B., Dempsey, G. T. & Zhuang, X. Multicolor Super-Resolution Imaging with Photo-Switchable Fluorescent Probes. *Science* **317**, 1749 (2007). https://doi.org/10.1126/science.1146598

47 Heilemann, M., van de Linde, S., Mukherjee, A. & Sauer, M. Super-Resolution Imaging with Small Organic Fluorophores. *Angewandte Chemie International Edition* **48**, 6903-6908 (2009). https://doi.org/10.1002/anie.200902073

48 Endesfelder, U. & Heilemann, M. in *Advanced Fluorescence Microscopy: Methods and Protocols* (ed Peter J. Verveer) 263-276 (Springer New York, 2015).

49 Sharonov, A. & Hochstrasser, R. M. Wide-field subdiffraction imaging by accumulated binding of diffusing probes. *Proceedings of the National Academy of Sciences* **103**, 18911 (2006). https://doi.org/10.1073/pnas.0609643104

50 Giannone, G. *et al.* Dynamic Superresolution Imaging of Endogenous Proteins on Living Cells at Ultra-High Density. *Biophysical Journal* **99**, 1303-1310 (2010). https://doi.org/10.1016/j.bpj.2010.06.005

51 Riera, R. *et al.* Single-molecule imaging of glycan–lectin interactions on cells with Glyco-PAINT. *Nature Chemical Biology* **17**, 1281-1288 (2021). https://doi.org/10.1038/s41589-021-00896-2

52 Tholen, M. M. E., Riera, R., Izquierdo-Lozano, C. & Albertazzi, L. Multiplexed Lectin-PAINT super-resolution microscopy enables cell glycotyping. *Communications Biology* **8**, 267 (2025). https://doi.org/10.1038/s42003-025-07626-7

53 Riedl, J. *et al.* Lifeact: a versatile marker to visualize F-actin. *Nature Methods* **5**, 605-607 (2008). https://doi.org/10.1038/nmeth.1220

54 Eklund, A. S. & Jungmann, R. Optimized Coiled-Coil Interactions for Multiplexed Peptide-PAINT. *Small* **19**, 2206347 (2023). https://doi.org/10.1002/smll.202206347

55 Maity, B. K., Nall, D., Lee, Y. & Selvin, P. R. Peptide-PAINT Using a Transfected-Docker Enables Live- and Fixed-Cell Super-Resolution Imaging. *Small Methods* **7**, 2201181 (2023). https://doi.org/10.1002/smtd.202201181

56 Watson, J. D. & Crick, F. H. C. Molecular Structure of Nucleic Acids: A Structure for Deoxyribose Nucleic Acid. *Nature* **171**, 737-738 (1953). https://doi.org/10.1038/171737a0

57 Franklin, R. E. & Gosling, R. G. Molecular Configuration in Sodium Thymonucleate. *Nature* **171**, 740-741 (1953). https://doi.org/10.1038/171740a0

58 Wang, A. H. J. *et al.* Molecular structure of a left-handed double helical DNA fragment at atomic resolution. *Nature* **282**, 680-686 (1979). https://doi.org/10.1038/282680a0

59 Sahayasheela, V. J., Ooga, M., Kumagai, T. & Sugiyama, H. Z-DNA at the crossroads: untangling its role in genome dynamics. *Trends in Biochemical Sciences* **50**, 267-279 (2025). https://doi.org/10.1016/j.tibs.2025.01.001

60 Geertsema, H. J. *et al.* Left-handed DNA-PAINT for improved super-resolution imaging in the nucleus. *Nature Biotechnology* **39**, 551-554 (2021). https://doi.org/10.1038/s41587-020-00753-y

61 Urata, H., Ogura, E., Shinohara, K., Ueda, Y. & Akagi, M. Synthesis and properties of mirror-image DNA. *Nucleic Acids Research* **20**, 3325-3332 (1992). https://doi.org/10.1093/nar/20.13.3325

62 Kool, E. T. Hydrogen Bonding, Base Stacking, and Steric Effects in DNA Replication. *Annual Review of Biophysics* **30**, 1-22 (2001). https://doi.org/10.1146/annurev.biophys.30.1.1

63 Seeman, N. C. Nucleic acid junctions and lattices. *Journal of Theoretical Biology* **99**, 237-247 (1982). https://doi.org/10.1016/0022-5193(82)90002-9

64 Rothemund, P. W. K. Folding DNA to create nanoscale shapes and patterns. *Nature* **440**, 297-302 (2006). https://doi.org/10.1038/nature04586

65 Dey, S. *et al.* DNA origami. *Nature Reviews Methods Primers* **1**, 13 (2021). https://doi.org/10.1038/s43586-020-00009-8

66 Jungmann, R. *et al.* Single-Molecule Kinetics and Super-Resolution Microscopy by Fluorescence Imaging of Transient Binding on DNA Origami. *Nano Letters* **10**, 4756-4761 (2010). https://doi.org/10.1021/nl103427w

67 Jungmann, R. *et al.* Quantitative super-resolution imaging with qPAINT. *Nature methods* **13**, 439-442 (2016). 10.1038/nmeth.3804

68 Schueder, F. *et al.* An order of magnitude faster DNA-PAINT imaging by optimized sequence design and buffer conditions. *Nature Methods* **16**, 1101-1104 (2019). https://doi.org/10.1038/s41592-019-0584-7

69 Strauss, S. & Jungmann, R. Up to 100-fold speed-up and multiplexing in optimized DNA-PAINT. *Nature Methods* **17**, 789-791 (2020). https://doi.org/10.1038/s41592-020-0869-x

70 Jungmann, R. *et al.* Multiplexed 3D cellular super-resolution imaging with DNA-PAINT and Exchange-PAINT. *Nature Methods* **11**, 313-318 (2014). https://doi.org/10.1038/nmeth.2835

71 Agasti, S. S. *et al.* DNA-barcoded labeling probes for highly multiplexed Exchange-PAINT imaging. *Chemical Science* **8**, 3080-3091 (2017). 10.1039/C6SC05420J

72 Banerjee, A., Srivastava, M., Vidwath, V. S. & Ganji, M. High-speed 10-plex DNA-PAINT with a larger sequence repertoire. *bioRxiv*, 2024.2012.2021.629871 (2024). https://doi.org/10.1101/2024.12.21.629871

73 Schueder, F. *et al.* Unraveling cellular complexity with transient adapters in highly multiplexed super-resolution imaging. *Cell* **187**, 1769-1784.e1718 (2024). https://doi.org/10.1016/j.cell.2024.02.033

74 Unterauer, E. M. *et al.* Spatial proteomics in neurons at single-protein resolution. *Cell* **187**, 1785-1800.e1716 (2024). https://doi.org/10.1016/j.cell.2024.02.045

75 Elliott, A. D. Confocal Microscopy: Principles and Modern Practices. *Current Protocols in Cytometry* **92**, e68 (2020). https://doi.org/10.1002/cpcy.68

76 Huang, B., Wang, W., Bates, M. & Zhuang, X. Three-Dimensional Super-Resolution Imaging by Stochastic Optical Reconstruction Microscopy. *Science* **319**, 810-813 (2008). https://doi.org/10.1126/science.1153529
77 Murphy, K. W., Casey. *Janeway's Immunobiology*. (Garland Science, 2016).
78 Thermo Fisher Scientific. *Monoclonal vs Polyclonal Antibodies*, <https://www.thermofisher.com/de/de/home/life-science/antibodies/primary-antibodies/monoclonal-vs-polyclonal-antibodies.html> (2024).
79 Harris, L. J., Skaletsky, E. & McPherson, A. Crystallographic structure of an intact IgG1 monoclonal antibody11Edited by I. A. Wilson. *Journal of Molecular Biology* **275**, 861-872 (1998). https://doi.org/10.1006/jmbi.1997.1508
80 Vidarsson, G., Dekkers, G. & Rispens, T. IgG Subclasses and Allotypes: From Structure to Effector Functions. *Frontiers in Immunology* **5** (2014). https://doi.org/10.3389/fimmu.2014.00520
81 Sadiki, A. *et al.* Site-specific conjugation of native antibody. *Antibody Therapeutics* **3**, 271-284 (2020). 10.1093/abt/tbaa027
82 Pleiner, T., Bates, M. & Görlich, D. A toolbox of anti–mouse and anti–rabbit IgG secondary nanobodies. *Journal of Cell Biology* **217**, 1143-1154 (2017). https://doi.org/10.1083/jcb.201709115
83 Schlichthaerle, T. *et al.* Site-Specific Labeling of Affimers for DNA-PAINT Microscopy. *Angewandte Chemie International Edition* **57**, 11060-11063 (2018). https://doi.org/10.1002/anie.201804020
84 Tiede, C. *et al.* Affimer proteins are versatile and renewable affinity reagents. *Elife* **6**, e24903 (2017). https://doi.org/10.7554/eLife.24903
85 Strauss, S. *et al.* Modified aptamers enable quantitative sub-10-nm cellular DNA-PAINT imaging. *Nature methods* **15**, 685-688 (2018). https://doi.org/10.1038/s41592-018-0105-0
86 Jin, B.-k., Odongo, S., Radwanska, M. & Magez, S. NANOBODIES®: A Review of Diagnostic and Therapeutic Applications. *International Journal of Molecular Sciences* **24** (2023).
87 Banerjee, A., Anand, M. & Ganji, M. Labeling approaches for DNA-PAINT super-resolution imaging. *Nanoscale* **15**, 6563-6580 (2023). https://doi.org/10.1039/D2NR06541J
88 Schlichthaerle, T. *et al.* Direct Visualization of Single Nuclear Pore Complex Proteins Using Genetically-Encoded Probes for DNA-PAINT. *Angewandte Chemie International Edition* **58**, 13004-13008 (2019). https://doi.org/10.1002/anie.201905685
89 Virant, D. *et al.* A peptide tag-specific nanobody enables high-quality labeling for dSTORM imaging. *Nature Communications* **9**, 930 (2018). https://doi.org/10.1038/s41467-018-03191-2
90 Götzke, H. *et al.* The ALFA-tag is a highly versatile tool for nanobody-based bioscience applications. *Nature Communications* **10**, 4403 (2019). https://doi.org/10.1038/s41467-019-12301-7
91 Moore, R. P. & Legant, W. R. Improving probes for super-resolution. *Nature Methods* **15**, 659-660 (2018). https://doi.org/10.1038/s41592-018-0120-1
92 Ganji, M., Schlichthaerle, T., Eklund, A. S., Strauss, S. & Jungmann, R. Quantitative Assessment of Labeling Probes for Super-Resolution Microscopy Using Designer DNA Nanostructures. *ChemPhysChem* **22**, 911-914 (2021). https://doi.org/10.1002/cphc.202100185
93 Hermanson, G. T. in *Bioconjugate Techniques (Third Edition)* (ed Greg T. Hermanson) 229-258 (Academic Press, 2013).
94 Baskin, J. M. *et al.* Copper-free click chemistry for dynamic in vivo imaging. *Proceedings of the National Academy of Sciences* **104**, 16793-16797 (2007). https://doi.org/10.1073/pnas.0707090104
95 Agard, N. J., Prescher, J. A. & Bertozzi, C. R. A Strain-Promoted [3 + 2] Azide−Alkyne Cycloaddition for Covalent Modification of Biomolecules in Living

Systems. *Journal of the American Chemical Society* **126**, 15046-15047 (2004). https://doi.org/10.1021/ja044996f
96 Luu, T., Gristwood, K., Knight, J. C. & Jörg, M. Click Chemistry: Reaction Rates and Their Suitability for Biomedical Applications. *Bioconjugate Chemistry* **35**, 715-731 (2024). https://doi.org/10.1021/acs.bioconjchem.4c00084
97 Ravasco, J. M. J. M., Faustino, H., Trindade, A. & Gois, P. M. P. Bioconjugation with Maleimides: A Useful Tool for Chemical Biology. *Chemistry – A European Journal* **25**, 43-59 (2019). https://doi.org/10.1002/chem.201803174
98 Smith, N. J. *et al.* Fast, irreversible modification of cysteines through strain releasing conjugate additions of cyclopropenyl ketones. *Organic & Biomolecular Chemistry* **16**, 2164-2169 (2018). https://doi.org/10.1039/C8OB00166A
99 Xue, Y., Si, X., Yin, D., Zhang, S. & Dai, H. Integrating PLOR and SPAAC Click Chemistry for Efficient Site-Specific Fluorescent Labeling of RNA. *International Journal of Molecular Sciences* **26** (2025).
100 Chen, L. *et al.* Improved variants of SrtA for site-specific conjugation on antibodies and proteins with high efficiency. *Scientific Reports* **6**, 31899 (2016). https://doi.org/10.1038/srep31899
101 Guimaraes, C. P. *et al.* Site-specific C-terminal and internal loop labeling of proteins using sortase-mediated reactions. *Nature Protocols* **8**, 1787-1799 (2013). https://doi.org/10.1038/nprot.2013.101
102 Honsa, M. *et al.* Imaging Ligand-Receptor Interactions at Single-Protein Resolution with DNA-PAINT. *Small Methods* **9** (2025). https://doi.org/10.1002/smtd.202401799
103 Zou, Z., Ji, Y. & Schwaneberg, U. Empowering Site-Specific Bioconjugations In Vitro and In Vivo: Advances in Sortase Engineering and Sortase-Mediated Ligation. *Angewandte Chemie International Edition* **63**, e202310910 (2024). https://doi.org/10.1002/anie.202310910
104 Alberts, B. J., Alexander; Lewis, Julian; Raff, Martin; Roberts, Keith; Walter, Peter. *Molecular Biology of the Cell*. Vol. 4th edition (Garland Science, 2002).
105 Overington, J. P., Al-Lazikani, B. & Hopkins, A. L. How many drug targets are there? *Nature Reviews Drug Discovery* **5**, 993-996 (2006). https://doi.org/10.1038/nrd2199
106 Lorente, J. S. *et al.* GPCR drug discovery: new agents, targets and indications. *Nature Reviews Drug Discovery* (2025). https://doi.org/10.1038/s41573-025-01139-y
107 Moran, A. E., Kovacsovics-Bankowski, M. & Weinberg, A. D. The TNFRs OX40, 4-1BB, and CD40 as targets for cancer immunotherapy. *Current Opinion in Immunology* **25**, 230-237 (2013). https://doi.org/10.1016/j.coi.2013.01.004
108 Du, Z. & Lovly, C. M. Mechanisms of receptor tyrosine kinase activation in cancer. *Molecular Cancer* **17**, 58 (2018). https://doi.org/10.1186/s12943-018-0782-4
109 Oda, K., Matsuoka, Y., Funahashi, A. & Kitano, H. A comprehensive pathway map of epidermal growth factor receptor signaling. *Molecular Systems Biology* **1**, 2005.0010 (2005). https://doi.org/10.1038/msb4100014
110 Cohen, S. Isolation of a Mouse Submaxillary Gland Protein Accelerating Incisor Eruption and Eyelid Opening in the New-born Animal. *Journal of Biological Chemistry* **237**, 1555-1562 (1962). https://doi.org/10.1016/S0021-9258(19)83739-0
111 Hynes, N. E. & Lane, H. A. ERBB receptors and cancer: the complexity of targeted inhibitors. *Nature Reviews Cancer* **5**, 341-354 (2005). https://doi.org/10.1038/nrc1609
112 Hubbard, S. R. & Miller, W. T. Receptor tyrosine kinases: mechanisms of activation and signaling. *Current Opinion in Cell Biology* **19**, 117-123 (2007). https://doi.org/10.1016/j.ceb.2007.02.010

113 Schlessinger, J. Ligand-Induced, Receptor-Mediated Dimerization and Activation of EGF Receptor. *Cell* **110**, 669-672 (2002). https://doi.org/10.1016/S0092-8674(02)00966-2
114 Zhang, X., Gureasko, J., Shen, K., Cole, P. A. & Kuriyan, J. An Allosteric Mechanism for Activation of the Kinase Domain of Epidermal Growth Factor Receptor. *Cell* **125**, 1137-1149 (2006). https://doi.org/10.1016/j.cell.2006.05.013
115 Popović, L. *et al.* Profiling of ERBB receptors and downstream pathways reveals selectivity and hidden properties of ERBB4 antagonists. *iScience* **27**, 108839 (2024). https://doi.org/10.1016/j.isci.2024.108839
116 Yarden, Y. & Pines, G. The ERBB network: at last, cancer therapy meets systems biology. *Nature Reviews Cancer* **12**, 553-563 (2012). https://doi.org/10.1038/nrc3309
117 Kovacs, E., Zorn, J. A., Huang, Y., Barros, T. & Kuriyan, J. A Structural Perspective on the Regulation of the Epidermal Growth Factor Receptor. *Annual Review of Biochemistry* **84**, 739-764 (2015). https://doi.org/10.1146/annurev-biochem-060614-034402
118 Huang, Y. *et al.* Molecular basis for multimerization in the activation of the epidermal growth factor receptor. *Elife* **5**, e14107 (2016). https://doi.org/10.7554/eLife.14107
119 Needham, S. R. *et al.* EGFR oligomerization organizes kinase-active dimers into competent signalling platforms. *Nature Communications* **7**, 13307 (2016). https://doi.org/10.1038/ncomms13307
120 Yarden, Y. & Sliwkowski, M. X. Untangling the ErbB signalling network. *Nature Reviews Molecular Cell Biology* **2**, 127-137 (2001). https://doi.org/10.1038/35052073
121 Holbro, T. *et al.* The ErbB2/ErbB3 heterodimer functions as an oncogenic unit: ErbB2 requires ErbB3 to drive breast tumor cell proliferation. *Proceedings of the National Academy of Sciences* **100**, 8933-8938 (2003). https://doi.org/10.1073/pnas.1537685100
122 Oh, D.-Y. & Bang, Y.-J. HER2-targeted therapies — a role beyond breast cancer. *Nature Reviews Clinical Oncology* **17**, 33-48 (2020). https://doi.org/10.1038/s41571-019-0268-3
123 Hudis Clifford, A. Trastuzumab — Mechanism of Action and Use in Clinical Practice. *New England Journal of Medicine* **357**, 39-51 https://doi.org/10.1056/NEJMra043186
124 Kirkpatrick, P., Graham, J. & Muhsin, M. Cetuximab. *Nature Reviews Drug Discovery* **3**, 549-550 (2004). https://doi.org/10.1038/nrd1445
125 Salles, G. *et al.* Rituximab in B-Cell Hematologic Malignancies: A Review of 20 Years of Clinical Experience. *Adv Ther* **34**, 2232-2273 (2017). https://doi.org/10.1007/s12325-017-0612-x
126 Gabriela, P. & Marek, M. The regulation and function of CD20: an “enigma” of B-cell biology and targeted therapy. *Haematologica* **105**, 1494-1506 (2020). https://doi.org/10.3324/haematol.2019.243543
127 Schuh, E. *et al.* Features of Human CD3+CD20+ T Cells. *The Journal of Immunology* **197**, 1111 (2016). https://doi.org/10.4049/jimmunol.1600089
128 Hultin, L. E., Hausner, M. A., Hultin, P. M. & Giorgi, J. V. Cd20 (pan-B cell) antigen is expressed at a low level on a subpopulation of human T lymphocytes. *Cytometry* **14**, 196-204 (1993). https://doi.org/10.1002/cyto.990140212
129 Hauser Stephen, L. *et al.* B-Cell Depletion with Rituximab in Relapsing–Remitting Multiple Sclerosis. *New England Journal of Medicine* **358**, 676-688 https://doi.org/10.1056/NEJMoa0706383
130 Klein, C. *et al.* Epitope interactions of monoclonal antibodies targeting CD20 and their relationship to functional properties. *MAbs* **5**, 22-33 (2013). https://doi.org/10.4161/mabs.22771

131 Bubien, J. K., Zhou, L. J., Bell, P. D., Frizzell, R. A. & Tedder, T. F. Transfection of the CD20 cell surface molecule into ectopic cell types generates a Ca2+ conductance found constitutively in B lymphocytes. *Journal of Cell Biology* **121**, 1121-1132 (1993). https://doi.org/10.1083/jcb.121.5.1121
132 Polyak, M. J., Li, H., Shariat, N. & Deans, J. P. CD20 Homo-oligomers Physically Associate with the B Cell Antigen Receptor. *Journal of Biological Chemistry* **283**, 18545-18552 (2008). https://doi.org/10.1074/jbc.M800784200
133 Rougé, L. *et al.* Structure of CD20 in complex with the therapeutic monoclonal antibody rituximab. *Science* **367**, 1224 (2020). https://doi.org/10.1126/science.aaz9356
134 Li, H. *et al.* The CD20 Calcium Channel Is Localized to Microvilli and Constitutively Associated with Membrane Rafts: ANTIBODY BINDING INCREASES THE AFFINITY OF THE ASSOCIATION THROUGH AN EPITOPE-DEPENDENT CROSS-LINKING-INDEPENDENT MECHANISM*. *Journal of Biological Chemistry* **279**, 19893-19901 (2004). https://doi.org/10.1074/jbc.M400525200
135 Uchida, J. *et al.* Mouse CD20 expression and function. *International Immunology* **16**, 119-129 (2004). https://doi.org/10.1093/intimm/dxh009
136 Kuijpers, T. W. *et al.* CD20 deficiency in humans results in impaired T cell–independent antibody responses. *The Journal of Clinical Investigation* **120**, 214-222 (2010). https://doi.org/10.1172/JCI40231
137 Morsy, D. E. D. *et al.* Reduced T-Dependent Humoral Immunity in CD20-Deficient Mice. *The Journal of Immunology* **191**, 3112 (2013). https://doi.org/10.4049/jimmunol.1202098
138 Franke, A., Niederfellner, G. J., Klein, C. & Burtscher, H. Antibodies against CD20 or B-Cell Receptor Induce Similar Transcription Patterns in Human Lymphoma Cell Lines. *PLOS ONE* **6**, e16596 (2011). https://doi.org/10.1371/journal.pone.0016596
139 Petrie, R. J. & Deans, J. P. Colocalization of the B Cell Receptor and CD20 Followed by Activation-Dependent Dissociation in Distinct Lipid Rafts. *The Journal of Immunology* **169**, 2886 (2002). https://doi.org/10.4049/jimmunol.169.6.2886
140 Kläsener, K., Maity, P. C., Hobeika, E., Yang, J. & Reth, M. B cell activation involves nanoscale receptor reorganizations and inside-out signaling by Syk. *Elife* **3**, e02069-e02069 (2014). https://doi.org/10.7554/eLife.02069
141 Gold, M. R. & Reth, M. G. Antigen Receptor Function in the Context of the Nanoscale Organization of the B Cell Membrane. *Annual Review of Immunology* **37**, 97-123 (2019). https://doi.org/10.1146/annurev-immunol-042718-041704
142 Gupta, N. *et al.* Quantitative proteomic analysis of B cell lipid rafts reveals that ezrin regulates antigen receptor–mediated lipid raft dynamics. *Nature Immunology* **7**, 625-633 (2006). https://doi.org/10.1038/ni1337
143 Kläsener, K. *et al.* CD20 as a gatekeeper of the resting state of human B cells. *Proceedings of the National Academy of Sciences* **118**, e2021342118 (2021). 10.1073/pnas.2021342118
144 Pierpont, T. M., Limper, C. B. & Richards, K. L. Past, Present, and Future of Rituximab—The World's First Oncology Monoclonal Antibody Therapy. *Frontiers in Oncology* **8** (2018). https://doi.org/10.3389/fonc.2018.00163
145 Looney, R., Anolik, J. & Sanz, I. Treatment of SLE with anti-CD20 monoclonal antibody. *Curr Dir Autoimmun* **8**, 193-205 (2005). https://doi.org/10.1159/000082104
146 Florou, D., Katsara, M., Feehan, J., Dardiotis, E. & Apostolopoulos, V. Anti-CD20 Agents for Multiple Sclerosis: Spotlight on Ocrelizumab and Ofatumumab. *Brain Sci* **10**, 758 (2020). https://doi.org/10.3390/brainsci10100758

147 Korhonen, R. & Moilanen, E. Anti-CD20 Antibody Rituximab in the Treatment of Rheumatoid Arthritis. *Basic & Clinical Pharmacology & Toxicology* **106**, 13-21 (2010). https://doi.org/10.1111/j.1742-7843.2009.00452.x
148 Meyer, S. *et al.* New insights in Type I and II CD20 antibody mechanisms-of-action with a panel of novel CD20 antibodies. *British Journal of Haematology* **180**, 808-820 (2018). https://doi.org/10.1111/bjh.15132
149 Herter, S. *et al.* Preclinical Activity of the Type II CD20 Antibody GA101 (Obinutuzumab) Compared with Rituximab and Ofatumumab In Vitro and in Xenograft Models. *Molecular Cancer Therapeutics* **12**, 2031 (2013). https://doi.org/10.1158/1535-7163.MCT-12-1182
150 Singh, V., Gupta, D. & Almasan, A. Development of Novel Anti-Cd20 Monoclonal Antibodies and Modulation in Cd20 Levels on Cell Surface: Looking to Improve Immunotherapy Response. *J Cancer Sci Ther* **7**, 347-358 (2015). https://doi.org/10.4172/1948-5956.1000373
151 Barth, M. J., Mavis, C., Czuczman, M. S. & Hernandez-Ilizaliturri, F. J. Ofatumumab Exhibits Enhanced In Vitro and In Vivo Activity Compared to Rituximab in Preclinical Models of Mantle Cell Lymphoma. *Clinical Cancer Research* **21**, 4391 (2015). https://doi.org/10.1158/1078-0432.CCR-15-0056
152 Unruh, T. L. *et al.* Cholesterol depletion inhibits src family kinase-dependent calcium mobilization and apoptosis induced by rituximab crosslinking. *Immunology* **116**, 223-232 (2005). https://doi.org/10.1111/j.1365-2567.2005.02213.x
153 Seyfizadeh, N., Seyfizadeh, N., Hasenkamp, J. & Huerta-Yepez, S. A molecular perspective on rituximab: A monoclonal antibody for B cell non Hodgkin lymphoma and other affections. *Critical Reviews in Oncology/Hematology* **97**, 275-290 (2016). https://doi.org/10.1016/j.critrevonc.2015.09.001
154 Chan, H. T. C. *et al.* CD20-induced Lymphoma Cell Death Is Independent of Both Caspases and Its Redistribution into Triton X-100 Insoluble Membrane Rafts. *Cancer Research* **63**, 5480 (2003).
155 Kumar, A., Planchais, C., Fronzes, R., Mouquet, H. & Reyes, N. Binding mechanisms of therapeutic antibodies to human CD20. *Science* **369**, 793 (2020). https://doi.org/10.1126/science.abb8008
156 Crescioli, S. *et al.* Antibodies to watch in 2025. *MAbs* **17**, 2443538 (2025). https://doi.org/10.1080/19420862.2024.2443538
157 Reichert, J. M. Metrics for antibody therapeutics development. *MAbs* **2**, 695-700 (2010). https://doi.org/10.4161/mabs.2.6.13603
158 Dantal, J. & Soulillou, J.-P. Use of monoclonal antibodies in human transplantation. *Current Opinion in Immunology* **3**, 740-747 (1991). https://doi.org/10.1016/0952-7915(91)90106-B
159 Kimball, J. A. *et al.* The OKT3 antibody response study: a multicentre study of human anti-mouse antibody (HAMA) production following OKT3 use in solid organ tranplantation. *Transplant Immunology* **3**, 212-221 (1995). https://doi.org/10.1016/0966-3274(95)80027-1
160 Reff, M. E. *et al.* Depletion of B Cells In Vivo by a Chimeric Mouse Human Monoclonal Antibody to CD20. *Blood* **83**, 435-445 (1994). https://doi.org/10.1182/blood.V83.2.435.435
161 Sawyers, C. L. Herceptin: A First Assault on Oncogenes that Launched a Revolution. *Cell* **179**, 8-12 (2019). https://doi.org/10.1016/j.cell.2019.08.027
162 Lonberg, N. Fully human antibodies from transgenic mouse and phage display platforms. *Current Opinion in Immunology* **20**, 450-459 (2008). https://doi.org/10.1016/j.coi.2008.06.004
163 Wypych, J. *et al.* Human IgG2 antibodies display disulfide-mediated structural isoforms. *J Biol Chem* **283**, 16194-16205 (2008). https://doi.org/10.1074/jbc.M709987200

164 Liu, H. & and May, K. Disulfide bond structures of IgG molecules. *MAbs* **4**, 17-23 (2012). https://doi.org/10.4161/mabs.4.1.18347
165 Saito, S., Namisaki, H., Hiraishi, K., Takahashi, N. & Iida, S. A stable engineered human IgG3 antibody with decreased aggregation during antibody expression and low pH stress. *Protein Science* **28**, 900-909 (2019). https://doi.org/10.1002/pro.3598
166 Wang, W., Erbe, A. K., Hank, J. A., Morris, Z. S. & Sondel, P. M. NK Cell-Mediated Antibody-Dependent Cellular Cytotoxicity in Cancer Immunotherapy. *Frontiers in Immunology* **6** (2015). https://doi.org/10.3389/fimmu.2015.00368
167 Van Wagoner, C. M. *et al.* Antibody-mediated phagocytosis in cancer immunotherapy. *Immunological Reviews* **319**, 128-141 (2023). https://doi.org/10.1111/imr.13265
168 Kolev, M. *et al.* Inside-Out of Complement in Cancer. *Frontiers in Immunology* **13** (2022). https://doi.org/10.3389/fimmu.2022.931273
169 Roumenina, L. T., Daugan, M. V., Petitprez, F., Sautès-Fridman, C. & Fridman, W. H. Context-dependent roles of complement in cancer. *Nature Reviews Cancer* **19**, 698-715 (2019). https://doi.org/10.1038/s41568-019-0210-0
170 Diebolder, C. A. *et al.* Complement Is Activated by IgG Hexamers Assembled at the Cell Surface. *Science* **343**, 1260 (2014). https://doi.org/10.1126/science.1248943
171 de Jong, R. N. *et al.* A Novel Platform for the Potentiation of Therapeutic Antibodies Based on Antigen-Dependent Formation of IgG Hexamers at the Cell Surface. *PLOS Biology* **14**, e1002344 (2016). https://doi.org/10.1371/journal.pbio.1002344
172 Merck & Co. *Selected Indications for KEYTRUDA® (pembrolizumab)*, <https://www.keytrudahcp.com/approved-indications/> (2025).
173 Wang, B. T. *et al.* Multimeric Anti-DR5 IgM Agonist Antibody IGM-8444 Is a Potent Inducer of Cancer Cell Apoptosis and Synergizes with Chemotherapy and BCL-2 Inhibitor ABT-199. *Molecular Cancer Therapeutics* **20**, 2483-2494 (2021). https://doi.org/10.1158/1535-7163.MCT-20-1132
174 Yu, X. *et al.* Complex Interplay between Epitope Specificity and Isotype Dictates the Biological Activity of Anti-human CD40 Antibodies. *Cancer Cell* **33**, 664-675.e664 (2018). https://doi.org/10.1016/j.ccell.2018.02.009
175 Yu, X. *et al.* TNF receptor agonists induce distinct receptor clusters to mediate differential agonistic activity. *Communications Biology* **4**, 772 (2021). https://doi.org/10.1038/s42003-021-02309-5
176 Dadas, O., Ertay, A. & Cragg, M. S. Delivering co-stimulatory tumor necrosis factor receptor agonism for cancer immunotherapy: past, current and future perspectives. *Frontiers in Immunology* **14** (2023). https://doi.org/10.3389/fimmu.2023.1147467
177 Chen, Y., Jiang, M. & Chen, X. Therapeutic potential of TNFR2 agonists: a mechanistic perspective. *Frontiers in Immunology* **14** (2023). https://doi.org/10.3389/fimmu.2022.931273
178 Hünig, T. The rise and fall of the CD28 superagonist TGN1412 and its return as TAB08: a personal account. *The FEBS Journal* **283**, 3325-3334 (2016). https://doi.org/10.1111/febs.13754
179 Zhang, D., Goldberg, M. V. & Chiu, M. L. Fc Engineering Approaches to Enhance the Agonism and Effector Functions of an Anti-OX40 Antibody. *Journal of Biological Chemistry* **291**, 27134-27146 (2016). https://doi.org/10.1074/jbc.M116.757773
180 Ridgway, J. B. B., Presta, L. G. & Carter, P. 'Knobs-into-holes' engineering of antibody CH3 domains for heavy chain heterodimerization. *Protein Engineering* **9**, 617-621 (1996). https://doi.org/10.1093/protein/9.7.617
181 Merchant, A. M. *et al.* An efficient route to human bispecific IgG. *Nature Biotechnology* **16**, 677-681 (1998). https://doi.org/10.1038/nbt0798-677

182 Surowka, M., Wolfgang, S. & and Klein, C. Ten years in the making: application of CrossMab technology for the development of therapeutic bispecific antibodies and antibody fusion proteins. *MAbs* **13**, 1967714 (2021). https://doi.org/10.1080/19420862.2021.1967714
183 Hale, G. Living in LALA land? Forty years of attenuating Fc effector functions. *Immunological Reviews* **328**, 422-437 (2024). https://doi.org/10.1111/imr.13379
184 Mössner, E. *et al.* Increasing the efficacy of CD20 antibody therapy through the engineering of a new type II anti-CD20 antibody with enhanced direct and immune effector cell–mediated B-cell cytotoxicity. *Blood* **115**, 4393-4402 (2010). https://doi.org/10.1182/blood-2009-06-225979
185 Reinhardt, S. C. M. *et al.* Ångström-resolution fluorescence microscopy. *Nature* **617**, 711-716 (2023). https://doi.org/10.1038/s41586-023-05925-9
186 Stehr, F., Stein, J., Schueder, F., Schwille, P. & Jungmann, R. Flat-top TIRF illumination boosts DNA-PAINT imaging and quantification. *Nature Communications* **10**, 1268 (2019). https://doi.org/10.1038/s41467-019-09064-6
187 Almitairi, J. O. M. *et al.* Structure of the C1r–C1s interaction of the C1 complex of complement activation. *Proceedings of the National Academy of Sciences* **115**, 768-773 (2018). https://doi.org/10.1073/pnas.1718709115
188 Mortensen, S. A. *et al.* Structure and activation of C1, the complex initiating the classical pathway of the complement cascade. *Proceedings of the National Academy of Sciences* **114**, 986-991 (2017). https://doi.org/10.1073/pnas.1616998114
189 Reid, K. B. M. Complement Component C1q: Historical Perspective of a Functionally Versatile, and Structurally Unusual, Serum Protein. *Frontiers in Immunology* **9** (2018). https://doi.org/10.3389/fimmu.2018.00764
190 Nguyen, T. T. *et al.* Efficacy and safety of add-on anti-CD20 monoclonal antibody to Bruton tyrosine kinase inhibitor treatment for chronic lymphocytic leukemia: a meta-analysis. *Scientific Reports* **13**, 9775 (2023). https://doi.org/10.1038/s41598-023-36279-x
191 Ghosh, A. *et al.* Decoding the molecular interplay of CD20 and therapeutic antibodies with fast volumetric nanoscopy. *Science* **387**, eadq4510 (2025). https://doi.org/10.1126/science.adq4510
192 Saltukoglu, D. *et al.* Plasma membrane topography governs the 3D dynamic localization of IgM B cell antigen receptor clusters. *The EMBO Journal* **42**, e112030 (2023). https://doi.org/10.15252/embj.2022112030
193 Juette, M. F. *et al.* Three-dimensional sub–100 nm resolution fluorescence microscopy of thick samples. *Nature Methods* **5**, 527-529 (2008). https://doi.org/10.1038/nmeth.1211
194 Zaza, C. *et al.* Super-resolution imaging in whole cells and tissues via DNA-PAINT on a spinning disk confocal with optical photon reassignment. *Nature Communications* **16**, 4991 (2025). https://doi.org/10.1038/s41467-025-60263-w
195 Chung, K. K. H. *et al.* Fluorogenic DNA-PAINT for faster, low-background super-resolution imaging. *Nature Methods* **19**, 554-559 (2022). https://doi.org/10.1038/s41592-022-01464-9
196 Wassie, A. T., Zhao, Y. & Boyden, E. S. Expansion microscopy: principles and uses in biological research. *Nature Methods* **16**, 33-41 (2019). https://doi.org/10.1038/s41592-018-0219-4
197 Zwettler, F. U. *et al.* Molecular resolution imaging by post-labeling expansion single-molecule localization microscopy (Ex-SMLM). *Nature Communications* **11**, 3388 (2020). https://doi.org/10.1038/s41467-020-17086-8
198 Rocha Tapia, A. *et al.* Site-directed conjugation of single-stranded DNA to affinity proteins: quantifying the importance of conjugation strategy. *Chemical Science* **15**, 8982-8992 (2024). https://doi.org/10.1039/D4SC01838A

199 Wang, G. & Xu, X. S. Peptide nucleic acid (PNA) binding-mediated gene regulation. *Cell Research* **14**, 111-116 (2004). https://doi.org/10.1038/sj.cr.7290209
200 Paludan, Søren R. & Bowie, Andrew G. Immune Sensing of DNA. *Immunity* **38**, 870-880 (2013). https://doi.org/10.1016/j.immuni.2013.05.004
201 Young, T. S. & Schultz, P. G. Beyond the Canonical 20 Amino Acids: Expanding the Genetic Lexicon *. *Journal of Biological Chemistry* **285**, 11039-11044 (2010). https://doi.org/10.1074/jbc.R109.091306
202 Masullo, L. A. *et al.* Ångström-resolution imaging of cell-surface glycans. *bioRxiv*, 2025.2002.2007.637003 (2025). https://doi.org/10.1101/2025.02.07.637003
203 Watson, J. L. *et al.* De novo design of protein structure and function with RFdiffusion. *Nature* **620**, 1089-1100 (2023). https://doi.org/10.1038/s41586-023-06415-8
204 Diwanji, D. *et al.* Structures of the HER2–HER3–NRG1β complex reveal a dynamic dimer interface. *Nature* **600**, 339-343 (2021). https://doi.org/10.1038/s41586-021-04084-z
205 Singh, P. K., Kim, S. & Smith, A. W. HER4 is a high-affinity dimerization partner for all EGFR/HER/ErbB family proteins. *Protein Science* **33**, e5171 (2024). https://doi.org/10.1002/pro.5171
206 Garrett, J. T., Tendler, S., Feroz, W., Kilroy, M. K. & Yu, H. Emerging importance of HER3 in tumorigenesis and cancer therapy. *Nature Reviews Clinical Oncology* **22**, 348-370 (2025). https://doi.org/10.1038/s41571-025-01008-y
207 Lucas, L. M. *et al.* The Yin and Yang of ERBB4: Tumor Suppressor and Oncoprotein. *Pharmacological Reviews* **74**, 18-47 (2022). https://doi.org/10.1124/pharmrev.121.000381
208 Gaboriaud, C., Frachet, P., Thielens, N. & Arlaud, G. The Human C1q Globular Domain: Structure and Recognition of Non-Immune Self Ligands. *Frontiers in Immunology* **2** (2012). https://doi.org/10.3389/fimmu.2011.00092
209 Keyt, B. A., Baliga, R., Sinclair, A. M., Carroll, S. F. & Peterson, M. S. Structure, Function, and Therapeutic Use of IgM Antibodies. *Antibodies* **9** (2020).
210 Divine, R. *et al.* Designed proteins assemble antibodies into modular nanocages. *Science* **372**, eabd9994 (2021). https://doi.org/10.1126/science.abd9994
211 Yi, M. *et al.* Targeting cytokine and chemokine signaling pathways for cancer therapy. *Signal Transduction and Targeted Therapy* **9**, 176 (2024). https://doi.org/10.1038/s41392-024-01868-3
212 Codarri Deak, L. *et al.* PD-1-cis IL-2R agonism yields better effectors from stem-like CD8+ T cells. *Nature* **610**, 161-172 (2022). https://doi.org/10.1038/s41586-022-05192-0
213 Li, H., Chang, Y., Jin, T. & Zhang, M. Progress of PD-1/PD-L1 immune checkpoint inhibitors in the treatment of triple-negative breast cancer. *Cancer Cell International* **25**, 139 (2025). https://doi.org/10.1186/s12935-025-03769-z
214 Lim, S. H., Beers, S. A., Al-Shamkhani, A. & Cragg, M. S. Agonist Antibodies for Cancer Immunotherapy: History, Hopes, and Challenges. *Clinical Cancer Research* **30**, 1712-1723 (2024). https://doi.org/10.1158/1078-0432.CCR-23-1014

6. Acknowledgements

I first and foremost thank Ralf for giving me the opportunity to pursue a PhD in his lab, investigating cell surface receptors and therapeutic antibodies with DNA-PAINT. Thank you for trusting me, for exposing me to exciting research questions, for pushing me outside of my comfort zone, and providing all the resources I needed to pursue my projects in the lab.

I also thank Christian for being my internal supervisor, for the great scientific collaboration, and for introducing me to the fascinating world of therapeutic antibodies. I am grateful for your timely feedback and your guidance throughout.

Thank you to my thesis advisory committee: Ralf Jungmann, Christian Klein, Michael Reth, Søren Degn, and Roland Beckmann, as well as to the members of my defense committee at the LMU Faculty of Chemistry and Biochemistry: Lukas Milles and Johanna Klughammer.

I am very grateful for the supportive and inspiring environment in the Jungmann lab. The team spirit and helpful culture will always be my benchmark for what a work environment should be like.

Sebastian and Alexa, thank you for your training and support at the beginning of my PhD.

Eduard, thank you for showing me all the tips and tricks in the lab and for always being there for me. I really enjoy our conversations, both in and outside of the lab, and I hope we stay friends in the future.

Shuhan, it was great working and discussing with you, you are such an inspiring scientist.

Thank you to the old girls' office: Kimberly, Taisha, and Ana. We always had so much fun together! Taisha, you were my desk neighbor for a long time, and I still miss having you in the office, I hope we stay in touch.

To the new girls' office: Monique and Eva, it has been great working with you. Monique, it has been amazing to both mentor you and learn from you over the past years. Eva, I really appreciate the team spirit you bring to the lab.

To the RESI team, Susanne, Luciano, and Philipp: we've been through all the challenges and fun together. You are all amazing scientists, and it was an honor to work with you!

Thank you Luciano for being such a great mentor! Your unique ability to combine scientific excellence with genuine people skills will always be an inspiration to me.

Thank you Rafal for always being a fun colleague and for your support with data analysis questions.

Thank you Larissa for the amazing teamwork and for being such an efficient and reliable scientist. I am sure you will have a great start to your PhD.

Ondřej, thank you for all the insights into protein biochemistry, it has been great working and discussing with you.

Jisoo, without you the lab would fall apart. Thank you for being such a warm and friendly person.

Megan and Clemens, it was great working with you at the beginning of your postdocs! You are both incredibly talented and skilled. With you, I see a bright future for the lab.

Hannah, it was an honor to have you as a Master's student, and it has been wonderful to witness your development over the past years. I am very excited to see the science you will bring to the world.

Thank you, Eduard and Peter, for proofreading my thesis.

To all my friends who supported me throughout my PhD: Thank you for the distractions, for keeping me grounded, and for always believing in me.

To my parents and my brother: Thank you for providing the best environment to grow up in. Without your support and belief in me, I would have never made it this far.

To my husband Ludwig: Thank you for being my rock and for sharing both the tough and joyful moments of this journey. You have always reminded me of my worth, encouraged me to stand my ground, and inspired me to prioritize not just hard work, but also fun and balance in life. I cannot wait for our future together.

7. Appendix

7.1 Publication 1

Ångström-resolution fluorescence microscopy

Susanne C. M. Reinhardt*, Luciano A. Masullo*, **Isabelle Baudrexel***, Philipp R. Steen*, Rafal Kowalewski, Alexandra S. Eklund, Sebastian Strauss, Eduard M. Unterauer, Thomas Schlichthaerle, Maximilian T. Strauss, Christian Klein & Ralf Jungmann. (* equal contribution)

Published in Nature

2023

Reprinted from Springer Nature.[185]

Article

Ångström-resolution fluorescence microscopy

https://doi.org/10.1038/s41586-023-05925-9

Received: 21 July 2022

Accepted: 7 March 2023

Published online: 24 May 2023

Open access

Check for updates

Susanne C. M. Reinhardt[1,2,5], Luciano A. Masullo[1,5], Isabelle Baudrexel[1,3,5], Philipp R. Steen[1,2,5], Rafal Kowalewski[1,2], Alexandra S. Eklund[1,3], Sebastian Strauss[1,2], Eduard M. Unterauer[1,2], Thomas Schlichthaerle[1,2], Maximilian T. Strauss[1,2], Christian Klein[3,4] & Ralf Jungmann[1,2]✉

Fluorescence microscopy, with its molecular specificity, is one of the major characterization methods used in the life sciences to understand complex biological systems. Super-resolution approaches[1–6] can achieve resolution in cells in the range of 15 to 20 nm, but interactions between individual biomolecules occur at length scales below 10 nm and characterization of intramolecular structure requires Ångström resolution. State-of-the-art super-resolution implementations[7–14] have demonstrated spatial resolutions down to 5 nm and localization precisions of 1 nm under certain in vitro conditions. However, such resolutions do not directly translate to experiments in cells, and Ångström resolution has not been demonstrated to date. Here we introdue a DNA-barcoding method, resolution enhancement by sequential imaging (RESI), that improves the resolution of fluorescence microscopy down to the Ångström scale using off-the-shelf fluorescence microscopy hardware and reagents. By sequentially imaging sparse target subsets at moderate spatial resolutions of >15 nm, we demonstrate that single-protein resolution can be achieved for biomolecules in whole intact cells. Furthermore, we experimentally resolve the DNA backbone distance of single bases in DNA origami with Ångström resolution. We use our method in a proof-of-principle demonstration to map the molecular arrangement of the immunotherapy target CD20 in situ in untreated and drug-treated cells, which opens possibilities for assessing the molecular mechanisms of targeted immunotherapy. These observations demonstrate that, by enabling intramolecular imaging under ambient conditions in whole intact cells, RESI closes the gap between super-resolution microscopy and structural biology studies and thus delivers information key to understanding complex biological systems.

The localization precision (σ_{SMLM}) of a target molecule in widefield single-molecule localization microscopy (SMLM)[15] is ultimately and fundamentally limited by the number of photons (N) collected per blinking event: $\sigma_{SMLM} \approx \frac{\sigma_{DIFF}}{\sqrt{N}}$ (σ_{DIFF} is the s.d. of the point spread function (PSF) of the optical imaging system[16]; Fig. 1a). Multiple localizations of the same target (Fig. 1b, top) are distributed around the true position due to their finite precision. Two or more points not resolvable by SMLM produce overlapping distributions of localizations, thus precluding unique assignment of localizations to respective targets (Fig. 1b, bottom). However, if each localization could be assigned to a specific target by colour, barcode or any other molecular identity, they could be unambiguously grouped per target[2].

The centre of each group of localizations can be calculated with a precision far better than σ_{SMLM}. In essence, applying the principle of localization microscopy to distinguishable groups of K super-resolved localizations, precision is increased from the s.d. (σ_{SMLM}) to the s.e.m. ($\frac{\sigma_{SMLM}}{\sqrt{K}}$). Collecting an arbitrarily large number of localizations yields an arbitrary increase in precision. Notably, this increase in precision occurs regardless of the precision achieved in individual localizations (σ_{SMLM}).

We introduce a straightforward implementation of this concept using Exchange-PAINT[17], a variant of DNA-PAINT[18], for identical target molecules (Fig. 1c). DNA-PAINT uses the programmable, repetitive but transient binding of dye-labelled 'imager' strands to their complementary 'docking' strands on target molecules of interest[9,18]. The transient nature of the binding leads to an apparent 'blinking' of the target, necessary to perform SMLM. Exchange-PAINT uses orthogonal DNA barcodes combined with imaging and washing cycles to allow for sequential target multiplexing. In our implementation we 'multiplex' a single target species by separating it into multiple, sparser subsets. By imaging them sequentially, sufficiently spaced and isolated groups of localizations are measured. Determining the centre of each group of localizations yields a resolution enhancement (Fig. 1d). We call this implementation resolution enhancement by sequential imaging (RESI), and the resulting localizations RESI localizations.

[1]Max Planck Institute of Biochemistry, Planegg, Germany. [2]Faculty of Physics and Center for NanoScience, Ludwig Maximilian University, Munich, Germany. [3]Department of Chemistry and Biochemistry, Ludwig Maximilian University, Munich, Germany. [4]Roche Innovation Center Zurich, Roche Pharma Research and Early Development, Schlieren, Switzerland. [5]These authors contributed equally: Susanne C. M. Reinhardt, Luciano A. Masullo, Isabelle Baudrexel, Philipp R. Steen. ✉e-mail: jungmann@biochem.mpg.de

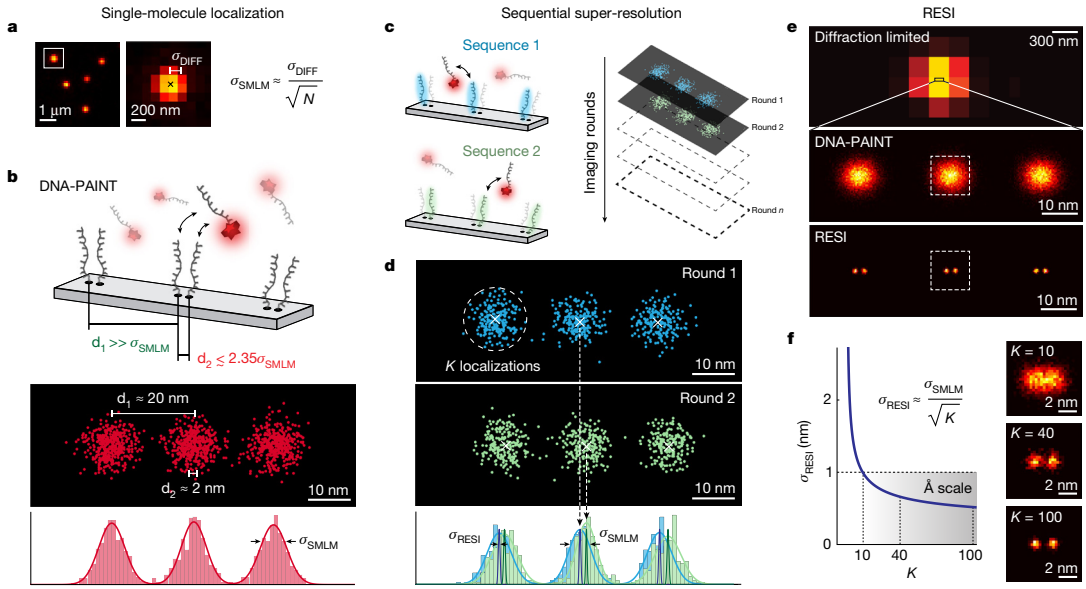

Fig. 1 | RESI concept. a, In SMLM, σ_{SMLM} of a single dye scales with $\frac{\sigma_{DIFF}}{\sqrt{N}}$, ultimately limiting the achievable spatial resolution. **b**, SMLM approaches such as DNA-PAINT feature approximately 10 nm spatial resolution (resolution approximated as full-width at half-maximum ≈ 2.35 σ_{SMLM}). Whereas targets separated by 20 nm (d_1) can thus be routinely resolved, objects spaced 2 nm apart (d_2) are unresolvable because the resulting distributions of localizations overlap. **c**, Using orthogonal DNA sequences (blue and green) and sequential acquisition as in Exchange-PAINT, localizations from targets spaced more closely than the SMLM resolution limit can be unambiguously assigned for each target. **d**, Combining all localizations per target (K) for each imaging round improves localization precision from s.d. (σ_{SMLM}) to s.e.m. (σ_{RESI}). **e**, As super-resolution revolutionized fluorescence microscopy, RESI results in another paradigm shift by reapplying the concept of localization to super-resolution data. **f**, Localization precision in RESI scales with $\frac{1}{\sqrt{K}}$, and thus resolution improvement in RESI is independent of σ_{SMLM}, reaching localization precision on the Ångström scale.

By application of RESI in silico (Methods), we demonstrated a resolution improvement (Extended Data Fig. 1) over super-resolution akin to the improvement of super-resolved over diffraction-limited measurements (Fig. 1e). For routinely obtainable DNA-PAINT localization precision (approximately 3 nm) and number of localizations per target (in the order of hundreds), RESI could achieve precision well below one nanometre, thus entering the Ångström scale (Fig. 1f) according to $\sigma_{RESI} = \frac{\sigma_{SMLM}}{\sqrt{K}}$.

For an experimental proof of principle of RESI we used self-assembled DNA origami structures to precisely position orthogonal DNA strands[9,19]. We first designed DNA origami featuring two docking strands spaced 5 nm apart, a distance previously resolved with DNA-PAINT[7,9], to verify the accuracy and precision of RESI. Using two sequential imaging rounds and an alignment procedure (Methods) to conduct RESI, we were able to accurately recapitulate the 5 nm point-to-point distance with precision improved by a factor of $\sqrt{K_{average}} = \sqrt{381} \approx 20$ (Extended Data Figs. 2 and 3).

We next performed RESI in three dimensions (3D) using recently developed 3D DNA origami disk structures[20] and measured distances between docking strands of 2.5 ± 0.4 nm in xy and 11.3 ± 0.8 nm in z. This demonstrates that RESI resolution enhancement applies in all three dimensions, surpassing current state-of-the-art 3D super-resolution capabilities (Extended Data Figs. 4 and 5; for imaging parameters see Extended Data Table 1).

RESI resolves single nuclear pore complex proteins

To demonstrate the applicability of RESI in a cellular context, we next imaged structural proteins of the nuclear pore complex (NPC). As the major gatekeeper of nucleocytoplasmic transport, the NPC is a key target for structural biology research[21]. We furthermore chose the NPC as a model system because it has been well studied using a variety of imaging approaches, including cryo-electron microscopy (cryo-EM)[22], fluorescence microscopy and super-resolution techniques[23,24]. Figure 2a presents a typical diffraction-limited and DNA-PAINT image of Nup96 molecules (tagged with monomeric enhanced green fluorescent protein (mEGFP)) labelled with DNA-conjugated anti-GFP nanobodies. Nup96 is a structural NPC protein (part of the so-called Y-complex) present in eight pairs exhibiting an eight-fold symmetry on both cytoplasmic and nuclear rings, totalling 32 copies per NPC (Fig. 2b). Individual pairs of Nup96 proteins, spaced approximately 10 nm laterally and 3 nm axially, cannot be routinely resolved with current state-of-the-art super-resolution implementations[25–28]. To enable RESI, neighbouring copies of Nup96 proteins must be labelled with orthogonal DNA sequences. To this end, we opted for a stochastic labelling approach by incubating the sample with anti-GFP nanobodies, each conjugated with one out of four orthogonal sequences (Fig. 2c). We note that, with an increasing number of expected targets below the classical DNA-PAINT resolution limit, a larger number of orthogonal labelling sequences[29]—and thus imaging rounds—is necessary to guarantee sufficiently spaced groups of localizations (for details on this requirement see Methods). Sequential 3D image acquisition in four rounds led to sufficiently spaced localization groups representing single Nup96 target molecules (Fig. 2d). Subsequent RESI super-localization of these groups allowed us to routinely visualize individual copies of Nup96 proteins (Fig. 2e). We note that this was achieved across the whole field of view (roughly 67 × 67 µm^2) totalling over 1,000 NPCs during a total image acquisition time of

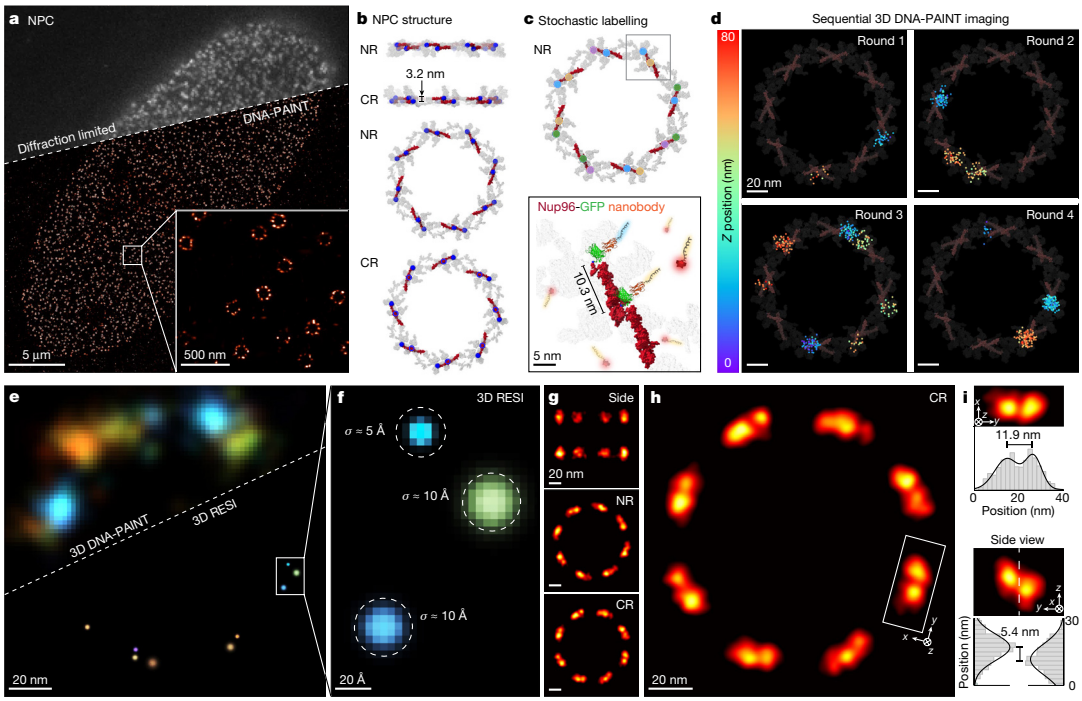

Fig. 2 | NPC proteins in whole cells resolved with Ångström precision by RESI. a, Diffraction-limited and DNA-PAINT overview image of Nup96-mEGFP labelled with DNA-conjugated anti-GFP nanobodies. Zoomed-in view (bottom right) shows high labelling efficiency and image quality for standard DNA-PAINT conditions, recapitulating the eight-fold symmetry of the NPC. **b**, Cryo-EM structure representation of the location of Nup96 proteins (red; C-terminal mEGFP position marked in blue) as part of the Y-complex in nuclear and cytoplasmic rings (NR and CR, respectively). Adapted from PDB 7PEQ. Nup96 is present in 32 copies per NPC. **c**, To enable RESI, Nup96-mEGFP proteins were stochastically labelled with orthogonal DNA sequences by incubation of the sample with anti-GFP nanobodies, each conjugated with one of four orthogonal sequences (represented by blue, yellow, magenta and green dots). **d**, Sequential 3D imaging (colour represents *z* position) of the four labels yielded sufficiently spaced localization distributions. The average number of localizations per target is $K_{average}$ = 38 (background represents cryo-EM structure from **b** for context). **e**, Comparison of 3D DNA-PAINT (top left) and 3D RESI (bottom right) for the same NPC illustrating improvement in spatial resolution by RESI. Localizations are rendered as gaussians with $\sigma_{DNA\text{-}PAINT}$ and σ_{RESI}, respectively. **f**, Localization precision (σ_{RESI}) as good as 5 Å was achieved by combining *K* localizations for each target, unambiguously resolving single Nup96 proteins. **g**, The 3D NPC cryo-EM structure was recapitulated using optical microscopy by applying a model-free average[30] of 1,217 NPCs from a single nucleus. **h**, RESI resolved adjacent Nup96 in a structural average by optical microscopy. **i**, Consistent with the cryo-EM structure (taking into account linkage error arising from label size), adjacent Nup96 proteins were spaced 11.9 ± 1.2 nm apart laterally (top) and 5.4 ± 0.4 nm axially (bottom).

100 min (see Extended Data Fig. 6 for representative data). The reconstructed RESI image features an average lateral localization precision of approximately 1 nm, representing a sixfold improvement over the individual DNA-PAINT acquisition rounds. We therefore achieved label-size-limited resolution, allowing us to resolve individual Nup96 molecules (Fig. 2f). Generally, label size not only limits spatial resolution but furthermore could lead to inaccuracies such as biased observed distances due to linkage errors.

We then performed unbiased 3D averaging of 1,217 NPCs using a recently developed model-free approach for SMLM data[30]. The resulting 3D average (Fig. 2g) not only allows recapitulation of the eight-fold symmetry of Nup96 in both cytoplasmic and nuclear rings (which has previously been achieved with super-resolution[23–28]), but enables resolution of individual Nup96 proteins in a structural average (Fig. 2h). Enabled by RESI's unprecedented spatial resolution, we were able to recapitulate distances of Nup96 proteins of 11.9 ± 1.2 nm laterally and 5.4 ± 0.4 nm axially from the structural average image (Fig. 2i). Both lateral and axial orientation, as well as tilt, of Nup96 pairs are consistent with cryo-EM data[22]. We resolved this spatial arrangement for most Nup96 protein pairs (Extended Data Fig. 7), which was previously out of reach for optical microscopy.

Imaging DNA bases at Ångström resolution

To assay the ultimately achievable spatial resolution by RESI, we designed a flat, rectangular DNA origami structure featuring six pairs (spaced 20 nm apart) of directly adjacent orthogonal docking strands at a distance of only one DNA base pair (red and blue strands in Fig. 3a). This yielded a designed in-plane distance of around 7 Å along the backbone of one strand of the DNA double helix[31]. The structures also contain DNA-PAINT docking strands for precise alignment between sequential imaging rounds (green strands in Fig. 3a). State-of-the-art DNA-PAINT image acquisition[32] at approximately 5 nm spatial resolution yielded six localization clouds in a 20 nm grid arrangement but failed to resolve the individual docking strands at subnanometre single-base-pair distances (Fig. 3b).

Remarkably, RESI resolves the individual docking strand positions (Fig. 3c) in all DNA origami structures. We note that RESI achieved this

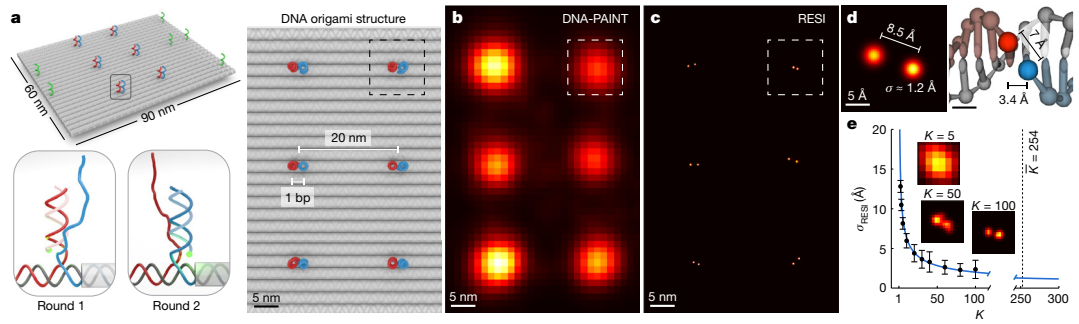

Fig. 3 | RESI resolves the distance of single DNA base pairs at Ångström resolution. a, DNA origami with docking strands spaced by a single base pair (bp; red and blue strands, with alignment markers in green) provided a platform to demonstrate the highest resolution achievable by RESI. **b**, DNA-PAINT resolved 20 nm spacing but the resolution was insufficient to distinguish individual docking sites, spaced one base apart. **c**, RESI resolves the adjacent docking strands. **d**, A Euclidean distance of 8.5 ± 1.7 Å was calculated from individual localizations with an average precision of 1.2 Å (left) for the single-base-pair backbone distance, which is within 1 s.d. of the expected value of roughly 7 Å (right). **e**, Experimental localization precision in RESI is in good agreement with $\frac{\sigma_{SMLM}}{\sqrt{K}}$ (blue line, K), yielding an average localization precision of 1.3 Å for the experimental data from all $n = 42$ DNA origami (insets correspond to exemplary point pair in **d**). Error bars represent mean ± 1 s.d.

in an image acquisition time of 100 min featuring an approximately 67 × 67 µm² field of view containing more than 2,000 DNA origami structures (see Extended Data Fig. 8 for representative DNA origami structures). RESI allows us to routinely resolve strands spaced apart by only one DNA base pair. Strikingly, we measured a distance of 8.5 ± 1.7 Å between two single docking strands in an individual DNA origami structure (Fig. 3d). This demonstrates an unprecedented resolution in optical microscopy by distinguishing structures closer than one nanometre. We note that our resolution claim is based on the most fundamental and strict definition: the ability to spatially distinguish point objects. We measured a distance of 9.5 ± 2.6 Å between adjacent docking strands in an average of 42 DNA origami (Extended Data Fig. 9), which is within 1 s.d. of the expected backbone distance[31] of around 7 Å.

To quantify resolution gain, we calculated RESI localizations for different values of K underlying DNA-PAINT localizations (Methods). We demonstrate that the effective localization precision scales as $\sigma_{RESI} = \frac{\sigma_{SMLM}}{\sqrt{K}}$, yielding an average localization precision of 1.3 Å for an average $K = 254$ (Fig. 3e), experimentally confirming the in silico results (Fig. 1f). RESI not only yields virtually unlimited numbers of localizations per target, but also avoids detrimental photophysical effects caused by spatial proximity of fixed-dye labels because, in DNA-PAINT imaging, two adjacent dyes are never present simultaneously. It has recently been reported[33] that, at sub-10-nm distances, photophysical near-field interactions play a major role in modulation of photoswitching kinetics, thus effectively preventing fixed-dye SMLM techniques from accessing this resolution scale. This ultimately limits the achievable resolution of even the most photon-efficient techniques available for single-molecule localization, such as MINFLUX or MINSTED, despite their subnanometre precision, unless combined with DNA-PAINT. The experimentally demonstrated subnanometre resolution illustrates the capacity of RESI to enable structural biology studies using DNA-based imaging at hitherto elusive scales.

CD20 receptor organization

Finally, we applied RESI to address and resolve a cell-biological question currently under debate that has so far been beyond reach for both cryo-EM in a native cellular context and incumbent super-resolution techniques. Specifically we studied the organization of CD20 membrane receptors, which are prime targets for therapeutic antibody treatment of B cell-derived blood cancers and autoimmune diseases[34].

In the case of the most frequently used therapeutic anti-CD20 antibody, rituximab (RTX), the spatial rearrangement of CD20 in the cell membrane is thought to play an important role in its efficacy[35,36]. Recent cryo-EM studies detected CD20 as a dimer in complex with two individual RTX-fragment antigen-binding regions[37,38], suggesting a linear chain-like assembly of CD20 in the presence of the full antibody[38]. On the other hand, when incubated with the full RTX antibody, a trimeric ring of alternating RTX molecules and CD20 dimers was detected in EM images[37]. The fact that cryo-EM experiments are performed in detergent solution raises the question about which molecular arrangements are actually present in the cell. Currently CD20 organization when bound to full RTX antibodies in intact cells cannot be assessed, thus precluding the investigation of whether CD20 clusters are of linear or circular nature. Moreover, even though in vitro studies showed that CD20 dimers can form without antibody binding, the quantitative assessment of CD20 dimerization in untreated cells is currently limited.

Here we applied RESI to study the molecular arrangement of CD20 in Chinese hamster ovary (CHO) cells transiently transfected with mEGFP-CD20, using four rounds of probe exchange in a total imaging time of 4.4 h. In the diffraction-limited overview and DNA-PAINT super-resolution image of untreated cells, CD20 appeared homogeneously distributed (Fig. 4a,b (top) and Extended Data Fig. 10a) whereas RTX-treated cells exhibited apparent CD20 clusters (Fig. 4b (bottom) and Extended Data Figs. 11a and 12a).

Comparison of DNA-PAINT and RESI for both untreated and RTX-treated cells shows sub-10-nm-spaced CD20 pairs in the RESI images (Fig. 4c, right) that were unresolvable with DNA-PAINT (Fig. 4c, left). RESI images suggest that CD20 is present in dimers and chain-like, higher-order structures in untreated and RTX-treated cells, respectively (Fig. 4d).

To quantitatively assess the existence of dimers in untreated cells, we performed first nearest-neighbour distance (NND) analysis for both DNA-PAINT and RESI data, demonstrating nonrandom distributions in both cases (Fig. 4e). RESI at 1 nm localization precision shows a substantial fraction of sub-10-nm distances in the NND histogram, which enables quantitative assessment of the degree of CD20 dimerization. We performed numerical simulations and a least-squares fit (Methods) that yielded a composition of 53 ± 1% monomers and 47 ± 1% dimers with average intradimer distance of 13.5 ± 0.3 nm (Fig. 4f, solid line). For comparison, we simulated NND distributions corresponding to a population of 100% monomers (Fig. 4f, dotted line),

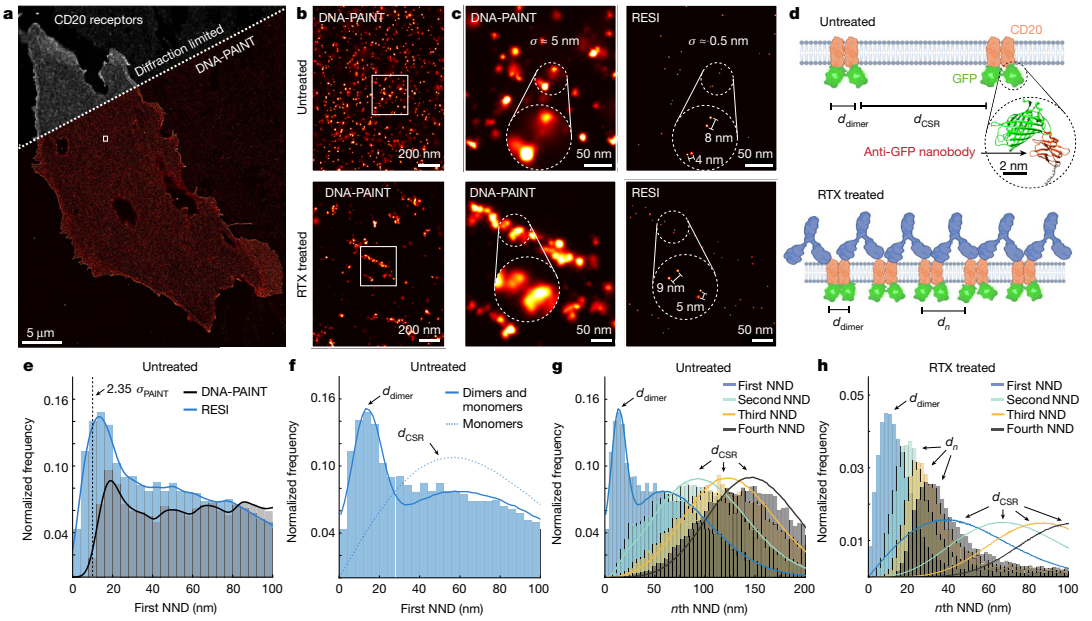

Fig. 4 | RESI shows CD20 receptor (re)organization at subnanometre precision following drug treatment. a, Diffraction-limited and DNA-PAINT overview image of CHO cells expressing mEGFP-CD20 labelled with anti-GFP nanobodies. **b**, Zoomed-in DNA-PAINT image showing apparently randomly distributed CD20 receptors for untreated cells (top) and clustered receptor arrangement for RTX-treated cells (bottom). **c**, Comparison of DNA-PAINT and RESI for both untreated and RTX-treated cells showing sub-10-nm-spaced receptor pairs in the RESI images, which are unresolvable with DNA-PAINT. **d**, RESI data suggest that CD20 proteins occur in dimers (spaced at d_{dimer}), which are in turn distributed according to complete spatial randomness (CSR; distances between dimers, d_{CSR}) in untreated cells. Chains of dimers were observed following administration of RTX. **e**, Whole-cell analysis of first NNDs of CD20 receptors (histograms of distances and kernel density estimation are shown). Only RESI, but not DNA-PAINT, allows the routine detection of sub-10-nm distances between proteins. Whereas DNA-PAINT overestimates dimer distance, RESI shows a label-limited distance of 13.5 nm (see main text for discussion). **f**, Fitting RESI NND data from **e** to a numerical model reveals CD20 dimers and monomers. **g**, CD20 receptors in untreated cells showed second to fourth NNDs consistent with CSR, thus excluding the presence of higher-order protein complexes. **h**, CD20 receptors in RTX-treated cells, however, showed first to fourth NNDs, inconsistent with complete spatial randomness.

further demonstrating that CD20 molecules are not present solely as monomers. Because all NND distributions except for the first order are consistent with a complete spatial random (CSR) distribution at the experimentally measured density, we exclude the presence of higher-order assemblies for untreated CD20 (Fig. 4g). Our findings present quantitative experimental evidence that CD20 exists as dimers in an intact cell membrane.

By contrast, RESI analysis of CD20 in RTX-treated cells yielded first to fourth NND distributions inconsistent with a CSR model (Fig. 4h and Extended Data Fig. 12d,e). This suggests a higher-order arrangement of CD20 molecules after RTX treatment and confirms recent cryo-EM-derived models[37,38].

Finally we probed the existence of hexameric, ring-like arrangements by comparison with numerical simulations (Extended Data Fig. 13). The characteristics of the experimentally detected CD20 clusters suggest the absence of isolated hexamers and support the hypothesis of predominantly linear, chain-like structures (Extended Data Fig. 13h).

Discussion

We introduce RESI, a conceptually new approach in SMLM to improve the spatial resolution of optical microscopy to the Ångström scale. RESI achieves this by combining multiple localizations from single targets to obtain a 'super-super-resolution' image after separating their localizations by sequential imaging (for example, using DNA-barcoded probes).

In this way RESI precision—and thus resolution—scales not only with the number of photons (N) detected per localization but also with the number of localizations (K) acquired per target. RESI thus provides a new precision scaling law: $\sigma_{RESI} = \frac{\sigma_{SMLM}}{\sqrt{K}} \approx \frac{\sigma_{DIFF}}{\sqrt{K}\cdot\sqrt{N}}$. This applies if a sufficiently large number of orthogonal labelling sequences and thus imaging rounds guarantee adequately spaced groups of localizations (Extended Data Fig. 14). Importantly, resolution enhancement is isotropic in three dimensions. For our current experimental implementation, RESI approaches structural biology resolution with an all-optical approach in intact cells using off-the-shelf labelling reagents and a simple inverted fluorescence microscope operated under ambient conditions. We were able to experimentally demonstrate Ångström spatial resolution below the physical size of a dye. This was achieved due to three specific advantages of DNA-PAINT leading to unbiased target sampling: (1) the rotational flexibility of the target-bound docking strand (even in the case of longer repetitive-sequence motifs[32]); (2) the freely rotating dipole of the dye attached to the imager sequence; and (3) the fact that two adjacent imagers are never present simultaneously.

Furthermore, because RESI images are not obtained from single localizations but from groups of localizations per target, the method presents a uniquely robust feature compared with other SMLM techniques: it shifts the focus from enhancement of only optical precision (σ_{OPT}) to improvement in overall precision ($\sigma_{SMLM} \approx \sqrt{\sigma_{OPT}^2 + \sigma_{MEC}^2}$) by averaging out the uncertainty effects of mechanical instability (σ_{MEC}), provided the latter is normally distributed.

With RESI we measured areas of 67 × 67 μm² in 100 min, making it applicable as a sufficiently high-throughput tool for cell biology. Resolving receptor patterns at single-protein resolution could enable 'spatial diagnostics' as a prescreening method for personalized treatments, and serve as a tool for biomedical discovery of patterned therapeutics—for example, by guiding drug design principles.

RESI performance and accuracy could be further improved by advances in intramolecular labelling approaches such as orthogonal unnatural amino acids[39]. RESI is thus poised to close the gap between 3D fluorescence super-resolution microscopy in whole intact cells and cryo-EM structural studies of individual supramolecular complexes, introducing a paradigm shift in fluorescence imaging by pushing optical microscopy to Ångström resolutions.

Online content

Any methods, additional references, Nature Portfolio reporting summaries, source data, extended data, supplementary information, acknowledgements, peer review information; details of author contributions and competing interests; and statements of data and code availability are available at https://doi.org/10.1038/s41586-023-05925-9.

1. Hell, S. W. & Wichmann, J. Breaking the diffraction resolution limit by stimulated emission: stimulated-emission-depletion fluorescence microscopy. *Opt. Lett.* **19**, 780–782 (1994).
2. Betzig, E. Proposed method for molecular optical imaging. *Opt. Lett.* **20**, 237–239 (1995).
3. Klar, T. A., Jakobs, S., Dyba, M., Egner, A. & Hell, S. W. Fluorescence microscopy with diffraction resolution barrier broken by stimulated emission. *Proc. Natl Acad. Sci. USA* **97**, 8206–8210 (2000).
4. Betzig, E. et al. Imaging intracellular fluorescent proteins at nanometer resolution. *Science* **313**, 1642–1645 (2006).
5. Rust, M. J., Bates, M. & Zhuang, X.Sub-diffraction-limit imaging by stochastic optical reconstruction microscopy (STORM). *Nat. Methods* **3**, 793–795 (2006).
6. Sharonov, A. & Hochstrasser, R. M. Wide-field subdiffraction imaging by accumulated binding of diffusing probes. *Proc. Natl Acad. Sci. USA* **103**, 18911–18916 (2006).
7. Dai, M., Jungmann, R. & Yin, P. Optical imaging of individual biomolecules in densely packed clusters. *Nat. Nanotechnol.* **11**, 798–807 (2016).
8. Balzarotti, F. et al. Nanometer resolution imaging and tracking of fluorescent molecules with minimal photon fluxes. *Science* **355**, 606–612 (2017).
9. Schnitzbauer, J., Strauss, M. T., Schlichthaerle, T., Schueder, F. & Jungmann, R. Super-resolution microscopy with DNA-PAINT. *Nat. Protoc.* **12**, 1198–1228 (2017).
10. Reymond, L. et al. SIMPLE: structured illumination based point localization estimator with enhanced precision. *Opt. Express* **27**, 24578–24590 (2019).
11. Gu, L. et al. Molecular resolution imaging by repetitive optical selective exposure. *Nat. Methods* **16**, 1114–1118 (2019).
12. Cnossen, J. et al. Localization microscopy at doubled precision with patterned illumination. *Nat. Methods* **17**, 59–63 (2020).
13. Weber, M. et al. MINSTED fluorescence localization and nanoscopy. *Nat. Photonics* **15**, 361–366 (2021).
14. Masullo, L. A. et al. An alternative to MINFLUX that enables nanometer resolution in a confocal microscope. *Light Sci. Appl.* **11**, 199 (2022).
15. Lelek, M. et al. Single-molecule localization microscopy. *Nat. Rev. Methods Primers* https://doi.org/10.1038/s43586-021-00038-x (2021).
16. Mortensen, K. I., Churchman, L. S., Spudich, J. A. & Flyvbjerg, H. Optimized localization analysis for single-molecule tracking and super-resolution microscopy. *Nat. Methods* **7**, 377–381 (2010).
17. Jungmann, R. et al. Multiplexed 3D cellular super-resolution imaging with DNA-PAINT and Exchange-PAINT. *Nat. Methods* **11**, 313–318 (2014).
18. Jungmann, R. et al. Single-molecule kinetics and super-resolution microscopy by fluorescence imaging of transient binding on DNA origami. *Nano Lett.* **10**, 4756–4761 (2010).
19. Rothemund, P. W. Folding DNA to create nanoscale shapes and patterns. *Nature* **440**, 297–302 (2006).
20. Eklund, A. S., Comberlato, A., Parish, I. A., Jungmann, R. & Bastings, M. M. C. Quantification of strand accessibility in biostable DNA origami with single-staple resolution. *ACS Nano* **15**, 17668–17677 (2021).
21. Beck, M. & Hurt, E. The nuclear pore complex: understanding its function through structural insight. *Nat. Rev. Mol. Cell Biol.* **18**, 73–89 (2017).
22. Schuller, A. P. et al. The cellular environment shapes the nuclear pore complex architecture. *Nature* **598**, 667–671 (2021).
23. Loschberger, A. et al. Super-resolution imaging visualizes the eightfold symmetry of gp210 proteins around the nuclear pore complex and resolves the central channel with nanometer resolution. *J. Cell Sci.* **125**, 570–575 (2012).
24. Szymborska, A. et al. Nuclear pore scaffold structure analyzed by super-resolution microscopy and particle averaging. *Science* **341**, 655–658 (2013).
25. Heydarian, H. et al. 3D particle averaging and detection of macromolecular symmetry in localization microscopy. *Nat. Commun.* **12**, 2847 (2021).
26. Wang, W., Heydarian, H., Huijben, T., Stallinga, S. & Rieger, B. Joint registration of multiple point clouds for fast particle fusion in localization microscopy. *Bioinformatics* **38**, 3281–3287 (2022).
27. Gwosch, K. C. et al. Reply to: Assessment of 3D MINFLUX data for quantitative structural biology in cells. *Nat. Methods* **20**, 52–54 (2023).
28. Weber, M. et al. MINSTED nanoscopy enters the Angstrom localization range. *Nat. Biotechnol.* https://doi.org/10.1038/s41587-022-01519-4 (2022).
29. Agasti, S. S. et al. DNA-barcoded labeling probes for highly multiplexed Exchange-PAINT imaging. *Chem. Sci.* **8**, 3080–3091 (2017).
30. Wu, Y. L. et al. Maximum-likelihood model fitting for quantitative analysis of SMLM data. *Nat. Methods* **20**, 139–148 (2023).
31. Drew, H. R. et al. Structure of a B-DNA dodecamer: conformation and dynamics. *Proc. Natl Acad. Sci. USA* **78**, 2179–2183 (1981).
32. Strauss, S. & Jungmann, R. Up to 100-fold speed-up and multiplexing in optimized DNA-PAINT. *Nat. Methods* **17**, 789–791 (2020).
33. Helmerich, D. A. et al. Photoswitching fingerprint analysis bypasses the 10-nm resolution barrier. *Nat. Methods* **19**, 986–994 (2022).
34. Pavlasova, G. & Mraz, M. The regulation and function of CD20: an "enigma" of B-cell biology and targeted therapy. *Haematologica* **105**, 1494–1506 (2020).
35. Glennie, M. J., French, R. R., Cragg, M. S. & Taylor, R. P. Mechanisms of killing by anti-CD20 monoclonal antibodies. *Mol. Immunol.* **44**, 3823–3837 (2007).
36. Pierpont, T. M., Limper, C. B. & Richards, K. L. Past, present, and future of rituximab—the world's first oncology monoclonal antibody therapy. *Front. Oncol.* **8**, 163 (2018).
37. Rouge, L. et al. Structure of CD20 in complex with the therapeutic monoclonal antibody rituximab. *Science* **367**, 1224–1230 (2020).
38. Kumar, A., Planchais, C., Fronzes, R., Mouquet, H. & Reyes, N. Binding mechanisms of therapeutic antibodies to human CD20. *Science* **369**, 793–799 (2020).
39. Beliu, G. et al. Bioorthogonal labeling with tetrazine-dyes for super-resolution microscopy. *Commun. Biol.* **2**, 261 (2019).

Methods

Materials

Unmodified DNA oligonucleotides, as well as DNA oligonucleotides modified with C3-azide and Cy3B, were purchased from MWG Eurofins and Metabion. The M13mp18 and p7560 scaffold was obtained from Tilibit. Magnesium chloride (1 M, no. AM9530G), sodium chloride (5 M, no. AM9759), ultrapure water (no. 10977-035), Tris (1 M, pH 8.0, no. AM9855G), EDTA (0.5 M, pH 8.0, no. AM9260G) and 10× PBS (no. 70011051) were purchased from Thermo Fisher Scientific. BSA (no. A4503-10G) was ordered from Sigma-Aldrich. Triton X-100 (no. 6683.1) was purchased from Carl Roth. Sodium hydroxide (no. 31627.290) was purchased from VWR. Paraformaldehyde (no. 15710) and glutaraldehyde (no. 16220) were obtained from Electron Microscopy Sciences. Tween-20 (no. P9416-50ML), glycerol (no. 65516-500 ml), methanol (no. 32213-2.5L), protocatechuate 3,4-dioxygenase pseudomonas (PCD, no. P8279), 3,4-dihydroxybenzoic acid (PCA, no. 37580-25G-F) and (±)-6-hydroxy-2,5,7,8-tetra-methylchromane-2-carboxylic acid (trolox, no. 238813-5G) were ordered from Sigma-Aldrich. Neutravidin (no. 31000) was purchased from Thermo Fisher Scientific. Biotin-labelled BSA (no. A8549) and sodium azide (no.769320) were obtained from Sigma-Aldrich. Coverslips (no. 0107032) and glass slides (no. 10756991) were purchased from Marienfeld and Thermo Fisher Scientific, respectively. Fetal bovine serum (FBS, no. 10500-064), 1× PBS (pH 7.2, no. 20012-019), 0.05% trypsin-EDTA (no. 25300-054), salmon sperm DNA (no. 15632011), OptiMEM (no. 31985062) and Lipofectamine LTX (no. A12621) were purchased from Thermo Fisher Scientific. Gold nanoparticles (90 nm, no. G-90-100) were ordered from Cytodiagnostics. Nanobodies against GFP (clone 1H1) with a single ectopic cysteine at the C terminus for site-specific conjugation were purchased from Nanotag Biotechnologies. DBCO-PEG4-Maleimide (no. CLK-A108P) was purchased from Jena Bioscience.

Buffers

The following buffers were used for sample preparation and imaging.

- Buffer A: 10 mM Tris pH 8.0, 100 mM NaCl and 0.05% Tween-20
- Buffer B: 10 mM $MgCl_2$, 5 mM Tris-HCl pH 8.0, 1 mM EDTA and 0.05% Tween-20 pH 8.0
- Buffer C: 1× PBS, 1 mM EDTA, 500 mM NaCl pH 7.4, 0.02% Tween, optionally supplemented with 1× trolox, 1× PCA and 1× PCD
- Blocking buffer: 1× PBS, 1 mM EDTA, 0.02% Tween-20, 0.05% NaN_3, 2% BSA, 0.05 mg ml^{-1} sheared salmon sperm DNA
- Two-dimensional (2D) DNA origami folding buffer: 10 mM Tris, 1 mM EDTA, 12.5 mM $MgCl_2$ pH 8.0
- 3D DNA origami folding buffer: 5 mM Tris, 1 mM EDTA, 5 mM NaCl, 20 mM MgCl2 pH 8.0
- 1× TA buffer: 40 mM Tris pH 8.0, 20 mM acetic acid

PCA, PCD and trolox

Trolox (100×) was made by the addition of 100 mg of trolox to 430 µl of 100% methanol and 345 µl of 1 M NaOH in 3.2 ml of water. PCA (40×) was made by mixing 154 mg of PCA in 10 ml of water and NaOH and adjustment of pH to 9.0. PCD (100×) was made by the addition of 9.3 mg of PCD to 13.3 ml of buffer (100 mM Tris-HCl pH 8.0, 50 mM KCl, 1 mM EDTA, 50% glycerol).

DNA-PAINT docking and imager sequences

Four orthogonal DNA sequence motifs were used to label targets in four RESI rounds. The docking strands were 5xR1 (TCCTCCT CCTCCTCCTCCT), 5xR2 (ACCACCACCACCACCACCA), 7xR3 (CTCTCTCTCTCTCTCTCTC) and 7xR4 (ACACACACACACACACACA). The respective imagers were R1 (AGGAGGA-Cy3B), R2 (TGGTGGT-Cy3B), R3 (GAGAGAG-Cy3B) and R4 (TGTGTGT-Cy3B). The design of 2D RESI origami required extension of the R1 site at the 5′ end such that the adjacent R1 and R3 docking strands could be spaced apart by a single base pair. Thus, the docking strand 5′ 5xR1 (TCCTCCTCCTCCTCCTCCT) and the 5′ R1 imager (Cy3B-AGGAGGA) were used rather than the 3′ versions for both 2D DNA origamis.

DNA origami self-assembly (2D)

All 2D DNA origami structures were designed in caDNAno[40]. Self-assembly of DNA origami was accomplished in a one-pot reaction mix with a total volume of 40 µl, consisting of 10 nM scaffold strand (for sequence, see Supplementary Data 2), 100 nM folding staples (Supplementary Data 1), 500 nM biotinylated staples (Supplementary Data 1) and 1 µM staple strands with docking site extensions (Supplementary Data 1) in 2D DNA origami folding buffer. The reaction mix was then subjected to a thermal annealing ramp using a thermocycler. First, it was incubated at 80 °C for 5 min, cooled using a temperature gradient from 60 to 4 °C in steps of 1 °C per 3.21 min and finally held at 4 °C.

DNA origami self-assembly (3D)

The 3D DNA origami disk structure was designed in caDNAno[40]. Self-assembly of the DNA origami disk was accomplished in a one-pot reaction mix of 50 µl total volume, consisting of 20 nM scaffold strand p7560 (for sequence, see Supplementary Data 3), 200 nM core folding staples (Supplementary Data 1), 200 nM staple sequences without handle extension (Supplementary Data 1), 500 nM biotinylated staples (Supplementary Data 1), 2 µM staple strands with R4 docking site extensions and 4 µM staple strands with R1 or R3 docking site extensions (Supplementary Data 1) in 3D DNA origami folding buffer. The reaction mix was then subjected to a thermal annealing ramp using a thermocycler. It was first incubated at 80 °C for 5 min then cooled using a temperature gradient from 60 °C to 20 °C in steps of 1 °C h^{-1} and finally held at 20 °C.

DNA origami purification

After self-assembly, structures were purified by agarose gel electrophoresis (1.5% agarose, 1× TA, 10 mM $MgCl_2$, 0.5× SybrSafe) at 4.5 V cm^{-1} for 1.5 h. Gel bands were cut, crushed and the origami stored in low-binding Eppendorf tubes at −20 °C.

DNA origami sample preparation and imaging

For sample preparation, a bottomless six-channel slide (ibidi, no. 80608) was attached to a coverslip. First, 80 µl of biotin-labelled BSA (1 mg ml^{-1}, dissolved in buffer A) was flushed into the chamber and incubated for 5 min. The chamber was then washed with 360 µl of buffer A. A volume of 100 µl of neutravidin (0.1 mg ml^{-1}, dissolved in buffer A) was then flushed into the chamber and allowed to bind for 5 min. After washing with 180 µl of buffer A and subsequently with 360 µl of buffer B, 80 µl of biotin-labelled DNA structures (approximately 200 pM) in buffer B was flushed into the chamber and incubated for 5 min. For measurement of the DNA origami disk, additional 2D DNA origami structures with 12 target sites[9] spaced 20 nm apart were incubated together, with the 3D disk origami serving as fiducials for drift correction. After DNA origami incubation the chamber was washed with 540 µl of buffer B. For DNA origami disk structures, 150 µl of gold nanoparticles (diluted 1:10 in buffer B) was flushed through and incubated for 5 min before washing with 540 µl of buffer B. Finally, 180 µl of the imager solution in buffer B was flushed into the chamber. The chamber remained filled with imager solution and imaging was then performed. Between imaging rounds, the sample was washed three times with 1 ml of buffer B until no residual signal from the previous imager solution was detected. Then, the next imager solution was introduced. For RESI, two imaging rounds were performed with imagers R1 and R4 present in round 1 and the imagers R3 and R4 in round 2 (R1 and R3 probe the sites of interest for RESI and R4 serves alignment purposes).

Nanobody–DNA conjugation

Nanobodies were conjugated as described previously[32]. Unconjugated nanobodies were thawed on ice, then 20-fold molar excess of

bifunctional DBCO-PEG4-Maleimide linker was added and reacted for 2 h on ice. Unreacted linker was removed by buffer exchange to PBS using Amicon centrifugal filters (10,000 MWCO). The DBCO-modified nanobodies were reacted with 5× molar excess of azide-functionalized DNA (R1, R2, R3 and R4) overnight at 4 °C. Unconjugated protein and free DNA were removed by anion exchange chromatography using an ÄKTA pure system equipped with a Resource Q 1 ml column.

Cell culture

CHO cells (CCL-61, ATCC) were cultured in Gibco Ham's F-12K (Kaighn's) medium supplemented with 10% FBS (no. 11573397, Gibco). U2OS-CRISPR-Nup96-mEGFP cells (a gift from the Ries and Ellenberg laboratories) were cultured in McCoy's 5A medium (Thermo Fisher Scientific, no. 16600082) supplemented with 10% FBS. Cells were passaged every 2–3 days using trypsin-EDTA.

Nup96 EGFP imaging

U2OS-CRISPR-Nup96-mEGFP cells were seeded on ibidi eight-well high glass-bottom chambers (no. 80807) at a density of 30,000 cm^{-2}. Cells were fixed with 2.4% paraformaldehyde in PBS for 30 min at room temperature. After fixation, cells were washed three times with PBS. Gold nanoparticles (200 µl) were incubated for 5 min and washed three times with PBS. Blocking and permeabilization were performed with 0.25% Triton X-100 in blocking buffer for 90 min. After washing with PBS, cells were incubated with 100 nM anti-GFP nanobodies in blocking buffer for 60 min at room temperature. To enable RESI, the nanobody solution consisted of 25 nM R1, R2, R3 and R4 docking-strand-coupled anti-GFP nanobodies with a total nanobody concentration of 100 nM. Unbound nanobodies were removed by washing three times with PBS, followed by washing once with buffer C for 10 min. Postfixation was performed with 2.4% paraformaldehyde in PBS for 15 min. After washing 3× with PBS, the imager solution in buffer C was flushed into the chamber. Between imaging rounds the sample was washed with 1–2 ml of PBS until no residual signal from the previous imager solution was detected. Then, the next imager solution was introduced. First, imagers R1, R2, R3 and R4 were added simultaneously to the sample to perform a standard DNA-PAINT measurement; then, RESI imaging was conducted via four subsequent imaging rounds with only one of the imagers.

Cloning

mEGFP-Alfa-CD20 was cloned by insertion of Alfa-CD20 into the mEGFP-C1 plasmid (no. 54759, Addgene). An Alfa-CD20 gblock (obtained from Integrated DNA Technologies) was amplified with primers cggcatggacgagct and gtacaagtccgga and, after cutting with restriction enzymes BsrGI and BamHI, Gibson assembly was performed (2× mix, NEB).

mEGFP-CD20 imaging

CHO cells were seeded on ibidi eight-well high glass-bottom chambers (no. 80807) the day before transfection at a density of 15,000 cm^{-2}. Transfection with mEGFP-CD20 was carried out with Lipofectamine LTX as specified by the manufacturer. CHO cells were allowed to express mEGFP-CD20 for 16–24 h. Then, the medium was replaced with fresh F-12K medium + 10% FBS (in the untreated case) or with F-12K medium + 10% FBS + 10 ug ml^{-1} RTX-Alexa 647 (a gift from Roche Glycart) (in the RTX-treated case), followed by incubation for 30 min. After washing two times with fresh medium for 5 min, cells were fixed with 250 µl of prewarmed 4% PFA + 0.1% glutaraldehyde in PBS for 15 min. CHO cells were washed three times with PBS and quenched with 100 mM Tris pH 8.0 for 5 min. Permeabilization was carried out for 5 min with 0.2% Triton X-100 in PBS, followed by three washes with PBS. Cells were blocked in blocking buffer for 1 h at room temperature (RT). Anti-GFP nanobodies were incubated at a total concentration of 25 nM overnight at 4 °C; for RESI with four rounds this yielded 6.25 nM each of GFP-Nb-R1/2/3/4. After washing three times with PBS at RT for 15 min, cells were postfixed with 4% PFA at RT for 10 min followed by washing and postfixation as described above. Gold nanoparticles (90 nm) were diluted 1:3 in PBS and incubated for 10 min at RT and the sample was washed two times with PBS to remove unbound gold. The imager solution in buffer C for the first round was incubated for 5 min and then replaced with fresh imager, after which the first acquisition round was started. Between imaging rounds the sample was washed with at least 2 ml of PBS until no residual signal from the previous imager solution was detected. Then, the next imager solution was introduced. RESI imaging was conducted via four subsequent imaging rounds with only one of the imagers. In the final imaging round, imagers R1, R2, R3 and R4 were added simultaneously to the sample to perform a standard DNA-PAINT measurement.

Microscopy setup

Fluorescence imaging was carried out using an inverted microscope (Nikon Instruments, Eclipse Ti2) with the Perfect Focus System, applying an objective-type TIRF configuration equipped with an oil-immersion objective (Nikon Instruments, Apo SR TIRF ×100/numerical aperture 1.49, oil). A 560 nm laser (MPB Communications, 1 W) was used for excitation. The laser beam was passed through a cleanup filter (Chroma Technology, no. ZET561/10) and coupled to the microscope objective using a beam splitter (Chroma Technology, no. ZT561rdc). Fluorescence was spectrally filtered with an emission filter (Chroma Technology, nos. ET600/50m and ET575lp) and imaged on an sCMOS camera (Andor, Zyla 4.2 Plus) without further magnification, resulting in an effective pixel size of 130 nm (after 2 × 2 binning). The readout rate was set to 200 MHz. Images were acquired by choosing a region of interest of size 512 × 512 pixels. 3D imaging was performed using a cylindrical lens (Nikon Instruments, N-STORM) in the detection path. Raw microscopy data were acquired using µManager[41] (v.2.0.1). Total internal reflection illumination was used for 2D and 3D DNA origami data, as well as for CD20 acquisition. Highly inclined and laminated optical sheet (HILO) illumination was employed for the acquisition of NPC data. Detailed imaging conditions for the respective experiments are shown in Extended Data Table 1.

Imaging parameters and duration

Due to target and sample heterogeneity the optimal imager concentration, c, used to achieve sparse blinking varies. Here we used concentrations from 100 pM (Nup96) to 800 pM (DNA origami). Optimal imager concentrations were determined visually for each sample. Concentrations were altered until blinking was frequent but sufficiently sparse to achieve good DNA-PAINT resolution.

The average number of expected binding events per binding site during a DNA-PAINT measurement is given by the duration of the measurement $t_{\mathrm{measurement}}$ and the mean dark time τ_{dark} (defined as $\tau_{\mathrm{dark}} = \frac{1}{k_{\mathrm{on}} \times c}$, with k_{on} being the on-rate of a given imager strand) as:

$$n_{\mathrm{binding\,events}} = \left(\frac{t_{\mathrm{measurement}}}{\tau_{\mathrm{dark}}}\right) = t_{\mathrm{measurement}} \times k_{\mathrm{on}} \times c.$$

The average number of localizations per binding event is given by the mean bright time τ_{bright} and camera exposure time t_{exposure} as

$$n_{\mathrm{locs\,per\,binding\,event}} = \left(\frac{\tau_{\mathrm{bright}}}{t_{\mathrm{exposure}}}\right).$$

Therefore, the average number of localizations expected per binding site over the course of the measurement is

$$n_{\mathrm{loc}} = \left(\frac{t_{\mathrm{measurement}}}{\tau_{\mathrm{dark}}}\right) \times \left(\frac{\tau_{\mathrm{bright}}}{t_{\mathrm{exposure}}}\right) = t_{\mathrm{measurement}} \times k_{\mathrm{on}} \times c \times \left(\frac{\tau_{\mathrm{bright}}}{t_{\mathrm{exposure}}}\right).$$

It follows that the total acquisition time necessary to collect n_{loc} localizations is, on average,

$$t_{measurement} = \frac{t_{exposure} \times n_{loc}}{\tau_{bright} \times k_{on} \times c}.$$

The necessary number of localizations, n_{loc}, is calculated using $\sigma_{RESI} = \frac{\sigma_{DNA\text{-}PAINT}}{\sqrt{n_{loc}}}$, and thus $n_{loc} = \left(\frac{\sigma_{DNA\text{-}PAINT}}{\sigma_{RESI}}\right)^2$ with the DNA-PAINT localization precision $\sigma_{DNA\text{-}PAINT}$.

For expected imager concentrations between 50 and 800 pM, exposure times between 100 and 200 ms and kinetics reported previously[32], the times required to collect 16 localizations (1 nm RESI precision given $\sigma_{DNA\text{-}PAINT}$ = 4 nm) vary between 42 s (R2, 800 pM, 100 ms exposure time) and 314 min (R5, 50 pM, 200 ms exposure time).

DNA-PAINT analysis

Raw fluorescence data were subjected to super-resolution reconstruction using the Picasso software package[9] (latest version available at https://github.com/jungmannlab/picasso). Drift correction was performed with a redundant cross-correlation and gold particles as fiducials for cellular experiments, or with single DNA-PAINT docking sites as fiducials for origami experiments.

Channel alignment

Alignment of subsequent imaging rounds was performed iteratively in Picasso[9], starting with a redundant cross-correlation and followed by gold fiducial alignment for cellular experiments. Every DNA origami was equipped with additional DNA-PAINT docking sites that were imaged simultaneously with the sites of interest in all imaging rounds, thus enabling their use as fiducials. First, redundant cross-correlation (2D and 3D origami measurements) and gold alignment (3D measurements) were performed in Picasso Render. To correct for nanoscopic movement of individual DNA origami during buffer exchange, channel alignment was not only performed on the full field of view but, additionally, small regions of interest containing only one DNA origami were selected. Within each region of interest, alignment was then conducted via the fiducial docking sites of the DNA origami. This was performed outside of Picasso in a custom Python script, not only to find the optimal translation between channels but also to correct for possible rotations of the DNA origami.

Clustering and RESI

Clustering of DNA-PAINT localizations. After channel alignment, DNA-PAINT data were analysed using a custom clustering algorithm for each imaging round. This algorithm is based on the fact that, in DNA-PAINT, localizations are independent measurements of the position of a target molecule and are observed to be Gaussian distributed. To assign localizations to a specific target molecule, we first used a gradient ascent method to find the centre of a localization cloud for each target. We then assigned all localizations circularly distributed around the centre point to the same target molecule. This is a valid approximation because, due to the reduction of effective target density by RESI's sequential imaging approach, the majority of localization clouds from single targets are spaced sufficiently apart.

The clustering algorithm uses two input parameters: radius r, which sets the final size of the clusters and defines a circular environment around each localization, and the minimal number of localizations, n_{min}, representing a lower threshold for the number of DNA-PAINT localizations in any cluster.

First, the number of neighbouring localizations within distance r from each localization is calculated. If a given localization has more neighbours within its r radius than all neighbouring localizations, it is considered a local maximum. If there are more than n_{min} localizations within a circle of radius r around such a local maximum, these localizations are assigned to the same cluster; the remainder are not considered to be part of a cluster and are omitted from further analysis.

Further filtering of clusters is performed to exclude clusters that originate from unspecific sticking of imagers to the sample. Firstly, the mean frame (mean value of the frame numbers in which localizations occurred) of all localizations assigned to the same cluster is calculated. In the case of repetitive blinking the mean frame is expected to be around half the total number of frames[42]. The algorithm therefore excludes all clusters with a mean frame in the first or last 20% of frames. Secondly, sticking events in the middle of the acquisition time can be identified by dividing the acquisition time into 20 time windows each containing 5% of frames. If any of these time windows contains more than 80% of localizations in the cluster, it is excluded as a sticking event.

The choice of the clustering radius r and the threshold n_{min} depend on the respective experimental conditions. A suitable value for n_{min} can be estimated by picking localization clouds originating from single target molecules (that is, well separated) in Picasso Render, exporting pick properties and plotting a histogram of the number of localizations in each pick. n_{min} is chosen to differentiate between populations corresponding to single targets and to background localizations.

The radius r scales with the size of the localization clouds and thus the localization precision. If too large a value is chosen, adjacent clusters might not be separated; if r is too small, 'subclustering' within one localization can occur. The latter also translates to a peak in NND at twice the clustering radius. A good a priori starting value for r is represented by approximately twofold the localization precision of the underlying DNA-PAINT measurement. Picasso Render offers a tool (Test Clusterer) in which the effect of different clustering parameters can be tested for a small region of interest.

For 3D clustering, an additional radius for the z direction is introduced because the spread of localizations in z is approximately twofold greater compared with x and y.

Calculation and rendering of RESI localization. Following cluster analysis, the centres of the DNA-PAINT localization groups were calculated as weighted (wtd) means by employing the squared inverse localization precisions ($\frac{1}{lp^2}$) as weights. For x and y coordinates:

$$\bar{x}_{wtd} = \frac{\sum_{i=1}^{N} w_i x_i}{\sum_{i=1}^{N} w_i}, \; w_i = \frac{1}{lp^2}.$$

For z coordinates a standard mean without weights is used to calculate z positions. The precision of the resulting RESI localization is the weighted s.e.m. of the underlying grouped localizations:

$$\begin{aligned}(s_{\bar{x}})_{wtd} &= \frac{(s_x)_{wtd}}{\sqrt{N}} \\ &= \sqrt{\frac{\mathrm{Var}(x)_{wtd}}{N}}, \text{ where } \mathrm{Var}(x)_{wtd} \\ &= \frac{N}{N-1} \frac{\sum_{i=1}^{N} w_i (x_i - \bar{x}_{wtd})^2}{\sum_{i=1}^{N} w_i}.\end{aligned}$$

The choice for $1/lp^2$ as weights is based on the following argument: under the hypothesis that localizations are independent and normally distributed with the same mean, the weighted mean based on inverse variances as weights is the maximum likelihood estimator of the mean of the whole set of localizations. Therefore, the variance of the weighted mean is minimal (the estimator is optimal) when the inverse variances of individual measurements $1/lp^2$ are chosen as weights.

Finally, we take the average of the resulting x and y s.e.m. as the final precision of each RESI localization. For z coordinates the precision is estimated to be two times xy precision. Saving RESI localizations in a Picasso hdf5 file allowed us to render them as Gaussians with s.d. corresponding to their respective precision.

RESI resolution estimation

Evaluation of in silico RESI precision with numerical simulations. To evaluate the performance of RESI, in silico numerical simulations were performed. The algorithm consists of the following steps.

(1) A grid of defined positions of the binding sites (ground truth) is generated. Typically, a grid of positions was generated (Extended Data Fig. 1a, top left).
(2) SMLM (DNA-PAINT) localizations are simulated as samples from a 2D Gaussian distribution with $\sigma = \sigma_{SMLM}$. A large number (M) of localizations is generated per binding site (Extended Data Fig. 1a, top right).
(3) For each binding site, subsets of K localizations are randomly selected ($K << M$). This results in $n = \frac{M}{K}$ subsets of SMLM localizations (Extended Data Fig. 1a, bottom left) that are then averaged to generate n RESI localizations (Extended Data Fig. 1a, bottom right).
(4) The resulting RESI localizations are then shown in a histogram (Extended Data Fig. 1b) and the trace (tr) of the covariance matrix is calculated. RESI precision is estimated as $\sigma_{RESI} = \sqrt{\frac{1}{2} tr(\mathrm{cov}(x, y))}$ (Extended Data Fig. 1c). This definition has been used before in the field as a scalar metric for 2D variance[8].
(5) Steps 3 and 4 are repeated for different values of K to numerically study $\sigma = \sigma_{RESI}(K)$.

Evaluation of experimental RESI precision by resampling of localizations. To evaluate the precision of RESI in experimental data, an analogous method was used. Briefly, the M total of DNA-PAINT localizations of each group corresponding to a single binding site was randomly resampled into subsets of K localizations, then steps 4 and 5 above were performed to evaluate σ_{RESI}. The plotted σ_{RESI} in Fig. 3d is the average value of all single binding sites in the dataset. Error bars represent the s.d. of the different σ_{RESI} values calculated for different binding sites.

Note that this analysis can be performed only for $K << M$ to have sufficient $n = \frac{M}{K}$ RESI localizations for a statistically significant estimation. Because final RESI localization takes into account all M DNA-PAINT localizations, final precision is extrapolated as $\sigma_{RESI} = \frac{\sigma_{SMLM}}{\sqrt{M}}$.

Stochastic labelling: simulations and user guidelines

In RESI, the sparsity of binding sites in the sample is achieved by labelling a single species of biomolecules with different orthogonal DNA sequences. The labelling process is performed in a stochastic manner: n different labels (for example, DNA-conjugated nanobodies) targeting the same protein species are simultaneously incubated in the sample and thus the probability of each single protein being labelled with a certain sequence i ($i = 1, \ldots, n$) is $p_i = \frac{1}{n}$, given that the same concentration of each label is used. Subsequently, n imaging rounds are performed to record all groups of localizations required to obtain the final RESI image.

The minimum number of labels (n) and rounds necessary to achieve sufficient sparsity of binding sites in each imaging round will depend mainly on three factors: SMLM localization precision and density and the molecular arrangement of the protein of interest. Here we describe how these parameters affect the final RESI results using a few practical examples.

Case 1: protein structure with oligomers not resolvable with DNA-PAINT. A typical study case is that of single proteins arranged in dimers, which in turn present another specific spatial organization in space. This is the case, for example, of the Nup96 in the NPC. In this case stochastic labelling has to be such that the probability of labelling two proteins forming a dimer with different sequences is sufficiently high. For n rounds of labelling/imaging, the probability is

$$P(\text{diff. seq.}) = 1 - p_i = 1 - \frac{1}{n}$$

for $n = 4$ labelling/imaging rounds $P(\text{diff. seq.}) \approx 75\%$. We chose $n = 4$ to demonstrate that it provides a relatively high P(diff. seq.) with only a few imaging rounds. We note, however, that $n > 4$ could be used to increase P(diff. seq.) and hence to maximize the sparsity of labelled binding sites in each round.

To resolve a set of an arbitrary number of molecules, m, spaced more closely than the resolution of DNA-PAINT, they must be labelled with n orthogonal sequences. In general, the proportion of m molecules labelled with n orthogonal sequences, and thus the proportion of resolvable sets of molecules, follows the equation

$$P(m, n) = \frac{n!}{(n - m)!\, n^m}.$$

Case 2: proteins distributed similarly to CSR at a certain density. This is a common case—for example, for membrane receptors. If proteins are distributed in a CSR fashion (Extended Data Fig. 14a) at a given density, DNA-PAINT can already resolve single proteins that are sufficiently spaced from their NNs. We will consider that proteins at a distance $d = 4 \times \sigma_{\text{DNA-PAINT}}$ are reliably resolved (note that this criterion is significantly stricter than $2.35 \times \sigma_{\text{DNA-PAINT}}$). Then, for a given density, the NND histogram can be computed and the fraction of distances below d calculated (Extended Data Fig. 14b). This represents the fraction of single proteins, F, that will not be resolved by DNA-PAINT. Here we plot F as a function of both density and resolution (Extended Data Fig. 14c). Such a map already provides a tool to understand the level of SMLM resolution needed to resolve single proteins at a given density.

RESI can be interpreted here as a way to reduce the effective density by splitting targets into different stochastically labelled subsets. Hence, the effective density of each round will be reduced according to the formula $\rho = \frac{\text{density}}{n}$. Extended Data Fig. 14d shows one-dimensional cuts of the 2D map to provide guidelines to choosing the number of orthogonal sequences (and hence imaging rounds) needed to be able to perform RESI efficiently. For example, for an initial resolution of 20 nm ($\sigma = 5$ nm), which is typical for DNA-PAINT in a cellular context, and a density of density = $200 \frac{\text{molecules}}{\mu\text{m}^2}$ (relatively high), $n = 4$ different sequences are sufficient to provide P(diff. seq.) $\approx 90\%$ for proteins below d (Extended Data Fig. 14d). These proteins will then be resolvable by RESI.

Model-free averaging

Model-free averaging of Nup96 data was performed for both DNA-PAINT and RESI measurement of the same nucleus, as described by Wu et al.[30]. The respective Picasso hdf5 files were segmented in SMAP[43] and saved in a file format compatible for averaging by employing plugins *segmentNPC*, *NPCsegmentCleanup* and *sitenumbers2loc*. Model-free averaging was then performed on the resulting _sml.mat files with default parameters by running the particleFusion.m script in Matlab (available with the SMAP source code). The averages shown correspond to the result of the final iteration, in which each point is rendered with a Gaussian of $\sigma = 2$ nm in x, y and z.

Numerical simulations for CD20 distribution

To interpret the results of the NND data in untreated cells, numerical simulations were performed. Briefly, two populations, one of CD20 monomers and one of dimers with a CSR distribution, were simulated and then their NNDs calculated. The algorithm can be summarized as follows:

(1) Choice of parameters. Density of monomers: number of monomers per unit area; density of dimers: number of dimers per unit area; dimer distance: expected distance between the two molecules including the labelling construct; uncertainty: variability in the position of each molecule due to labelling and localization errors; labelling efficiency: fraction of ground-truth molecules that will actually be

labelled and measured. The observed density, which has to match the experimental parameter, then becomes observed density = (density of monomers + density of dimers) × labelling efficiency. For quantification of the labelling efficiency of the DNA-conjugated GFP nanobody we used a transiently transfected CHO cell line expressing a GFP- and Alfa-tag at the C terminus of a monomeric membrane protein (for example, CD86). We then labelled GFP- and Alfa-tag using their cognate nanobodies conjugated to two orthogonal docking sequences and performed two rounds of Exchange-PAINT. We then obtained the best-fitting parameters for a sample comprising pairs of GFP/Alfa-tag, and isolated Alfa-tags, similarly to how CD20 dimer/monomer analysis is performed. The ratio of these two populations is then used as an estimation of labelling efficiency. Full details of the quantification approach will be available in a manuscript currently in preparation.

(2) Simulation of monomers: a set of spatial coordinates with CSR distribution and given density are drawn; simulation of dimers: a set of spatial coordinates with CSR distribution are drawn, representing the centre of each dimer. For each dimer centre, two positions are generated with a random orientation and a distance with expected value dimer distance. The position of each pair of molecules is drawn, taking into account the uncertainty parameter (drawn from a Gaussian distribution).

(3) A random subset of 'detectable' molecules is taken from the ground-truth set (fraction = labelling efficiency) to simulate the labelling process.

(4) NNDs are calculated on the subset of detectable molecules.

The parameters density of monomers = 212 μm^{-2}, density of dimers = 0 μm^{-2}, uncertainty = 5 nm and labelling efficiency = 50% were used to compare data for RTX-treated cells with a CSR distribution of monomers.

For the untreated case, the best-fit parameters were obtained through an iterative, nonlinear, least-squares algorithm. The experimentally observed density (50 molecules μm^{-2}) is used for the simulation.

Description of the iterative nonlinear, least-squares algorithm

For every set of parameters a simulation is performed, NNDs are histogrammed and the sum of the squared differences between the simulation and experimental histogram are computed. A fit consists of finding the parameters that minimize the sum of the squared differences.

Parameters

- D, average dimer distance (nm)
- σ_label, variability introduced by the labelling (nm)
- frac_of_dimers, fraction of dimers (%)

Note: frac_of_monomers = 100 − frac_of_dimers

Estimation of parameters.

(1) Coarse-fit over a large range of parameters to determine the range of the best-fit parameters. Range D = 1–20 nm, σ_label = 1–20 nm, frac_of_dimers = 0–100%.

(2) Fine-fit over a reduced parameter space around the best-fit results in the previous step.

The parameters D_opt, σ_label_opt and frac_of_dimers_opt that best match the proposed model and the data are now found. In this case it resulted in D_opt = 13.5 nm, σ_label_opt = 5.5 nm, frac_of_dimers_opt = 47% (Fig. 4e,f).

Estimation of parameter uncertainty.

(1) *M* is created (in this case, *M* = 100), simulated (using datasets D_opt, σ_label_opt, frac_of_dimers_opt) with the same number of molecules as the experimental data (around 21,000).

(2) *M* datasets are fine-fitted and the best-fit parameters D_opt, σ_label_opt and frac_of_dimers_opt are obtained. Three sets are obtained: D_opt, σ_label_opt and frac_of_dimers_opt.

(3) The distributions of D_opt, σ_label_opt and frac_of_dimers_opt are studied. Standard deviation can be used as an estimation of the parameter uncertainties obtained in b.

The uncertainties of the parameters D_opt, σ_label_opt and frac_of_dimers_opt are now obtained.

Data availability

Localization data from this study are available at Zenodo (https://doi.org/10.5281/zenodo.7795826). Raw microscopy data obtained during this study are available from the corresponding author on reasonable request.

Code availability

RESI can be performed using Picasso v.0.6.0, available at https://github.com/jungmannlab/picasso with documentation provided at https://picassosr.readthedocs.io/en/latest/render.html. The custom-written scripts used in this study are available at https://github.com/jungmannlab/resi.

40. Douglas, S. M. et al. Rapid prototyping of 3D DNA-origami shapes with caDNAno. *Nucleic Acids Res.* **37**, 5001–5006 (2009).
41. Edelstein, A. D. et al. Advanced methods of microscope control using muManager software. *J. Biol. Methods* **1**, e10 (2014).
42. Wade, O. K. et al. 124-Color super-resolution imaging by engineering DNA-PAINT blinking kinetics. *Nano Lett.* **19**, 2641–2646 (2019).
43. Ries, J. SMAP: a modular super-resolution microscopy analysis platform for SMLM data. *Nat. Methods* **17**, 870–872 (2020).

Acknowledgements We thank Y.-L. Wu and J. Ries for valuable assistance with model-free averaging. We thank J. Schmied and F. Schueder for helpful discussions. We thank M. K. Steen-Mueller and I. Glueck for proofreading the manuscript. This research was funded in part by the European Research Council through an ERC Consolidator Grant (ReceptorPAINT, grant agreement no. 101003275), the German Research Foundation through SFB1032 (project A11, no. 201269156), the Danish National Research Foundation (Centre for Cellular Signal Patterns, DNRF135), the Human Frontier Science Program through a Young Investigator Grant (no. HFSP RGY0065/2018), the Volkswagen Foundation through the initiative 'Life?—A Fresh Scientific Approach to the Basic Principles of Life' (grant no. 98198), the Max Planck Foundation and the Max Planck Society. S.S. and T.S. acknowledge support by the QBM graduate school. S.C.M.R., I.B., P.R.S., A.S.E., E.M.U. and M.T.S. acknowledge support by the IMPRS-LS graduate school. I.B. acknowledges funding support by Roche. L.A.M. acknowledges a postdoctoral fellowship from the European Union's Horizon 20212022 research and innovation programme under Marie Skłodowska-Curie grant agreement no. 101065980.

Author contributions S.C.M.R. designed and conducted 2D and 3D DNA origami as well as Nup96 experiments, developed the analysis software and analysed DNA origami and Nup96 data. L.A.M. designed and conducted computer simulations, contributed to analysis software and analysed DNA origami, Nup96 and CD20 data. I.B. designed and conducted CD20 experiments and analysed CD20 data. P.R.S. designed and conducted 2D DNA origami experiments, contributed to analysis software and analysed DNA origami and Nup96 data. R.K. and T.S. contributed to analysis software. S.S. developed labelling probes. A.S.E., S.S., E.M.U. and M.T.S. performed preliminary RESI experiments. C.K. contributed to the design of studies targeting CD20 and their interpretation. S.C.M.R., L.A.M., I.B., P.R.S. and R.J. interpreted data and wrote the manuscript. R.J. conceived the concept, designed experiments and supervised the study. S.C.M.R., L.A.M., I.B. and P.R.S. contributed equally. All authors reviewed and approved the final manuscript.

Funding Open access funding provided by the Max Planck Society.

Competing interests C.K. declares employment, patents (unrelated to this work) and stock ownership with Roche.

Additional information

Supplementary information The online version contains supplementary material available at https://doi.org/10.1038/s41586-023-05925-9.

Correspondence and requests for materials should be addressed to Ralf Jungmann.

Peer review information *Nature* thanks Alistair Curd and the other, anonymous, reviewer(s) for their contribution to the peer review of this work. Peer reviewer reports are available.

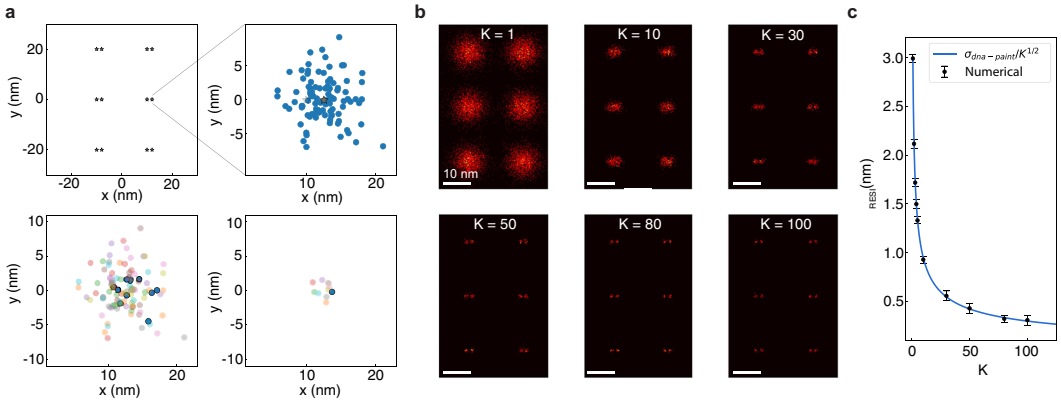

Extended Data Fig. 1 | RESI resolution estimation. a, A grid of defined positions of binding sites is generated (top left), SMLM (DNA-PAINT) localizations are simulated as samples from a gaussian distribution (top right). Localizations for only one binding site were plotted for clarity. For each binding site, subsets of K localizations are randomly selected (bottom left) and averaged (bottom right). One exemplary subset and its average is highlighted. **b**, Resulting RESI-localizations are histogrammed to produce images at different resolutions (K values). **c**, RESI-localization precision σ_{RESI} vs K. Analytical dependence on $\sqrt{K}$ (blue line) and numerical results (black dots). A total of 1200 SMLM localizations per site are simulated. Error bars represent mean ± 1 s.d.

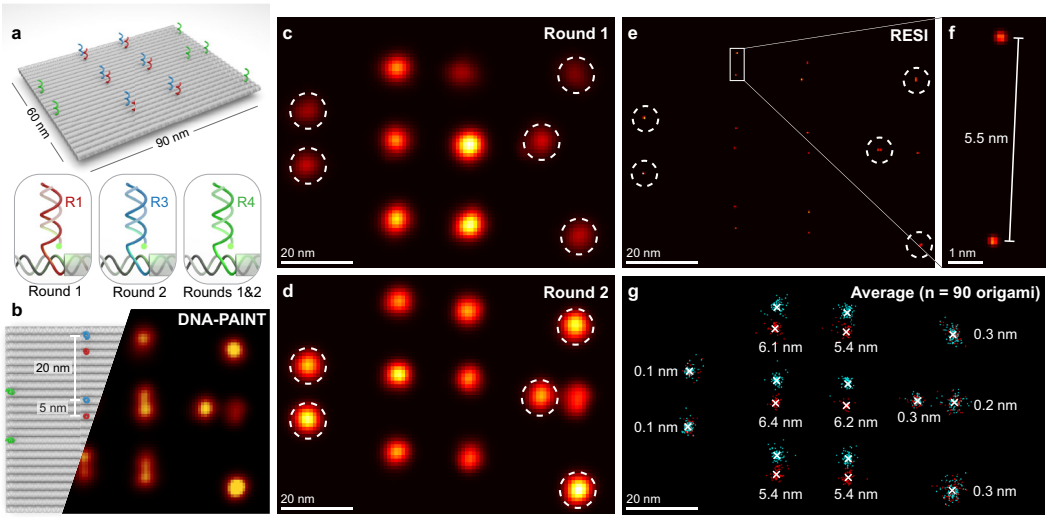

Extended Data Fig. 2 | RESI in 2D DNA origami. a, DNA origami design featuring six 5 nm-spaced orthogonal docking strand pairs (red R1, blue R3) and six alignment docking strands (green R4). See Methods for sequence details. **b**, DNA-PAINT acquisition parameters were tuned such that 5 nm were not consistently resolvable. **c**, First imaging round conducted with R1 (target) and R4 imagers (alignment, sites circled). **d**, Second imaging round conducted with R3 (target) and alignment imagers (R4, sites circled). The alignment sites were used for translational and rotational alignment between rounds. **e**, RESI resolves the 5 nm distances. **f**, The distance and orientation between R1 and R3 docking strands are consistent with the design. **g**, An average of 90 DNA origami structures reveals consistent results and excellent alignment performance. The numbers indicate the distance between rounds.

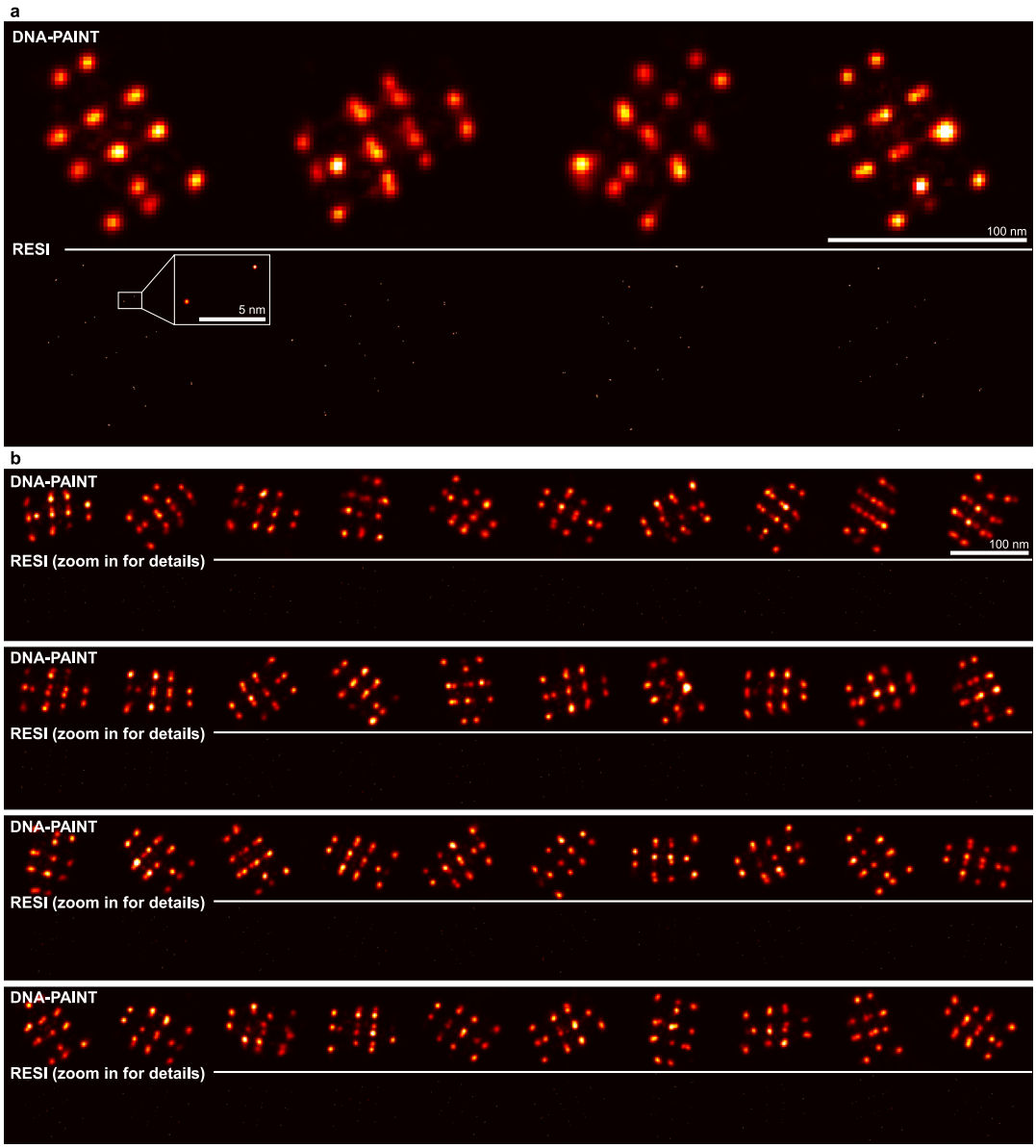

Extended Data Fig. 3 | 2D DNA origami. Representative DNA origami from across the field of view of the measurement. **a**, Four DNA origami, shown at DNA-PAINT resolution (upper row) and RESI resolution (lower row). The insert depicts a pair of docking strands spaced at approx. 5 nm. **b**, 40 additional DNA origami, shown at DNA-PAINT resolution (upper rows) and RESI resolution (lower rows).

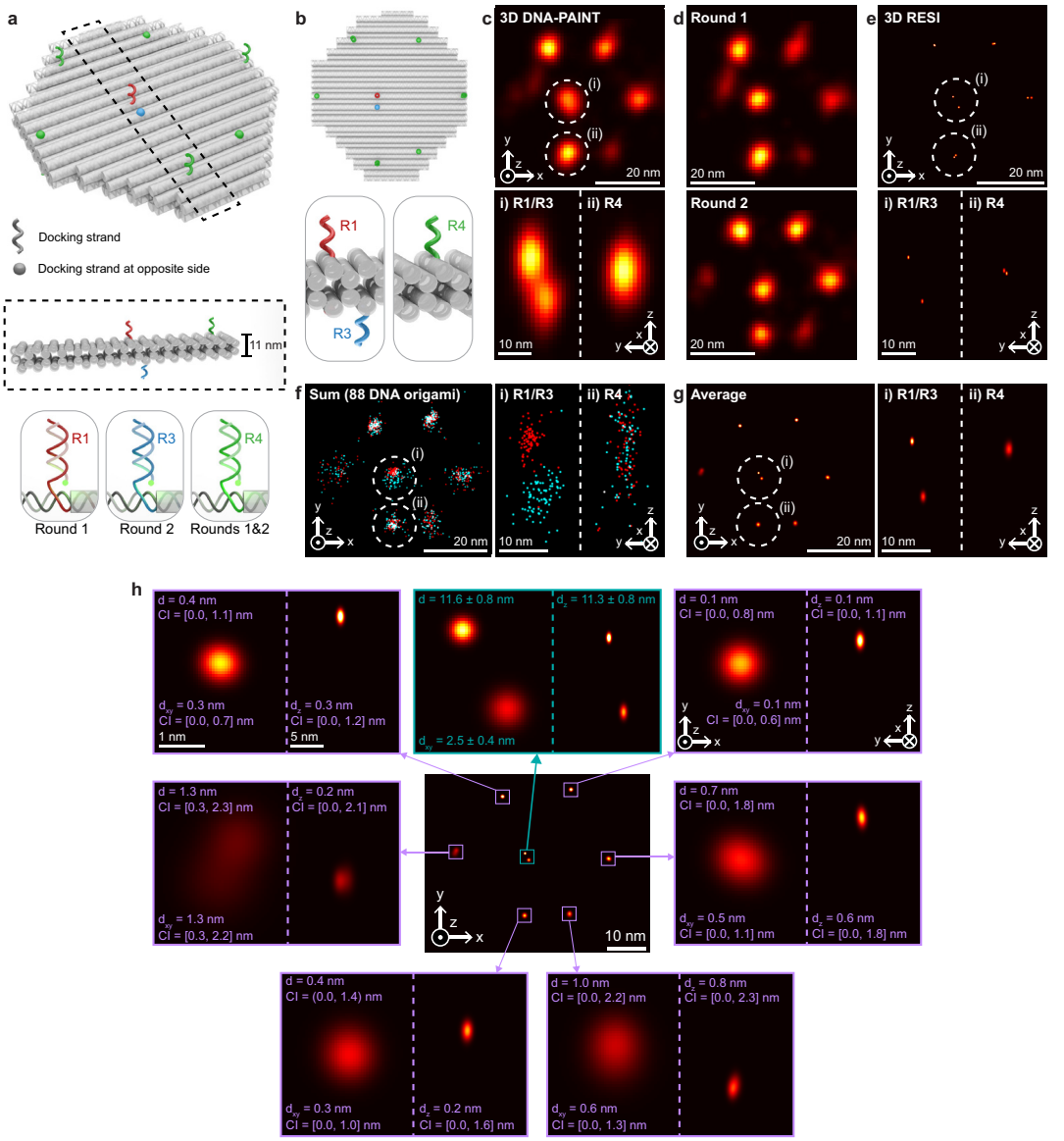

Extended Data Fig. 4 | RESI in 3D DNA origami. a, DNA origami design featuring one pair of orthogonal docking strands (red R1, blue R3) as well as six alignment docking strands (green R4). Docking strands extend from both the top and bottom surface of the DNA origami (insert). **b**, The design ensures that all but the R1/R3 docking strand pair are spaced sufficiently to be resolved by DNA-PAINT. **c**, 3D DNA-PAINT imaging resolves R4 alignment sites, barely resolves R1/R3 axially and does not resolve R1/R3 laterally. **d**, Sequential 3D DNA-PAINT imaging with R4 sites used for alignment. **e**, RESI resolves R1/R3 both axially and laterally. **f**, An overlay of 88 DNA origami reveals overall good alignment despite structural heterogeneity. **g**, Average of 88 DNA origamis. **h**, The particle average recovers the structure with an alignment uncertainty of 0.7 nm CI = [0, 1.6] nm, showing a distance between the average R1/R3 positions of 11.6 ± 0.8 nm (xy-distance: 2.5 ± 0.4 nm, z-distance: 11.3 ± 0.8 nm), matching the designed distances[20]. Same scale applies to all magnification panels. CI describes 68% confidence interval.

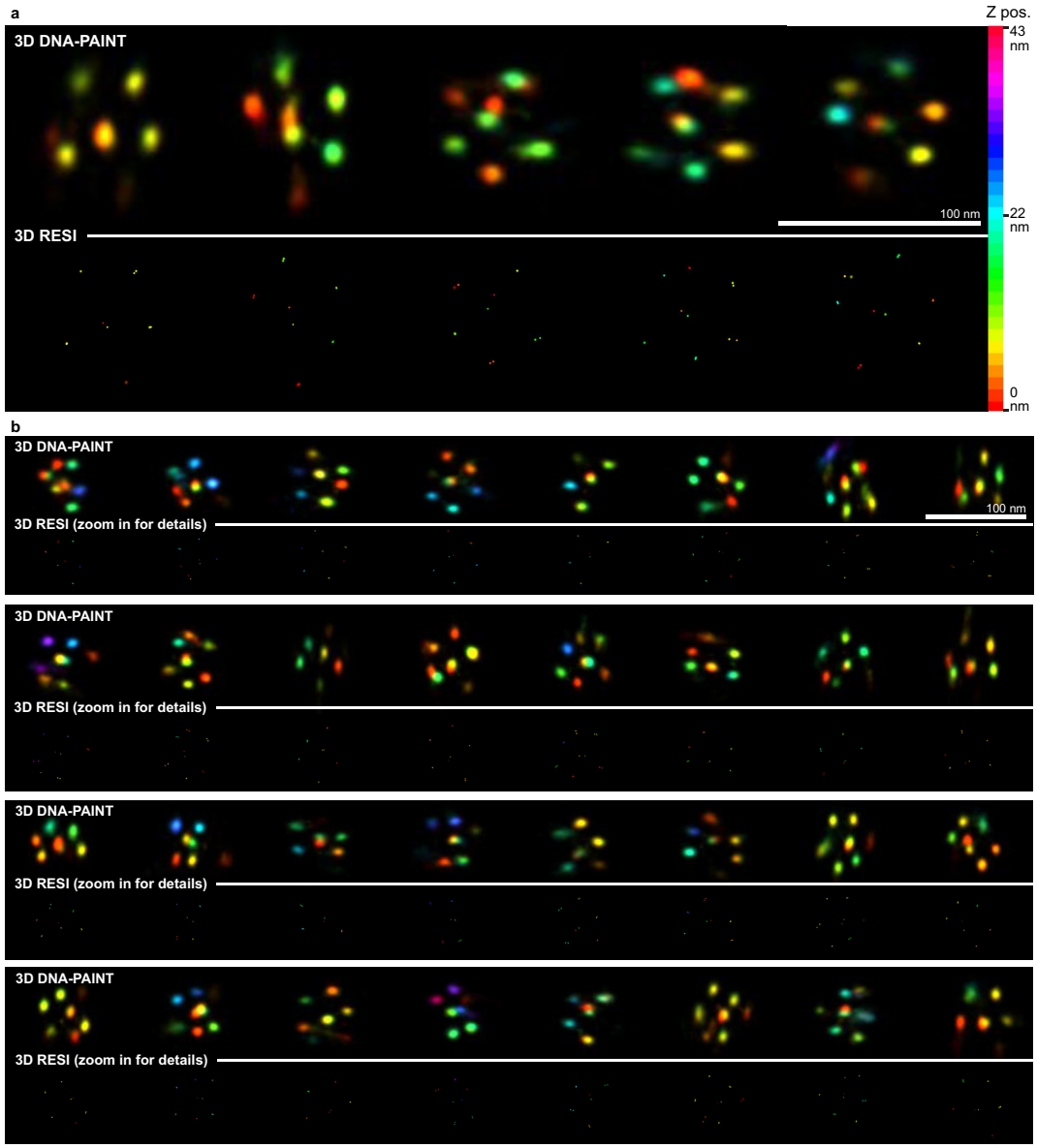

Extended Data Fig. 5 | 3D DNA origami. Representative 3D DNA origami from across the field of view of the measurement. **a**, Five DNA origami, shown at DNA-PAINT resolution (upper row) and RESI resolution (lower row). The color scale to the right represents the z position of localizations. The measured z coordinates for each DNA origami have been shifted by a constant such that the lowest localization for a given structure is defined to be at z = 0. This ensures full use of the color range. **b**, 32 additional DNA origami, shown at DNA-PAINT resolution (upper rows) and RESI resolution (lower rows). The z positions are colored according to the color scale in panel **a**.

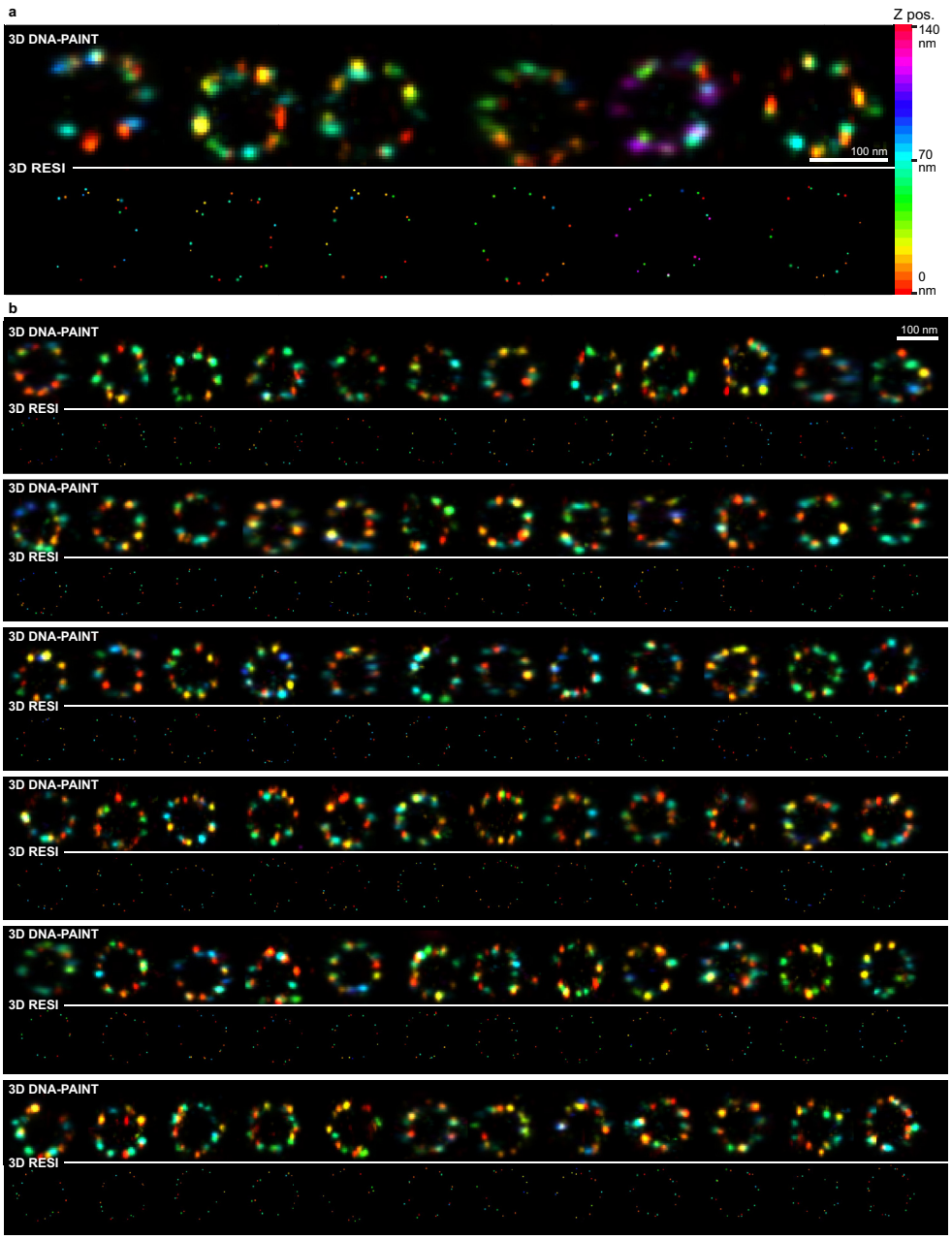

Extended Data Fig. 6 | U2OS Nup96-mEGFP. Representative NPCs from across the field of view of the measurement. **a**, Six NPCs, measured using DNA-PAINT (upper row) and RESI (lower row). The color scale to the right represents the z position of localizations. The measured z coordinates for each NPC have been shifted by a constant such that the lowest localization for a given structure is defined to be at z = 0. This ensures full use of the color range. **b**, 72 additional NPCs, measured using DNA-PAINT (upper rows) and RESI (lower rows). The z positions are colored according to the color scale in panel **a**.

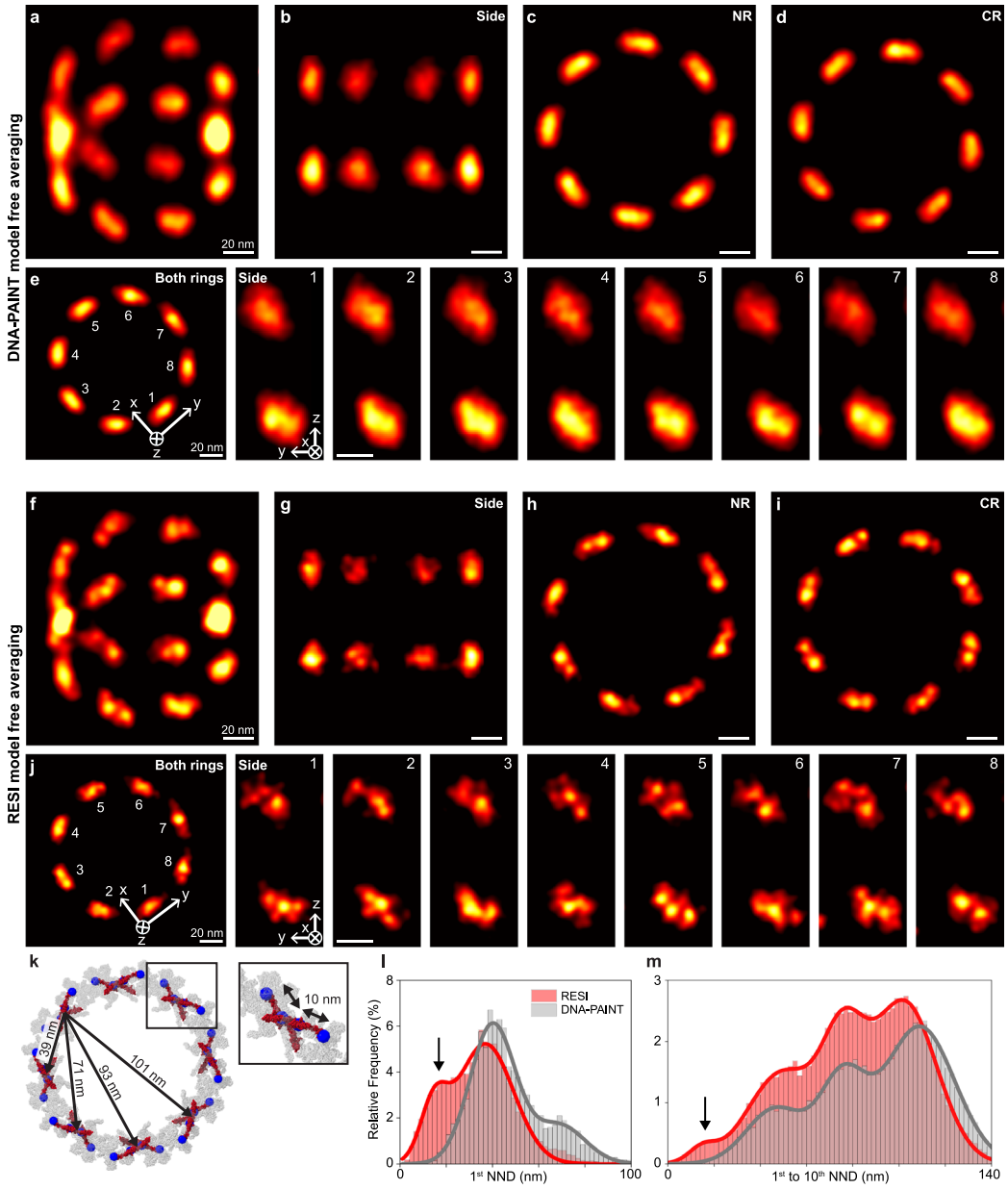

Extended Data Fig. 7 | Averaging of Nup96 proteins. a, Model-free averaging for DNA-PAINT measurements of Nup96 (N = 1045 NPCs). An angled isometric view is shown. **b**–**d**, DNA-PAINT resolves nucleoplasmic and cytoplasmic rings and recapitulates their eight-fold symmetry, but fails to resolve individual Nup96 proteins. **e**, Side views of all Nup96 pairs in both rings reveal the angled orientation but do not resolve individual Nup96 proteins. **f**, Model-free averaging for RESI measurements of Nup96 (N = 1190 NPCs). **g**–**i**, RESI recapitulates nucleoplasmic and cytoplasmic rings as well as their eight-fold symmetry and resolves individual adjacent Nup96 proteins in the majority of cases. **j**, Side views of all eight Nup96 pairs in both rings reveal the angled orientation as well as, in some cases, adjacent individual Nup96 proteins. **k**, The Cryo-EM structure of the nuclear pore complex indicates that a given Nup96 protein will have neighbors spaced at 11 nm, 39 nm, 71 nm, 93 nm and 101 nm. **l**, Performing clustering and nearest neighbor analysis for DNA-PAINT data reveals a peak at approx. 40 nm, corresponding to the distance between two Nup96 pairs, but not below that. RESI, on the other hand, features a first peak at approx. 15 nm, corresponding to the distance between adjacent Nup96 while taking linkage error (label size) into account. **m**, Analysis of first to tenth nearest neighbor distances for RESI and DNA-PAINT recapitulates the distances from (**k**), but only RESI resolves the smallest distance. All scale bars: 20 nm.

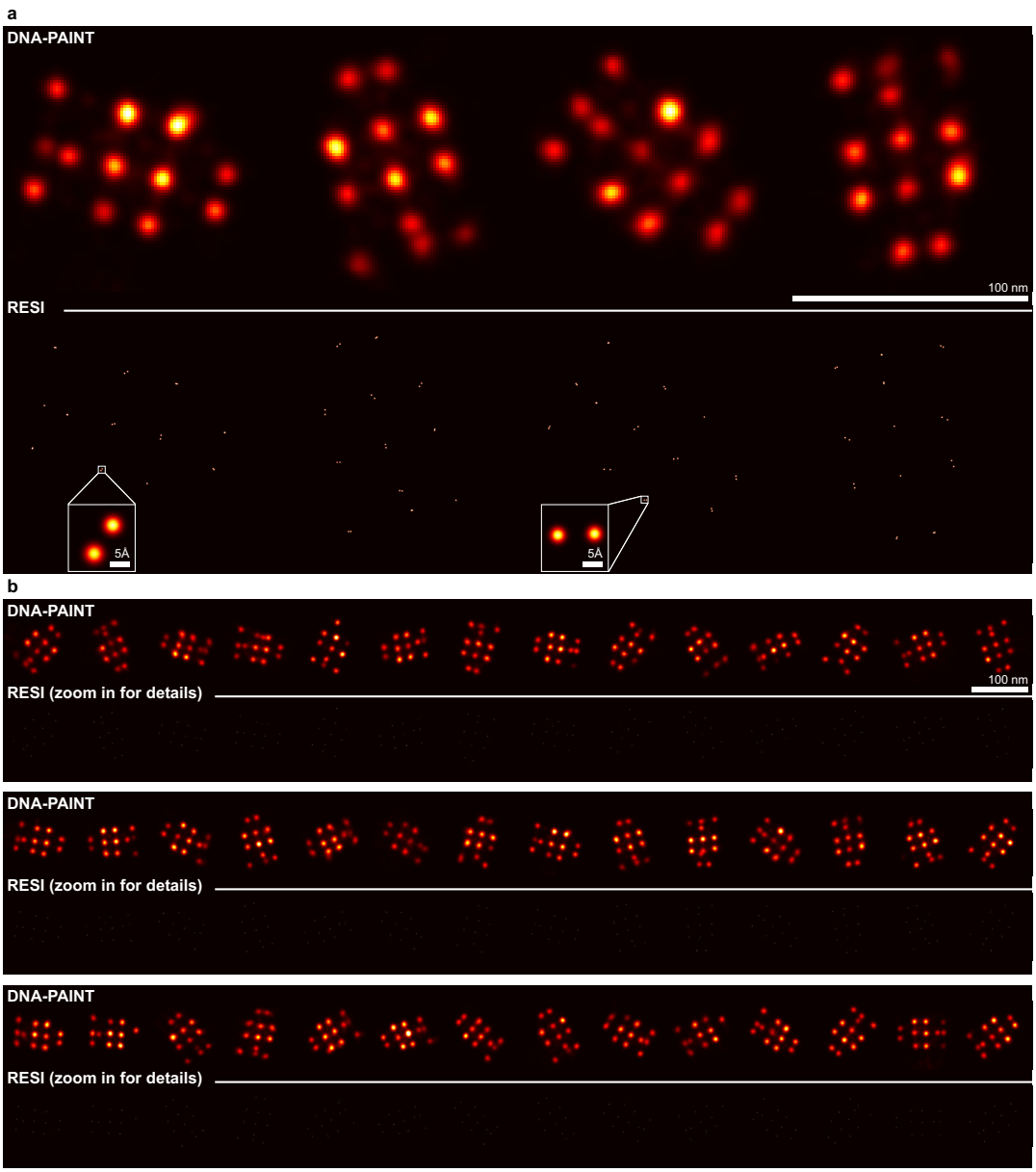

Extended Data Fig. 8 | Sub-nm DNA origami. Representative DNA origami from across the field of view of the measurement. **a**, Four DNA origami, shown at DNA-PAINT resolution (upper row) and RESI resolution (lower row). The inserts show pairs of directly adjacent docking strands resolved by RESI. **b**, 42 additional DNA origami, shown at DNA-PAINT resolution (upper rows) and RESI resolution (lower rows).

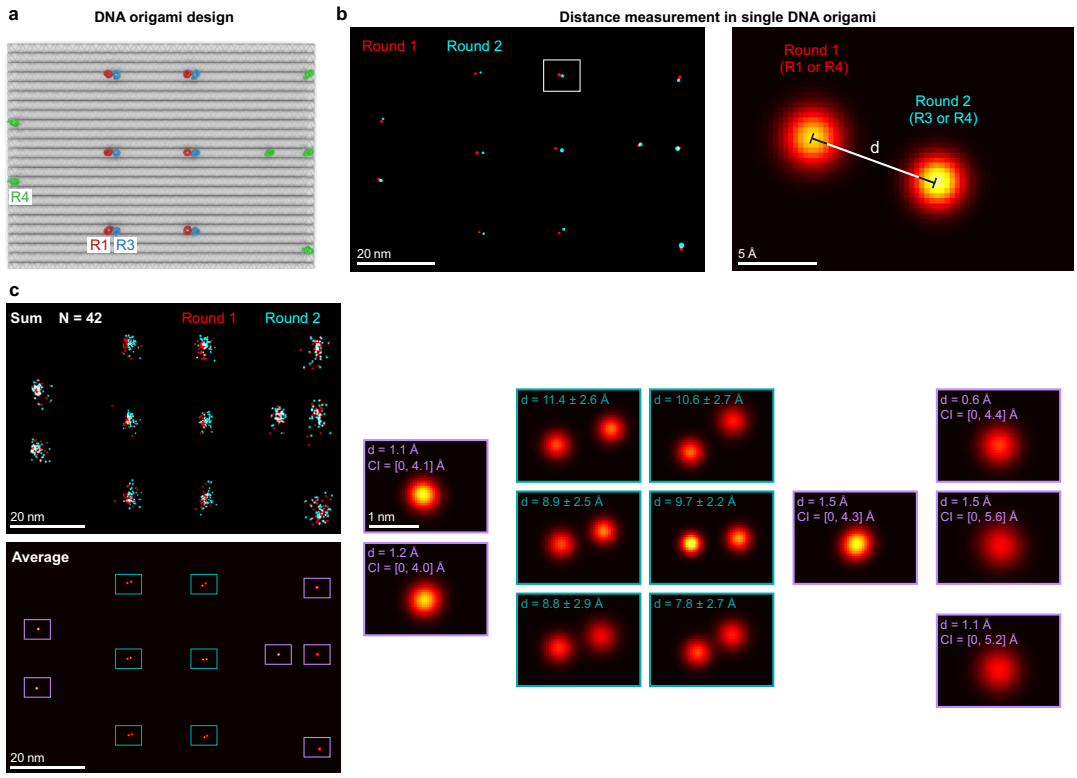

Extended Data Fig. 9 | Sub-nm RESI measurements. a, DNA origami featuring six alignment strands (green R4) and six pairs of orthogonal docking strands (red R1, blue R3) spaced one base pair apart. **b**, RESI representation with RESI-localizations from round 1 in red and round 2 in blue illustrates excellent alignment. The distances between RESI-localizations from round 1 and 2 are defined as illustrated. **c**, Overlaying 42 DNA origami and performing a particle average recovers the structure with an alignment uncertainty of 1.2 Å CI = [0, 4.6] Å, showing distances between the average positions of the sites at 9.5 ± 2.6 Å (mean over six distances in the average ± mean over the error-propagated uncertainties of the six distances). Same scale applies to all magnification panels. CI describes 68% confidence interval.

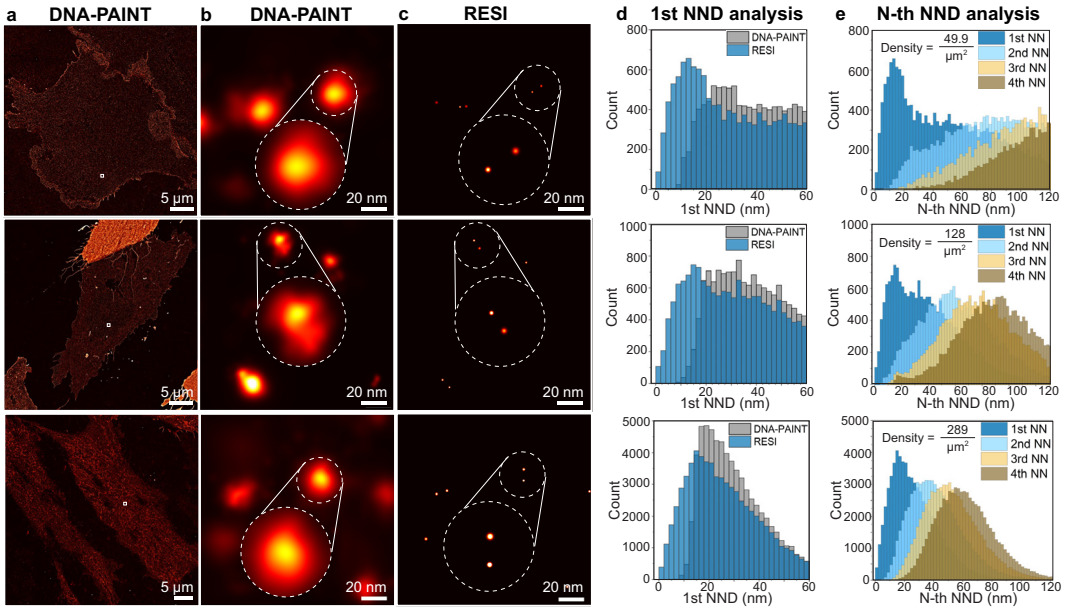

Extended Data Fig. 10 | RESI resolves CD20 dimers in untreated CHO cells for different expression levels. a, DNA-PAINT imaging of whole mEGFP-CD20-expressing CHO cells, labeled with anti-GFP-nanobodies, shows homogeneously distributed molecules for three independent experiments. **b**, Zoom-in regions of DNA-PAINT show cases in which dimers could not be resolved. **c**, RESI reveals sub-10-nm spaced receptor pairs, which are unresolvable in the DNA-PAINT cases. **d**, Whole-cell analysis of first nearest neighbor distances (1st NNDs) of CD20 receptors (histograms of the distances are displayed). Only RESI, but not DNA-PAINT, allows the routine detection of sub-10-nm distances between proteins. **e**, RESI-localization precision below 1 nm allows for routine detection of sub-10-nm distances, resulting in an accurate assessment of the first NND.

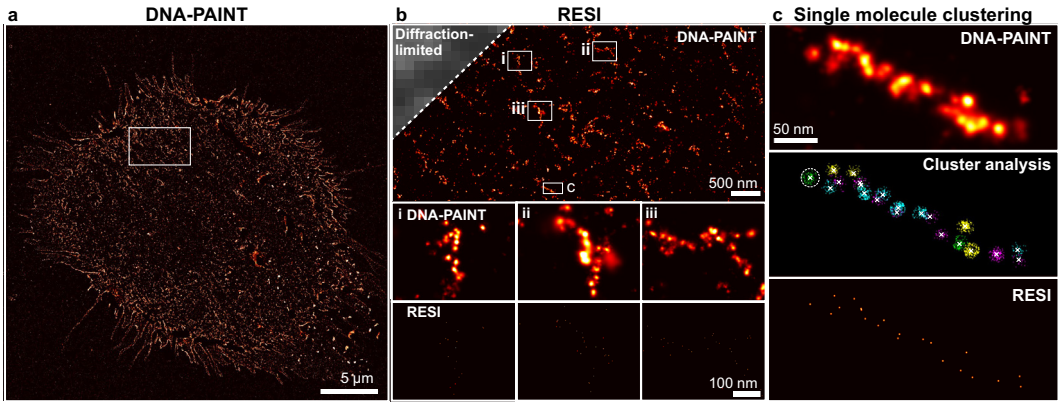

Extended Data Fig. 11 | RESI resolves the substructure in RTX-induced chain-like arrangements of CD20 receptors with sub-nanometer precision. **a**, DNA-PAINT overview image of mEGFP-CD20 expressing CHO cells treated with RTX. **b**, Labeling with DNA-conjugated anti-GFP-nanobodies and imaging with DNA-PAINT reveals higher-order organization after RTX-treatment. RESI (insets i–iii) achieves molecular resolution and thereby resolves the molecular arrangement of mEGFP-CD20. **c**, DNA-PAINT imaging shows clustered CD20 molecules. Performing RESI with sequences R1, R2, R3 and R4 in four separate imaging rounds (color-coded) allows for clustering of localizations originating from a single target. From the clustered localizations, RESI-localizations were calculated, enabling true single-protein resolution.

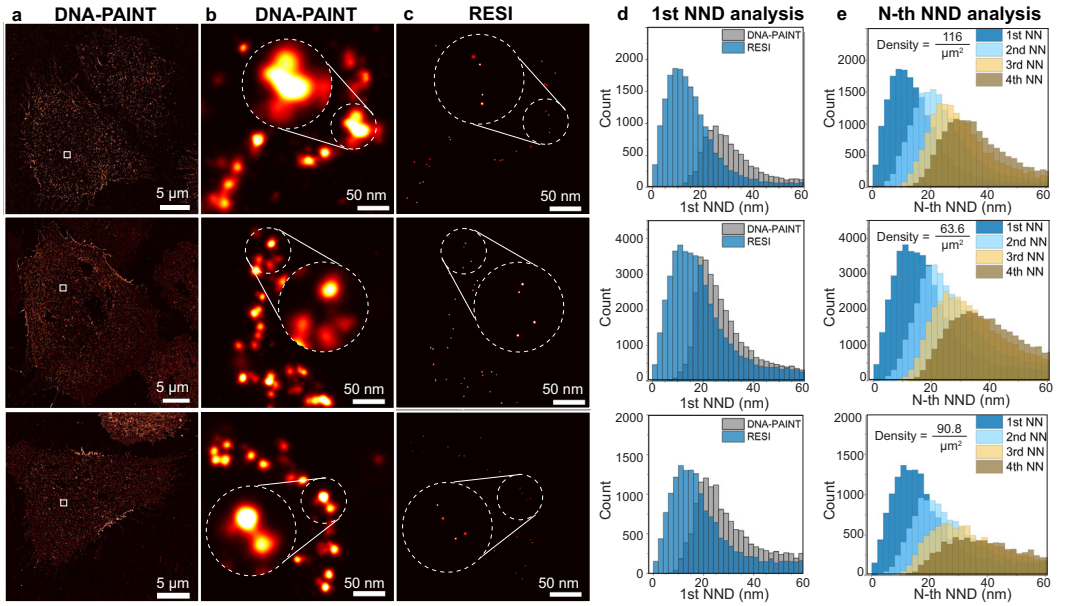

Extended Data Fig. 12 | RESI reveals higher order arrangement of CD20 dimers in Rituximab-treated CHO cells. a, DNA-PAINT imaging of whole mEGFP-CD20-expressing CHO cells, labeled with anti-GFP-nanobodies, shows clustered CD20- molecules in Rituximab-treated cells for three independent experiments. **b**, Zoom-in regions of DNA-PAINT show mEGFP- CD20 clustered into chain-like arrangements. **c**, RESI reveals sub-10-nm spaced receptor pairs within the clusters, unresolvable by DNA-PAINT. **d**, Whole-cell analysis of first nearest neighbor distances (1st NNDs) of CD20 receptors bound to Rituximab (histograms of the distances are displayed). Only RESI, but not DNA-PAINT, allows the routine detection of sub-10-nm distances between proteins. **e**, Routine detection of sub-10-nm distances by RESI recapitulates the first NND measured in the untreated case. Notably the NND peaks measured in the three repeats are consistent, independently of the protein density.

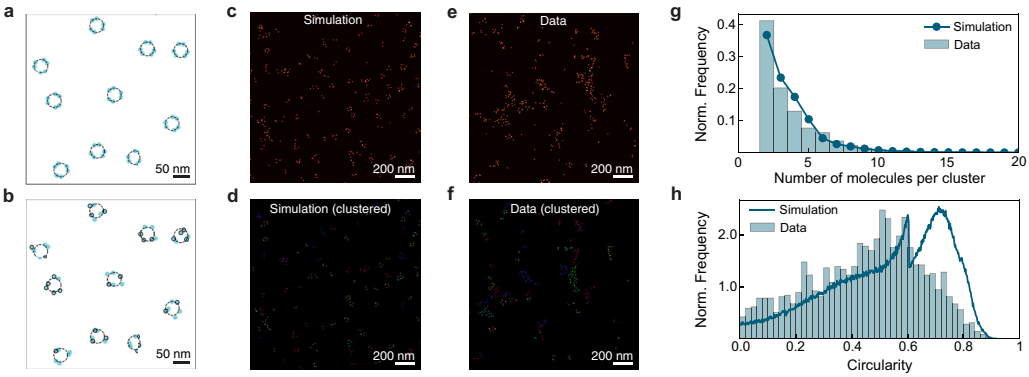

Extended Data Fig. 13 | Comparison of Rituximab treated CD20 data to simulated CD20 hexamer arrangements. a, Example of ground truth simulated CD20 hexamers (light blue circles, simulated as triangles of dimers with intra-dimer distances of 13.5 nm as measured experimentally) with random distribution and orientation on a 2D surface at the experimentally determined density. **b**, Label uncertainty and labeling efficiency (black circles indicate labeled molecules) are taken into account in the simulation for a realistic comparison. **c**, Simulated proteins in hexameric arrangements represented as gaussians. **d**, Hexamers after DBSCAN cluster analysis (colors indicate clusters). **e**, RESI image of CD20 data after RTX-treatment. **f**, RESI-localizations of CD20 data after DBSCAN cluster analysis (colors indicate clusters). **g**, Number of molecules per detected cluster for the experimental data and the simulated hexamers. **h**, Circularity metric of experimental data and the simulated hexamers after convex hull analysis of the clusters. We note that the sharp drop at 0.605 stems from the maximum circularity metric for clusters where the convex hull is defined by three molecules. Notably, the absence of a circularity peak at ~0.7 in the experimental data suggests that CD20 molecules are not arranged in isolated ring-like hexameric structures.

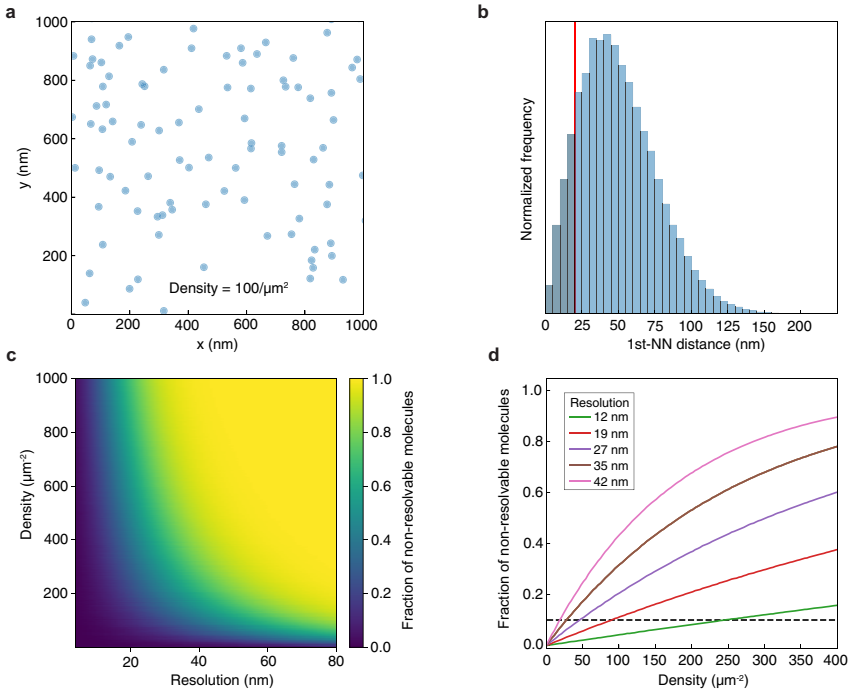

Extended Data Fig. 14 | Stochastic labeling. a, Exemplary simulation of proteins with a Complete Spatial Random (CSR) distribution of a given density. **b**, Histogram of Nearest Neighbor Distances (NNDs). The red line indicates the smallest distance (*d*) that can be resolved by DNA-PAINT for a given set of imaging parameters. The fraction of molecules with a NN below this distance threshold (blue, shaded) can be computed for a given density and a given DNA-PAINT resolution. **c**, 2D map of the fraction of non-resolvable molecules as a function of density and resolution. **d**, 1D cuts of c at different resolutions (color-coded) can be used as a user guide to estimate the number of multiplexing rounds needed to perform RESI efficiently given a certain target fraction of non-resolvable distances.

Extended Data Table 1 | Imaging and RESI parameters

Data	Round	Exposure time (ms)	Number of frames	Power (at objective, mW)	Power density (W / cm^2)	Imagers	Buffer	Cluster Radius xy (nm)	Cluster Radius z (nm)	Cluster N_{min}	K_mean
Extended Data Figure 2	Round 1	100	40 000	52	260	700 pM 5' R1, 700 pM R4	B+ (PCA, PCD, Trolox)	4	-	50	423
	Round 2					700 pM R3, 700 pM R4					338
Extended Data Figure 4	Round 1	100	40 000	56	280	500 pM R1, 250 pM R4	B+ (PCA, PCD, Trolox)	7	20	30	114
	Round 2					350 pM R3, 250 pM R4					112
Figure 2, Extended Data Figure 6, Extended Data Figure 7	DNA PAINT	150	40 000	18	90	15 pM R1, 15 pM R2, 15 pM R3, 15 pM R4	C+ (PCA, PCD, Trolox)	11	22	10	-
	Round 1		10 000			150 pM R1		11	22	10	23
	Round 2					100 pM R2					50
	Round 3					100 pM R3					31
	Round 4					100 pM R4					43
Figure 3 & Extended Data Figure 9	Round 1	100	30 000	56	280	500 pM 5' R1, 800 pM R4	B+ (PCA, PCD, Trolox)	4	-	50	250
	Round 2					300 pM R3, 800 pM R4					258
Figure 4 (Untreated) & Extended Data Figure 10	DNA PAINT	100	160000	30	150	100 pM R1, 100 pM R2, 50 pM R3, 100 pM R4	C (PCA, PCD, Trolox)	9	-	15	-
	Round 1	100	40000			400 pM R1		9	-	15	80
	Round 2					400 pM R2					59
	Round 3					200 pM R3					87
	Round 4					400 pM R4					119
Figure 4 (RTX treated), Extended Data Figure 11, Extended Data Figure 12	Round 1	100	40000	30	150	300 pM R1		9	-	15	58
	Round 2					300 pM R2					46
	Round 3		35000			300 pM R3					94
	Round 4					300 pM R4					121

Overview of DNA-PAINT image acquisition parameters alongside clustering and RESI parameters.

7.2 Publication 2

Resolving the structural basis of therapeutic antibody function in cancer immunotherapy with RESI

Isabelle Pachmayr, Luciano A. Masullo, Susanne C.M. Reinhardt, Jisoo Kwon, Maite Llop, Ondřej Skořepa, Sylvia Herter, Marina Bacac, Christian Klein & Ralf Jungmann.

Accepted in Nature Communications

2025

Resolving the structural basis of therapeutic antibody function in cancer immunotherapy with RESI

Isabelle Pachmayr[1,2], Luciano A. Masullo[1], Susanne C.M. Reinhardt[1,3], Jisoo Kwon[1], Maite Llop[4], Ondřej Skořepa[1,5], Sylvia Herter[4], Marina Bacac[4], Christian Klein[2,4], Ralf Jungmann[1,3,*]

[1]Max Planck Institute of Biochemistry, Planegg, Germany, [2]Department of Biochemistry, Ludwig Maximilian University, Munich, Germany, [3]Faculty of Physics and Center for Nanoscience, Ludwig Maximilian University, Munich, Germany, [4]Roche Innovation Center Zurich, Roche Pharma and Early Development, Schlieren, Switzerland, [5]Department of Biochemistry, Charles University, Prague, Czech Republic.
*Correspondence should be addressed to R.J. (jungmann@biochem.mpg.de)

Abstract

Monoclonal antibodies (mAb) are key therapeutic agents in cancer immunotherapy and exert their effects through Fc receptor-dependent and -independent mechanisms. However, the nanoscale receptor reorganization resulting from mAb binding and its implications for the therapeutic mode of action remain poorly understood. Here, we present a multi-target 3D RESI super-resolution microscopy technique that directly visualizes the structural organization of CD20 receptors and the Type I (e.g., Rituximab) and Type II (e.g., Obinutuzumab) anti-CD20 therapeutic antibodies and quantitatively analyze these interactions at single-protein resolution in situ. We discover that, while Type I mAbs promote higher-order CD20 oligomerization, Type II mAbs induce limited clustering, leading to differences in therapeutic function. Correlating RESI with functional studies for Type II antibodies with different hinge region flexibilities, we show that the oligomeric CD20 arrangement determines the Type I or Type II function. Thus, the nanoscale characterization of CD20-mAb complexes enhances our understanding of the structure-function relationships of therapeutic antibodies and offers insights into the design of next-generation mAb therapies.

Introduction

Immunotherapies based on therapeutic monoclonal antibodies (mAb) have revolutionized cancer treatment in the last 30 years. Tumor cell killing by mAbs is mediated by various mechanisms: On the one hand, Fc recognition by cellular Fc receptors can lead to antibody-dependent cellular cytotoxicity and phagocytosis, and Fc recognition by soluble complement proteins can activate complement-dependent cytotoxicity (**Fig. 1a**). On the other hand, binding of mAbs to their membrane receptor targets can directly exert function on the treated cells, independent of Fc functionality (**Fig. 1a**)[1,2]. In both the Fc-dependent and the Fc-independent mechanisms, the nanoscale receptor reorganization caused by mAb binding has likely a strong impact on their downstream function. This is also thought to be the case for tumor necrosis factor receptor mAbs, for which mAbs exert agonism or antagonism, depending on their clustering behavior, as well as for growth factor receptors, such as EGFR and C-Met, in which different mAb clones either lead to activation or silencing[3-6].

A prominent example of this hypothesized mAb structure-function relationship are anti-CD20-mAbs, used for treatment in B-cell malignancies and depletion of B cells in autoimmune diseases[7]. CD20-targeting mAbs can be separated into two groups – Type I and Type II – that exert therapeutic functions to a different degree: Type I mAbs lead to CD20 clustering and complement activation, whereas Type II mAbs lead to potent effector cell-mediated killing as well as to direct cytotoxicity.[8,9] Cryo-EM structures indicate a relationship of structure and function for Type I vs. Type II mAbs: Type I Rituximab (RTX) fragment antigen-binding (Fab) exhibit a shallow binding angle and a 2:2 Fab:CD20 stoichiometry, suggesting a potential bridging of CD20 dimers upon Type I mAb treatment (**Fig. 1b, top**). In contrast, Type II Obinutuzumab (OBZ) Fabs have a steeper CD20 binding angle and a 1:2 Fab:CD20 stoichiometry[10], suggesting a maximum of tetramers after Type II mAb binding (**Fig. 1b, bottom**)[11,12]. However, for both Type I and Type II treatment, the nanoscale structural arrangement of CD20 together with the complete mAbs in a cellular environment is not fully understood. Additionally, there is a lack of insight into the nanoscale organizational requirements for Type I or Type II function. To address these questions, we need (1) molecular specificity, (2) the ability to image proteins in the context of intact cells, (3) molecular spatial resolution and (4) multiplexing capability. Cryo-EM, mass spectrometry and traditional super-resolution microscopy methods, such as stimulated emission depletion microscopy, stochastic optical reconstruction microscopy (STORM) or photoactivated localization microscopy, are limited because they cannot achieve single-protein resolution *in situ* for dense assemblies[13-15]. With the recent development of resolution enhancement by sequential imaging (RESI), we can achieve single-protein resolution in intact cells, complementing structural biology data in a cellular context[16]. Given the unresolved link between the nanoscale organization of CD20 and therapeutic functions, we aim to elucidate how therapeutic mAbs modulate CD20 spatial arrangements and how these, in turn, influence functional outcomes.

To this end, we introduce multi-target 3D RESI imaging to directly and simultaneously visualize the nanoscale organization of CD20 receptors and their bound therapeutic mAbs at the intact cell membrane. We find that Type I and Type II mAbs induce distinct receptor arrangements in situ, and that the degree of CD20 oligomerization correlates with a functional transition between the two mAb types. Our findings establish a generalizable framework for linking receptor nanoscale organization to the therapeutic antibody function and offer new avenues for optimizing antibody design. This approach paves the way for structure-guided development of next-generation immunotherapies across diverse receptor systems.

Results

Single-protein resolution imaging of antibody-receptor complexes

To directly visualize both CD20 and the mAbs in the cellular context, we implemented a specific and quantitative multi-target labeling system for RESI imaging. RESI is based on DNA-PAINT (DNA Points Accumulation for Imaging in Nanoscale Topography)[17,18], a super-resolution microscopy technique that utilizes the transient binding of fluorescently labeled DNA probes to complementary target sequences to achieve ~10 nm spatial resolution through single-molecule localization. By stochastically labeling and sequentially imaging sparse target subsets at this resolution, RESI allows us to enhance the precision of the DNA-PAINT measurements by averaging localizations, therefore achieving Ångström spatial resolution[16].

For CD20, this is achieved by tagging the receptors with monomeric enhanced GFP (mEGFP) and labeling with the cognate nanobody (GFP-Nb) (**Fig. 1c, top left**). For the therapeutic mAbs, we made use of a small and specific peptide tag (ALFA-tag)[19] that can be stoichiometrically labeled with its cognate nanobody and genetically encoded to be expressed at the C-terminus of the heavy chain of therapeutic antibodies RTX and OBZ (**Fig. 1c, top right**). To achieve RESI for two protein targets, we implemented stochastic labeling and sequential readout featuring two sets of four orthogonal DNA sequences to label CD20 and mAbs, respectively.

Each separate imaging round resulted in DNA-PAINT localizations, originating from repetitive detection of single molecules by stochastic blinking (**Fig. 1c, bottom**). Multiple DNA-PAINT localizations (K) were grouped according to spatial proximity ("clustered") to obtain RESI localizations with improved precision according to $\sigma_{\mathrm{RESI}} = \sigma_{\mathrm{DNA\text{-}PAINT}}/\sqrt{K}$. To achieve this, two adjacent molecules must be labeled with orthogonal docking strands. An image resolving individual molecules was then reconstructed from the individual RESI localizations of CD20 and the mAb.

To observe the CD20 nanoscale organization independently of the downstream cellular functions in B lymphocytes, we established two-target RESI in CHO-K1 cells transfected with mEGFP-CD20 and treated with

ALFA-tagged mAbs. After mAb treatment and fixation, we performed stochastic labeling according to **Fig. 1c** and performed whole-cell 3D RESI with 0.6 nm localization precision (**Fig. 2** and **Supplementary Figure 1**). We achieved an effective resolution of ~2 to ~5 nm, limited by the size of the ALFA-tag-Nb or the mEGFP-tag-Nb complex, respectively.

Type I and Type II antibodies show distinct nanoscale arrangements.

Classical DNA-PAINT imaging shows that Type I-RTX and CD20 form co-clusters of 50-300 nm in the cell membrane (**Fig. 2a, b**). Only RESI, however, allowed us to faithfully resolve single proteins of both CD20 receptors and mAbs (**Fig. 2b**). When inspecting single clusters in 3D, it can be observed that RTX and CD20 organize in the membrane in a coplanar manner, with no apparent membrane bending induced by RTX binding (**Fig 2c, d** and **Supplementary Figure 2**). We detect RTX and CD20 with an average axial distance of 32 $\pm$ 11 nm, consistent with RTX bound outside of the cell membrane **(Supplementary Figure 3a)**.

In contrast, OBZ and CD20 co-cluster with a similar axial distance of 27 $\pm$ 9 nm **(Supplementary Figure 3b)**, but do not form >50 nm assemblies (**Fig. 2e, f**). RESI reveals the 3D oligomerization of CD20, forming a maximum of tetramers, when bound to OBZ (**Fig. 2g, h**). Excitingly, we were able to resolve two ALFA-Nbs bound to a single OBZ mAb, thus visualizing intramolecular distances within a protein (**Fig. 2g**). Interestingly, CD20 and OBZ do not seem to organize in a coplanar manner, suggesting potential membrane bending.

This detailed visualization with RESI highlights the different modes of interaction between CD20 and the therapeutic antibodies, RTX and OBZ, with implications for their mechanisms of action at the molecular level. To quantitatively analyze the properties of individual RTX-CD20 molecular assemblies, we first applied a cluster detection algorithm (Density-based spatial clustering of applications with noise, DBSCAN[20]) to the two-target RESI images (**Fig. 3a**). The stoichiometry of RTX:CD20, i.e. the number of RTX molecules per CD20 molecules, can be directly determined for each RTX-CD20 cluster, as RESI allows us to resolve single protein copies of both receptors and mAbs. The number of CD20 molecules per cluster in RTX-treated cells ranges from a single CD20 molecule to over 40 molecules per cluster (**Fig. 3b**). Furthermore, **Figure 3b** shows a clear linear correlation between the number of RTX molecules and the number of CD20 molecules in these clusters. When taking into account the labeling efficiency of ALFA- and GFP-Nbs (see Methods), a linear fit reveals approximately one RTX per two CD20 molecules (**Fig. 3b**, red line; **Supplementary Figure 4a**), suggesting that CD20 dimers are linked by RTX molecules.

To further quantitatively evaluate the precise molecular arrangement of the RTX-CD20 assemblies, we analyzed the first to sixth nearest-neighbor distances (NND) for CD20 (**Fig. 3c**, histogram). Only with RESI, and not with DNA-PAINT we were able to routinely detect sub-10 nm distances, allowing us to recover the actual first-NND peak (**Supplementary Figure 5**). To assess oligomeric CD20 and RTX arrangements, we then compared the NND

histograms of the data to those of simulated point patterns (**Fig. 3c**, solid line; for simulation details, see the Methods section). RTX-treated CD20 shows higher-order arrangements for all NNDs when compared to complete spatial random (CSR) simulations (**Supplementary Figure 3c-d**.). Notably, CD20 NNDs after treatment with ALFA-tagged and untagged RTX are comparable, showing that the ALFA-tag does not affect the mAb's CD20 binding properties[16]. Consistently, our NND data aligns well with a flexible chain model, taking into account the highly flexible hinge region of human IgG1 antibodies[21] (see Methods) (**Fig. 3d** and **Supplementary Figure 6a-c**). We obtained an average chain segment length of 23±2 nm for the RTX hinge-to-hinge region distance (**Supplementary Figure 3e**), which is longer than the expected length[22] of approx. 21 nm (see Methods). This is in line with the shallow binding angle for RTX-Fabs (**Fig. 1b**), leading to an increased Fab-to-Fab distance within the mAb[11,12].

We further assessed whether the flexible nature of RTX-CD20 chains can explain how RTX assemblies organize to form C1q binding platforms (**Fig. 3e**, top). C1q is a multimeric 460 kDa protein with six head domains, capable of activating the cytotoxic complement cascade upon binding to hexameric platforms of six mAbs.[23]

We have previously shown that isolated hexameric circular platforms of CD20 and RTX, as postulated by Cryo-EM studies, are not compatible with our RESI data showing highly concatenated linear RTX-CD20 clusters[11,12,16]. Although circular arrangements may be present in limited amounts on the cell membrane, this suggests that an alternative structural organization leads to compatible C1q binding platforms.

For instance, U-shaped chains of ≥6 CD20 dimers could position ≥6 RTX-Fc domains in close proximity, allowing for efficient C1q binding. To test this hypothesis, we analyzed the number of C1q-compatible binding sites per RTX-cluster (see Methods) and indeed, we detected several platforms compatible with C1q binding (**Fig. 3e**, bottom; **Supplementary Figure 4b**). Importantly, Fc-Fc interaction blockade does not change the structural RTX-CD20 arrangements observed with RESI, suggesting that this RTX-mediated CD20-clustering and the formation of C1q-binding platforms are independent of RTX Fc-Fc interactions (**Supplementary Figure 7**).

In contrast to Type I RTX, analyzing Type II OBZ-CD20 co-clusters reveals no higher-order oligomerization and no linear relationship between the number of OBZ molecules and the number of CD20 molecules (**Fig. 3f, g** and **Supplementary Figure 4c**). Instead, the frequencies of OBZ:CD20 stoichiometries result in discrete values, pointing towards limited oligomerization with one OBZ bound to one, two, three, or four CD20 molecules (**Fig. 3g**). To determine the oligomeric state of CD20, we first analyzed the 1st to 6th NNDs by comparing them with a simulated distribution of CD20 molecules according to CSR (**Supplementary Figure 3f** and **Supplementary Figure 6d**. For details on the CSR simulations, refer to Methods section "CD20 low order oligomerization simulations"). This comparison revealed specific peaks at distances below 20 nm for 1st to 3rd NNDs, which cannot be explained by a pure CSR distribution. These results indicate the presence of monomers, dimers, trimers, and tetramers of CD20 molecules on the cell surface (**Fig. 3h**). To assess the oligomeric state of the OBZ mAb when bound to CD20, we

analyzed the NNDs of the ALFA-Nb used for OBZ-labeling (**Fig. 3 h**, bottom right). The ALFA-Nb to ALFA-Nb distances only show a non-random peak in the first NND, corresponding to the expected labeling with two ALFA-Nbs per single OBZ-molecule (**Fig. 3h**, right and **Supplementary Figure 3g**). Moreover, the fact that the second NND peak is distributed according to CSR allows us to exclude the presence of higher-order assemblies of OBZ upon CD20 binding (**Fig. 3h** and **Supplementary Figure 6e**), contrary to what we observed in the RTX case. Accordingly, we detected only a few compatible C1q binding platforms for OBZ (**Supplementary Figure 3h**) as compared to RTX.

To quantitatively assess the experimental distribution of CD20 oligomers we compared our data with a simulated model of oligomers (monomers, dimers, trimers and tetramers) taking into account experimental factors such as labeling efficiency and linkage error (see Methods) (**Fig. 3h**). The proportions of each kind of oligomer are free parameters of the model that are retrieved from the fit to the data. We obtained a composition of 35% monomers, 48% dimers, 10% trimers and 7% tetramers of CD20 after OBZ binding (**Fig. 3i** and **Supplementary Figure 6c**).

Contrary to the proposed terminal complex of CD20 tetramers[11], we detected fewer trimers and tetramers than expected after OBZ binding. Even though the detection efficiency of oligomers in RESI may be reduced due to two adjacent DNA-PAINT-unresolvable molecules labeled with the same DNA docking strand sequence, this cannot explain a trimer and tetramer proportion below 30 %.[16] It could however be the case that the steep binding angle of OBZ-Fab (**Fig. 1b, bottom**) observed in Cryo-EM[11] necessitates membrane bending to allow for OBZ binding to two CD20 dimers simultaneously (**Fig. 3j**, top). To assess this experimentally, we measured the angle of the OBZ-CD20 complex, comprising CD20 trimers or tetramers, relative to the 2D plane of observation. Interestingly, we found an average angle of 25 ° (**Fig. 3j**, bottom and **Supplementary Figure 3i**), suggesting local nanoscale bending of the cell membrane; however, we cannot exclude that tilting of the whole complex contributes to this phenomenon (**Supplementary Figure 4d**). This energetically unfavorable membrane bending, which occurs when binding to two CD20 dimers happens simultaneously, likely accounts for the lower frequency of OBZ-induced CD20 tetramers.

CD20 oligomeric arrangement determines Type II function

Intrigued by this finding, we next hypothesized that there is a potential to increase CD20 tetramerization by introducing a more flexible hinge region in the mAb. For this purpose, we focused on OBZ-based CD20-CD3-T cell engagers (TCEs)[24]. The TCEs were evaluated in two distinct formats. The classical format (c-TCE) resembles the anti-CD20 Fab arrangement of Type II OBZ, with an additional anti-CD3-Fab attached externally to one OBZ-Fab for T cell binding, while the inverted format (i-TCE) exchanges the positions of the anti-CD3-Fab and OBZ-Fab, placing the anti-CD3-Fab internally and the OBZ-Fab externally (**Fig. 4a**). After treatment with c- or i-TCE, we

performed RESI imaging for CD20 like above. The RESI results show qualitatively comparable CD20 arrangements for both cases, with monomers, dimers, trimers and tetramers detected in the proximity of the mAbs (**Fig. 4b, c** and **Supplementary Figure 8**). However, more detailed analysis using NND histograms yields a higher degree of oligomerization for i-TCE compared to c-TCE (**Fig. 4d,e** and **Supplementary Figure 9**). By quantitatively comparing NNDs of the experimental data with NNDs of a numerical model simulating CD20 monomers, dimers, trimers and tetramers, we determine different trimer and tetramer proportions for both mAb formats, although the inter-CD20 dimer distance remains conserved (**Fig. 4d, e** and **Supplementary Figure 10**). Strikingly, i-TCE is significantly more efficient in trimer and tetramer formation (49.6 ± 6.2 %) compared to c-TCE (27.2 ± 10.5 %), demonstrating that an increased linker flexibility through introducing the anti-CD3-Fab between the OBZ-Fabs indeed allows for more efficient CD20 tetramer formation (**Fig. 4f**).

To test whether this difference in CD20 trimerization and tetramerization capabilities for both TCE formats also results in a difference in CD20-directed function, we correlated the nanoscale molecular organization of CD20 with results obtained by functional assays in living cells. In a direct cell killing assay, assessing only the CD20-mediated cytotoxicity, (see Methods) only Type II, but not Type I mAbs potently induce direct cell death in CD20-positive cells (**Fig. 4g** and **Supplementary Figure 11**). In agreement with its Type II functionality, treatment with c-TCE results in potent direct cell killing in CD20-positive cells (**Fig. 4g** and **Supplementary Figure 11**). Conversely, the direct cell killing ability of i-TCE is significantly reduced, thus exhibiting more Type I-like functions (**Fig. 4g** and **Supplementary Figure 11**). Moreover, i-TCE approaches Type I-like cell binding capabilities by engaging with about twice as many mAbs than c-TCE (**Fig. 4h**) in accordance with previously described Type I vs. Type II characteristics[25]. These two assays show that the function of c-TCE is comparable to that of Type II OBZ, whereas i-TCE exhibits a Type I-like function. Additionally, as we observed no higher-order oligomers beyond tetramers in the RESI images for either format, we conclude that CD20 concatenation, as seen in the RTX case, is not required for the shift from Type II toward Type I functionality. Rather than higher-order oligomerization, we demonstrate that the efficient formation of CD20 trimers and tetramers induced by certain therapeutic mAbs is what drives the shift from Type II to Type I function.

Therapeutic antibody function correlates with CD20 arrangement

To test if the CD20 oligomeric arrangement is a general determinant of Type I vs. Type II functionality, we next investigated CD20 oligomerization for additional Type I and Type II anti-CD20 mAbs. Type I Ofatumumab (OFA) leads to even stronger complement binding than RTX[26,27] and has also been shown to bind with two individual Fabs to CD20 dimers, albeit with a steeper binding angle[11,12]. Similar to RTX-treatment, RESI images acquired after OFA treatment show CD20 oligomerization (**Fig. 5a** and **Supplementary Figure 12a-b**). In addition, the NND

histograms reveal linear higher-order CD20 arrangements for all first to sixth NNDs, like RTX (**Fig. 5b**). Comparing the NND data to the same flexible chain-like model as for RTX allowed us to faithfully fit the CD20-NND data, albeit featuring a shorter (17±2 nm) chain-segment length compared to RTX (23 nm) (**Fig. 5b** and **Supplementary Figure 12c**). This in fact agrees with the steeper binding angle of OFA-Fabs to CD20 dimers, effectively reducing the intra-IgG1 Fab-Fab distance (**Fig. 5c**) while also forming platforms compatible with C1q binding (**Supplementary Figure 12d**). Furthermore, we evaluated the Type I mAb 2H7, which shows higher-order oligomerization of up to hexamers (**Supplementary Figure 12e-g**).

In addition to OBZ and c-TCE, we evaluated the CD20 oligomerization after treatment with the Type II clone H299. The RESI images of CD20 after H299 treatment reveal oligomers up to tetramers, comparable to OBZ data (**Fig. 5d**). NND histograms for H299 show a non-CSR first, second, and third NND peak, indicative of oligomers up to tetramers (**Fig. 5e**). These results are consistent with trimer and tetramer proportions that we previously detected for Type II mAbs (**Fig. 4**), yielding less than 30 % of CD20 trimers and tetramers upon H299 binding (**Fig. 5f**).

Taken together, the unique ability of RESI to directly observe and quantify *in situ* molecular changes in CD20 arrangements allows us to propose a general model to correlate the mAb-induced CD20 oligomerization with their Type I or Type II function (**Fig. 5g**). Type II function, characterized by direct cell death, correlates with limited CD20 oligomerization of dimers, trimers and tetramers (**Fig. 5g**, left side). On the contrary, full Type I-like function, characterized by less efficient cell killing, is accompanied by the ability to form higher-order concatenated structures of at least hexamers, as shown by imaging of RTX, OFA, as well as 2H7 (**Fig. 5g**, right side). Notably, modifying the Type II-like c-TCE to the more flexible i-TCE, generates a transition from Type II-like to Type I-like function, as detected by a reduction of direct cytotoxicity. This is accompanied by a significant increase in the ability to form CD20 trimers and tetramers upon binding, thereby defining the molecular requirements for Type I and II function of therapeutic mAbs.

Discussion

Our data highlights the importance of assessing the nanoscale organization of therapeutic monoclonal antibodies (mAb) and their target proteins during binding to gain a comprehensive understanding of the molecular mechanisms underlying their therapeutic action. We have developed a sensitive and versatile assay using RESI microscopy to quantitatively analyze the impact of monoclonal antibody mAbs binding to their cognate receptors on the nanoscale structural organization of receptor-mAb complexes within cells. RESI microscopy enables the imaging of individual molecules with Ångström-scale precision within intact cells, allowing for spatial analysis and modeling of the molecular functions of anti-CD20 mAbs. Our study reveals that Type I mAbs induce higher-order

CD20 oligomerization with a minimum of hexamers, whereas Type II mAbs lead to limited CD20 oligomerization, forming up to tetramers. We evaluated the effect of changing the relative orientation of the two OBZ-Fab arms by inverting the anti-CD3 and anti-CD20 Fab arms in the OBZ-like CD20-CD3-TCE. When using CD20-CD3 TCEs in the presence of T cells, i-TCE is a more potent bispecific T cell engager than c-TCE, most likely due to the highly efficient CD20 binding and closer spatial contact of cancer cells with T cells[24]. Interestingly, when only investigating the CD20-mediated direct cytotoxicity, independent of T cell-mediated effects, we found that i-TCE reduces the original direct cytotoxicity of c-TCE while it increases the formation of CD20 trimers and tetramers. This suggests that a higher abundance of CD20 trimers and tetramers inversely correlates with the direct cytotoxicity of anti-CD20 antibodies. This partial loss of direct cytotoxicity while also showing a partial increase in CD20 oligomer formation in the case of i-TCE suggests a continuum in both therapeutic function and CD20 oligomerization between Type I and Type II mAbs, rather than two distinct categories.

According to Type I-like gain of function with increasing CD20 oligomerization, Type II OBZ has previously been shown to mainly activate cell death inducing pathways, while Type I RTX has a dual function in activating both pro-apoptotic and anti-apoptotic signaling pathways within the B-cell receptor (BCR) cascade[28,29]. This suggests that increasing CD20 oligomerization by Type I mAbs promotes pro-survival effects induced by CD20-mediated signaling. The extent to which therapeutic mAb-modulated CD20 oligomerization influences BCR signaling cascades needs further investigation, as this has important implications on personalized medicine or combination therapy with drugs influencing the BCR cascade[30].

Only with RESI, we were able to image the macromolecular assembly of CD20 and mAbs in the cellular context, revealing that Type I mAbs can form platforms compatible with C1q binding within chain-like arrangements, without the need for closed rings (**Fig. 2** and **3**).[31] Shorter antigen-to-antigen distances correlate with C1q deposition and activation[32], which is in agreement with the shorter chain segment length we deduced for OFA vs. RTX, as OFA is known to lead to more stable C1q binding[27]. Furthermore, the flexible chain model explains how adjacent C1q platforms within a chain could allow for C1-complex (C1q with proteases C1r and C1s bound) cross-activation.[33,34]

Our findings demonstrate the universal applicability of our RESI imaging and analysis workflow for any membrane protein that holds potential as an immunotherapeutic target. We can elucidate oligomeric as well as nano- to microscale structural arrangements of membrane proteins in complex with their cognate antibodies *in situ*, i.e. in whole intact cells, a capability thus far out of reach for super-resolution microscopy. RESI features a dynamic range spanning almost five orders of magnitude, from whole cells (10-100 µm) to intermolecular distances of protein dimers (1-10 nm).

MINFLUX and related techniques achieve localization precisions of 1–2 nm (sub-5 nm resolution), comparable to RESI and sufficient to resolve single proteins[35-39]. When combined with DNA-PAINT, MINFLUX also allows for high multiplexing[40]. However, throughput is currently a major limitation in MINFLUX: areas of a few hundred nanometers are acquired sequentially (several minutes of acquisition each), thus requiring hours for fields-of-view spanning only a few micrometers[35,40]. While whole-cell imaging with MINFLUX is theoretically possible, it has not yet been demonstrated. In contrast, RESI can acquire ~100 x 100 µm² fields-of-view—covering multiple cells—in similar timeframes, yielding a ~1000-fold higher throughput.

The current throughput of RESI enables imaging of more than 10 cells per day, making it a powerful tool for screening therapeutic mAb candidates at molecular resolution. Moreover, automation and parallelized measurements in multiple microscopes could extend the throughput beyond hundreds of cells per day. Training machine learning models on RESI data could enable the prediction of mAb functions based on their oligomeric patterns, offering potential for biosimilar and generic drug screening, as well as quality control. To further refine the relationship between the structure and function of anti-CD20 mAbs, future studies could investigate those mAbs that have been shown to unify Type I and Type II functionalities[41].

RESI microscopy will not only enhance our understanding of existing therapies but also pave the way for the rational design of next generation mAbs with optimized therapeutic profiles. Future research could focus on the relationship between mAb structure and function across different cancer types and treatment contexts to fully exploit the potential of these biological agents.

Methods

Materials

Right-handed DNA oligonucleotides, modified with C3-azide or 5'-Cy3B, were ordered from Metabion. Left-handed DNA sequences were purchased from Biomers. Ultrapure water (cat: 10977-035), Tris 1 M pH 8 (cat: AM9855G), EDTA 0.5 M pH 8.0 (cat: AM9260G) and 10×PBS pH 7.4 (cat: 70011051) were purchased from Thermo Fisher Scientific. Sodium chloride 5M (cat: AM9759), Bovine serum albumin (cat: A9647) and sodium azide (cat: 71289 were ordered from Sigma-Aldrich. Lipofectamine LTX (A12621) and 16% Formaldehyde methanol-free (cat: 28908) and sheared salmon sperm DNA (cat: AM9680) were obtained from Thermo Fisher Scientific. Glutaraldehyde (25%, cat: 4157.1) and NH_4Cl (cat: K298.1) were ordered from Carl Roth. Triton X-100 (10 % solution) (cat: 93443), Tween 20 (cat: P9416-50ML), glycerol (cat: 65516-500ML), protocatechuate 3,4-dioxygenase pseudomonas (PCD) (cat: P8279), 3,4-dihydroxybenzoic acid (PCA) (cat: 37580-25G-F) and (+−)-6-hydroxy-2,5,7,8- tetra-methylchromane-2-carboxylic acid (Trolox) (cat: 238813-5 G) were ordered from Sigma-Aldrich. Fetal Bovine Serum (FBS) (cat. A5669701, Gibco), 1× Phosphate Buffered Saline (PBS) pH 7.2 (cat: 20012-019), 0.05 % Trypsin–EDTA (cat: 25300-054), Lipofectamine 3000 (cat: L3000015) were purchased from Thermo Fisher Scientific. 90 nm diameter Gold Nanoparticles (cat: G-90-100) were ordered from Cytodiagnostics. µ-Slide 8 Well high Glass Bottom (cat: 80807) was purchased from ibidi. Amicon Ultra-0.5 and Amicon Ultra-2 centrifugal filter units with 10k and 50k MWCO (cat: UFC5010, UFC 5050, UFC201024, UFC205024) were purchased from Merck.

Cloning

mEGFP-CD20 was cloned by insertion of CD20 into the mEGFP-C1 plasmid (no. 54759, Addgene). A CD20 gblock (obtained from Integrated DNA Technologies) was inserted with Gibson assembly after cutting with restriction enzymes BsrGI and BamHI (2× Gibson Assembly mix, New England Biolabs cat: E2611).

Nanobody-DNA conjugation via a single cysteine

Nanobodies against GFP, ALFA, and human IgG were ordered with a single ectopic cysteine at the C-terminus for site-specific and quantitative conjugation. The conjugation to DNA-PAINT docking sites (see **Supplementary Table 1 and 2**) was performed as described previously[16]. First, buffer was exchanged to 1× PBS + 5 mM EDTA, pH 7.0 using Amicon centrifugal filters (10k MWCO) and free cysteines were reacted with 20-fold molar excess of bifunctional maleimide-PEG_4-DBCO linker (Sigma-Aldrich, cat: 760668) for 2-3 hours on ice. Unreacted linker was removed by buffer exchange to PBS using Amicon centrifugal filters. Azide-functionalized DNA was added with 3-5 molar excess to the DBCO-nanobody and reacted overnight at 4°C. Unconjugated nanobody and free azide-DNA were removed by anion exchange chromatography using an ÄKTA Pure liquid chromatography system equipped with a Resource Q 1 ml column. Nanobody-DNA concentrations were adjusted to 5-10 µM (in 1xPBS, 50% glycerol, 0.05% NaN_3) and stored at -20°C for 1-6 months or at -80°C for >6 months.

Cell culture

CHO-K1 cells (CCL-61, ATCC) were cultured in Gibco Ham's F-12K (Kaighn's) medium (Thermo Fisher Scientific, cat: 21127030), supplemented with 10 % FBS (cat. A5669701, Gibco). Cells were passaged every 2–3 days using trypsin-EDTA.

ALFA-tagged therapeutic antibodies

The ALFA-tag was fused genetically to the C-terminus of the heavy chain of rituximab and obinutuzumab via a G5S linker (GGGGGSPSRLEEELRRRLTE). The respective antibodies were transiently expressed in HEK239 cells and purified via protein A. Their identity and activity were confirmed (**Supplementary Table 3**).

Expression and purification of SpA-B

A plasmid (pET-30b(+)_SpA-B) enabling bacterial expression of *Staphylococcus aureus* Protein A, subunit B (SpA-B), was constructed by Gibson Assembly, inserting the codon-optimized gene (Uniprot entry P38507, A212-K269) into a pET-30b(+) (Novagen, cat: 69910) plasmid previously digested with NdeI and XhoI endonucleases. The resulting construct included a C-terminal Sortase A (LPETGG) sequence, followed by a hexahistidine tag to facilitate subsequent purification and functionalization.

An aliquot of *Escherichia coli* BL21(DE3) (New England Biolabs, cat: C2527H) was transformed with pET-30b(+)_SpA-B and a single colony was picked and inoculated into 1 L of LB_KAN medium, followed by incubation at 37 °C, 200 RPM. When the OD600 reached 0.5, protein expression was induced by adding IPTG to a final concentration of 0.2 mM, and incubation was continued at 37 °C, 200 RPM for 4 hours. Cells were harvested by centrifugation (10,000 × g, 15 minutes), resuspended in 40 mL of PBS, and lysed by sonication (3 minutes, 40% amplitude, 1 s on/off pulses) on ice. The lysate was centrifuged (15,000 × g, 30 minutes), filtered, and the supernatant was loaded onto a Ni-NTA (HisTrap FastFlow 5ml, Cytiva, cat: 17528601) column pre-equilibrated with PBS. The column was washed with 20 mM imidazole in PBS, and the protein was eluted with 250 mM imidazole in PBS.

The eluate was concentrated using a 3 kDa cut-off filter and loaded onto a Superdex 75 Increase 10/300 GL column (Cytiva, cat: 17517401), with PBS as the mobile phase. The protein eluted as a single peak, and the corresponding fractions were pooled (5.8 mg/mL), aliquoted, frozen in liquid nitrogen, and stored at -20 °C

Binding of SpA-B to IgG1

Specific binding of SpA-B to IgG1 was assessed by first immobilizing 3 mg SpA-B in His-Incubation buffer (Supplementary Table 4) on Ni-NTA beads (Ni-NTA Spin Purification Kit, Thermo Scientific, 88227) for 30 min at RT. Then, Ni-NTA beads were washed 4 times with His-Washing buffer (Supplementary Table 4). The SpA-B loaded beads were incubated with RTX-IgG1 in His-Incubation buffer for 30min at RT. After incubation, SpA-B and RTX-IgG1 coated beads were again washed 4 times with His-Washing buffer before elution with His-Elution buffer (Supplementary Table 4). To control for unspecific binding of both SpA-B and RTX-IgG1 to Ni-NTA beads, 3mg BSA instead of SpA-B were incubated on Ni-NTA beads, followed by washing as above. The BSA coated beads were subsequently incubated with RTX-IgG1, followed by washing and elution as above. Samples were analyzed on an SDS-PAGE.

Treatment with therapeutic antibodies

CHO-K1 cells were seeded on 8 Well high Glass Bottom chambers the day prior to transfection at a density of 10,000 cells per well. CHO cells were transfected with mEGFP-CD20 using Lipofectamine LTX as specified by the manufacturer. CHO cells were allowed to express receptors overnight. Therapeutic antibodies were thawed on ice, subjected to a spin at >20000xg at 4°C for 10 min and the supernatant was kept on ice until cell treatment. F12K medium + 10% FBS was heated to 37°C. All therapeutic antibodies (RTX-Alfa and OBZ-Alfa, OFA, 2H7, CD20-CD3-TCEs) were diluted to 66.7 nM in medium (**Supplementary Table 3**). For the experiments assessing the effect of Fc-Fc interaction blockade, SpA-B was incubated with RTX or OBZ at a 20-fold molar excess for 15 min at RT, before adding the mAbs to the pre-heated medium. Cells were incubated with therapeutic antibodies for 30 min at 37°C. Next, cells were washed 2x with 250 μL F12K medium. 16% PFA was diluted 1:4 in 1xPBS and pre-heated to 37°C for 10 min. The medium was removed, and cells were immediately fixed with 250 μL 4% PFA for 15 minutes and washed 3x with PBS. Cells were permeabilized in 0.1% TritonX-100 in PBS for 5 minutes and washed with PBS followed by incubation with Blocking buffer (Supplementary Table 4) for 1h at RT.

RESI sample preparation

The RESI staining mix was prepared as follows: anti-GFP Nbs (clone 1H1), conjugated with DNA-docking strands 5xR1, 5xR2, 7xR3, or 7xR4 were added in equimolar amounts to a final concentration of 50 nM in Blocking buffer, and ALFA-tag nanobodies conjugated with DNA-docking strands 5xR5, 5xR6, 7xL1 or 7xL4 were added to the GFP-

Nb-mix in Blocking buffer to a final concentration of 50 nM. 200 µL RESI staining mix was added per well and incubated overnight at 4 °C. The next day, unbound binders were removed by washing with the Washing buffer (Supplementary Table 4), followed by a single wash with PBS. Post-fixation was performed with 4% PFA in PBS + 0.1% glutaraldehyde for 10 min. Quenching was performed with 0.2 M NH_4Cl in PBS, followed by washing with PBS. Gold nanoparticles, freshly diluted 1:3 in PBS, were vortexed thoroughly, and 250 µL of the gold suspension was added and incubated for 7 min before washing with PBS.

RESI imaging

mEGFP-CD20 transfected cells were selected by screening for homogenous, low GFP-fluorescence in TIRF mode, using a 488 nm excitation laser with 1 mW at the objective. Next, the Imaging buffer (Supplementary Table 4) was freshly prepared, and R4 imager strands were added at a concentration of 500 pM. Using the 561 nm excitation laser at 30 mW at the objective, cells were further selected for sufficiently sparse, homogenous blinking density. Afterwards, the first RESI image acquisition round was initiated with imager concentration ranging from 500 pM to 1 nM. Imagers were washed off with PBS, and imager strands for the next RESI imaging round were added in a freshly prepared Imaging buffer (Supplementary Table 4). All other imagers were added with the same procedure until 8 rounds of RESI imaging were completed. A detailed overview of imaging parameters is listed in **Supplementary Table 5**.

Microscope setup

2D and 3D Fluorescence imaging was carried out on an inverted microscope (Nikon Instruments, Eclipse Ti2) with the Perfect Focus System, applying an objective-type TIRF configuration equipped with an oil-immersion objective (Nikon Instruments, Apo SR TIRF ×100, numerical aperture 1.49, oil). 488 nm and 560 nm lasers (MPB Communications, 1 W) were used for excitation and coupled into the microscope via a Nikon manual TIRF module. The laser beams were passed through cleanup filters (Chroma Technology, ZET488/10× for 488 nm excitation, ZET561/10× for 560 nm excitation) and coupled into the microscope objective using a beam splitter (Chroma Technology, ZT488rdc-UF2 for 488 nm excitation, ZT561rdc-UF2 for 560 nm excitation). Fluorescence was spectrally filtered with an emission filter (Chroma Technology, ET525/50 m and ET500lp for 488 nm excitation, ET600/50 m and ET575lp for 560 nm excitation and ET705/72 m) and imaged on an sCMOS camera (Hamamatsu, ORCA-Fusion BT) without further magnification, resulting in an effective pixel size of 130 nm (after 2 × 2 binning). The central 1,152 × 1,152 pixels (576 × 576 after binning) of the camera were used as the region of interest, and the scan mode was set to lowest noise (≥100ms) for 100ms integration time and low noise (≥25ms) for 75 ms integration time. Three-dimensional (3D) imaging was performed using an astigmatism lens (Nikon Instruments, N-STORM) in the detection path[42]. Raw microscopy data were acquired using µManager (Version 2.0.1)[43].

Image analysis for RESI

Raw fluorescence data were subjected to super-resolution reconstruction using the Picasso software package[7] (latest version available at https://github.com/jungmannlab/picasso). Drift correction was performed with redundant cross-correlation and gold particles as fiducials for cellular experiments. Gold NPs were also used to align all rounds for 8-plex exchange. After channel alignment with RCC and gold NPs, whole cell regions of the DNA-PAINT data were picked and analyzed using the Picasso SMLM clustering algorithm (latest version available at https://github.com/jungmannlab/picasso) for each target individually.

Clustering of DNA-PAINT localizations

Cluster analysis was performed according to a previously published method[16]. After channel alignment, DNA-PAINT data were analyzed using a custom clustering algorithm in 'Picasso: Render'. First, localization cloud centers were identified via gradient ascent. Localizations surrounding each center could be grouped, due to sufficient spacing between localization clouds in RESI.

The algorithm requires two input parameters: radius r, defining the cluster size and circular area around each localization, and n_{min}, the minimum number of localizations per cluster. The number of neighbors within distance r of each localization is counted. If a localization has more neighbors than its surrounding points, it is marked as a local maximum. Clusters are formed if there are more than n_{min} localizations within r of a local maximum; non-clustered localizations are discarded. RESI localizations are the centers of the localization groups, calculated as weighted mean by employing the squared inverse localization precisions as weights.
Clusters are filtered in two ways to exclude those of non-specific "sticking" of imagers. First, the mean frame of localizations in each cluster is calculated, and clusters with a mean frame in the first or last 20% of frames are excluded. Second, clusters containing over 80% of localizations within 5% of the frames are also excluded.
The clustering radius (r) and threshold (n_{min}) depend on experimental conditions. A suitable n_{min} can be determined by selecting localization clouds from single target molecules, plotting a histogram, and distinguishing between targets and background. Radius r should be approximately 1.5× to 2× the NeNa localization precision to avoid overlapping clusters or sub-clustering. Picasso Render provides a tool to test different clustering parameters on small regions of interest.
For 3D clustering, the xy-clustering radius r is doubled to be used as the z radius, as the z the spread of localizations in z is approximately two-fold greater compared with x and y.

3D visualization
Regions of interest, i.e. single clusters for RTX/CD20 or OBZ/CD20 were picked from the 2-target image and individually displayed as a 2-target image in the 3D window in Picasso Render. For visualization in 3D, the individual picks were rotated by 90° or 270° around the x- or the z-axis. 3D DNA-PAINT data was displayed as clustered localizations or as RESI localizations.

DBSCAN two-target cluster analysis of RESI data
2-target RESI images of RTX/CD20 and OBZ/CD20 were subjected to DBSCAN[20] co-clustering with a radius of 40 nm and a minimum of at least 1 Alfa-Nb and 1 GFP-Nb detected. Non-clustered localizations were discarded for 2-target analysis.

Ratio analysis
After DBSCAN co-clustering, ALFA-Nb to GFP-Nb ratios were determined on a per cluster basis and the histogram was plotted. Moreover, counts of ALFA-Nbs per cluster were plotted versus GFP-Nb counts and represented in a 2D histogram. To determine the correlation, a linear fit was performed with Python polyfit and the slope of the linear fit was determined. The slope was normalized for Alfa-Nb and GFP-Nb labeling efficiencies (40 % and 50%, respectively) to determine the mAb to CD20 ratio[44]. Graphs in **Fig. 3** were normalized so that 2 ALFA-Nbs equals 1 therapeutic antibody (RTX or OBZ).

C1q platform analysis
C1q is a complex with 6 head domains, each capable of binding to one antibody-Fc domain and a hexameric platform of Fc domains is the most efficient[32] in capturing C1q. Consequently, 6 therapeutic antibodies in spatial proximity were approximated as ≥5 ALFA-Nbs within 25 nm, as ALFA-Nbs were previously measured to label with 40% labeling efficiency[44]. Importantly, C1q-binding platforms are defined as one possible configuration for binding, without removing clusters containing the same ALFA-Nb, to represent the apparent gain in avidity.

Angle analysis
For each OBZ-CD20 co-cluster containing more than 3 CD20 molecules, the center of mass for both the mAb and the CD20 cluster was determined. Then, the vector from mAb-center of mass to CD20-center of mass was calculated and the angle between this vector and the normal vector on the xy-plane (which corresponds to the

plane of a flat membrane on the coverslip) was determined (see **Fig. 3h**). Therefore, an angle of 0° means a perfectly perpendicular mAb over the CD20 cluster.

Distance analysis
The vector from mAb-center of mass to CD20-center of mass was determined for each cluster, as described in **angle analysis** and the absolute value of the vector was determined (see **Fig. 3h**).

DBSCAN one-target cluster analysis
CD20 RESI data was subjected to DBSCAN clustering with a radius of 20 nm and a minimum of at least 2 GFP-Nb detected per cluster. Individual clusters were identified, and non-clustered molecules were discarded.

CD20 chain-like oligomerization simulations
CD20 cluster size frequencies and the density of CD20 clusters were extracted from the DBSCAN one-target cluster analysis data. Then, a random set of x-y coordinates was generated as chain-starting points. For each individual chain, the number of chain segments was randomly selected according to the experimentally evaluated cluster size frequency. Then, for each chain-starting point, a random angle was chosen to simulate the next hinge point. From this hinge point, an angle between 30 and 330 was randomly chosen to simulate the next hinge point. This process was repeated for each chain, until the maximum number of chain-segments was simulated. Each center of mass between two hinge points was used to simulate 2 GFP-Nbs labeling a CD20 dimer. The hinge points were used to simulate two ALFA-Nbs labeling the therapeutic antibody. The resulting GFP-CD20 and Alfa-Nb coordinates were subjected to labeling efficiency and uncertainty corrections and the nearest-neighbor distance histograms were analyzed. Fixed parameters for simulations were experimentally determined chain-lengths and chain-frequencies, the hinge angles, as estimated to be between 30° and 330° from the domain plane angle analysis of Individual Particle Electron Tomography data[21], the experimentally determined 13.5 nm GFP-Nb to GFP-Nb dimer distance[16] and the experimentally determined ALFA-Nb to ALFA-Nb distances of 4 nm. Segment length was a free parameter (i.e. hinge point to hinge point distance) and was optimized starting from an estimated distance of <21 nm, considering a ~16 nm Fab-to-Fab distance[22] plus contributions of the ~5nm CD20 dimer distance[11,12].

Monte-Carlo simulations to determine the uncertainty of the chain segment length
Three separate "optimal" CD20 chain simulations with the optimal chain segment length (RTX: 23 nm, OFA: 17 nm) were generated from the experimental data. Each of the simulated data sets were subjected to cluster analysis to obtain cluster sizes. According to the cluster sizes of these "optimal" simulations, chain simulations iterating through different chain segment lengths, were performed. The 1st to 10th NNDs of "optimal" and "iterating" simulations were determined. Then, the sum of least squares between the "iterating" NNDs and the respective "optimal" simulation were calculated. The results are displayed in the respective Extended Data Figures. Significant differences between the sum of least squares were assessed with an unpaired t-test. The first significant difference in the chain segment lengths was defined as the uncertainty of the deduced chain segment length.

CD20 low order oligomerization simulations
Expected coordinates of CD20 oligomers, such as monomers, dimers, trimers, tetramers were generated. Simulations of variable proportions of CD20 oligomers were performed. For the data and for each simulation, NND analysis was performed. The most likely proportions of populations of oligomers were obtained through a least-squares optimization procedure. Simulation and analysis were performed with the Picasso module SPINNA[45].

The algorithm for optimizing oligomer proportions of the simulation can be summarized as follows:

- Simulation of monomers: a set of spatial coordinates with CSR distribution and given density are drawn.

- Simulation of dimers: a set of spatial coordinates with CSR distribution are drawn, representing the center of each dimer. For each center, two positions are generated with a random orientation and expected distances.
- Simulation of trimers: a set of spatial coordinates with CSR distribution are drawn, representing the center of each trimer. For each center, three positions are generated with a random orientation and expected distances.
- Simulation of tetramers: a set of spatial coordinates with CSR distribution are drawn, representing the center of each tetramer. For each center, four positions are generated with a random orientation and expected distances.
- The final position of each molecule is computed taking into account the *Uncertainty* parameter (in all cases 5 nm) drawn from a gaussian distribution.
- NNDs are calculated on the subset of detectable molecules, corrected by the published labeling efficiencies[44].
- The number of dimers, trimers and tetramers per unit area are simulated such that the *total density* of molecules is set to match the observed experimental density after taking into account the labeling efficiency of the molecules.

Cell Culture for cell binding and direct cell killing assays
Raji (ECACC #85011429) were cultivated in DMEM supplemented with 10 % FCS and 1 % Glutamax (Invitrogen/Gibco # 35050-038), SU-DHL-6 (ATCC #CRL-2959) and OCI-LY18 (DSMZ #ACC699) were cultivated in RPMI1640 supplemented with 10 % FCS and 1 % Glutamax.

CD20 binding assay
CD20 binding of obinutuzumab, rituximab, glofitamab and CD10 classical TCB was assessed on OCILY18, SUDHL6 and Raji B cell lines. The cell lines were resuspended at 1 x 10^6/ml in FACS Buffer and 100 µl/well (100000/well) were seeded into 96-U-bottom plates. Antibody dilutions were prepared in FACS Buffer (200 nM down to 0.01 nM, 1:4 dilution steps). 25 µl/well of the pre-diluted antibodies or PBS were added after centrifugation to the cell pellets and incubated for 1 h at 4°C. Afterwards, cells were washed and incubated with a PE-labelled secondary antibody (PE-conjugated AffiniPure F(ab)'$_2$ Fragment goat anti-human IgG Fcg Fragment specific (Jackson Immunoresearch Lab 109-116-170) in the presence of a live/dead marker (NIR) for 30 min at 4°C. Cells were washed twice and re-suspended in 150 µl/well FACS Buffer/PBS and measured using a BD FACS CantoII.

Assessment of direct cell death
Phosphatidylserine exposure and cell death were assessed by FACS analysis of Annexin V- (Annexin V FLUOS Staining Kit, Roche Applied Science #11828681001) and PI (Sigma Aldrich #P4864)-stained cells. Briefly, 1 × 10^5 target cells/well (190 µL/well) were seeded in 96-well plates and incubated with mAb (12.5 nM) for 24 h (untreated samples were used as negative control). Cells were then washed with Annexin V binding buffer (10mM HEPES/NAOH pH7.4, 140 mM NaCl, 2.5mM $CaCl_2$), stained with Annexin V FITC for 15 min at room temperature in the dark, then washed again and re-suspended in Annexin V binding buffer (200 µL/well) containing PI. Samples were analyzed immediately on a BD FACSCantoTM II.

Data availability

All data are included in the Supplementary Information or available from the authors, as are unique reagents used in this Article. The raw numbers for charts and graphs are available in the Source Data file whenever possible. Localization data are available on Zenodo (https://dx.doi.org/10.5281/zenodo.15552356).

Code Availability

Picasso can be downloaded from GitHub: https://github.com/jungmannlab/picasso. Oligomer analysis was performed with the Picasso module SPINNA[45].

References

1 Pavlasova, G. & Mraz, M. The regulation and function of CD20: an "enigma" of B-cell biology and targeted therapy. *Haematologica* **105**, 1494-1506 (2020). https://doi.org/10.3324/haematol.2019.243543

2 Tsao, L. C., Force, J. & Hartman, Z. C. Mechanisms of Therapeutic Antitumor Monoclonal Antibodies. *Cancer Res* **81**, 4641-4651 (2021). https://doi.org/10.1158/0008-5472.CAN-21-1109

3 Greenall, S. A. *et al.* Non-agonistic bivalent antibodies that promote c-MET degradation and inhibit tumor growth and others specific for tumor related c-MET. *PLoS One* **7**, e34658 (2012). https://doi.org/10.1371/journal.pone.0034658

4 Tebbutt, N., Pedersen, M. W. & Johns, T. G. Targeting the ERBB family in cancer: couples therapy. *Nat Rev Cancer* **13**, 663-673 (2013). https://doi.org/10.1038/nrc3559

5 Yu, X. *et al.* Complex Interplay between Epitope Specificity and Isotype Dictates the Biological Activity of Anti-human CD40 Antibodies. *Cancer Cell* **33**, 664-675 e664 (2018). https://doi.org/10.1016/j.ccell.2018.02.009

6 Jones, S. *et al.* Targeting of EGFR by a combination of antibodies mediates unconventional EGFR trafficking and degradation. *Sci Rep* **10**, 663 (2020). https://doi.org/10.1038/s41598-019-57153-9

7 Marshall, M. J. E., Stopforth, R. J. & Cragg, M. S. Therapeutic Antibodies: What Have We Learnt from Targeting CD20 and Where Are We Going? *Front Immunol* **8**, 1245 (2017). https://doi.org/10.3389/fimmu.2017.01245

8 Cragg, M. S. & Glennie, M. J. Antibody specificity controls in vivo effector mechanisms of anti-CD20 reagents. *Blood* **103**, 2738-2743 (2004). https://doi.org/10.1182/blood-2003-06-2031

9 Niederfellner, G. *et al.* Epitope characterization and crystal structure of GA101 provide insights into the molecular basis for type I/II distinction of CD20 antibodies. *Blood* **118**, 358-367 (2011). https://doi.org/10.1182/blood-2010-09-305847

10 Mossner, E. *et al.* Increasing the efficacy of CD20 antibody therapy through the engineering of a new type II anti-CD20 antibody with enhanced direct and immune effector cell-mediated B-cell cytotoxicity. *Blood* **115**, 4393-4402 (2010). https://doi.org/10.1182/blood-2009-06-225979

11 Kumar, A., Planchais, C., Fronzes, R., Mouquet, H. & Reyes, N. Binding mechanisms of therapeutic antibodies to human CD20. *Science* **369**, 793-799 (2020). https://doi.org/10.1126/science.abb8008

12 Rouge, L. *et al.* Structure of CD20 in complex with the therapeutic monoclonal antibody rituximab. *Science* **367**, 1224-1230 (2020). https://doi.org/10.1126/science.aaz9356

13 Klar, T. A., Jakobs, S., Dyba, M., Egner, A. & Hell, S. W. Fluorescence microscopy with diffraction resolution barrier broken by stimulated emission. *Proc Natl Acad Sci U S A* **97**, 8206-8210 (2000). https://doi.org/10.1073/pnas.97.15.8206

14 Rust, M. J., Bates, M. & Zhuang, X. Sub-diffraction-limit imaging by stochastic optical reconstruction microscopy (STORM). *Nat Methods* **3**, 793-795 (2006). https://doi.org/10.1038/nmeth929

15 Betzig, E. *et al.* Imaging intracellular fluorescent proteins at nanometer resolution. *Science* **313**, 1642-1645 (2006). https://doi.org/10.1126/science.1127344

16 Reinhardt, S. C. M. *et al.* Angstrom-resolution fluorescence microscopy. *Nature* **617**, 711-716 (2023). https://doi.org/10.1038/s41586-023-05925-9

17 Jungmann, R. *et al.* Single-molecule kinetics and super-resolution microscopy by fluorescence imaging of transient binding on DNA origami. *Nano Lett* **10**, 4756-4761 (2010). https://doi.org/10.1021/nl103427w

18 Schnitzbauer, J., Strauss, M. T., Schlichthaerle, T., Schueder, F. & Jungmann, R. Super-resolution microscopy with DNA-PAINT. *Nat Protoc* **12**, 1198-1228 (2017). https://doi.org/10.1038/nprot.2017.024

19 Gotzke, H. *et al.* The ALFA-tag is a highly versatile tool for nanobody-based bioscience applications. *Nat Commun* **10**, 4403 (2019). https://doi.org/10.1038/s41467-019-12301-7

20 Ester, M., Kriegel, H.-P., Sander, J. & Xu, X. in *Proceedings of the Second International Conference on Knowledge Discovery and Data Mining* 226–231 (AAAI Press, Portland, Oregon, 1996).

21 Zhang, X. *et al.* 3D Structural Fluctuation of IgG1 Antibody Revealed by Individual Particle Electron Tomography. *Sci Rep* **5**, 9803 (2015). https://doi.org/10.1038/srep09803

22 Shaw, A. *et al.* Binding to nanopatterned antigens is dominated by the spatial tolerance of antibodies. *Nat Nanotechnol* **14**, 184-190 (2019). https://doi.org/10.1038/s41565-018-0336-3

23 Diebolder, C. A. *et al.* Complement is activated by IgG hexamers assembled at the cell surface. *Science* **343**, 1260-1263 (2014). https://doi.org/10.1126/science.1248943

24 Bacac, M. *et al.* CD20-TCB with Obinutuzumab Pretreatment as Next-Generation Treatment of Hematologic Malignancies. *Clin Cancer Res* **24**, 4785-4797 (2018). https://doi.org/10.1158/1078-0432.CCR-18-0455

25 Teeling, J. L. *et al.* Characterization of new human CD20 monoclonal antibodies with potent cytolytic activity against non-Hodgkin lymphomas. *Blood* **104**, 1793-1800 (2004). https://doi.org/10.1182/blood-2004-01-0039

26 Pawluczkowycz, A. W. *et al.* Binding of submaximal C1q promotes complement-dependent cytotoxicity (CDC) of B cells opsonized with anti-CD20 mAbs ofatumumab (OFA) or rituximab (RTX): considerably higher levels of CDC are induced by OFA than by RTX. *J Immunol* **183**, 749-758 (2009). https://doi.org/10.4049/jimmunol.0900632

27 Bondza, S. *et al.* Complement-Dependent Activity of CD20-Specific IgG Correlates With Bivalent Antigen Binding and C1q Binding Strength. *Front Immunol* **11**, 609941 (2020). https://doi.org/10.3389/fimmu.2020.609941

28 Franke, A., Niederfellner, G. J., Klein, C. & Burtscher, H. Antibodies against CD20 or B-cell receptor induce similar transcription patterns in human lymphoma cell lines. *PLoS One* **6**, e16596 (2011). https://doi.org/10.1371/journal.pone.0016596

29 Edelmann, J. *et al.* Rituximab and obinutuzumab differentially hijack the B cell receptor and NOTCH1 signaling pathways. *iScience* **24**, 102089 (2021). https://doi.org/10.1016/j.isci.2021.102089

30 Nguyen, T. T. *et al.* Efficacy and safety of add-on anti-CD20 monoclonal antibody to Bruton tyrosine kinase inhibitor treatment for chronic lymphocytic leukemia: a meta-analysis. *Sci Rep* **13**, 9775 (2023). https://doi.org/10.1038/s41598-023-36279-x

31 Strasser, J. *et al.* Unraveling the Macromolecular Pathways of IgG Oligomerization and Complement Activation on Antigenic Surfaces. *Nano Lett* **19**, 4787-4796 (2019). https://doi.org/10.1021/acs.nanolett.9b02220

32 Abendstein, L. *et al.* DNA Nanostructure-Templated Antibody Complexes Provide Insights into the Geometric Requirements of Human Complement Cascade Activation. *J Am Chem Soc* **146**, 13455-13466 (2024). https://doi.org/10.1021/jacs.4c02772

33 Mortensen, S. A. *et al.* Structure and activation of C1, the complex initiating the classical pathway of the complement cascade. *Proc Natl Acad Sci U S A* **114**, 986-991 (2017). https://doi.org/10.1073/pnas.1616998114

34 Reid, K. B. M. Complement Component C1q: Historical Perspective of a Functionally Versatile, and Structurally Unusual, Serum Protein. *Front Immunol* **9**, 764 (2018). https://doi.org/10.3389/fimmu.2018.00764

35 Gwosch, K. C. *et al.* MINFLUX nanoscopy delivers 3D multicolor nanometer resolution in cells. *Nat Methods* **17**, 217-224 (2020). https://doi.org/10.1038/s41592-019-0688-0

36 Balzarotti, F. *et al.* Nanometer resolution imaging and tracking of fluorescent molecules with minimal photon fluxes. *Science* **355**, 606-612 (2017). https://doi.org/10.1126/science.aak9913

37 Masullo, L. A. *et al.* An alternative to MINFLUX that enables nanometer resolution in a confocal microscope. *Light Sci Appl* **11**, 199 (2022). https://doi.org/10.1038/s41377-022-00896-4

38 Sahl, S. J. *et al.* Direct optical measurement of intramolecular distances with angstrom precision. *Science* **386**, 180-187 (2024). https://doi.org/10.1126/science.adj7368

39 Weber, M. *et al.* MINSTED fluorescence localization and nanoscopy. *Nat Photonics* **15**, 361-366 (2021). https://doi.org/10.1038/s41566-021-00774-2

40 Ostersehlt, L. M. *et al.* DNA-PAINT MINFLUX nanoscopy. *Nat Methods* **19**, 1072-1075 (2022). https://doi.org/10.1038/s41592-022-01577-1

41 Li, B. *et al.* Characterization of a rituximab variant with potent antitumor activity against rituximab-resistant B-cell lymphoma. *Blood* **114**, 5007-5015 (2009). https://doi.org/10.1182/blood-2009-06-225474

42 Huang, B., Wang, W., Bates, M. & Zhuang, X. Three-dimensional super-resolution imaging by stochastic optical reconstruction microscopy. *Science* **319**, 810-813 (2008). https://doi.org/10.1126/science.1153529

43 Edelstein, A. D. *et al.* Advanced methods of microscope control using muManager software. *J Biol Methods* **1** (2014). https://doi.org/10.14440/jbm.2014.36

44 Hellmeier, J. *et al.* Quantification of absolute labeling efficiency at the single-protein level. *Nat Methods* **21**, 1702-1707 (2024). https://doi.org/10.1038/s41592-024-02242-5

45 Masullo, L. A. *et al.* Spatial and stoichiometric in situ analysis of biomolecular oligomerization at single-protein resolution. *Nat Commun* **16**, 4202 (2025). https://doi.org/10.1038/s41467-025-59500-z

Acknowledgements

We thank Cindy Schulenburg for expressing ALFA-tagged versions of Rituximab and Obinutuzumab. Therapeutic antibodies were provided by Roche Glycart. This research was funded in part by the European Research Council through an ERC Consolidator Grant (ReceptorPAINT, Grant agreement number 101003275, R.J.), the BMBF (Project IMAGINE, FKZ: 13N15990, R.J.), the Volkswagen Foundation through the initiative ‘Life?—A Fresh

Scientific Approach to the Basic Principles of Life' (grant no. 98198, R.J.), the Max Planck Foundation, and the Max Planck Society. IP and SCMR acknowledge support by the IMPRS-ML graduate school. LAM acknowledges a postdoctoral fellowship from the European Union's Horizon 20212022 research and innovation program under Marie Skłodowska-Curie grant agreement no. 101065980. O.S. acknowledges support from the Czech Science Foundation grant no. 24-12553O. Molecular graphics were generated with UCSF ChimeraX, developed by the Resource for Biocomputing, Visualization, and Informatics at the University of California, San Francisco, with support from National Institutes of Health R01-GM129325 and the Office of Cyber Infrastructure and Computational Biology, National Institute of Allergy and Infectious Diseases. Part of the schematics were generated with the help of BioRender (www.biorender.com).

Author contributions

I.P. conceived and performed all experiments except the functional studies, designed analysis software and analyzed the data. L.A.M. designed and wrote the analysis software and analyzed the data. S.C.M.R. wrote analysis software. J.K. produced DNA-conjugated labeling reagents. O.S. expressed and purified the SpA-B protein. M.L., S.H. and M.B. designed and performed functional studies. C.K. contributed to the design of studies targeting CD20 and interpretation. I.P., L.A.M., and R.J. interpreted data and wrote the manuscript. R.J. conceived and supervised the study. All authors reviewed and approved the final manuscript.

Competing interests

M.L., S.H., M.B. and C.K. declare employment, patents (unrelated to this work), and stock ownership with Roche. The other authors declare no competing interests.

Figures

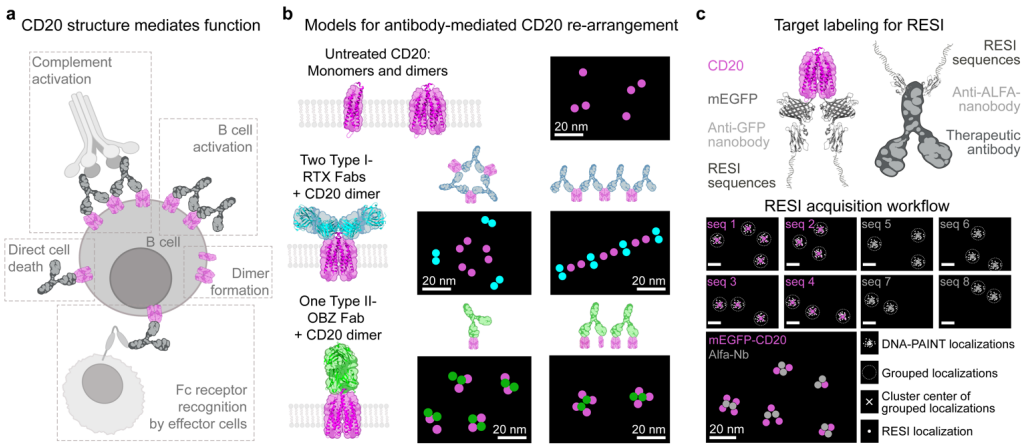

Fig. 1 | Assessing the structure-function relationship of anti-CD20 therapeutic antibodies in the cellular context using RESI microscopy. **a**, The structural configuration of CD20 proteins and their interactions with therapeutic antibodies on the cell membrane influence the therapeutic efficacy of the antibodies. **b**, CD20 proteins (magenta) in the membrane exist as a mixture of monomers and pre-formed dimers[1]. Rituximab (RTX) (cyan) can bind with 2 Fabs per CD20 dimer, thereby inducing higher-order arrangements of CD20 dimers[2,3]. However, the quantitative nature of the 3D cluster organization is still unknown. In contrast, Obinutuzumab (OBZ) (green) can bind with one Fab per single CD20 dimer, suggesting a terminal complex of up to CD20 tetramers by bridging two CD20 dimers. However, the resulting structural organization of CD20 – potentially forming monomers, dimers, trimers, or tetramers – remains to be fully elucidated. **c,** We use two-target RESI super-resolution microscopy with four rounds per target to visualize and correlate the locations of mEGFP-tagged CD20 and ALFA-tagged therapeutic antibodies at single-protein resolution (sub-5 nm). CD20 is labeled in 1:1 stoichiometry and mAbs are labeled in a 2:1 stoichiometry. By performing eight consecutive DNA-PAINT imaging rounds and clustering localizations, we achieve precise RESI localizations (σ ≈ 0.6 nm) of the targets in their cellular context. Created with the help of BioRender (https://BioRender.com/y76v9f4 and https://BioRender.com/5575210)

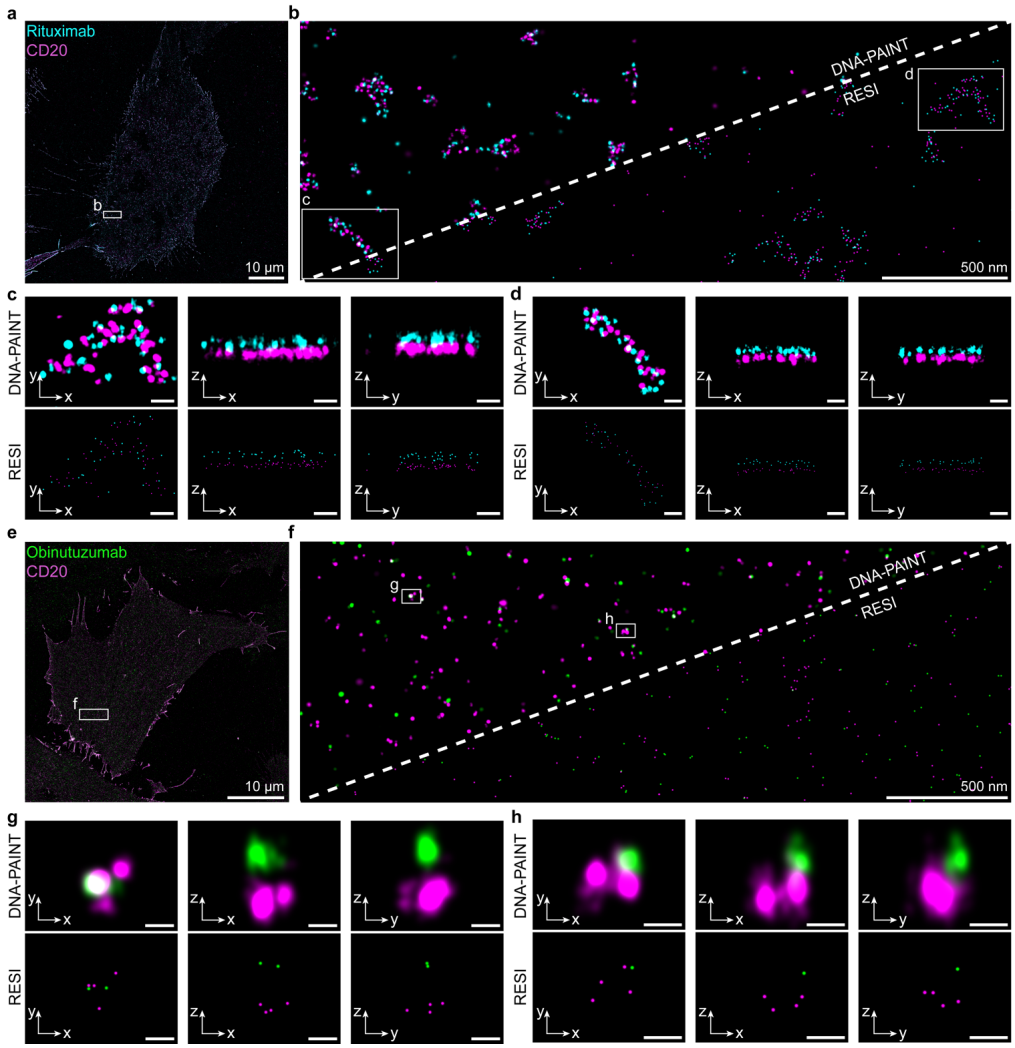

Fig. 2 | Super-resolution imaging of CD20-therapeutic antibody complexes using RESI. Imaging of cells treated with Rituximab (**a**) and Obinutuzumab (**e**) shows the distribution of CD20 and these therapeutic antibodies. Rituximab (cyan) colocalizes with CD20 (magenta), forming distinct higher-order structures on the cell membrane. In contrast, Obinutuzumab (green) and CD20 colocalize, yet appear homogeneously distributed without forming such structures. Transitioning from DNA-PAINT super-resolution (left side of dashed line) to RESI resolution (right side of dashed line) allows visualization of individual proteins in complexes. In (**b**), Rituximab-CD20 complexes exhibit clustered formations, while in (**f**), Obinutuzumab-CD20 complexes appear as few colocalizing molecules without evident higher-order clustering. 3D rotational views of the complexes reveal further structural details. For Rituximab-CD20 complexes (**c**, **d**), the 3D view shows that clusters are generally planar, suggesting a two-dimensional organization in the cell membrane. In contrast, Obinutuzumab-CD20 complexes (**g**, **h**) show up to four CD20 molecules colocalized with a single Obinutuzumab molecule, lacking the distinct planar higher-order structures observed in Rituximab-treated cells. Images are representative of three independent experiments. Scale bars in (**c**, **d**): 50 nm. Scale bars in (**g**, **h**): 20 nm.

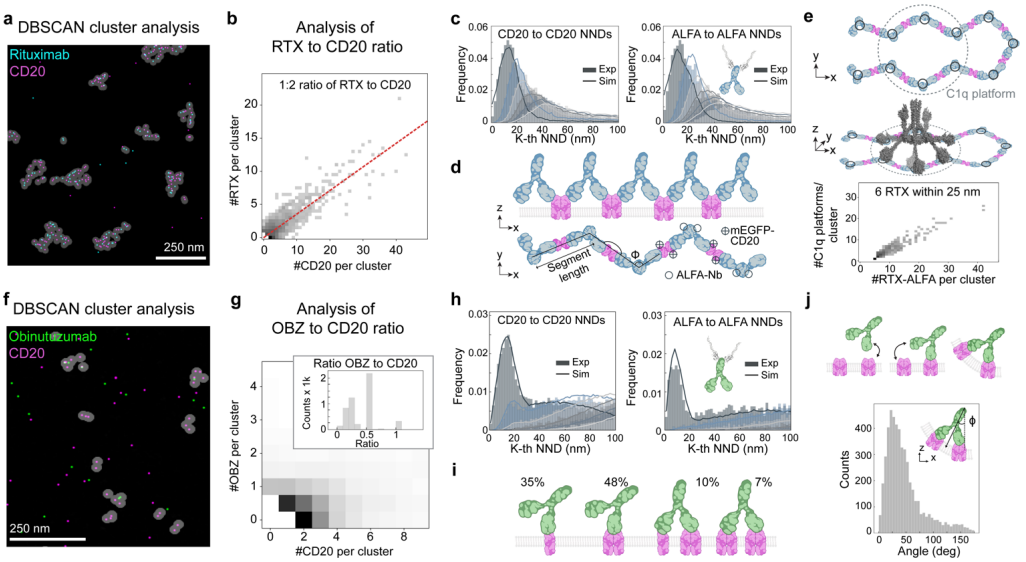

Fig. 3 | Quantitative analysis and structural modeling of therapeutic antibody-CD20 complexes a, DBSCAN analysis (marked in gray) of RTX (cyan)-CD20 (magenta) clusters shows distinct higher-order structures in 2D. **b,** Quantitative analysis in 2D reveals a linear relationship between the number of RTX molecules and CD20 dimers. Two ALFA-Nbs correspond to one RTX per cluster. A linear fit yields 0.38, suggesting that approximately one RTX binds per CD20 dimer, when correcting for the labeling efficiency (for details, see Methods). **c,** Nearest-Neighbor Distance (NND) analysis indicates a higher-order organization, which can be modeled by a flexible-chain arrangement. **d,** The model includes anchor points at the RTX hinge regions, linear segments connecting these points, CD20 dimers located centrally along these segments and ALFA-Nbs located at the hinge regions. **e,** The flexible-chain model can explain how RTX-CD20 interactions lead to the formation of U-shaped clusters to facilitate C1q binding. The number of hexameric RTX platforms was determined by counting each possible binding configuration of C1q (see Methods). **f,** DBSCAN cluster analysis for OBZ (green) with CD20 in 2D shows smaller clusters compared to RTX-CD20. **g,** Quantitative analysis reveals specific OBZ to CD20 stoichiometries, without a linear relationship between the number of OBZ and CD20 molecules. Two ALFA-Nbs correspond to one OBZ per cluster. **h,** NND analysis for CD20 complexes suggests that CD20 does not form higher-order structures beyond tetramers at the cell surface. NND analysis of the ALFA-Nbs labeling OBZ reveals only a first NND peak, representing two ALFA-Nbs bound per single OBZ. The absence of a second NND peak excludes a higher-order arrangement of OBZ-CD20 clusters. **i,** Simulations with CD20 monomers, dimers, trimers and tetramers, taking into account the labeling efficiency of the GFP-Nb, for this representative cell result in 35 % monomers, 48 % dimers, 10 % trimers and 7 % tetramers after OBZ treatment. **j,** We observe a 25° angle between OBZ bound to CD20 and the xy-plane of the cell membrane, suggesting the necessity of membrane bending to allow for OBZ binding to CD20 with two Fab arms simultaneously. Created with the help of BioRender (https://BioRender.com/y76v9f4 and https://BioRender.com/5575210).

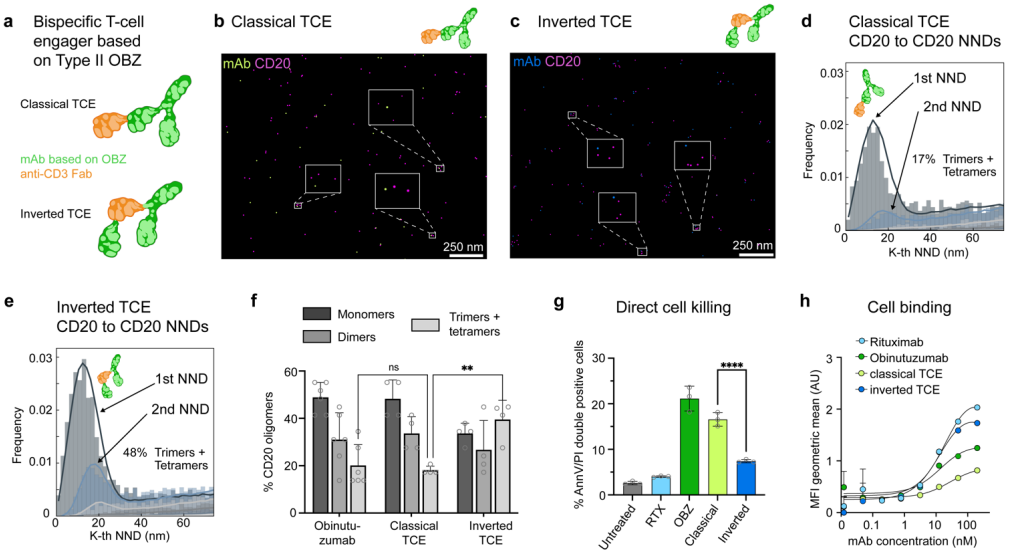

Fig. 4 | Assessing the structure-function relationship of anti-CD20 antibodies. a, Schematic representation of CD20-CD3 TCE configurations: classical (c-TCE) and inverted (i-TCE), featuring an anti-CD20 monoclonal antibody (mAb) based on OBZ and an anti-CD3 Fab fragment at two different positions in the molecule. **b** and **c,** RESI images of mAb-CD20 clusters when treated with c-TCE (b) and i-TCE (c). **d** and **e,** Nearest-Neighbor Distance (NND) analysis of CD20 clusters treated with c-TCE (d) and i-TCE (e), showing increased frequencies of non-random sub-25-nm distances in the second and third NND histograms for i-TCE. Least-squares fit (solid lines) of monomers, dimers, trimers and tetramers shows an increased trimer- and tetramerization for i-TCE compared to c-TCE. **f,** Bar graph depicting the percentage of CD20 oligomers in monomeric, dimeric, and higher-order forms (trimers and tetramers) for OBZ, c-TCE, and i-TCE. The frequency of trimers and tetramers is increased for i-TCE compared to c-TCE. The bars and error bars represent the mean and standard deviation, respectively. The number of biological replicates is n(OBZ)=3, n(c-TCE)=n(i-TCE)=4. Statistical significance was tested using a two-way ANOVA, adjusting for multiple comparisons (p=0.0027). Source data are provided as a Source Data file. **g,** Direct cell killing assay of CD20-positive Raji cells in untreated condition, and upon treatment with untagged versions of Rituximab (RTX), Obinutuzumab (OBZ), c-TCE, and i-TCE. i-TCE has a reduced killing efficiency compared to c-TCE, approaching values for Type I-RTX. The number of biological replicates is n=3. The height of the bar and error bars represent mean and standard deviation, respectively. Statistical significance was tested using a one-way ANOVA, adjusting for multiple comparisons (p<0.0001). Source data are provided as a Source Data file. **h,** Graph depicting cell binding affinity in Raji cells across a range of mAb concentrations (0.01 to 100 nM) for untagged versions of RTX, OBZ, c-TCE, and i-TCE, measured as Mean Fluorescence Intensity (MFI) geometric mean. The results show an increased binding for i-TCE compared to c-TCE. The data points and error bars represent mean and standard deviation, respectively. The number of biological replicates is n=3. Source data are provided as a Source Data file. Created with the help of BioRender (https://BioRender.com/y76v9f4 and https://BioRender.com/5575210).

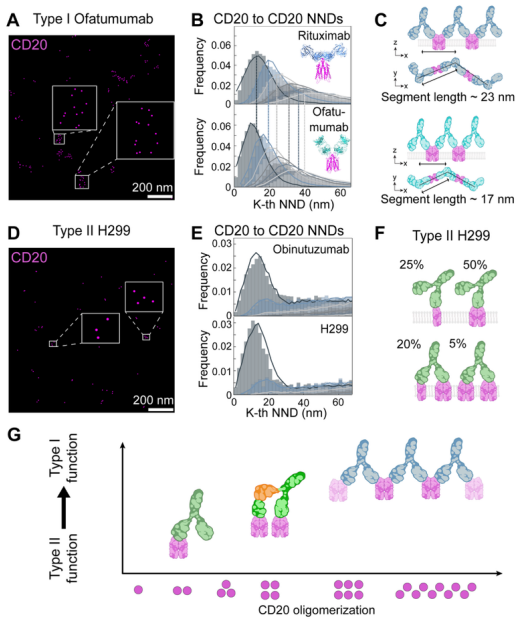

Fig. 5 | 2-plex RESI imaging and quantitative analysis shows a structure-function relationship of Type I and Type II anti-CD20 therapeutic antibodies. a, RESI image of CD20 treated with Type I Ofatumumab shows higher-order CD20 arrangements. **b,** NND analysis (histogram) and fitting with CD20-flexible chain model (solid line). Image is representative of three independent experiments. **c,** Type I Ofatumumab forms flexible chains with a shorter segment length than Rituximab, i.e. 17±2 nm. **d,** RESI image of CD20 treated with Type II H299 (clone used for therapeutic antibody Tositumomab) shows limited CD20 oligomerization. Image is representative of three independent experiments. **e,** NND analysis (histogram) and fitting with a model of monomers, dimers, trimers and tetramers (solid line). **f,** Type II H299 forms oligomers similarly to Obinutuzumab. **g,** Correlation of CD20 Type I or Type II-like function with CD20 oligomerization. Created with the help of BioRender (https://BioRender.com/y76v9f4 and https://BioRender.com/5575210)

Supplementary Information

Resolving the structural basis of therapeutic antibody function in cancer immunotherapy with RESI

Isabelle Pachmayr[1,2], Luciano A. Masullo[1], Susanne C.M. Reinhardt[1,3], Jisoo Kwon[1], Maite Llop[4], Ondřej Skořepa[1,5], Sylvia Herter[4], Marina Bacac[4], Christian Klein[2,4], Ralf Jungmann[1,3,*]

[1]Max Planck Institute of Biochemistry, Planegg, Germany, [2]Department of Biochemistry, Ludwig Maximilian University, Munich, Germany, [3]Faculty of Physics and Center for Nanoscience, Ludwig Maximilian University, Munich, Germany, [4]Roche Innovation Center Zurich, Roche Pharma and Early Development, Schlieren, Switzerland, [5]Department of Biochemistry, Charles University, Prague, Czech Republic. Correspondence should be addressed to R.J. (jungmann@biochem.mpg.de)

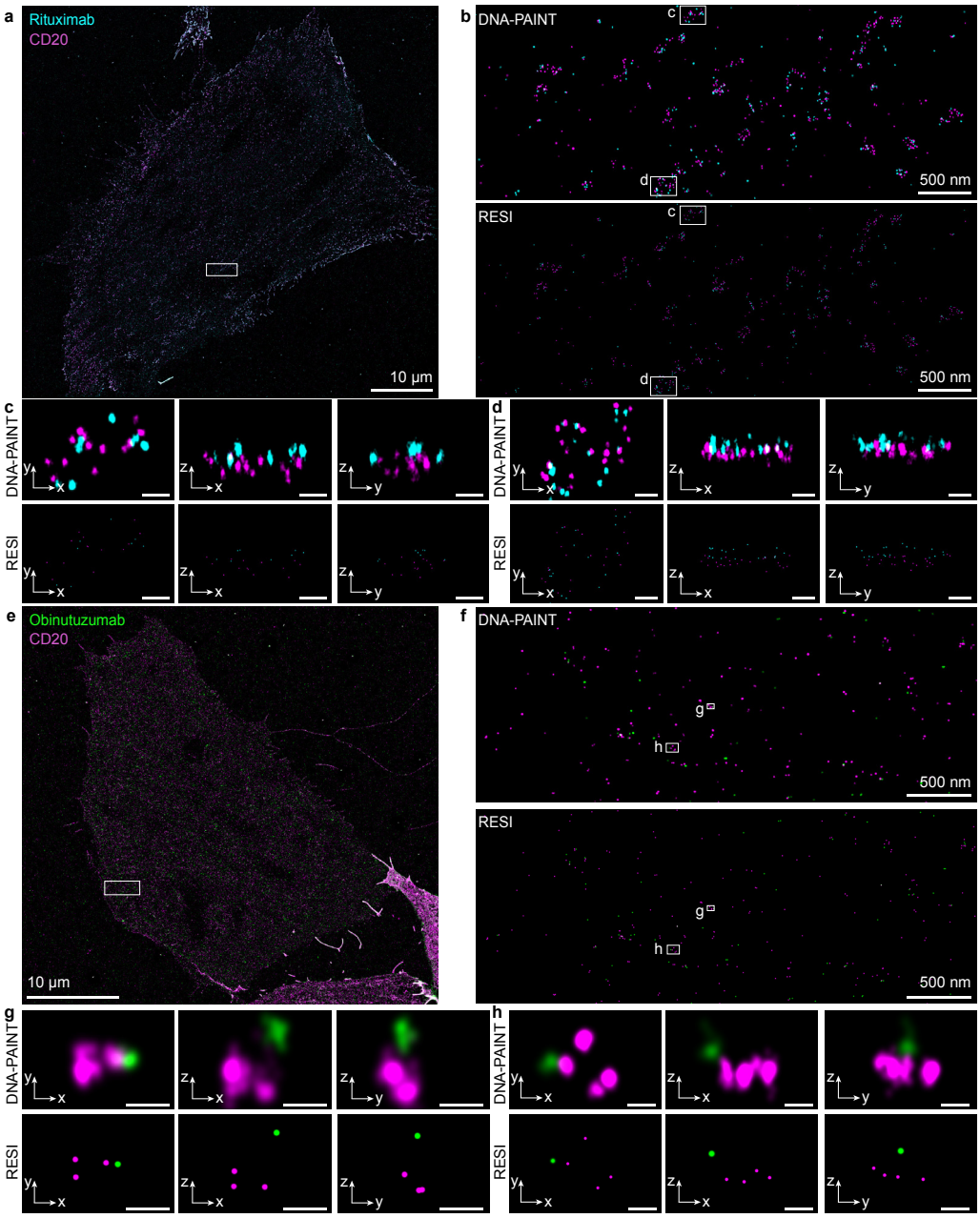
a
Rituximab
CD20
10 µm
b
DNA-PAINT
c
d
500 nm
RESI
c
d
500 nm
c
DNA-PAINT
RESI
d
DNA-PAINT
RESI
e
Obinutuzumab
CD20
10 µm
f
DNA-PAINT
g
h
500 nm
RESI
g
h
500 nm
g
DNA-PAINT
RESI
h
DNA-PAINT
RESI

Supplementary Fig. 1 | Replicate for super-resolution imaging of CD20-therapeutic antibody complexes using RESI. **a**, DNA-PAINT imaging shows that Rituximab (RTX) (cyan) colocalizes with CD20 (magenta), forming distinct higher-order structures. **b**, RTX-CD20 complexes exhibit clustered formations. RESI resolution allows visualization of individual proteins. **c** and **d**, 3D view of individual RTX-CD20 complexes. **e**, DNA-PAINT imaging shows that Obinutuzumab (OBZ) (green) and CD20 (magenta), are homogeneously distributed in the cell. **f**, Transitioning from DNA-PAINT super-resolution to RESI resolution allows visualization of OBZ-CD20 complexes without evident higher-order clustering. **g** and **h**, 3D view of individual OBZ-CD20 complexes, lacking the distinct planar higher-order structures observed in RTX-treated cells. Scale bars in (**c**, **d**): 50 nm. Scale bars in (**g**, **h**): 20 nm.

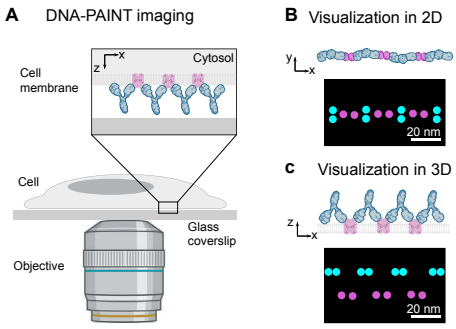

Supplementary Fig. 2 | Visualization of mAb-CD20 complexes in adherent cells. a, DNA-PAINT imaging with an inverted microscope. **b,** For 2D visualization, images are displayed in the x-y-plane. **c,** For 3D visualization, images are rotated around the x-axis. Created with the help of BioRender (https://BioRender.com/y76v9f4 and https://BioRender.com/5575210)

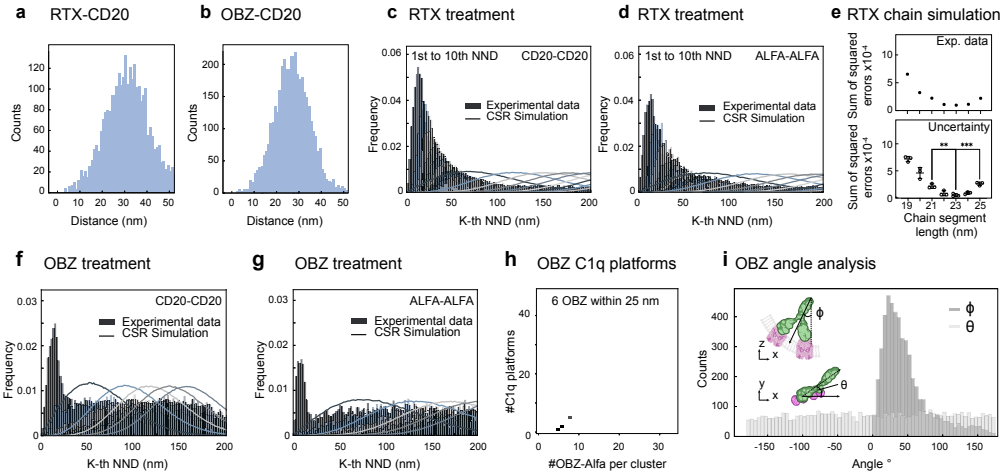

Supplementary Fig. 3 | Quantitative analysis of therapeutic Antibody-CD20 complexes. a, Axial RTX to CD20 distances within RTX-CD20 complexes are 32 nm ± 11 nm (mean ± std). **b,** Axial OBZ to CD20 distances within OBZ-CD20 complexes are 27 nm ± 9 nm (mean ± std). **c,** Nearest-Neighbor Distance (NND) analysis of CD20 after RTX treatment shows non-CSR distributions for all shown NNDs. **d,** Nearest-Neighbor Distance (NND) analysis of ALFA-Nbs after RTX treatment shows non-CSR distributions for all shown NNDs. **e**, Optimizing the chain segment length in the flexible-chain model by calculating the sum of squared errors yields a chain segment length of 23 nm ± 2 nm. Monte-Carlo simulations (bottom) reveal an uncertainty of ± 2 nm. Centered vertical lines represent the means, and the error bars represent the standard deviations. Statistical significance was assessed using an unpaired t-test, with $p_{21,23}$=0.0043 and $p_{23,25}$=0.009. **f,** NND analysis of CD20 after OBZ treatment shows non-CSR distributions for 1st to 3rd NNDs. **g,** NND analysis of ALFA-Nb after OBZ treatment of CD20 shows non-CSR distribution for 1st NNDs only. **h**, C1q platform analysis for OBZ shows almost no platforms as most OBZ clusters are < 6 OBZ. **i,** Angle analysis for OBZ-CD20 clusters shows a 25° angle for ϕ (like in **Fig. 3**) and a random angle for θ. Created with the help of BioRender (https://BioRender.com/y76v9f4 and https://BioRender.com/5575210)

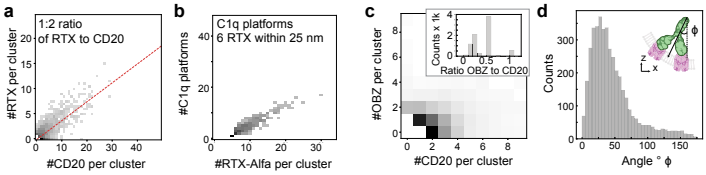

Supplementary Fig. 4 | Replicate for quantitative analysis of therapeutic antibody-CD20 complexes. a, Quantitative analysis of RTX-CD20 clusters reveals a linear relationship between the number of RTX molecules and CD20 dimers, suggesting that approximately one RTX molecule binds per CD20 dimer. **b**, There are multiple C1q-binding platforms within RTX-CD20 clusters, featuring at least 6 RTX within 25 nm. **c**, Quantitative analysis of OBZ-CD20 clusters reveals specific OBZ to CD20 stoichiometries, without a linear relationship between the number of OBZ and CD20 molecules. **d**, OBZ is bound to CD20 in a 25° angle over the xy-plane of the cell membrane. Created with the help of BioRender (https://BioRender.com/y76v9f4 and https://BioRender.com/5575210)

a DNA-PAINT and RESI NNDs after RTX-treatment

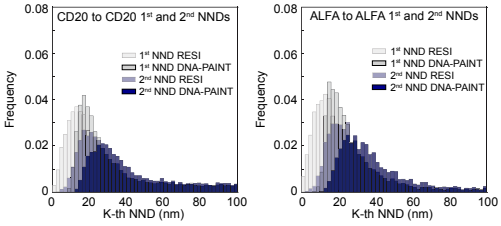

b DNA-PAINT and RESI NNDs after OBZ-treatment

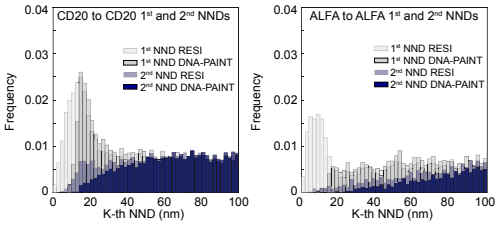

Supplementary Fig. 5 | NND analysis of DNA-PAINT and RESI data for RTX and OBZ treated cells. a, CD20 to CD20 and ALFA to ALFA NNDs obtained from analysis of DNA-PAINT and RESI data of RTX-ALFA-treated cells. Only first and second NNDs are displayed for clarity. The RESI NND histograms (high opacity) and the DNA-PAINT histograms (low opacity) are directly compared in one plot. After RTX treatment, DNA-PAINT NND data of CD20 shows first and second NND peaks (left). However, the resolution limit in DNA-PAINT limits the detection of sub-10 nm distances for the first NND. Only with RESI, these sub-10 nm distances are detected. Similar observations can be made for the ALFA to ALFA NNDs (right). **b**, CD20 to CD20 NNDs (left) and ALFA to ALFA NNDs (right) obtained from analysis of DNA-PAINT and RESI data of OBZ-ALFA-treated cells. Only first and second NNDs are displayed for clarity. The RESI NND histograms (high opacity) and the DNA-PAINT histograms (low opacity) are directly compared in one plot. After OBZ treatment, DNA-PAINT NND data of CD20 shows only a first NND peak. Only with RESI, a second NND peak, representing CD20 trimers and tetramers, can be detected. Sub-10 nm ALFA to ALFA NNDs for 2 ALFA-Nbs bound on one OBZ molecule (right) can only be detected with RESI but not with DNA-PAINT.

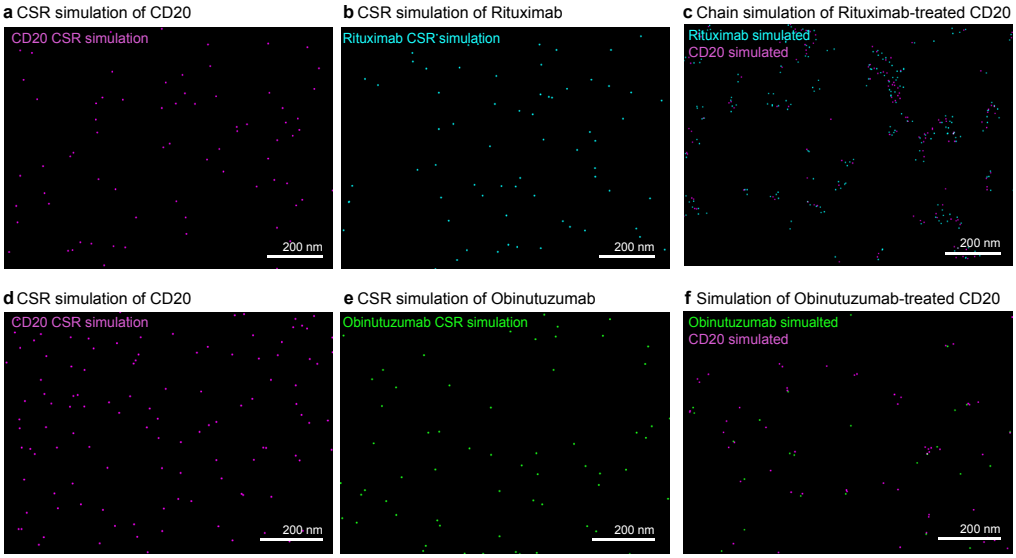

Supplementary Fig. 6 | Simulations of RTX-CD20 and OBZ-CD20 complexes for NND analysis. a, CSR monomer simulation of CD20 at the same density as measured in RESI data. **b**, CSR monomer simulation of ALFA labeling RTX at the same density as measured in RESI data. **c**, Chain simulation of CD20 and RTX with 23 nm chain segment length. **d**, CSR monomer simulation of CD20 at the same density as measured in RESI data. **e**, CSR monomer simulation of ALFA labeling OBZ at the same density as measured in RESI data. **f**, Simulation of OBZ bound to CD20 monomers, dimers, trimers and tetramers.

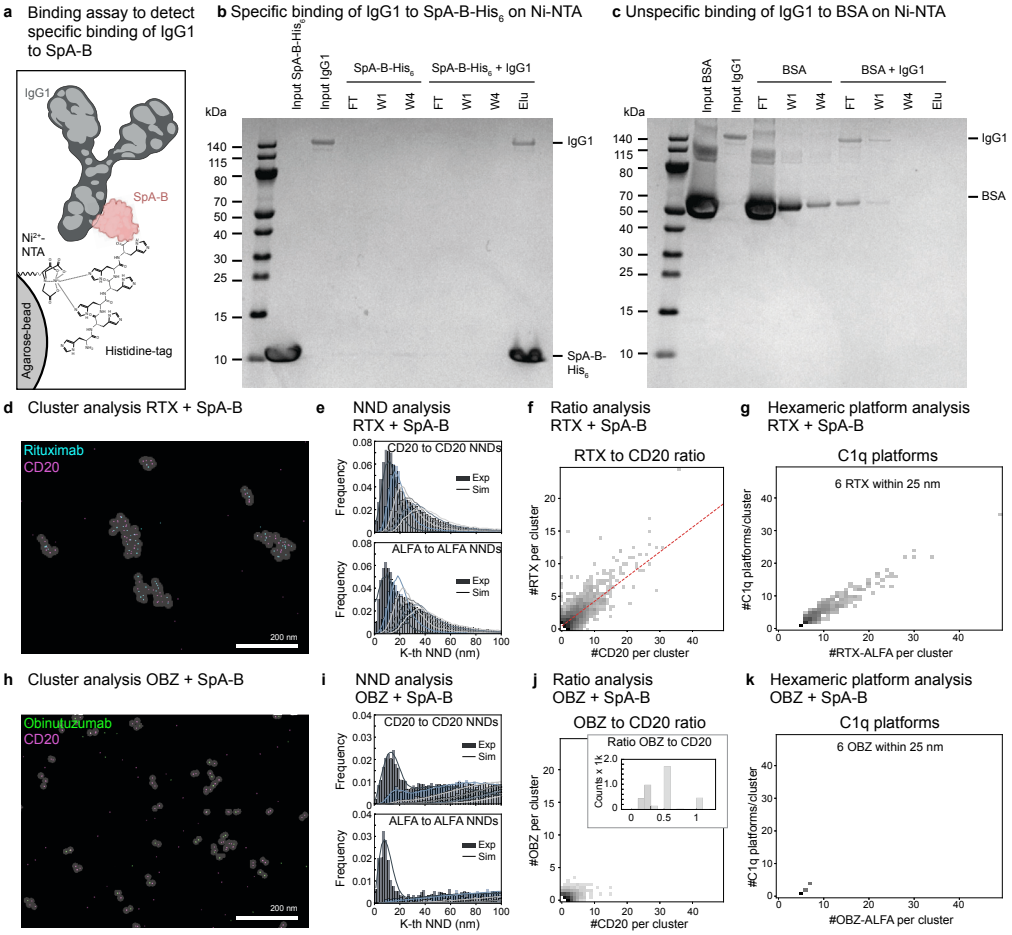

Supplementary Fig. 7 | CD20 and mAb organization upon Fc-Fc interaction blockade with SpA-B. a, Binding assay to test SpA-B binding to IgG1-Fc domain. SpA-B immobilized on Nickel-nitrilotriacetic acid (Ni-NTA) beads was incubated with IgG1. Created with the help of BioRender (https://BioRender.com/y76v9f4 and https://BioRender.com/5575210). **b**, SDS-PAGE analysis confirmed SpA-B binding to Ni-NTA beads, with no protein detected in flow-through (FT) and washes (W1, W4). After IgG1 incubation, neither SpA-B nor IgG1 were detected in FT or washes, indicating high-affinity binding. Elution confirmed specific binding of both proteins. **c**, SDS-PAGE of the negative control showed unspecific binding of BSA to Ni-NTA beads, as most protein appeared in FT and wash fractions. After IgG1 incubation, BSA and IgG1 were mostly detected in FT and washes, with no specific binding in elution. **d**, RESI imaging showed Rituximab (RTX)-CD20 clusters after SpA-B-blocked RTX treatment. DBSCAN analysis indicates similar higher-order structures to non-blocked samples. **e**, Nearest-Neighbor Distance (NND) analysis of blocked RTX-CD20 resembles non-blocked data, supported by flexible-chain simulations. **f**, Quantitative 2D cluster analysis indicates a linear relationship between RTX molecules and CD20 dimers. Two ALFA-Nbs corresponded to one RTX per cluster. When corrected for labeling efficiencies, this suggested ~1 RTX per CD20 dimer. g, Hexameric C1q platforms were equally detected in blocked and non-blocked RTX-CD20 samples. **h**, RESI imaging after SpA-B-blocked Obinutuzumab (OBZ) treatment showed dispersed clusters similar to non-blocked samples. **i**, NND analysis of blocked OBZ-CD20 identified peaks consistent with monomer to tetramer arrangements. NNDs of ALFA-Nbs labeling OBZ exluded higher-order clustering. **j**, Quantitative analysis revealed distinct OBZ-to-CD20 stoichiometries without linear relationships. Two ALFA-Nbs are displayed as one OBZ per cluster. **k**, Few C1q platforms were detected in OBZ-CD20 clusters, similar to non-blocked OBZ.

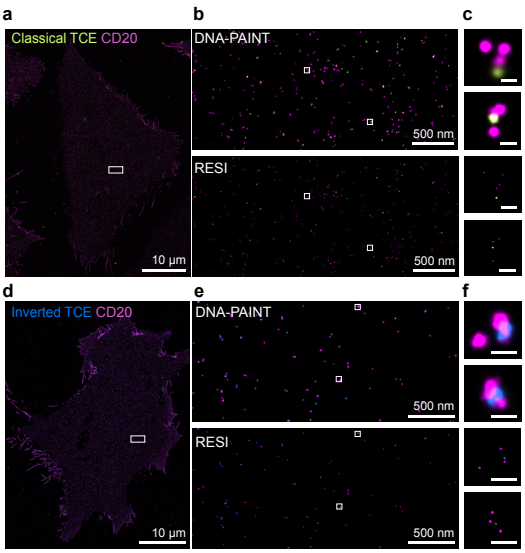

Supplementary Fig. 8 | Classical and inverted TCE bound to CD20. a, Whole cell DNA-PAINT image of c-TCE treated cells. **b,** Zoom in of c-TCE treated cells in DNA-PAINT (top) and RESI (bottom). **c,** Single c-TCE-CD20 complexes in DNA-PAINT and RESI (Scale bar: 20nm). **d,** Whole cell DNA-PAINT image of i-TCE treated cells. **e,** Zoom in of i-TCE treated cells in DNA-PAINT (top) and RESI (bottom). **f,** Single i-TCE-CD20 complexes in DNA-PAINT and RESI (Scale bar: 20nm).

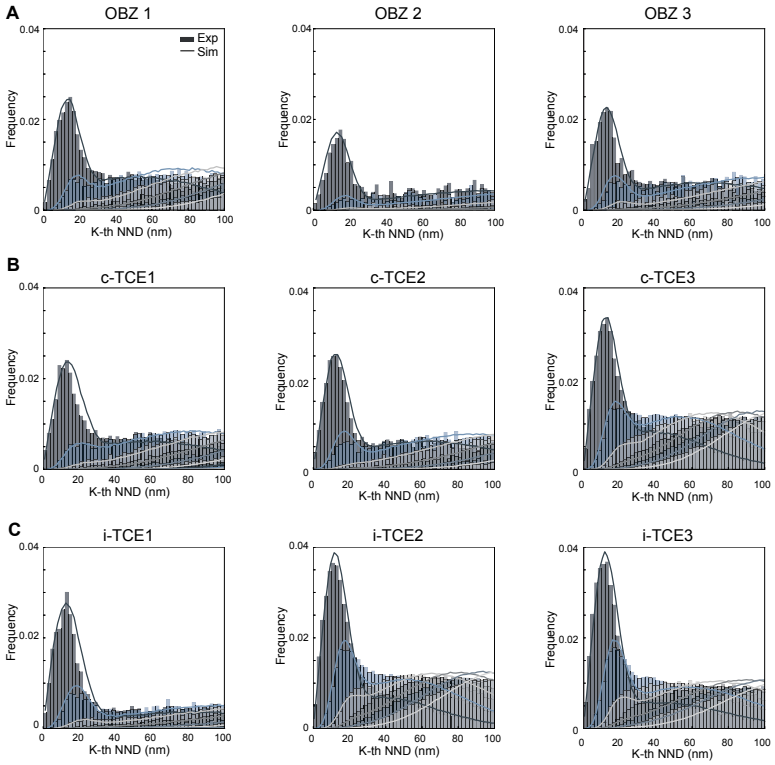

Supplementary Fig. 9 | Nearest-Neighbor Distance analysis of CD20 data upon mAb-treatment, depicting the low order oligomerization simulation results of Fig 4f. a, Three datasets of three individual OBZ-treated cells (Exp) with the simulation recapitulating the data (Sim). **b**, Three additional datasets of three individual c-TCE-treated cells (Exp) with the simulation recapitulating the data (Sim). **c**, Three additional datasets of three individual i-TCE-treated cells (Exp) with the simulation recapitulating the data (Sim).

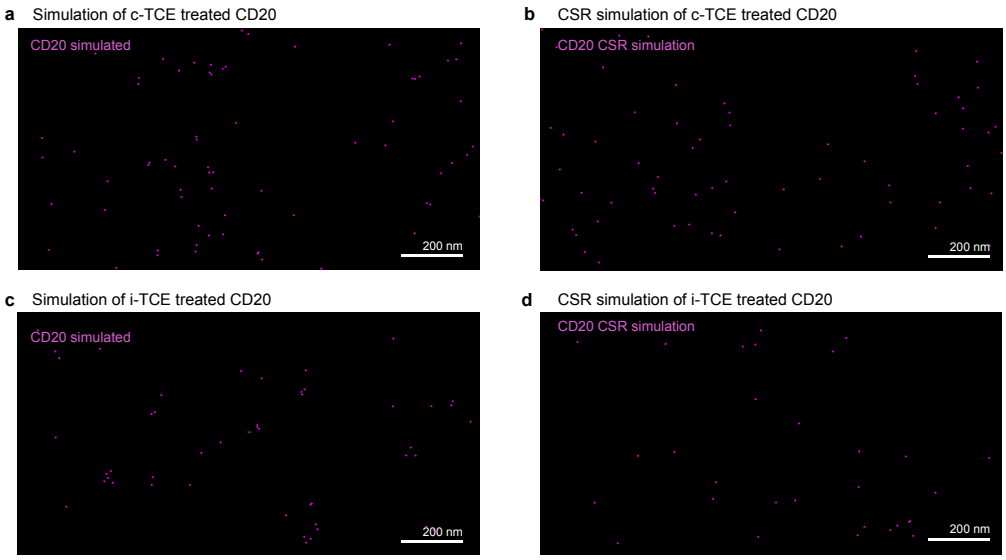

Supplementary Fig. 10 | Simulations of CD20 for NND analysis. a, Simulation of CD20 monomers, dimers, trimers and tetramers after c-TCE treatment. **b**, CSR monomer simulation of CD20 at the same density as measured for c-TCE treated CD20. **c**, Simulation of CD20 monomers, dimers, trimers and tetramers after i-TCE treatment. **d**, CSR monomer simulation of CD20 at the same density as measured for i-TCE treated CD20.

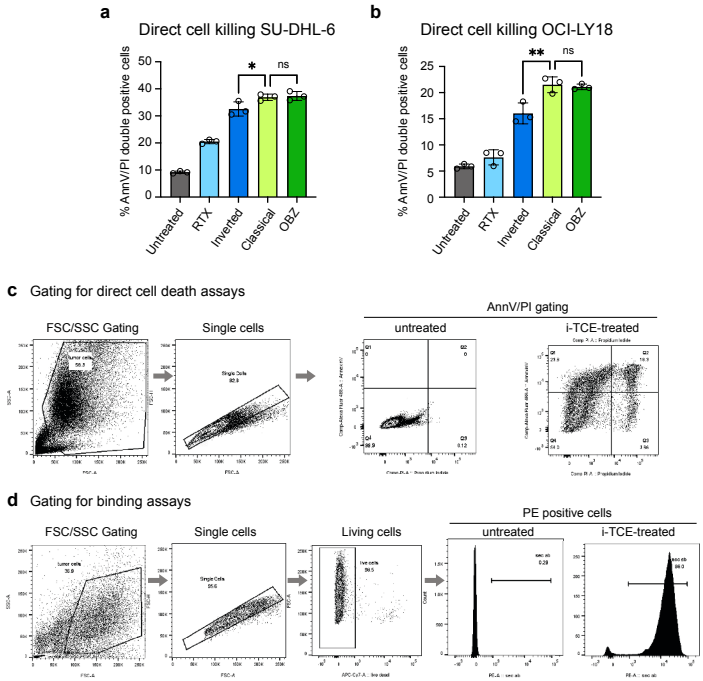

Supplementary Fig. 11 | Cell killing assays in CD20-positive cell lines. a, Direct cell killing FACS assay for untreated SU-DHL-6 cells, cells treated with Rituximab (RTX), classical TCE, inverted TCE and Obinutuzumab (OBZ). The results show a reduced killing efficiency for i-TCE vs c-TCE, trending toward values for Type I-RTX. The number of biological replicates is n=3. Statistical significance was tested using a one-way ANOVA, adjusting for multiple comparisons (p=0.0378). Source data are provided as a Source Data file. **b,** Direct cell killing FACS assay for untreated OCI-LY18 cells, cells treated with Rituximab (RTX), classical TCE, inverted TCE and Obinutuzumab (OBZ). The results show a reduced killing efficiency for i-TCE vs c-TCE, trending toward values for Type I-RTX. The number of biological replicates is n=3. Statistical significance was tested using a one-way ANOVA, adjusting for multiple comparisons (p=0.0037). Source data are provided as a Source Data file. **c,** Gating strategies for Fig. 4g. **d,** Gating strategies for Fig. 4h and Supplementary Fig. 11a,b.

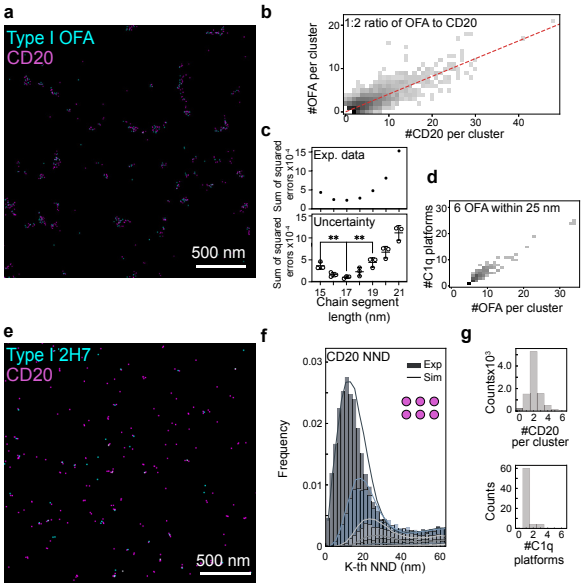

Supplementary Fig. 12 | Quantitative analysis of Type I therapeutic Antibody-CD20 complexes. a, RESI image of OFA-treated cells. **b,** Quantitative analysis of OFA-CD20 clusters reveals a linear relationship between the number of OFA molecules and CD20 dimers, suggesting that approximately one OFA molecule binds per CD20 dimer. **c,** Optimizing the chain segment length in the flexible-chain model by calculating the sum of squared errors yields a chain segment length of 17±2 nm. Monte-Carlo simulations (bottom) reveal an uncertainty of ±2 nm. Centered vertical lines represent the means, and the error bars represent the standard deviations. Statistical significance was assessed using an unpaired t-test, resulting in $p_{15,17}$=0.0063 and $p_{17,19}$=0.0064. **d,** Hexameric OFA platforms could facilitate complement component 1q (C1q) binding. **e,** RESI image of Type I 2H7-treated cells. **f,** NND analysis for CD20 complexes after 2H7-treatment shows linear chain-like hexameric CD20 complexes. **g,** The number of CD20 per cluster and the number of C1q platforms per cluster suggests the presence of CD20 hexamers after 2H7 treatment.

Supplementary Tables

Supplementary Table 1 | DNA-PAINT docking and imager sequences

Identity	Docking sequence	Imager sequence
5xR1	TCCTCCTCCTCCTCCTCCT	AGGAGGA-Cy3B
5xR2	ACCACCACCACCACCACCA	TGGTGGT-Cy3B
7xR3	CTCTCTCTCTCTCTCTCTC	GAGAGAG-Cy3B
7xR4	ACACACACACACACACACA	TGTGTGT-Cy3B
5xR5	CTTCTTCTTCTTCTTCTTC	GAAGAA-Cy3B
5xR6	AACAACAACAACAACAACAA	TGTTGTT-Cy3B
5xL1	left-handed TCCTCCTCCTCCTCCTCCT	left-handed AGGAGGA-Cy3B
7xL4	left-handed ACACACACACACACACACA	left-handed TGTGTGT-Cy3B

Supplementary Table 2 | DNA-conjugated Nanobodies

Name	Docking sequence	Stock Concentration (μM)
Anti-GFP-Nb-5xR1	TCCTCCTCCTCCTCCTCCT	5
Anti-GFP-Nb-5xR2	ACCACCACCACCACCACCA	5
Anti-GFP-Nb-7xR3	CTCTCTCTCTCTCTCTCTC	5
Anti-GFP-Nb-7xR4	ACACACACACACACACACA	5
Anti-GFP-Nb-7xL3	left-handed CTCTCTCTCTCTCTCTCTC	10
Anti-ALFA-Nb-5xR5	CTTCTTCTTCTTCTTCTTC	5
Anti-ALFA-Nb-5xR6	AACAACAACAACAACAACAA	5
Anti-ALFA-Nb-5xL1	left-handed TCCTCCTCCTCCTCCTCCT	10
Anti-ALFA-Nb-7xL4	left-handed ACACACACACACACACACA	10
Anti-human-IgG-Nb-7xR3 (2F2)	CTCTCTCTCTCTCTCTCTC	5
Anti-human-IgG-Nb-7xR3 (2H5)	CTCTCTCTCTCTCTCTCTC	5
Anti-mouse kappa light chain-Nb-7xR3	CTCTCTCTCTCTCTCTCTC	5

Supplementary Table 3 | Antibodies and Nanobodies

Name	Target	Format	Modification	Clone	Manufacturer	Cat.No.	Treatment/Staining	Concentration (nM)
Anti-GFP-Nb	GFP	Single domain antibody/ nanobody	C-terminal cysteine	1H1	NanoTag Biotechnologies	N0305	After PFA fixation	25
Anti-ALFA-Nb	ALFA	Single domain antibody/ nanobody	C-terminal cysteine	1G5	NanoTag Biotechnologies	N1505	After PFA fixation	25
Anti-Human IgG-Nb	Human IgG	Single domain antibody/ nanobody	C-terminal cysteine	2F3	NanoTag Biotechnologies	-	After PFA fixation	25
Anti-Human IgG-Nb	Human IgG	Single domain antibody/ nanobody	C-terminal cysteine	2H5	NanoTag Biotechnologies	-	After PFA fixation	25
Obinutuzumab	Human CD20	Human IgG1-defucosylated	ALFA-tag	GA101	Roche Glycart	-	Live	67
Rituximab	Human CD20	Human IgG1	ALFA-tag	Rituximab	Roche Glycart	-	Live	66.7
classical CD20-CD3-TCE	Human CD20, human CD3	Human IgG1, PG-LALA	-		Roche Glycart	-	Live	66.7
inverted CD20-CD3-TCE	Human CD20, human CD3	Human IgG1, PG-LALA	-		Roche Glycart	-	Live	6766.7
Ofatumumab	Human CD20	Human IgG1	-	2F2	Creative Biolabs	PABL-422	Live	66.7
Anti-CD20 (B1)	Human CD20	Mouse IgG2a, lambda	FITC	H299	Beckmann	6602381	Live	66.7
Ocrelizumab	Mouse IgG		-	2H7	eBioscience	14-0209-82	Live	66.7

Supplementary Table 4 | Buffer composition

Buffer name	Buffer composition
100× Trolox	100 mg Trolox, 430 µl 100 % Methanol, 345 µl 1M NaOH in 3.2 ml H_2O
40× PCA	154 mg PCA, 10 ml water and NaOH were mixed and pH was adjusted 9.0
100× PCD	9.3 mg PCD, 13.3 ml of buffer (100 mM Tris-HCl pH 8, 50 mM KCl, 1 mM EDTA, 50 % Glycerol)
Imaging buffer	1× PBS pH 7.4, 1 mM EDTA, 500 mM NaCl, 0.02% Tween; supplemented with 1× Trolox, 1× PCA and 1× PCD
Washing buffer	1× PBS pH 7.4, 0.02% Tween 20
Blocking buffer	1× PBS, 1 mM EDTA, 0.02% Tween-20, 0.05% NaN3, 2% BSA, 0.05 mg/ml sheared salmon sperm DNA
His-Incubation buffer	1xPBS pH 7.2, supplemented with 10 mM imidazole
His-Washing buffer	1xPBS pH 7.2, supplemented with 25 mM imidazole
His-Elution buffer	1xPBS pH 7.2, supplemented with 250 mM imidazole

Supplementary Table 5 | Imaging conditions and clustering parameters

Imager	Imager concentration [pM]	Integration time [ms] 2D	Integration time [ms] 3D	Frames	Clustering radius [nm]	Min number of locs
R1	500 pM	75	100	30000	6	15
R2	500 pM	75	100	30000	6	20
R3	500 pM	75	100	30000	6	15
R4	500 pM	75	100	30000	6	20
L3	500 pM	75	100	30000	6	15
R5	500 pM	100	100	30000	6	15
R6	500 pM	100	100	30000	6	15
L1	1000 pM	75	100	15000	6	15
L4	500 pM	75	100	30000	6	15

7.3 Publication 3

Imaging Ligand-Receptor Interactions at Single-Protein Resolution with DNA-PAINT

Monique Honsa*, **Isabelle Pachmayr***, Larissa Heinze*, Levent Bas, Luciano A. Masullo, Jisoo Kwon, Ana Perovic, Brenda Schulman & Ralf Jungmann. (* equal contribution)

Published in Small Methods

2025

Reprinted from Wiley-VCH GmbH.[102]

RESEARCH ARTICLE

small methods
www.small-methods.com

Imaging Ligand-Receptor Interactions at Single-Protein Resolution with DNA-PAINT

*Monique Honsa, Isabelle Pachmayr, Larissa Heinze, Levent Bas, Luciano A. Masullo, Jisoo Kwon, Ana Perovic, Brenda Schulman, and Ralf Jungmann**

Ligand-receptor interactions are critical for cell communication, with membrane receptors such as the Epidermal Growth Factor Receptor (EGFR) mediating responses to external signals. Super-resolution microscopy techniques in principle allow the visualization of these interactions at single-molecule resolution. While DNA-Points Accumulation for Imaging in Nanoscale Topography (DNA-PAINT) super-resolution microscopy has been successfully used to image receptors, specific labeling of cognate ligands, such as EGF, with DNA has remained challenging. Here, an approach to label and image the small extracellular ligand EGF using site-specific tagging and DNA modification is presented. Functional, site-specifically tagged EGF constructs, including DNA-conjugated and ALFA-tagged EGF, are generated. When compared to the native ligand, only the ALFA-tagged EGF maintains full functionality such as efficient EGFR clustering and internalization, while the DNA-conjugated EGF exhibits reduced EGFR oligomerization. 3D DNA-PAINT imaging of the ALFA-tagged EGF, when bound to EGFR, reveals spatial arrangements of EGF-EGFR complexes and captures different stages of receptor internalization. The labeling approach enables precise visualization of ligand-receptor interactions at high resolution and, in principle, can be extended to other ligand-receptor systems.

1. Introduction

Ligand-receptor interactions play a major role in intercellular communication and decision-making, with membrane receptors acting as key mediators to external signals.[1] Ligands binding to these receptors are the primary source by which cells interpret and respond to their environment. This binding event triggers a cascade of downstream signaling, often regulated by other small proteins, that directs crucial cellular processes such as growth, differentiation, and survival.[1] Understanding these interactions at the molecular level is essential, as ligand-receptor interactions are fundamental for numerous biological functions and disease mechanisms.

To date, quantitatively studying these systems with single-protein resolution is challenging, which limits our ability to fully understand their interactions and downstream effects on signaling pathways. Super-resolution fluorescence microscopy methods allow for sub-20 nm resolution imaging in situ and have enabled novel scientific discoveries in the last 20 years.[2] One way to achieve super-resolution is single-molecule localization microscopy (SMLM).[3–6] In this method, individual and well-separated fluorophores are imaged as they switch on and off stochastically over the sample. The super-resolved image is reconstructed using the positions of each measured fluorophore, which are obtained from fits of their individual images to the point spread function of the microscope. DNA-Points Accumulation for Imaging in Nanoscale Topography (DNA-PAINT) is an SMLM method in which the temporal separation of emitters is achieved by transient binding of dye-labeled imager strands (imager) to complementary DNA-docking strands (binding site) that are immobilized on the targets of interest in the sample.[7,8]

DNA-PAINT has several advantages over other SMLM approaches: 1) since the ON/OFF switching mechanism is decoupled from the photophysics of the fluorescent dye, the brightest fluorophores available can be used, yielding higher signal-to-noise ratio, which in turn leads to improved localization precisions[9] (up to 2–3 nm in cells), 2) repetitive and predictable sampling of the targets is achieved as a virtually unlimited pool of imager strands will transiently bind to the docking sites,[10] 3) unlimited multiplexing can be achieved by using different DNA orthogonal sequences.[11,12] Therefore, DNA-PAINT achieves a high-fidelity, multi-channel, 3D single-protein resolution in whole intact cells (Fields of view ≈100 × 100 μm2). Furthermore, resolution can be extended to the Ångström level by using the recently developed Resolution Enhancement by

M. Honsa, I. Pachmayr, L. Heinze, L. Bas, L. A. Masullo, J. Kwon, A. Perovic, B. Schulman, R. Jungmann
Max Planck Institute of Biochemistry
Am Klopferspitz 18, 82152 Planegg, Germany
E-mail: jungmann@biochem.mpg.de
M. Honsa, L. Heinze, R. Jungmann
Faculty of Physics and Center for Nanoscience
Ludwig Maximilian University
Geschwister-Scholl-Platz 1, 80539 Munich, Germany

The ORCID identification number(s) for the author(s) of this article can be found under https://doi.org/10.1002/smtd.202401799

DOI: 10.1002/smtd.202401799

Sequential Imaging (RESI) method.[13] Given these advantages, DNA-PAINT emerges as one of the methods of choice to directly image and quantify oligomerization and molecular organization of receptors and ligands in situ.

To robustly visualize membrane receptors with DNA-PAINT, efficient labeling of the targets of interest with DNA strands is required. Standard protein labeling approaches for DNA-PAINT include the use of primary antibodies with DNA-labeled secondary probes[14] as well as direct immunolabeling with DNA-conjugated affibodies,[15] aptamers[16] and nanobodies.[9,14] While antibodies are the most widely available labeling reagents, their relatively large size (150 kDa) limits the positional accuracy in DNA-PAINT measurements.[17] Affibodies, aptamers, and nanobodies are smaller, however, they are often not readily available for specific targets of interest. To address this issue in experiments requiring the simultaneous targeting of only a few protein species, one effective approach is to use genetically encoded tags, such as Green Fluorescent Protein (GFP)[18] or the ALFA tag,[19] which have readily available cognate nanobody binders. DNA-PAINT and RESI imaging of membrane receptors at single-protein resolution have successfully been demonstrated in the past.[13]

However, there are currently no optimized methods to specifically label extracellular ligands for efficient DNA-PAINT imaging while preserving their biological function. To demonstrate a universally applicable method for labeling and imaging ligands, we chose the well-known and extensively studied EGF-EGFR ligand-receptor system.[20] EGFR is one of four members of the EGFR receptor family, all of which play a crucial role in regulating cell proliferation, differentiation, and migration.[21,22] Additionally, EGFR family members are often mutated or dysregulated in cancers, such as those affecting the breast, lung, brain, and gastrointestinal tract.[21,22] As a result, drugs that modulate EGFR expression levels or EGFR activation—by targeting the extracellular or intracellular domains, respectively—are utilized in cancer therapy.

On a molecular level, EGFR activation is triggered by EGF-induced structural alterations and the formation of an EGFR-EGFR dimer interface, as shown by X-ray crystallography.[23] This leads to tyrosine autophosphorylation within the EGFR dimer's intracellular kinase domains.[24] Understanding these interactions at the molecular level is crucial not only for basic biological insights into how cells communicate and respond to external signals but also for informing the design of targeted therapies that can more precisely modulate these pathways. Improved molecular-level insights could therefore drive the development of more effective cancer treatments.

To date, direct stochastic optical reconstruction microscopy imaging showed EGF and EGFR co-clustering, with resolution limited to ≈20 nm.[25] Higher spatial resolutions were reached with Fluorescence resonance energy transfer and Fluorophore localization imaging with photobleaching studies of dye-labeled EGF, indirectly measuring ≈12 nm EGF-to-EGF distances in cells.[26,27] However, these approaches do not allow for direct imaging of EGF-to-EGF distances with sub-5 nm resolution and are mostly limited to single-target imaging.[28,29]

Determining the organization of EGF-EGFR in the activated state necessitates multiplexed imaging of both EGFR and EGF at sub-20 nm resolution, as the expected EGF-to-EGF distance when bound to an EGFR dimer is ≈11 nm. With the advancement of sub-5-nm imaging as in RESI, we can now visualize the molecular arrangement of EGF when bound to EGFR in a cellular context, in 3D. This capability promises to deepen our understanding of receptor-ligand interactions with an unparalleled level of detail, potentially paving the way for breakthroughs in therapeutic targeting. However, the imaging of EGF with DNA-PAINT has been limited by a lack of efficient labeling strategies. In this study, we thus developed a functional, site-specifically tagged human EGF ligand with high yields by utilizing two tags that enhance EGF expression and folding. We assess both the functionality and site-specific addressability of these ligands for DNA-PAINT imaging and propose a broadly applicable labeling method for small extracellular ligands.

2. Results

Labeling of EGF ligands for DNA-PAINT imaging has to mainly fulfill two requirements: 1) Conjugated EGF has to exhibit similar functionality (i.e., the ability to induce dimerization, activation, and internalization of EGFR) as native unconjugated EGF and 2) the EGF tag has to be fully accessible for DNA-PAINT imaging. Upon EGF treatment, EGFR oligomerizes, forming higher-order complexes that are crucial for effective signaling and internalization. The EGFR-EGF complex is internalized via vesicle formation (**Figure 1a**). Based on the structure of this EGF-EGFR complex[30] (PDB ID: 3NJP), the C-terminus of EGF is embedded into the binding pocket of EGFR (Figure 1b, inset). Thus, to minimize interference with the functionality of EGF and to maintain the addressability of EGF for subsequent DNA-PAINT imaging, we carried out specific tagging at the N-terminus.

In humans, EGF is first expressed as a single-pass transmembrane protein (pro-EGF), which undergoes proteolytic cleavage at the cell surface to release the mature and active N-terminal ectodomain as soluble EGF.[31] Thus, the correct folding of EGF depends on the expression as a fusion protein. To achieve this, we added the N-terminal B1 domain of *Streptococcal* protein G (GB1) facilitating expression[32] and an N-terminal Glutathione-S-Transferase (GST)-tag, enabling high yield of functional EGF after Tobacco-Etch Virus (TEV) cleavage (Figure 1c; Figure S1, Supporting Information).

We then developed two strategies (Figure 1d) for modifying EGF with DNA: 1) directly labeling EGF with DNA docking strands and 2) using an ALFA tag to which DNA-conjugated nanobodies could bind after incubation in a cellular context. To site-specifically add a DNA docking strand using the first strategy, we chose the Sortase system that allows enzyme-mediated coupling of poly-Glycine-tagged proteins to LPXTG-modified proteins.[33] GGSGGG-EGF (further referred to as GG-EGF) was first functionalized with Azide via an Azide-coupled peptide that could, in turn, be reacted with dibenzocyclooctyne (DBCO)-DNA using copper-independent click chemistry (Figure 1c; Figure S1, Supporting Information). To test the functionality of our site-specifically labeled EGF constructs, we used the human cancer cell line A549, stably expressing EGFR-GFP. After treating with 10 nM unconjugated EGF for 10 min, fixing, and imaging with total internal reflection fluorescence (TIRF) microscopy, we were able to detect EGFR-clustering in the diffraction-limited GFP-channel (Figure S2, Supporting Information). By labeling EGFR

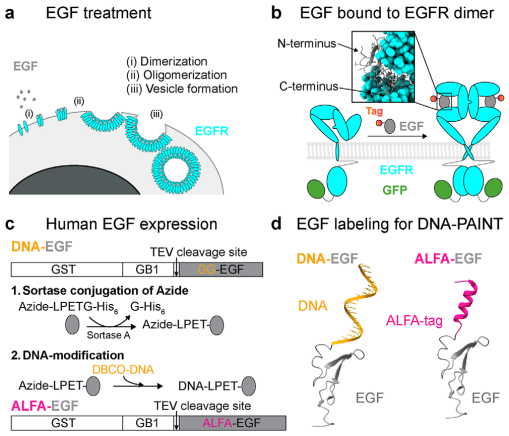

Figure 1. Labeling approaches of EGF. a) EGF treatment promotes receptor clustering through dimerization and oligomerization, eventually resulting in vesicle formation within cells. b) The EGF ligand binds to the EGF receptor (EGFR), inducing EGFR dimerization. Upon binding, the EGF C-terminus faces EGFR and the EGF N-terminus is accessible. EGFR is labeled with an intracellular C-terminal GFP-tag. c) Expression and purification of EGF involve an N-terminal GST-tag for stability and purification and a GB1-tag to enhance yield. For site-specific N-terminal labeling, a glycine-rich sequence (GG) enables Sortase-mediated conjugation of EGF with an azide-modified peptide Azide-LPETGG-HHHHHH. This azide-labeled EGF is subsequently coupled with DBCO-DNA, yielding DNA-EGF. An alternative version, ALFA-EGF, is expressed similarly, incorporating an ALFA-tag immediately upstream of EGF. d) DNA-EGF is directly labeled via a DNA conjugate, while ALFA-EGF features an N-terminal peptide tag, allowing for subsequent labeling with a DNA-linked ALFA nanobody.

with a DNA-conjugated anti-GFP-nanobody and imaging with DNA-PAINT, we measured EGFR clusters with 200–500 nm in diameter (Figure S2, Supporting Information). Similar to unconjugated EGF, both DNA-EGF and ALFA-EGF resulted in the expected EGFR clustering, as shown by diffraction-limited as well as DNA-PAINT imaging (**Figure 2**a–c; Figure S2, Supporting Information). In contrast, no EGFR clustering was detected in untreated cells.

To qualitatively evaluate the functionality and accessibility of the DNA-conjugated EGF and the ALFA-tagged EGF, we performed Exchange-PAINT experiments.[11] The DNA-conjugated EGF was directly measured with DNA-PAINT since it already carries the docking strand. The ALFA-EGF was imaged by incubating DNA-conjugated anti-ALFA-nanobodies on the fixed cell sample. EGFR and EGF were targeted with orthogonal docking strands and image acquisition was carried out using Exchange-PAINT. Since EGF induces oligomerization of EGFR, we assessed the functionality of the DNA-EGF and the ALFA-EGF by comparing their EGF-induced oligomerization of EGFR to cells treated with unconjugated EGF. For this, we determined the nearest neighbor distances (NND) for the different EGFs across multiple cells. Specifically, we analyzed 1) EGFR-EGFR NNDs to evaluate the EGF-induced EGFR oligomerization (Figure 2d–f), 2) EGF-EGFR cross-NND to quantify the accessibility of the EGF and thus the co-localization of EGFR with EGF (Figure 2g,h), and 3) EGF-EGF NND to further confirm the oligomerization behavior (Figure 2i,j). To further quantify the NND histograms, we simulated complete spatial randomness (CSR) of the measured receptor and ligand densities and calculated the area between the experimental NND plots and the CSR curves (Denoted as "Δ area", Figure 2k,l).

The EGFR-EGFR NND analysis revealed that ALFA-tagged EGF induces EGFR clustering behavior similar to that of unconjugated EGF and demonstrates increased co-localization with EGFR. This suggests that the ALFA-tag does not interfere with EGF's binding to the tight binding pocket of EGFR. In contrast, DNA-conjugated EGF showed reduced oligomerization (indicated by a smaller "Δ area"). The EGF-EGFR cross-NND also shows that we detect more co-localization of ALFA-EGF with EGFR compared to DNA-EGF to EGFR. ALFA-EGF led to more EGFR clustering compared to DNA-EGF. This is consistent with the apparent increased oligomerization of EGFR induced by ALFA-EGF, and the specific binding of ALFA-EGF to EGFR (Figure 2c). These findings indicate that DNA-conjugated EGF may not be fully functional, as it shows reduced oligomerization compared to unconjugated EGF and lower co-localization with EGFR. Adding the DNA docking strand to the azide-EGF after fixation led to a high non-specific background (Figure S3, Supporting Information), compromising the accuracy of this approach.

Using ALFA-tagged EGF, we are now able to study the interaction of ligands with their receptors at single-molecule resolution, gaining more insight into the spatial arrangement of EGFR and EGF. In a 3D measurement, we captured specific distinct stages of receptor internalization on one cell (**Figure 3**a). Here, we identified two axial layers (Figure 3b): one corresponding to intracellularly visualized EGFR and the other to extracellularly visualized EGF. The measured distance between these layers was ≈25 nm, aligning well with the thickness of the cell membrane when accounting for tag size and label position. We could observe specific phases of receptor internalization (Figure 3c, d), starting with receptor oligomerization and clustering on the membrane and progressing to fully internalized EGFR-EGF vesicles. These stages are reflected in the EGF-EGF nearest-neighbor distance (NND) histograms. As internalization progresses, the peaks in the EGF-EGF NND histograms shift toward shorter distances, indicating increased proximity.

Notably, we resolved the relative spatial arrangement of EGF and EGFR within these vesicles, with EGF positioned toward the vesicle interior and EGFR oriented outward, aligning with the anticipated internalization process. This ligand labeling protocol for EGF enabled us to directly resolve both ligand-to-ligand and ligand-to-receptor distances in 3D.

3. Conclusion

In this study, we introduced a method for site-specific labeling of the small extracellular ligand EGF, enabling its visualization using multiplexed DNA-PAINT super-resolution microscopy. Our results show that direct conjugation of EGF with DNA reduces its functional ability, partially impairing its capacity to induce EGFR oligomerization compared to the unconjugated ligand. This effect may stem from electrostatic interactions between the negatively charged DNA and EGF, which could hinder the binding or activation of EGFR. Additionally, the DNA-docking strand

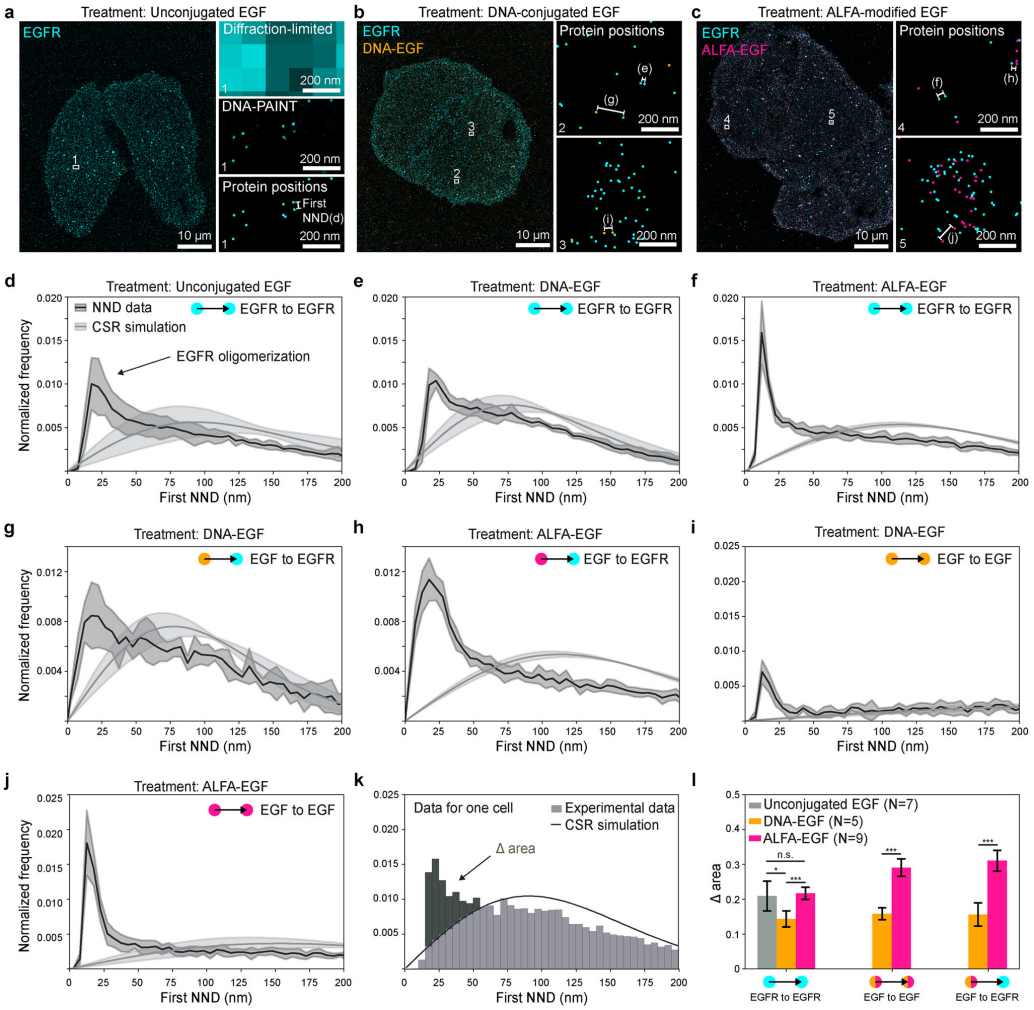

Figure 2. Visualization and functional analysis of DNA-EGF and ALFA-EGF labeling in EGFR-expressing cells. a–c) DNA-PAINT images of A549 cells expressing EGFR-mTagGFP2 treated with (a) unconjugated EGF, (b) DNA-EGF, and (c) ALFA-EGF. Insets show zoomed views of clustered localizations with protein positions determined by the center of mass of each cluster. DNA-EGF (b) shows minimal co-localization with EGFR across areas of varying EGFR density (2 and 3), while ALFA-EGF (c) exhibits a high degree of co-localization with EGFR in both low and high EGFR density regions (4 and 5). d–f) EGFR oligomerization was assessed by measuring the first-nearest neighbor distance (NND) of EGFR positions for cells treated with unconjugated EGF, DNA-EGF, and ALFA-EGF. Solid lines represent the mean NND for each treatment (N = 7 for unconjugated EGF, N = 5 for DNA-EGF, N = 9 for ALFA-EGF), with the shaded areas indicating standard deviation (STD). A completely spatially random (CSR) distribution is overlaid for comparison. g, h) Specific binding of DNA-EGF and ALFA-EGF to EGFR was evaluated through cross-NND measurements from EGF to EGFR positions, with CSR distributions included for reference. i, j) EGF-to-EGF NND histograms reveal a non-random peak for both DNA-EGF and ALFA-EGF compared to CSR, indicating non-random spatial proximity of the labeled EGF molecules. k) Quantitative analysis of binding interactions was performed by calculating the area above the CSR curve in the normalized NND histograms (Δ area) for experimental data. l) Bar plot comparing the mean values of "Δ areas" from the NND histograms in (d–j), highlighting differences in binding and clustering. The EGFR to EGFR NND shows that DNA-EGF promotes lower EGFR oligomerization (Δ area: 0.14 ± 0.02) compared to unconjugated EGF (0.21 ± 0.04), while ALFA-EGF (0.22 ± 0.02) induces a similar extent of EGFR oligomerization as unconjugated EGF. The EGF to EGFR cross-NND indicates higher colocalization for ALFA-EGF (Δ area: 0.31 ± 0.03) than DNA-EGF (0.16 ± 0.03), and EGF to EGF NND analysis demonstrates increased clustering with ALFA-EGF (Δ area: 0.29 ± 0.03) compared to DNA-EGF (0.16 ± 0.02), suggesting superior labeling and binding efficiency for ALFA-EGF. *p*-values were determined with one-sided ANOVA testing (***: $p < 0.001$; **: $p < 0.01$; *: $p < 0.05$; n.s.: $p > 0.05$).

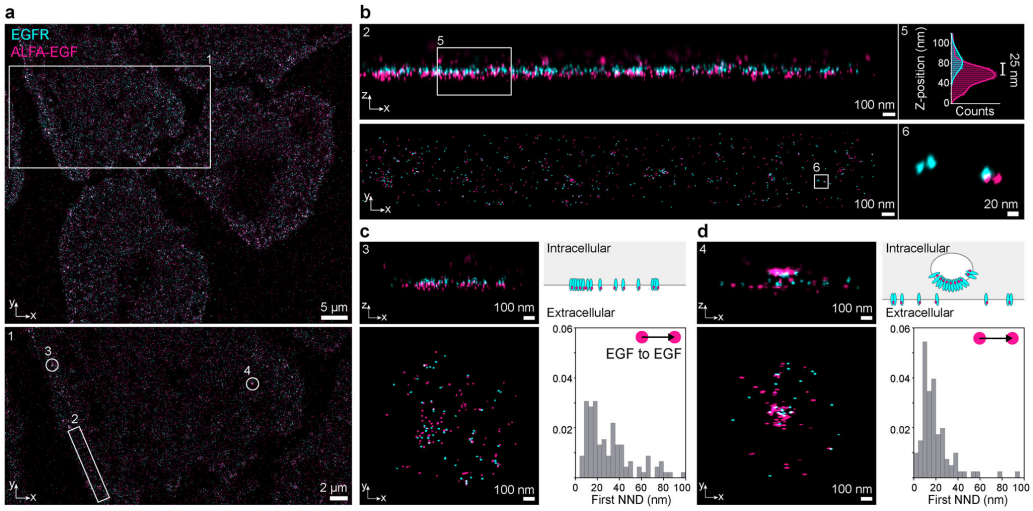

Figure 3. 3D visualization of ALFA-EGF and EGFR interactions in cells. a) 3D DNA-PAINT image of A549 cells, showing EGFR-GFP (cyan) and ALFA-EGF (magenta). The zoomed-in region (1) highlights clusters of EGFR and ALFA-EGF on the cell membrane. b) In a homogeneous cell area (zoom-in of the region (2) from (a, bottom)), the z-x view reveals two distinct layers: intracellularly-GFP-tagged EGFR visualized using GFP-Nanobodies (cyan) and extracellularly bound ALFA-EGF (magenta). A cross-sectional z-position histogram of area (5) shows a peak-to-peak distance of ≈25 nm between EGFR and ALFA-EGF, indicative of their axial spatial separation. c) In regions with EGFR and ALFA-EGF clustering (zoom-in of the region (3) from (a, bottom)), the EGF-to-EGF nearest neighbor distance histogram indicates clustering at short distances. d) In more mature vesicles (zoom-in of region (4) from (a, bottom)), shorter, non-random EGF-to-EGF distances become more prominent, as evidenced by the increased frequency of short NND peaks, suggesting a higher degree of ligand clustering in vesicles.

attached to EGF might become partially inaccessible when the ligand is bound to its receptor. To overcome these limitations, we employed an alternative labeling strategy using the small ALFA-tag, which does not affect EGF function. This approach preserved EGF's ability to induce EGFR oligomerization at wild-type levels (Figure 2). ALFA-EGF can be incubated with living cells to activate EGFR and then targeted with DNA-conjugated anti-ALFA nanobodies after fixation, yielding DNA-docking strands that are accessible for subsequent DNA-PAINT imaging. This novel ligand labeling approach enabled us for the first time to directly visualize the relative spatial arrangements of EGF and EGFR at single-protein resolution using DNA-PAINT. We found a close proximity of ALFA-EGF and EGFR (≈17 nm in 2D), as expected from the X-ray structure (Figure 2). In addition, the specific addressability of ALFA-EGF enabled us to introduce anti-ALFA single-domain antibodies, each labeled with one of three orthogonal DNA sequences, for RESI imaging in 3D. This allowed us to resolve two ALFA-EGFs bound to the same EGFR dimer with a distance of 11 nm, as predicted by the EGF-EGFR structure[30] (PDB ID: 3NJP) (Figure 3). Furthermore, we were able to visualize downstream steps in EGFR signaling by imaging vesicle formation and internalization after EGF-induced activation (Figure 3).

A detailed understanding of EGFR oligomerization upon EGF-mediated activation and their spatial arrangement could guide structure-specific drug design, by disrupting or enhancing oligomerization and thus modulating EGFR signaling.

We developed a general ligand expression strategy utilizing GST- and GB1-tags for high yields and efficient purification and the ALFA tag for efficient detection. Due to its small size of 14 amino acids and its independent folding, it minimally impacts ligand function. Unlike HA or myc tags, the ALFA-tag forms a stable alpha-helix and remains specifically addressable after fixation, making it ideal for super-resolution microscopy. It can be labeled with a high-affinity single-domain antibody (≈40% labeling efficiency in DNA-PAINT).[34] ALFA-tag's versatility allows placement at the N-terminus, C-terminus, or within a protein, enabling broad ligand applications. Beyond super-resolution microscopy, ALFA-tagged ligands can be used for immunoprecipitation, immunoblotting, and in vivo ligand detection.[19] Expanding orthogonal tag-binder pairs will enable multiplexed imaging of different ligands. Taken together, our ligand labeling method is a stepping stone to study – with an unprecedented level of detail – ligand-receptor interactions, offering new insights into complex signaling networks.

4. Experimental Section

Materials: DNA oligonucleotides modified with C3-azide, Cy3B, and DBCO were ordered from Metabion and MWG Eurofins. Sodium chloride (NaCl; 5 M; AM9760G), potassium chloride (KCl; 2 M; AM9640G), calcium chloride ($CaCl_2$; 1 M, 15445389), ultrapure water (10977-035), Tris (1 M, pH 8; AM9855G), ethylenediaminetetraacetic acid (EDTA; 0.5 M, pH 8.0; AM9260G), 1× phosphate-buffered saline (PBS; pH 7.2; 20012–019), 10× PBS (70011051), fetal bovine serum (FBS; 10500-064),

0.05% trypsin–EDTA (25300- 054), Dubecco's modified eagle medium (DMEM; 61965026) and Salmon Sperm DNA (15632011) were purchased from Thermo Fisher Scientific. Human EGF (E9644-.2MG), bovine serum albumin (BSA; A4503-10G), TritonX-100 (93443), and Millipore Millex 33 mm MCE 0.22 µm sterile filter (SLGS033) were ordered from Sigma–Aldrich. Ammonium chloride (NH_4Cl; K298.1) was purchased from Carl Roth. Sodium hydroxide (NaOH; 31627.290) was purchased from VWR. Methanol-free paraformaldehyde (PFA; 15710) was obtained from Electron Microscopy Sciences. Glutaraldehyde (23115.01) was purchased from SERVA. Tween-20 (P9416-50ML), glycerol (65516-500 mL), methanol (32213-2.5L), protocatechuate 3,4-dioxygenase *pseudomonas* (PCD; P8279), 3,4-dihydroxybenzoic acid (PCA; 37580-25G-F), (±)-6-hydroxy-2,5,7,8-tetra-methylchromane-2-carboxylic acid (trolox; 238813–5G), sodium azide (NaN_3; 769320) and A549 EGFR-TagGFP2 cells (CLL 1141) were obtained from Sigma–Aldrich. Ninety-nanometer gold nanoparticles (G-90-100) were ordered from Cytodiagnostics. PureCube 100 Ni-INDIGO Agarose was purchased from Cube Biotech (75103). Anion exchange column RESOURCE Q (17117701) and Glutathione Sepharose 4B (17075605) were obtained from Cytiva. Nanobodies against GFP (clone 1H1, N0305) and against ALFA (N1505) with a single ectopic cysteine at the C-terminus for site-specific conjugation were purchased from Nanotag Biotechnologies. DBCO-PEG4-Maleimide (CLK-A108P) was purchased from Jena Bioscience. Microscope slides were obtained from ibidi (µ-Slides with 8 wells with a glass bottom, 80801).

Buffers: The following buffers were used for sample preparation and imaging:

i) Imaging buffer: 1×PBS, 1 mM EDTA, 500 mM NaCl (pH 7.4), 0.02% Tween; supplemented with 1×Trolox, 1×PCA and 1×PCD, filtered with 0.2 µm filter
ii) Blocking buffer: 1xPBS, 1 mM EDTA, 0.02% Tween-20, 0.05% NaN_3, 2% BSA, 0.05 mg mL^{-1} salmon sperm DNA, filtered with 0.2 µm filter
iii) Quenching buffer: 2 M NH_4Cl in ultrapure water, filtered with 0.2 µm filter

Expression and Purification of EGF: GST-GSGS-GB1-TEV-GG-EGF or GST-GSGS-GB1-TEV-ALFA-GSGS-EGF were expressed in *Escherichia coli* T7 SHuffle Express strain that enables disulfide bridge formation.[35] After expression, cells were harvested and lysed by sonication. The lysate was clarified by centrifugation at 50000 g for 30 mins at 4 °C. For GST Affinity Purification, the clarified lysate was loaded onto a Glutathione Sepharose 4B column equilibrated with Tris-HCl (50 mM, pH 7.5) and NaCl (200 mM). After washing with 10 column volumes (CV) of binding buffer, elution of the GST fusion protein was performed by His-tagged TEV protease-cleavage (1 mg mL^{-1} in 50 mM Tris-HCl, 200 mM NaCl) of GST-GSGS-GB1-tag and overnight incubation at 4 °C. The cleaved protein was further purified using a Superdex 30 Increase GL 10/300 column equilibrated with Tris-HCl (50 mM, pH 7.5) and NaCl (150 mM). Fractions containing the purified GG-EGF or ALFA-EGF were pooled. ALFA-EGF was purified in the same way. Protein samples were analyzed by SDS-PAGE using 4–22% gradient gels under non-reducing conditions.

Sortase Conjugation of GG-EGF: To site-specifically functionalize GG-EGF an Azide-peptide was used. GG-EGF (100 µM) was reacted with the peptide (pep, Azide-LPETGG-HHHHHH) (1 mM), Sortase A (10 µM) in Tris-HCl (50 mM, pH 7.5), NaCl (150 mM), supplemented with $CaCl_2$ (10 mM). The reaction was incubated at 4 °C for 3 h. The conjugated product was purified by passing the mixture through Ni-INDIGO Agarose (200 µL) to remove His-tagged Sortase A and excess peptide.

DBCO-DNA Conjugation of GG-EGF: Azide-EGF was further conjugated with DBCO-7xR3. A reaction mixture of Azide-EGF (40 µM) was incubated with equimolar amounts of DBCO-DNA overnight at 4 °C. The conjugated product was purified using a ResourceQ 5/50 column. Elution was performed using a linear gradient of 0–50% Buffer B (1x PBS, 1 M NaCl, pH 7.4). Fractions containing the 7xR3-EGF conjugate were pooled and concentrated to 250 µL with Amicon Ultra 3 kDA filters (Figure S1, Supporting Information).

PCA, PCD, and Trolox: A 100× Trolox solution was prepared by dissolving Trolox (100 mg) in 100% methanol (430 µL) and NaOH (1 M, 345 µL) in water (3.2 mL). For the 40× PCA solution, PCA (154 mg) was mixed with water (10 mL), and the pH was adjusted to 9.0 using NaOH. The 100× PCD solution was made by dissolving PCD (9.3 mg) in 13.3 mL of buffer containing Tris-HCl (100 mM, pH 8), KCl (50 mM), EDTA (1 mM), and glycerol (50%).

Microscope Setup: Fluorescence imaging was carried out on an inverted microscope (Nikon Instruments, Eclipse Ti2) with the Perfect Focus System, applying an objective-type TIRF configuration equipped with an oil-immersion objective (Nikon Instruments, Apo SR TIRF×100, NA 1.49, Oil). A 560-nm laser (MPB Communications, 1 W) was used for excitation and coupled into the microscope via a Nikon manual TIRF module. The laser beam was passed through a cleanup filter (Chroma Technology, ZET561/10) and coupled into the microscope objective using a beam splitter (Chroma Technology, ZT561rdc). Fluorescence was spectrally filtered with an emission filter (Chroma Technology, ET600/50 m, and ET575lp) and imaged on an sCMOS camera (Hamamatsu Fusion BT) without further magnification, resulting in an effective pixel size of 130 nm (after 2×2 binning). TIR illumination was used for all measurements. The camera's central 1152×1152 pixels (576×576 after binning) were used as the region of interest. Raw microscopy data was acquired using µManager (Version 2.0.1). 3D imaging was performed using a cylindrical lens (Nikon Instruments, N-STORM) in the detection path.

Cell Culture: A549 EGFR-TagGFP2 cells were cultured at 37 °C and 5% CO_2 in DMEM medium supplemented with 10% FBS. Cells were passaged every 2–3 days using trypsin-EDTA. mTagGFP2 was further referred to as GFP.

Nanobody-DNA Conjugation: The anti-GFP nanobody and the anti-ALFA were conjugated to a DBCO-PEG4-Maleimide linker. After removing the unreacted linker with Amicon centrifugal filters (10 000 MWCO), the DBCO-nanobody was conjugated via DBCO-azide click chemistry to one of the DNA docking strands according to Table S1 (Supporting Information).[9]

Cell Sample Preparation: A549 GFP-EGFR cells (10 000 cm^{-2}) were seeded on eight-well high glass-bottom chambers. The next day, the cells were washed 3 times with serum-free DMEM medium and starved for 6h. Afterward, the cells were treated for 10 min with the specifically labeled EGF (10 nM) in a serum-free DMEM medium. The cells were then fixed with pre-warmed methanol-free PFA (4%) in 1xPBS for 15 min. After washing 3 times with 1xPBS, the cells were permeabilized with TritonX-100 (0.125%) in 1xPBS for 2 min. After washing 3 times with 1xPBS, the cells were blocked with blocking buffer at 4 °C overnight. For EGFR-GFP imaging 25 nM DNA-conjugated anti-GFP and anti-ALFA nanobodies in blocking buffer were incubated for 1 h at room temperature (RT), while RESI imaging requires R6 anti-GFP (25 nM) and orthogonally labeled R1-R3 anti-ALFA nanobodies (6.25 nM each) in blocking buffer were incubated overnight at 4 °C (for DNA sequences see Table S1, Supporting Information). The cells were washed 3 times with 1xPBS, post-fixed with PFA (4%) and glutaraldehyde (0.2%) in 1xPBS for 10 min. Then, the cells were quenched with freshly prepared NH_4Cl (200 mM) in 1xPBS from the quenching buffer for 5 min and washed 3 times with 1xPBS. 90 nm gold nanoparticles in 1:1 in 1xPBS were incubated for 5 min at RT. The cells were washed 3 times with 1xPBS

EGFR-GFP Imaging: The samples were imaged in an imaging buffer with 200 pM imager strand (sequences see Table S1, Supporting Information), for 40 000 frames with 100 ms exposure time per frame at 30 mW laser power after the objective, corresponding to a power density of 150 W cm^{-2}.

RESI 3D Imaging: The samples were imaged in an imaging buffer with 200 pM imager strands (for DNA sequences see Table S1, Supporting Information), for 40 000 frames with 100 ms exposure time per frame at 30 mW laser power after the objective, corresponding to a power density of 150 W cm^{-2}. In between every imaging round, the current imager strands were removed by washing the sample with 1xPBS until no blinking events were observed on the microscope.

Statistical Analysis: The raw fluorescence single-molecule localization data were processed for super-resolution reconstruction using the Picasso software package[8] (the latest version is available at https://github.com/jungmannlab/picasso). For this, single molecules were localized in

Picasso using the Gaussian least squares option. The z coordinate of 3D measurements was determined using a 3D calibration file, based on the degree of astigmatism.[36] Drift correction was performed using a redundant cross-correlation method with gold particles serving as fiducials. For measurement with multiple imaging rounds, all resulting channels were aligned with each other. After that, the protein positions were determined with a clustering algorithm for each channel individually. For this, circular clusters of localizations centered around local maxima were identified and grouped. The centers of the localization groups were calculated as a weighted mean, using the squared inverse localization precisions as the weights, as previously described.[13] RESI measurements of the ALFA-EGF were analyzed as described before.[13] The first nearest neighbor distances (NND) of the cluster centers were determined using the Python module Scikit Learn.[37] A set of molecules with complete spatial randomness (CSR) distribution was simulated using a custom Python script. For each dataset, the positions of 5 000 000 molecules were simulated based on the measured protein densities. For the analysis in Figure 2d–j, the normalized NND histograms of the experimental and simulated data (with a bin size of 5 nm) for each EGF were summarized by calculating the average (black line) and standard deviation (grey area) of the bar heights across multiple datasets ($N = 7$ for unconjugated EGF, $N = 5$ for DNA-EGF, $N = 9$ for ALFA-EGF). The binding interactions were estimated for each dataset by the area (Δ area) of the NND histogram that exceeded the CSR simulation. For this, the normalized histograms of both experimental and simulated data were generated using the same bin size. The positive differences between the simulated and experimental data for NNDs from 0 to 200 nm were summed and multiplied by the bin size to obtain the Δ area. The average and standard deviation of Δ areas of multiple cells were then calculated for each EGF and are shown as a bar graph in Figure 2l. To test the difference of the means of the Δ areas for statistical significance, a one-sided ANOVA test was performed with the python package scipy[38] (***: $p < 0.001$; **: $p < 0.01$; *: $p < 0.05$; n.s.: $p > 0.05$).

Supporting Information

Supporting Information is available from the Wiley Online Library or from the author.

Acknowledgements

The authors thank Susanne Reinhardt for her help with the data analysis. The authors thank the MPI peptide facility for Azide-peptide synthesis as well as the MPI protein facility, especially Emilie Song, for ALFA-EGF and Sortase A expression. M.H. and I.P. acknowledged support from the International Max Planck Research School for Molecules of Life (IMPRS-ML). L.A.M. acknowledges a postdoctoral fellowship from the European Union's Horizon 20212022 research and innovation program under Marie Skłodowska-Curie grant agreement no. 101065980. This research was funded in part by the European Research Council through an ERC Consolidator Grant (ReceptorPAINT, grant agreement number 101003275), the BMBF (Project IMAGINE, FKZ: 13N15990), the Volkswagen Foundation through the initiative 'Life?—A Fresh Scientific Approach to the Basic Principles of Life' (grant no. 98198), the Danish National Research Foundation (Centre for Cellular Signal Patterns, DNRF135), the Max Planck Foundation and the Max Planck Society.

Open access funding enabled and organized by Projekt DEAL.

Conflict of Interest

The authors declare no conflict of interest.

Author Contributions

M.H., I.P., and L.H. contributed equally to this work. M.H. designed and analyzed cell experiments, interpreted data, and wrote the manuscript. I.P. designed, performed, and analyzed the conjugation and purification of DNA-EGF and ALFA-EGF, interpreted data, and wrote the manuscript. L.H. performed and analyzed experiments and wrote the manuscript. L.A.M. interpreted data, provided input on the data analysis, and wrote the manuscript. L.B. designed the expression and purification strategy for EGF. J.K. and A.P. prepared samples. B.S. supervised the study. R.J. conceived and supervised the study, interpreted data, and wrote the manuscript. All authors reviewed and approved the manuscript.

Data Availability Statement

The data that support the findings of this study are available from the corresponding author upon reasonable request.

Keywords

DNA-PAINT, EGFR, ligand-receptor interactions, membrane receptors, single-molecule imaging, super-resolution imaging

Received: October 23, 2024
Revised: March 21, 2025
Published online: April 3, 2025

[1] J. Su, Y. Song, Z. Zhu, X. Huang, J. Fan, J. Qiao, F. Mao, *Signal Transduct. Target Ther.* **2024**, *9*, 196.
[2] S. J. Sahl, S. W. Hell, S. Jakobs, *Nat. Rev. Mol. Cell Biol.* **2017**, *18*, 685.
[3] M. J. Rust, M. Bates, X. Zhuang, *Nat. Methods* **2006**, *3*, 793.
[4] S. T. Hess, T. P. Girirajan, M. D. Mason, *Biophys. J.* **2006**, *91*, 4258.
[5] E. Betzig, G. H. Patterson, R. Sougrat, O. W. Lindwasser, S. Olenych, J. S. Bonifacino, M. W. Davidson, J. Lippincott-Schwartz, H. F. Hess, *Science* **2006**, *313*, 1642.
[6] M. Lelek, M. T. Gyparaki, G. Beliu, F. Schueder, J. Griffié, S. Manley, R. Jungmann, M. Sauer, M. Lakadamyali, C. Zimmer, *Nat. Rev. Methods Primers* **2021**, *1*, 39.
[7] R. Jungmann, C. Steinhauer, M. Scheible, A. Kuzyk, P. Tinnefeld, F. C. Simmel, *Nano Lett.* **2010**, *10*, 4756.
[8] J. Schnitzbauer, M. T. Strauss, T. Schlichthaerle, F. Schueder, R. Jungmann, *Nat. Protoc.* **2017**, *12*, 1198.
[9] S. Strauss, R. Jungmann, *Nat. Methods* **2020**, *17*, 789.
[10] R. Jungmann, M. S. Avendaño, M. Dai, J. B. Woehrstein, S. S. Agasti, Z. Feiger, A. Rodal, P. Yin, *Nat. Methods* **2016**, *13*, 439.
[11] R. Jungmann, M. S. Avendaño, J. B. Woehrstein, M. Dai, W. M. Shih, P. Yin, *Nat. Methods* **2014**, *11*, 313.
[12] E. M. Unterauer, S. Shetab Boushehri, K. Jevdokimenko, L. A. Masullo, M. Ganji, S. Sograte-Idrissi, R. Kowalewski, S. Strauss, S. C. M. Reinhardt, A. Perovic, C. Marr, F. Opazo, E. F. Fornasiero, R. Jungmann, *Cell* **2024**, *187*, 1785.
[13] S. C. M. Reinhardt, L. A. Masullo, I. Baudrexel, P. R. Steen, R. Kowalewski, A. S. Eklund, S. Strauss, E. M. Unterauer, T. Schlichthaerle, M. T. Strauss, C. Klein, R. Jungmann, *Nature* **2023**, *617*, 711.
[14] S. S. Agasti, Y. Wang, F. Schueder, A. Sukumar, R. Jungmann, P. Yin, *Chem. Sci.* **2017**, *8*, 3080.
[15] T. Schlichthaerle, A. S. Eklund, F. Schueder, M. T. Strauss, C. Tiede, A. Curd, J. Ries, M. Peckham, D. C. Tomlinson, R. Jungmann, *Angew. Chem. Int. Ed. Engl.* **2018**, *57*, 11060.
[16] S. Strauss, P. C. Nickels, M. T. Strauss, V. Jimenez Sabinina, J. Ellenberg, J. D. Carter, S. Gupta, N. Janjic, R. Jungmann, *Nat. Methods* **2018**, *15*, 685.
[17] M. Ganji, T. Schlichthaerle, A. S. Eklund, S. Strauss, R. Jungmann, *ChemPhysChem* **2021**, *22*, 911.

[18] J. Ries, C. Kaplan, E. Platonova, H. Eghlidi, H. Ewers, *Nat. Methods* **2012**, *9*, 582.
[19] H. Götzke, M. Kilisch, M. Martínez-Carranza, S. Sograte-Idrissi, A. Rajavel, T. Schlichthaerle, N. Engels, R. Jungmann, P. Stenmark, F. Opazo, S. Frey, *Nat. Commun.* **2019**, *10*, 4403.
[20] K. M. Ferguson, *Annu. Rev. Biophys.* **2008**, *37*, 353.
[21] N. E. Hynes, H. A. Lane, *Nat. Rev. Cancer* **2005**, *5*, 341.
[22] S. Halder, S. Basu, S. P. Lall, A. K. Ganti, S. K. Batra, P. Seshacharyulu, *Expert Opin. Ther. Targets* **2023**, *27*, 305.
[23] J. P. Dawson, M. B. Berger, C. Lin, J. Schlessinger, M. A. Lemmon, K. M. Ferguson, *Mol. Cell. Biol.* **2005**, *25*, 7734.
[24] J. H. Bae, J. Schlessinger, *Mol. Cells* **2010**, *29*, 443.
[25] C. C. Valley, D. J. Arndt-Jovin, N. Karedla, M. P. Steinkamp, A. I. Chizhik, W. S. Hlavacek, B. S. Wilson, K. A. Lidke, D. S. Lidke, *Mol. Biol. Cell* **2015**, *26*, 4087.
[26] P. Winckler, L. Lartigue, G. Giannone, F. De Giorgi, F. Ichas, J. Sibarita, B. Lounis, L. Cognet, *Sci. Rep.* **2013**, *3*, 2387.
[27] S. R. Needham, S. K. Roberts, A. Arkhipov, V. P. Mysore, C. J. Tynan, L. C. Zanetti-Domingues, E. T. Kim, V. Losasso, D. Korovesis, M. Hirsch, D. J. Rolfe, D. T. Clarke, M. D. Winn, A. Lajevardipour, A. H. A. Clayton, L. J. Pike, M. Perani, P. J. Parker, Y. Shan, D. E. Shaw, M. L. Martin-Fernandez, *Nat. Commun.* **2016**, *7*, 13307.
[28] J. Ichinose, M. Murata, T. Yanagida, Y. Sako, *Biochem. Biophys. Res. Commun.* **2004**, *324*, 1143.
[29] R. S. Iyer, S. R. Needham, I. Galdadas, B. M. Davis, S. K. Roberts, R. C. H. Man, L. C. Zanetti-Domingues, D. T. Clarke, G. O. Fruhwirth, P. J. Parker, D. J. Rolfe, F. L. Gervasio, M. L. Martin-Fernandez, *Nat. Commun.* **2024**, *15*, 2130.
[30] C. Lu, L. Mi, M. J. Grey, J. Zhu, E. Graef, S. Yokoyama, T. A. Springer, *Mol. Cell. Biol.* **2010**, *30*, 5432.
[31] M. P. Sanderson, P. J. Dempsey, A. J. Dunbar, *Groundwater* **2006**, *24*, 121.
[32] Y. Cheng, D. J. Patel, *Biochem. Biophys. Res. Commun.* **2004**, *317*, 401.
[33] Q. Wu, H. L. Ploegh, M. C. Truttmann, *ACS Chem. Biol.* **2017**, *12*, 664.
[34] J. Hellmeier, S. Strauss, S. Xu, L. A. Masullo, E. M. Unterauer, R. Kowalewski, R. Jungmann, *Nat. Methods* **2024**, *21*, 1702.
[35] J. Lobstein, C. A. Emrich, C. Jeans, M. Faulkner, P. Riggs, M. Berkmen, *Microb. Cell Fact.* **2012**, *11*, 56.
[36] B. Huang, W. Wang, M. Bates, X. Zhuang, *Science* **2008**, *319*, 810.
[37] F. Pedregosa, G. Varoquaux, A. Gramfort, V. Michel, B. Thirion, O. Grisel, M. Blondel, P. Prettenhofer, R. Weiss, V. Dubourg, J. Vanderplas, A. Passos, D. Cournapeau, M. Brucher, M. Perrot, E. Duchesnay, *J. Mach. Learn. Res.* **2011**, *12*, 2825.
[38] P. Virtanen, R. Gommers, T. E. Oliphant, M. Haberland, T. Reddy, D. Cournapeau, E. Burovski, P. Peterson, W. Weckesser, J. Bright, S. J. van der Walt, M. Brett, J. Wilson, K. J. Millman, N. Mayorov, A. R. J. Nelson, E. Jones, R. Kern, E. Larson, C. J. Carey, I. Polat, Y. Feng, E. W. Moore, J. VanderPlas, D. Laxalde, J. Perktold, R. Cimrman, I. Henriksen, E. A. Quintero, C. R. Harris, et al., *Nat. Methods* **2020**, *17*, 261.

WILEY-VCH

Supporting Information

Imaging ligand-receptor interactions at single-protein resolution with DNA-PAINT

*Monique Honsa, Isabelle Pachmayr, Larissa Heinze, Levent Bas, Luciano A. Masullo, Jisoo Kwon, Ana Perovic, Brenda Schulman, Ralf Jungmann**

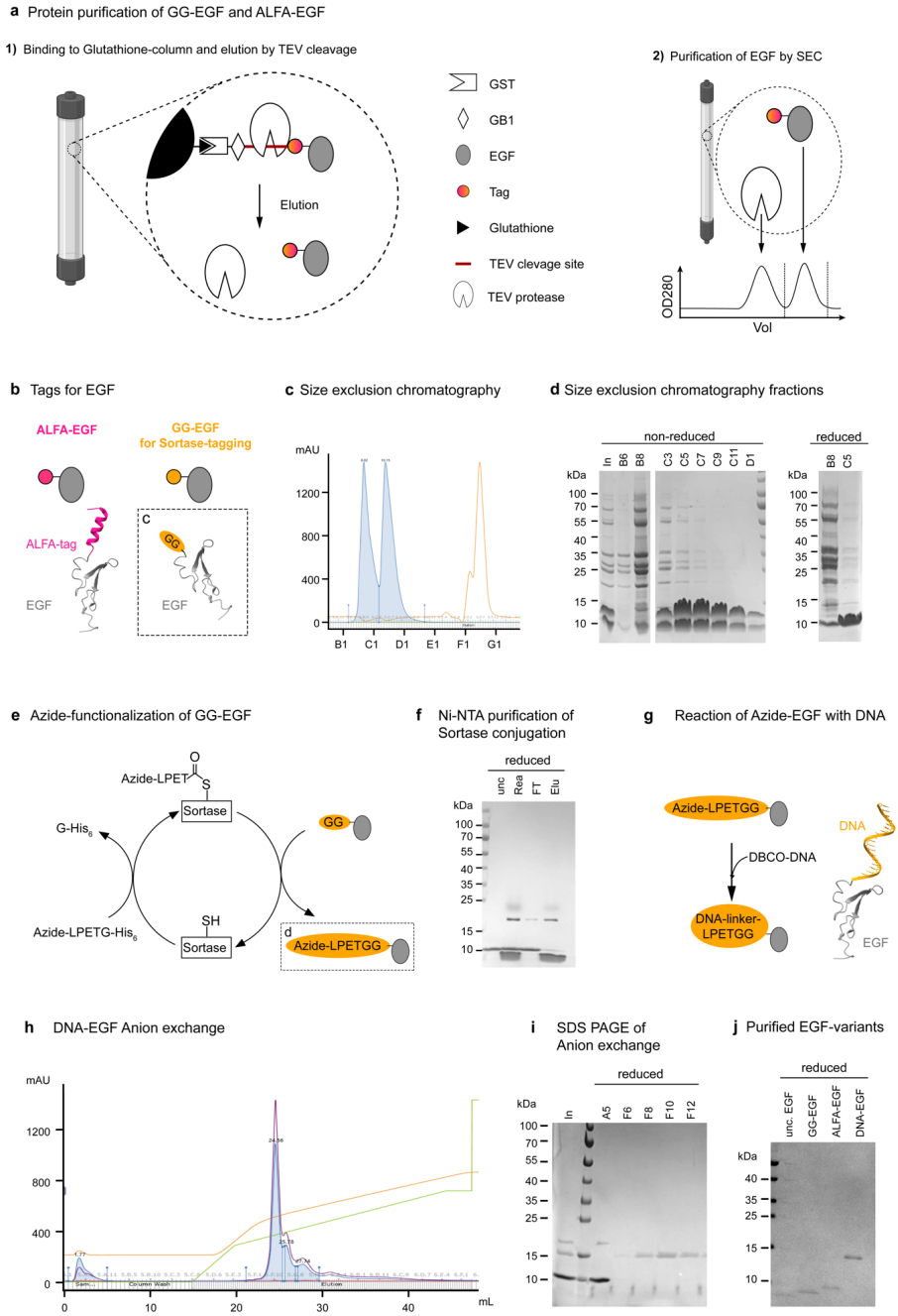
a Protein purification of GG-EGF and ALFA-EGF
1) Binding to Glutathione-column and elution by TEV cleavage
Elution
GST
GB1
EGF
Tag
Glutathione
TEV clevage site
TEV protease
2) Purification of EGF by SEC
OD280
Vol
b Tags for EGF
ALFA-EGF
GG-EGF
for Sortase-tagging
ALFA-tag
EGF
c Size exclusion chromatography
mAU
B1 C1 D1 E1 F1 G1
d Size exclusion chromatography fractions
non-reduced
reduced
kDa
e Azide-functionalization of GG-EGF
Azide-LPET
Sortase
G-His6
GG
Azide-LPETG-His6
SH
Azide-LPETGG
f Ni-NTA purification of Sortase conjugation
reduced
unc
Reac
FT
Elu
g Reaction of Azide-EGF with DNA
Azide-LPETGG
DBCO-DNA
DNA-linker-LPETGG
DNA
EGF
h DNA-EGF Anion exchange
mAU
mL
i SDS PAGE of Anion exchange
reduced
In
A5
F6
F8
F10
F12
j Purified EGF-variants
reduced
unc. EGF
GG-EGF
ALFA-EGF
DNA-EGF

Figure S1 | Purification, tagging, and functionalization of EGF for applications in DNA-PAINT imaging. (a) Purification of glycine-glycine-tagged EGF (GG-EGF) GG-EGF and ALFA-EGF by affinity purification and size exclusion chromatography. The GST-GB1-tag-EGF fusion protein binds to a glutathione column via the GST tag. A Tobacco-Etch Virus (TEV) protease cleavage site in between GB1 and the tag allows for on-column cleavage and elution of tag-EGF (1). Tag-EGF is further purified and separated from the TEV protease using size-exclusion chromatography (2). **(b)** EGF tagging strategies, including ALFA-tagged EGF (ALFA-EGF) and glycine-glycine-tagged EGF (GG-EGF) for sortase-mediated functionalization. **(c)** Size exclusion chromatography (SEC) of GG-EGF after TEV cleavage. Fractions C5-C12 were pooled. **(d)** SEC fractions of GG-EGF were analyzed on an SDS-PAGE gel. There are two bands due to variations in disulfide bridge formation. When analyzing GG-EGF on a reducing SDS-PAGE gel, only one band corresponding to the expected size of EGF is obtained. **(e)** Azide-functionalization of GG-EGF using sortase-mediated ligation, enabling site-specific conjugation of an azide-modified LPETGG peptide. **(f)** Ni-NTA based purification of the Sortase-mediated conjugation of GG-EGF. Unconjugated EGF (unc), the reaction mix (Rea), the flow through (FT, containing DBCO-conjugated EGF) and the Elution (Elu, containing His-tagged Sortase and His-tagged peptide) were analyzed on a reducing SDS-PAGE. **(g)** Bioorthogonal conjugation of Azide-EGF with DNA using a strain-promoted azide-alkyne cycloaddition reaction with Dibenzocyclooctyne (DBCO)-functionalized DNA. **(h)** DNA-conjugated EGF was separated from unconjugated EGF (in the flow-through) by Anion-exchange chromatography. **(i)** Reducing SDS-PAGE of anion exchange chromatography of DNA-EGF. Fractions F6-G1 were pooled. **(j)** Reducing SDS-PAGE of unconjugated EGF, GG-EGF, ALFA-EGF and DNA-EGF.

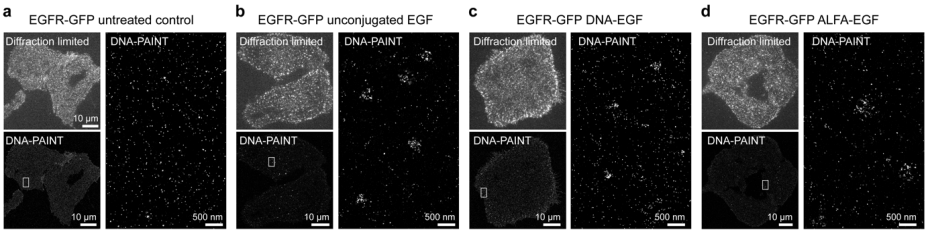

Figure S2 | Diffraction-limited and DNA-PAINT images of EGFR (untreated and EGF-treated). (a) Diffraction-limited and DNA-PAINT imaging of untreated EGFR-GFP shows homogeneous distribution of EGFR with no vesicles. **(b)** Diffraction-limited and DNA-PAINT imaging of EGF-treated EGFR-GFP shows vesicle formation of EGFR with ~500 nm in diameter. **(c)** Diffraction-limited and DNA-PAINT imaging of DNA-EGF-treated EGFR-GFP shows vesicle formation of EGFR with ~300 nm in diameter. **(d)** Diffraction-limited and DNA-PAINT imaging of ALFA-EGF-treated EGFR-GFP shows vesicle formation of EGFR with ~500 nm in diameter.

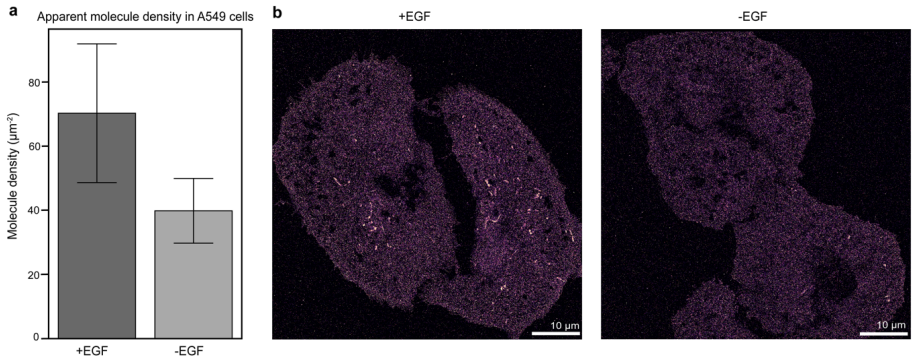

Figure S3 | DNA-PAINT images of DBCO-conjugated DNA chemically linked "clicked" to azide-EGF (untreated and EGF-treated) after cell fixation. (a) Measured DBCO-DNA density on A549 cells with DNA-PAINT under two conditions: Azide-EGF-treated (70 ± 22 μm^{-2}) and untreated (40 ± 10 μm^{-2}). Bars represent the mean and error bars indicate standard deviation (STD). N=8 (for each condition). **(b)** Representative DNA-PAINT images of the azide-EGF treated and untreated cases showing clear localizations in both, which indicates nonspecific binding of the DBCO-DNA to the cell. For the measurements, the cells were seeded, starved in serum- free medium for 6 h and then, depending on the condition, treated with 10 nM azide-EGF for 10 min. The cells were then fixed with 4% PFA for 15 min, permeabilized with 0.125% Triton-X for 2 min and blocked with an azide-free blocking buffer overnight at 4°C. DBCO click chemistry was performed by incubating 1µM DBCO-conjugated DNA on the sample for 3 hr at RT.

Supplementary Table S1 | Strand sequence of docking strands and imagers.

Sequence name	Docking site strand sequence (5' to 3')	Imager strand sequence (5' to 3')
R1	TCCTCCTCCTCCTCCTCCT	AGGAGGA-Cy3B
R2	ACCACCACCACCACCACCA	GGTGGT-Cy3B
R3	CTCTCTCTCTCTCTCTCTC	GAGAGAG-Cy3B
R4	ACACACACACACACACACA	GTGTGT-Cy3B
R5	CTTCTTCTTCTTCTTCTTC	GAAGAAG-Cy3B
R6	AACAACAACAACAACAACAA	TGTTGTT-Cy3B